Quantitative Methods in High Field MRI

by

Olivier Mougin

Thesis submitted to The University of Nottingham

for the degree of Doctor of Philosophy

August 2010

CONTENTS

Contents

Contents

Contents

Contents

ABSTRACT

The increased signal-to-noise ratio available at high magnetic field makes possible the acquisition of clinically useful MR images either at higher resolution or for quantitative methods. The work in this thesis is focused on the development of quantitative imaging methods used to overcome difficulties due to high field MRI systems (> 3T). The protocols developed and presented here have been tested on various studies aiming at discriminating tissues based on their NMR properties.

The quantities of interest in this thesis are the longitudinal relaxation time T_1, as well as the magnetization transfer process, particularly the chemical exchange phenomenon involving amide protons which is highlighted particularly well at 7T under specific conditions. Both quantities (T_1 and amide proton transfer) are related to the underlying structure of the tissues *in-vivo*, especially inside the white matter of the brain. While a standard weighted image at high resolution can provide indices of the extent of the pathology, a robust measure of the NMR properties of brain tissues can detect earlier abnormalities.

A method based on a 3D Turbo FLASH readout and measuring reliably the T_1 *in-vivo* for clinical studies at 7T is first presented. The other major part of this thesis presents magnetization transfer and chemical exchange phenomena. First a quantitative method is investigated at 7T, leading to a new model for exchange as well as contrast optimization possibility for imaging. Results using those methods are presented and applied in clinical setting, the main focus being to image reliably the brain of both healthy subjects and Multiple Sclerosis patients to look at myelin structures.

ACKNOWLEDGEMENT

INTRODUCTION

Since its introduction into clinical imaging, Magnetic Resonance Imaging (MRI) has proven to be a valuable tool for diagnosis, due to its ability to distinguish pathological tissue (such as a brain tumor) from healthy tissue. Not only is its harmless radiation in the radio-frequency range advantageous compared to ionizing radiation used in X-rays or Computed Tomography (CT) modalities, but it also provides remarkable contrast in the soft tissues, such as the kidney, the liver and the brain. The advent of Ultra-high field magnets, such as the 7T scanner installed in Nottingham allows imaging at a sub-millimetric scale due to the increased Signal to Noise Ratio (SNR) and provide remarkable and new contrasts particularly suitable for human neuroimaging.

While higher quality images can be produced with higher field strength scanners, clinical diagnosis stays subjective to the radiographer experience. By using quantitative imaging, it is possible to compare unbiased measures, to derive statistics out of clinical trial data set, in brief to obtain objective biomarkers sensible to minute changes in the imaged tissues. Moreover, it is necessary to quantify first specific magnetic properties of the brain tissues at high field in order to produce qualitative images of clinical use. This thesis presents the design, experiment and validation at high field of two of the most useful MR modalities in clinical settings, namely the longitudinal relaxation time (T_1) and the magnetization transfer ratio (MTR). Acquisition of high resolution images and derivation of quantitative maps, both for healthy subjects and patients, is presented here using methods especially designed for high magnetic field applications.

Chapters 1 and 2 provide a theoretical overview of the Nuclear Magnetic Resonance (NMR) phenomenon and Magnetic Resonance Imaging (MRI), describing the theory and the versatility of

1

this imaging modality. A basic overview of the fundamental theory behind MR quantities, such as relaxation times and magnetization transfer, is given in chapter 1, together with specificities of neuroimaging at high field. Chapter 2 then describes the basic pulse sequences used to reflect these MR quantities and presents an overview of the instrumentation used for image acquisition, focusing particularly on the Philips Achieva 7T system installed in the SPMMRC.

Chapter 3 presents the different methods used to map the relaxation time T_1, before describing the sequence implemented used to map and investigate the T_1 in the human brain at 7T. The signal model, the fitting procedure as well as the robustness of the quantification process is then evaluated and validated via comparison experiments, before being used for studies of diverse purposes, both in healthy subjects and patients.

Chapter 4 is focused on detecting and quantifying the Chemical Exchange Saturation Transfer (CEST), a Magnetization Transfer effect visible *in vivo* particularly at high field. The CEST effect coming from amide protons is particularly pronounced at 7T. Modelling of these MT effects based on a 3 compartment exchange is presented. Quantification is performed on phantoms (composed of exchangeable creatine protons) and in the white matter of volunteers.

Chapter 5 utilizes the results of the previous chapter to present the optimization of a Magnetization Transfer protocol producing high resolution MTR maps at 7T. After a presentation of the utility of a MT protocol at high field, the three-pool model described in chapter 4 is used to optimize the contrast obtainable *in vivo*. Robustness to inhomogeneities, minimization of contrast attenuation due to image acquisition as well as optimization of the final image quality via a specifically designed simulator is then presented. The chapter concludes with a range of applications of the designed protocol, as the detection of the stria of Gennari as well as visualisation of abnormalities in the cortex of multiple sclerosis patients, in preparation of clinical trials.

The conclusion chapter contains a brief summary of the results obtained and details the key findings of the work. Possible future directions for the project are also presented along with suggestions for applications of the work in different clinical settings.

SOURCE OF SIGNAL IN NMR

Nuclear Magnetic Resonance (NMR) is based on the independent discovery by Bloch and Purcell in 1946 of method of measuring the spin angular momentum of the nucleus and explaining its interaction with an external magnetic field. This discovery, awarded a shared Nobel Prize in 1952, has led to numerous applications in chemistry, and has the potential for studying the molecular structure of crystals and other materials. The absorption of radio frequency (RF) from such spin systems, as well as its interaction with both external and intrinsic fields, makes the detection of the resultant magnetic field a useful tool for non-invasive investigation of structures. The advance of NMR has moved to the exploration of more complex structures such as living tissues, and is nowadays applied in the clinics thanks to its potential to image the body at a millimetric scale. This chapter presents the basic NMR principles necessary to form the framework of this thesis. The origins of nuclear magnetisation are briefly discussed and the behaviour of a sample under an applied magnetic field is described. Using the spins as a source of contrast in imaging is then described and an introduction to magnetic resonance imaging at ultra-high field (7T) is given.

1.1 NMR: from the quantum theory to a classical description

The NMR effect arises from interaction between the angular momentum of a nucleus with an external magnetic field and so it is strictly a quantum phenomenon. The evolution of a single spin can be predicted by quantum mechanics, but becomes cumbersome as the number of spins in the system increases. The following section describes the quantum model before introducing the MR

phenomenon with the classical approach.

1.1.1 Nuclei, spins and angular momentum

An elementary particle possesses a variety of properties such as mass or charge, another being its intrinsic angular momentum, also known as spin. Electrons, protons and neutrons all possess spin, which is quantized and may be positive or negative, depending on its rotational direction. The spin angular momentum p of a particle is quantized and is related to the spin quantum number I by $p = \hbar\sqrt{I(I+1)}$, where $\hbar$ is Planck's constant divided by 2π and I may take half integer or integer value. An hydrogen atom consists of an electron orbiting a single proton, with I taking a value of $+1/2$ for the proton. The measurable values of the z-component of the angular momentum are given by $p_z = m_z \hbar$, where m_z is a quantum number with the following possible values $-I, -I + 1, \ldots, +I$. In the case of the proton, m_z can take the values $1/2$ and $-1/2$.

Moving charges generate a magnetic field. A nuclear spin with angular moment $\mathbf{p}$ is thus associated with a nuclear magnetic moment

$$\boldsymbol{\mu} = \gamma \mathbf{p} \tag{1.1}$$

where γ is the gyromagnetic ratio, a nucleus dependent constant. The behaviour of this magnetic moment under a magnetic field is the basis of the nuclear magnetic resonance phenomenon. For ^1H, the gyromagnetic ratio is $\gamma = 267.510^6 \text{rad}.s^{-1}.T^{-1}$. Most nuclei are however NMR insensitive, as it requires an odd number of protons and/or neutrons to create a nonzero spin. Nuclei present in the body with nonzero spins are ^{13}C, ^{15}N and ^{23}Na, with the most abundant being the isotope ^{1}H. Since all experiments in this thesis are based on ^{1}H NMR, this is the only nucleus that will be discussed in detail.

The rotational energy of a molecule is proportional to the square of the total angular momentum, and so the energy is also quantized. In the absence of an external magnetic field, the $2I + 1$ possible states of the spins are degenerate; they all possess the same energy. If the nuclei are placed inside an external magnetic field, the energy levels diverge for the $2I + 1$ states, due to a different interaction of the magnetic field determined by the quantum number of the spin. This energy splitting due to the

presence of an external magnetic field is called the Zeeman effect.

1.1.2   Predicting the energy of a system: the Boltzmann statistics

Considering all hydrogen nuclei situated inside a drop of water, each of the magnetic moments will point in a different direction, transferring energy between each other by random interaction, producing zero net magnetisation. In NMR, the numerous spins in a material cannot be considered individually, so only the net magnetisation is generally analysed. After placing this water droplet in a magnetic field for a time long enough so it has reached its thermal equilibrium, the bulk (or net) magnetisation of the sample is then given by the sum of magnetic moments of all the nuclei it contains, as shown in fig. 1.1. By convention the magnetic field applied in MRI is along the z-axis: $\mathbf{B_0} = B_0\hat{\mathbf{z}}$. The component of the magnetic moment parallel to the magnetic field is then: $\mu_z = \gamma\hbar m_z$. If N_s is the total number of spins in the system, the bulk magnetisation is then described by

$$\mathbf{M} = \sum_{n=1}^{N_s} \mu_{z,n}\hat{\mathbf{z}}.$$ (1.2)

For the hydrogen atom, only two possible energy states are possible for the z-component: $E = -\boldsymbol{\mu}\mathbf{B} = \gamma\hbar m_z B_0$, *i.e.* the spin orientation of the ^1H nucleus placed inside a magnetic field $\mathbf{B_0}$ will either align with or against the direction of the field, depending on the energy it has. The water droplet considered here possesses an ensemble of spins, some in the lower energy state $|\uparrow>$, some in the higher energy state $|\downarrow>$, while the rest is a superposition of the states $|\uparrow>$ and $|\downarrow>$. The energy difference from both states is proportional to the magnitude of the external magnetic field B_0:

$$\Delta E = \gamma\hbar B_0$$ (1.3)

The presence of an external field leads to a difference in spin population in each state, as presented in the fig. 1.1, with a preference of the spins for the lower energy eigenstate, *i.e.* the parallel or up state. This population difference however is very small and can be derived via the Boltzmann distribution:

$$\frac{N\uparrow}{N\downarrow} = \exp\left(\frac{\Delta E}{k_B T_s}\right)$$ (1.4)

5

1.1. NMR: from the quantum theory to a classical description
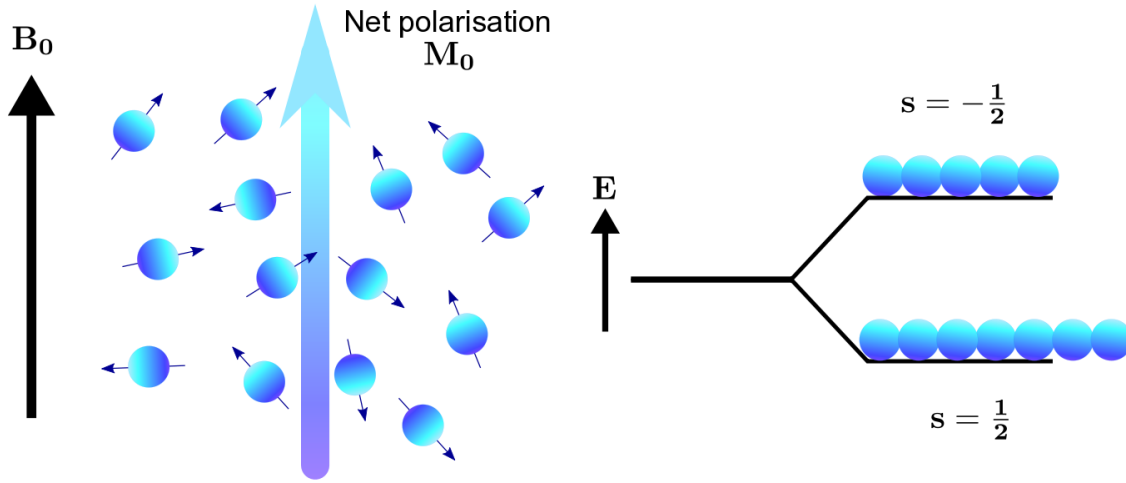
Figure 1.1: Bulk magnetisation of a spin system placed in an external magnetic field $\mathbf{B_0}$. At thermal equilibrium, the net polarisation is aligned with the field (the degree of polarisation is greatly exaggerated here). The Zeeman energy levels are represented on the right, with only two positions possible for these eigenstates.

where $N \uparrow$ and $N \downarrow$ are the number of spins whose z-component is aligned with and against the applied field, T_s is the temperature of the spin system and k_B is the Boltzmann constant. For hydrogen nuclei at 300 K and a 1 T magnetic field, the population difference is approximately 6 part per million (ppm). This relatively small difference can be increased, either with lower temperature (not realistic for clinical *in vivo* experiment) or with higher magnetic field. The low sensitivity of the technique, due to small detectability of the signal produced by a single proton, as well as the small difference between the two states, is counteracted by the huge amount of protons available in biological tissues, of the order of 10^{22} protons per cm^3 of living tissue.

This difference in population due to the static magnetic field induces the net magnetisation called the equilibrium magnetisation M_0. This magnetisation is proportional to the difference in the number of nuclei aligned with or against the field, and gives

$$M_0 = \frac{\gamma^2 \hbar^2 B_0 N_s}{4 k_B T_s}. \tag{1.5}$$

When looking at a spin placed in a magnetic field, the amplitude of nuclear magnetic moment μ is larger than the magnetic moment considered solely in the z-direction. It implies that the nuclear magnetic moment does not align exactly with $\mathbf{B_0}$, and rather precesses about $\mathbf{B_0}$ at a frequency ω_0

1.1. NMR: from the quantum theory to a classical description

called the Larmor frequency, giving the Larmor equation:

$$\omega_0 = \gamma B_0. \tag{1.6}$$

The resonant frequency of the system is determined by the energy gap between the up and down states (1.3) which, combined with Planck's law $E = \hbar\omega$ yields the resonant Larmor frequency $\omega_0 = -\gamma B_0$. By applying a radio-frequency magnetic field with an energy equal to the difference between the two states (1.3), *i.e.* the energy level splitting, a transition between the two eigenstates $|N \uparrow>$ and $|N \downarrow>$ is induced, with the absorption of a photon of energy $\Delta E = \hbar\gamma B_0$. This radio-frequency wave also makes the spin ensemble coherent, inducing a relative alignment of the phase of the spins. While the quantum mechanical theory is the only way to describe fully the evolution of a spin system, a classical approach describing the bulk magnetisation at a macroscopic scale is surprisingly effective, and intuitively easier to follow. For example, the Larmor equation can be equally demonstrated via a classical approach.

Classically, a magnetic moment $\mathbf{M}$ placed in a external magnetic field $\mathbf{B}$ experiences a torque $\mathbf{L}$, inducing a rotation proportional to the change in angular momentum:

$$\mathbf{L} = \mathbf{M} \times \mathbf{B} = \frac{d\mathbf{P}}{dt} \tag{1.7}$$

which, after substituting 1.1 into 1.7 leads to the Bloch equation [2]

$$\frac{d\mathbf{M}}{dt} = \gamma\mathbf{M} \times \mathbf{B}. \tag{1.8}$$

This states that when pushed out of alignment with the main magnetic field $\mathbf{B}$, the magnetisation $\mathbf{M}$ precesses about $\mathbf{B}$. With a stronger magnetic field, the rotation of the angular momentum around the magnetic field increases linearly with the main magnetic field B_0 following equation 1.6, also increasing the available M_0 (dependent on the magnetic field strength, as shown in equation 1.5). It is possible to derive the same equilibrium magnetisation M_0 from both approaches by using Boltzmann statistics/distribution for the classical/quantum approach (see [13, 12] for more details). The classical approach is generally employed to describe the evolution of the magnetisation $\mathbf{M}$, as it is the most

intuitive way to explain the macroscopic observations made via MRI.

1.1.3 Rotation via radiofrequency pulses

By applying a second magnetic field $\mathbf{B_1}$ to the sample, the spins now precess about the combined magnetic field axis. When the oscillating $\mathbf{B_1}(t)$ magnetic field is switched off, a signal emanating from the nuclei of the sample can be recorded. Although the amplitude B_1 of the radio-frequency (RF) pulse is very small compared with the main magnetic field B_0, this RF field is resonant with the precession of the spins and causes the phase of the spins to align, creating a sort of spiralling motion of the spin polarization (fig. 1.2.a.), also called nutation. To simplify the visualization of the NMR experiment, it is common to consider a reference frame rotating at the Larmor frequency about the z-axis. The new frame of reference is denoted (x', y', z) and is called the rotating frame. In this rotating frame of reference, $\mathbf{B_1}$ appears stationary, and $\mathbf{B_0}$ transforms to zero. The magnetisation vector $\mathbf{M}$ appears to tip around $\mathbf{B_1}$ from its equilibrium position toward the y'-axis (fig. 1.2.b.). The angle α by which the magnetisation is tipped around the x'-axis depends on the amplitude and the duration of the applied B_1 field:

$$\alpha = \int_0^{\tau} \gamma B_1(t) dt \tag{1.9}$$

where τ is the time the RF pulse is applied. A 90° pulse flips the magnetisation $\mathbf{M}$ entirely into the $x'y'$ plane and a 180° pulse inverts the bulk magnetisation. With an RF pulse, it is also possible to saturate the magnetisation, by destroying completely but temporarily $\mathbf{M}$. In fact, with a sufficiently long RF irradiation, the spin system settles into a steady-state value which equalizes the superposition of the two states and thus nulling the net magnetization, inducing the saturation. This state is dependent on the return to equilibrium from the spins, and the competing effect of irradiation with relaxation.

1.2 Signal acquisition methods

The signal recorded during an NMR experiment comes mainly from protons of water molecules (as it is the prominent species inside the sample). However an ensemble of spins such as a water droplet placed in a magnetic field that has reached its thermal equilibrium is silent and does not create
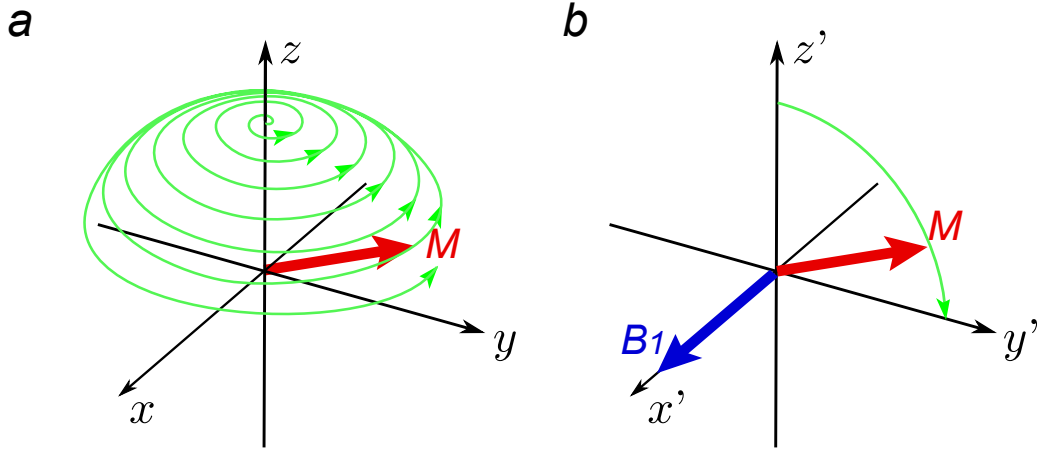
Figure 1.2: The evolution of the bulk magnetisation vector $\mathbf{M}$ under the application of an RF pulse $\mathbf{B_1}$ at the resonant frequency ω_0 in (a) the laboratory and (b) the rotating frame.

any signal to record. Using a RF pulse to excite the spins will create a signal dependant of the position and the NMR properties of each spin. Spins having the same properties and spatially restricted to a small volume can be modelled as isochromats, providing one magnetization vector for this ensemble of spins. Record of the signal coming out of a volume can be considered as a classical manner considering these isochromats instead of the spins. The next section review the principles necessary to obtain a signal during an NMR experiment.

1.2.1 Principle of the Free Induction Decay (FID)

The most basic NMR experiment is the generation of a Free Induction Decay (FID) signal. A sample placed in an uniform magnetic field B_0 reaches its thermal equilibrium before being excited via a transmitter coil at the Larmor frequency. This causes the magnetization of each isochromat to be tipped into the transverse plane. After switching off the radio-frequency pulse, a voltage can be detected on the receiver coil via Faraday induction. The result is an exponentially decaying signal at the resonant frequency, with the rate of the decay dependent on the T_2^* of the sample. This gives information about the environment of the spins, and is at the base of all NMR experiments. At the start of the FID the spins (or isochromats) are in phase (coherent); this coherence is lost due to the relaxation processes described in the next section and the signal decays in amplitude. However it is often difficult to read the early part of the FID since it is necessary to gate the receiver off during RF

transmission.

1.2.2 Principle of echo

Two types of rephasing methods are used routinely in MRI to produce echoes; gradient echos (GE) are formed using a linear gradient and spin echos (SE) are formed using refocusing pulses. Hahn in 1950 was the first to study the echoes [11], and observed that a constructive interference of the spins recreated a FID (*i.e.* the spins refocuses) after applying two consecutive 90° RF pulses. The first RF excitation pulse tips the magnetization towards the xy-plane, before the spins dephase naturally, causing the detectable signal to decay. For spin echo imaging, an 180° pulse is typically applied on the y-axis at a time τ after the 90° excitation pulse. The refocusing pulse flips the spins about the y-axis, reversing the sign of the phase shift. At a time 2τ from the excitation pulse the phase shift of the spins is zero and an echo is formed (fig. 1.3).
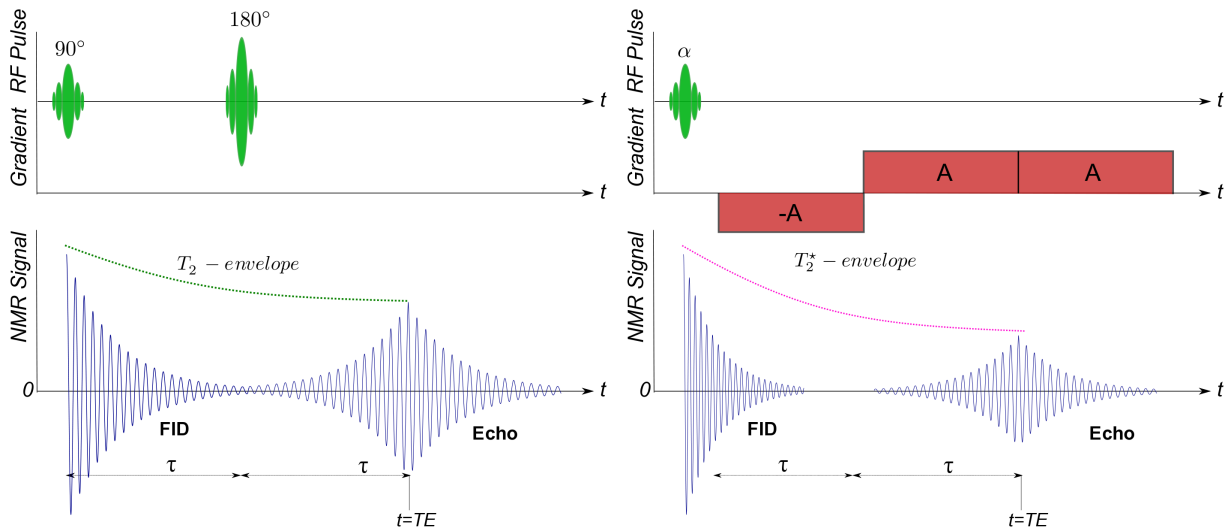
Figure 1.3: A spin echo sequence (left), together with a gradient echo sequence (right). The evolution of the magnetization is presented to show the effect of the refocusing, either created by the gradient, or the refocusing pulse.

The spins accumulate phase at different rates depending on their locations in the gradient field. A gradient echo is formed by applying a series of linear field gradients across the sample. After an RF pulse of angle θ, a negative gradient is applied, which causes spins to precess at different rates at different positions across the sample. The spins will suffer additional dephasing in relation with the

time τ the gradient has been applied for. Applying the same gradient with an opposite polarity reverses the direction of phase accumulation of the spins: rapidly dephasing spins come back into phase with slowly dephasing spins. The spins rephase and create an echo with a peak at a time $t = TE$ after the polarity of the gradient reverses (where the area under the positive gradient lobe equals the area under the negative gradient lobe), as illustrated in fig. 1.3. The echo contains frequency information about the spins, as well as phase coherency of the signal. As indicated in fig. 1.3, the echoes are attenuated by T_2 and T_2^*, two relaxation times that will be discussed below.

1.2.3 Chemical shift

The theory described here is for spins resonating at the Larmor frequency, experiencing subtle variation in the field due to neighbour tumbling molecules or small inhomogeneity of the main magnetic field strength. Another source of change of resonance frequency is the chemical shift, due to varying degree of electronic shielding of the nuclei depending on its environment. Spins resonating slightly off-resonance can create artefacts inside the echo, possibility misplacing the spins, but this off-resonance effect can also provide information about the chemical environment of the spins. In NMR spectroscopy techniques, information about the chemical environment of the nuclei in the sample is extracted from a single FID. The FID is Fourier transformed and the frequency spectrum analysed. Since the electronic shielding varies with the chemical environment, the variation of frequencies provides useful information, and forms the basis of NMR spectroscopy. In MRI such a range of precessional frequencies produces chemical shift artefacts, but can also be used to provide magnetization transfer contrast.

1.3 Spin interactions: source of NMR contrast

The flexibility of the spin dynamics in NMR provides a large variety of mechanisms to manipulate the image contrast. The diversity in water binding inside the different human body tissues makes them distinctive with NMR imaging, as the spins evolve differently depending on their environment, making NMR an useful tool to image the human body non invasively. In MRI, soft tissues such as

the brain yield particularly good signal due to their high concentration in water and proteins. The first factor defining signal is the spin density throughout the object, however the flexibility in proton spin density contrast between tissues in the body is low, making the acquisition time long, so other sources of contrast based on the variation of T_1, T_2 and $T_2^\star$ values are usually employed. Relaxation time weighted images are proton density images which have also been weighted by the rate of a relaxation time. The diverse MRI contrasts, which can be obtained by careful choice of imaging parameters, are reviewed hereafter.

Proton Density (PD)   When placed in a strong magnetic field, the spins precess along their polarization axis, producing a stable net magnetisation M_0 at thermal equilibrium. By manipulating this magnetization correctly, it is possible to measure the signal originating only from the spins of hydrogen nuclei resonating inside a region of interest. This concentration measure is thus called Proton Density (**PD**), as it shows only the amount of protons inside a volume of interest, such as a voxel. All imaging facilities are sensitive to **PD**, as half the number of protons inside a volume would only create half the signal. In human tissues, the proton density is very similar across tissues, apart from the Cerebro-Spinal Fluid (CSF), which is composed almost exclusively of water and thus very bright on **PD**-weighted images. Although the **PD** contrast is the primary source of contrast, **PD** changes often correlate closely with T_1 changes. Whilst protons (on a water molecule, bound to lipid complexes or in a mixed state) generally diffuse or exchange between the different states, this does not affect the overall density of protons. Other measures are necessary to display the dynamic of the spins.

1.3.1   Relaxation as a source of contrast

At equilibrium the spin system has a random phase and a spin population conforming to Boltzmann statistics, with the macroscopic nuclear magnetization M_0 along the direction of the external field, i.e. the z-axis. When the spins are disturbed from their equilibrium states by an RF pulse, the new magnetization $\mathbf{M}$ is flipped away from its alignment with the field $\mathbf{B_0}$. The bulk magnetization will subsequently tend to relax back to its equilibrium state, after the switch off of the RF pulse. The relevant time constants characterizing the relaxation phenomena are the principal source of contrast used in MRI.

1.3. Spin interactions: source of NMR contrast

1.3.1.1 Longitudinal relaxation time (T_1)

The recovery of the net magnetisation M_0 towards the z-axis involves an exchange of energy between the spin system and the surrounding thermal reservoir, defined historically as the 'lattice'. As the recovery of the magnetisation towards the longitudinal axis is not instantaneous, this phenomenon is characterized by the longitudinal relaxation time T_1, also called spin-lattice relaxation time. In the absence of any other effects, this recovery is described by the Bloch equation:

$$\frac{dM_z(t)}{dt} = \frac{M_0 - M_z(t)}{T_1} \tag{1.10}$$
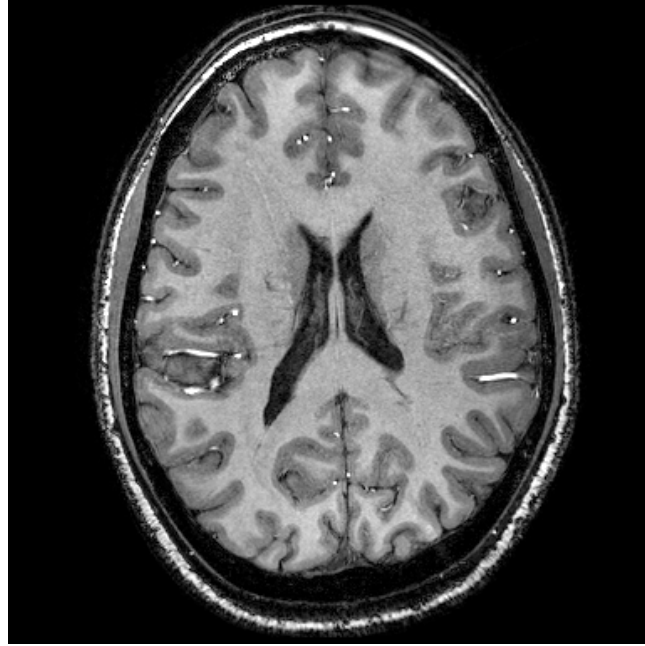
Figure 1.4: T_1-weighted image acquired with the MPRAGE sequence at an inversion time of 1.3s

The recovery is caused by the fluctuating magnetic fields arising largely from the motion of molecules in the neighbourhood of the magnetic moments (dipole-dipole interactions). The rate at which the energy is lost indicates how closely the spins are coupled to the lattice. Therefore the T_1 recovery rate can tell us about the mobility of the molecules (particularly water molecules) and hence the binding of those molecules to macromolecules, *e.g.* lipid molecules, large proteins or cells membranes. This is the cause of the T_1 contrast between the brain tissues: macromolecules such as myelin cause the protons in white matter to have a shorter T_1 than the grey matter, making it brighter

on a T_1-weighted image as shown in fig. 1.4. The Cerebro-Spinal Fluid (CSF), mainly composed of free water, has thus a much longer T_1 than grey or white matter. Other factors which can affect the T_1 of tissue are the magnetic field strength, pathology or exogenous molecules as contrast agents. Optimization of the final contrast generally requires mapping the T_1 of the tissue(s) of interest. This will be described in depth in the chapter 3, where the acquisition, as well as the possible applications of T_1 mapping will be discussed.

1.3.1.2 Transverse relaxation time (T_2)

To understand the transverse relaxation, it is easier to consider a spin system which undergoes a 90° RF pulse. The net magnetisation is tipped into the y direction when the RF pulse stops, and a transverse magnetisation $M_{x'y'}$ is created. The spins then precess as usual around the z-axis, nutating the bulk magnetisation M around the z-axis. However random interaction with the numerous neighbouring spins produces microscopic local magnetic fields, disturbing the precession of the spins of interest. The Larmor frequency of each spin is thus altered locally. This creates a dephasing of the spin system, and relaxes the transverse magnetisation $M_{x'y'}$ at a rate T_2 towards zero, *i.e.* its equilibrium state. The transverse relaxation time T_2 is thus characteristic of the time necessary for the system to lose coherency, or phase, acquired during the excitation. This loss is inherent to the spins system and occurs only in the transverse plane, leaving the longitudinal magnetisation unaffected. It is thus called the spin-spin relaxation time, and is always equal to or shorter than the longitudinal relaxation time. This leads to another part of the Bloch equation (valid on resonance and in the rotating frame):

$$\frac{dM_{xy}(t)}{dt} = -\frac{M_{xy}(t)}{T_2} \tag{1.11}$$

As described in 1.2.2, the spins can be forced to rephase to produce an echo of the FID signal, either via the use of a 180° or with the use of a gradient. Producing an echo via a refocusing RF pulse ensure that all the spins rephase at the time of the echo, giving a true T_2 contrast. The gradient echo technique however does not refocus the phase dispersion due to field inhomogeneities, giving a T_2^* contrast as described hereafter.

1.3.1.3 T2* contrast

Experimentally, the NMR signal decays faster than predicted by T_2 due to inhomogeneities in the local magnetic field experienced by the spins. These inhomogeneities cause shifts to the rotating frequency of the spins, thus creating off-resonant effects to the nearby spins and dephasing them further. This accelerated decay time is called T_2^* and is generally shorter at high field and can be directly related to the susceptibility of the tissues, *i.e.* a quantity describing how a bulk material is magnetized when exposed to an external magnetic field. T_2^* is related to T_2 by

$$\frac{1}{T_2^*} = \frac{1}{T_2} + \frac{1}{T_2'} \tag{1.12}$$

where T_2' accounts for processes arising from imperfections in the B_0 field.

Reduction of the T_2^* relaxation time can occur when the phase dispersion due to field inhomogeneities within a voxel is large, for instance close to air filled sinuses, giving rise to intravoxel dephasing. This decoherence is not a fully intrinsic relaxation mechanism, as it depends on the location of the spins inside the magnet, besides the intrinsic tissue susceptibility. The susceptibility can also be used as a direct source of contrast, *e.g.* in Susceptibility Weighting Imaging (SWI) and susceptibility mapping techniques. Differences in local tissue magnetic susceptibility can generate deviations in the static magnetic field of a few hundredth of ppm, giving rise to offsets in the spins resonant frequency. Susceptibility-induced field inhomogeneity scales linearly with static magnetic field strength, B_0 [7], therefore susceptibility induced image distortions and signal loss become more severe at high field. To reduce this artefact at 7T it is crucial to locally correct the field using shimming techniques.

These effects can all be combined to give the phenomenological Bloch equation

$$\frac{d\mathbf{M}}{dt} = -\frac{\mathbf{M_x}}{T_2}\hat{\mathbf{x}} - \frac{\mathbf{M_y}}{T_2}\hat{\mathbf{y}} + \left(\frac{\mathbf{M_0} - \mathbf{M_z}}{T_1}\right)\hat{\mathbf{z}} + \gamma\mathbf{M} \times (\mathbf{B_1} + \Delta\mathbf{B_0}) \tag{1.13}$$

with $\Delta\mathbf{B_0}$ defined as the difference in Tesla between the nominal magnetic field strength B_0 of the magnet, and the local magnetic field sensed by the spins.

Overall the Bloch equations can be used to model the NMR signal detected from a sample

using a given imaging sequence, and these equations will be used throughout the thesis to model the evolution of the magnetisation.

1.3.2 Spin dynamics as the origin of contrast

While the relaxation mechanisms depend closely on the environment of the spin, diffusion and exchange of the water molecules inside the tissue happen at a fast rate compared to the relaxation mechanisms. The proportion of time a spin spends in either a bound, mixed or free environment ultimately influences the observed relaxation time.

1.3.2.1 Correlation time τ_C

As the molecules of water move around inside a droplet, the protons sense randomly fluctuating background magnetic fields. Protons are thus precessing at various frequencies, and not just exactly at the Larmor frequency ω_0, also experiencing fields varying at the Larmor frequency. The spectral density $J(\omega)$ describes the fluctuations of frequency of the spins

$$J(\omega) = \frac{2\tau_C}{1 + (\omega\tau_C)^2} \tag{1.14}$$

where τ_c is the correlation time, a measure of the rate of movement of molecules. Bloembergen, Purcell and Pound [3] developed in 1948 the BPP theory which describes the effects the energy absorption of the system has on the spin state, with the primary parameter being the correlation time. This time τ_c defines the 'decay of memory' of the tumbling motion of the molecules, also defined as the time it takes the particle to rotate by one radian, this time being dependent on the particle size as well as on the viscosity of the surrounding. For example, if the transverse field of the molecule fluctuates rapidly, meaning the molecule is highly mobile and is changing its motional state with high frequency, then the correlation time is short, and the spectral density function is broad. Conversely, a slowly fluctuating field produces a narrow spectral density, with a long correlation time. This is illustrated in the fig. 1.5.

A short τ_c means a small number of water molecules tumbling at the Larmor frequency, hence

Spectral density $J(\omega)$

slow motion

$$J(\omega) = \frac{2\tau_c}{1+(\omega\tau_c)^2}$$

intermediate motion

c

fast motion

b

a

ω_0

$\log(\omega)$
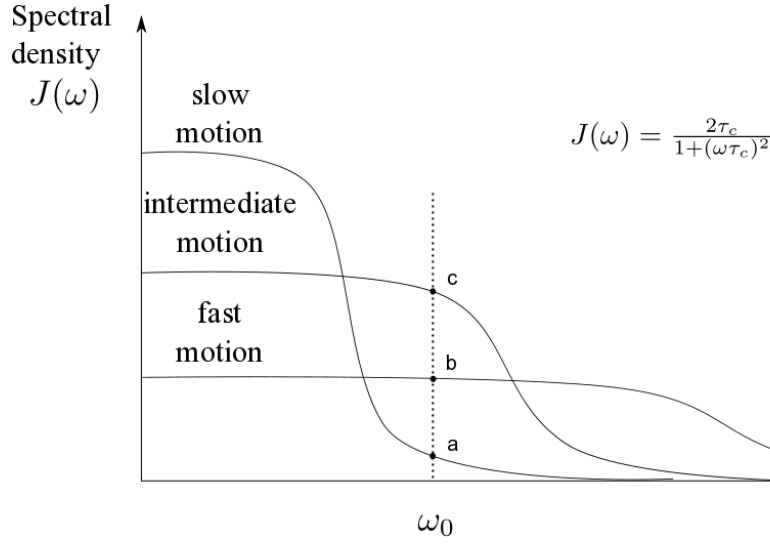
Figure 1.5: Spectral density function $J(\omega)$ for 3 substances of varying correlation time τ_c.

an inefficient T_1 and T_2 relaxation, as seen in CSF. For water molecules bound to macromolecules by forming hydration layer, the T_2 relaxation is very efficient due to rapid dephasing with respect to other protons. In the intermediate case ($\tau_c \sim 10^{-7}s$) the T_1 relaxation will be the most efficient, with a large number of protons tumbling at the Larmor frequency. This correlation time, as well as the viscosity of the media, are parameters influencing the spectral linewidth of the different spin species.

While the correlation time τ_c is a good indication of the environment and dynamic of the spins, it is not practically measurable. However diffusion and exchange of the magnetization can be measured separately, and will be described in the following sections.

1.3.2.2 Magnetisation Transfer Contrast (MTC)

As described earlier, the frequency of protons positioned in the hydration layer of large macromolecules is not always at the water Larmor frequency, due to a broad resonance linewidth. These protons have a very short T_2 and are thus invisible to direct imaging. Magnetisation Transfer Contrast (MTC), commonly used nowadays in clinical settings, manages to highlight those invisible spins indirectly. The measured signal is still from the water spins, but this signal is modulated by transfer of magnetization from saturated bound protons.

Spins inside the tissue are situated on mobile molecules which are interacting with their envi-

ronment. If one considers molecules being in movement or in exchange between two environments i and j, this can often be detected via an exchange of longitudinal magnetisation. In fact, a different chemical site for the proton means generally a different Larmor frequency, and thus different NMR chemical shifts. If the physical environment changes, then the relaxation times change. If a spin for example exchange from a proton in a highly free compartment to a proton in a more compact and bound pool, then the result will be a shortening of its T_2 with no effect on the T_1. But if the molecules exchange between the two compartments, part of the longitudinal magnetisation of the j spins will produce a response in the i spins in excess of that expected on the basis of cross-relaxation via dipolar interactions. The method used to record this phenomenon is to saturate the magnetisation of the j spins prior the excitation of the i spins. For this method, two images are acquired, one with and one without selective presaturation of the j spins. The two images are then subtracted and normalised (ratio), revealing where spin transfer has taken place. This normalized map (also called Magnetization Transfer Ratio map) depends on the amount of exchange taking place (*i.e.* the rate of exchange on both pools), but is also related to the average T_1 of the spins and the density of the protons. MTR depends on the details of the pulse sequence used as well as the imaging hardware. To produce any thorough quantitative measurements, one has to first model the exchange/transfer process and then obtain the adequate experiment necessary to probe it.

This modality can be used to quantify the amount of macromolecules in tissues such as the myelin in the white matter, but is also helpful to understand off-resonance effects, happening when the frequency of certain spins are not exactly at the Larmor frequency. It can induce a slight change in the effective flip angle, or bring out-of-view spins into resonance. A deeper analysis of these effects will be presented in the chapters 4 and 5.

1.3.2.3 Diffusion imaging

Inside the water droplet, the proton trajectory is dictated by random Brownian motion of the molecule and leads to an isotropic diffusion. If physical barriers restrict the diffusion of the water molecules in one or two directions, the diffusion become anisotropic, as for example for molecules close to cell membranes. The diffusion is defined by a coefficient D, measurable with a pulsed-gradient spin-echo (or gradient-echo) sequence (very similar to the sequences described in 1.2.2).

The mobility of the spins is encoded via strong, opposed, diffusion gradients, applied between the excitation pulse and the echo. These are either bipolar gradient lobes separated by a time T_D for the GE, or monopolar gradients separated by a time T_D and a spin echo pulse for the SE. The more the spin is restricted in the direction of the applied gradient, the stronger the measured signal, as most of the signal will be refocused. By repeating the experiment with several different gradient orientations and possibly strengths, it is feasible to recover the preferred direction the spins are diffusing inside a voxel. Diffusion Tensor Imaging (DTI) uses this to reconstruct the fibre tracts inside the brain, the water molecules diffusing preferably in the direction of the axons, being restricted spatially in the other directions by the fibre tracts.

1.4 Neuro-imaging at high field

The human brain is a key target for MRI due to its complexity, both in structure and function. Moreover, the NMR properties of the soft tissue composing the brain provide good contrast to delineate structures, as well as pathology. Commonly used Magnetic Resonance Imaging (MRI) scanners operate at field strengths of 1.5 or 3 Tesla (T), but increasing the field strength further improves the sensitivity (as described by equation 1.5), but not without posing technical challenges. Images obtained from the MRI system are generally contaminated by artefacts such as noise, distortion, contrast inhomogeneity, blurring due to subject movement, as any imaging modality would be. This section describes a number of the common image artefacts in MRI, highlighting the effects at high field, and the ways by which these artefacts can be reduced. This section also reviews the gains, but also the difficulties raised by using ultra-high field magnets to image the brain *in vivo*. An overview of the principal tissue relaxation quantities is also provided.

1.4.1 Advantages of high field

Increase in sensitivity   The image signal to noise ratio (SNR) available in MRI increases with the static magnetic field strength, $\mathbf{B_0}$. Theoretically, the SNR is linearly increasing with the magnetic field, but this is validated experimentally only up to 1.5T [6]. In fact, as the field increases, the

electromagnetic wavelength at the resonance frequency shortens as well as the penetration depth. At magnetic field up to 1T, the wavelength is very long compared to the size of the sample, and wavelength effects are negligible. At higher field strength, depending on the local dielectric properties of human tissues, the head can act as an RF resonator and can create standing wave patterns. The gain in sensitivity of the coil becomes dependent on position within the head, producing a complex pattern of the SNR with position. In one comparison between 4 and 7 T human brain imaging using a transverse electromagnetic (TEM) volume head coil, an average increase of 1.76 in SNR was recorded [18]. However, the increase was not spatially uniform, with the measured gain varying from a value of 2.1 at the centre of the head to 1.4 at the periphery. The overall increase in SNR at ultra-high field can be traded for increased spatial resolution or reduced image acquisition time, the upper limit of spatial resolution being dictated by the minimal volume required to produce a measurable NMR signal.

Increase in spectral resolution The amount of some species inside cells, such as certain proteins, lipids or also specific molecules (choline, creatine, amide groups, *etc.*) can be detected and even quantified thanks to an increase spectral resolution at high field for spectroscopy. It has made it possible to resolve previously overlapped compounds in the brain *in vivo*, such as the neurotransmitters glutamate and glutamine, part of the GABA-glutamine cycle necessary for the metabolic repletion of the neurons and its synapses [17]. Increase in sensitivity also provides the possibility of reducing the volume of interest and/or the scanning time of spectroscopic experiments. However the reduction of the T_2 with field strength means that the spectroscopic signal decays quicker, inducing new challenges for the acquisition of *in vivo* spectra.

1.4.2 Difficulties

Noise The noise affecting the recorded signal in NMR comes from electronic random fluctuations inside the electrical conductors involved during an NMR experiment, such as the coils recording the signal, but also the electrically conducting tissues of the patient. Brownian motion of electrons within a conductor is related to its temperature, which can be greatly reduced inside the coils by using superconductors wires. However, at field strength superior to 1.5T, the principal source of noise is the patient due to its high resistivity compared to the coils. For a uniform B_1 field, this creates a linear

relationship between the available SNR and the field strength B_0. In practice, other factors, such as signal bandwidth or coil proximity to the sample for example, will further influence the relationship. However, another source of noise present inside some MRI images is caused by the subject alone and is called physiological noise. It is created by respiration, cardiac pulsation and other temporal variations of the subject inside the scanner, and is particularly important for dynamic studies. The physiological noise scales linearly with B_0 and so can reduce the gain of using high field systems.

Field inhomogeneities   Building a magnet (described in 2.4.1) delivering a magnetic field five orders of magnitude larger than the earth's magnetic field requires high quality fabrication, with very low error tolerance. However, imperfections are inevitable, and lead to deviations from the main magnetic field (ΔB_0). Minimizing this error is possible as explained in 2.4.2, but will always lead to small field variations inside the volume of interest, generally negligible for general imaging purposes. As explained previously in 1.4.1, homogeneous transmission and reception of electromagnetic field at relatively high radio-frequency (hundreds of MHz) becomes difficult if the size of the volume to excite is equal or smaller than the wavelength. It can exhibit a standing wave behaviour, creating field cancellation due to interference. It has been noticed since the first brain images acquired at ultra-high field (4T and higher) that an RF coil with volume coverage produces images with an hyper-intense region at the centre of the brain, due to an decrease B_1 amplitude outside the $'$hotspot$'$. Various methods are being investigated to reduce these inhomogeneities in the transmit field B_1, such as RF shimming techniques or multi-transmit RF coils. Correction can also be performed post-acquisition, and generally necessitates mapping of the fields. Specific techniques will be described in the chapters 3, 4 and 5, providing basis for the correction of imperfections in the images due to inhomogeneity.

Increase in power deposition   Power deposition induced by RF excitation pulse is expected to increase quadratically with field strength up to 200 MHz. As estimated in [18] via the Maxwell model, a 90° flip angle necessitates 1.8 time more power at 7T compared to 4T to excite the spins equally in the centre of the brain, and was confirmed experimentally, while the standard square law would predict a factor of 3. This results in a higher power deposited inside the brain when imaging at ultra-high field, generally limiting the huge advantage of sensitivity for imaging methods using a large number of saturation pulses or refocusing pulses, such as spin echo refocusing methods and magnetization

transfer experiments. The limit of power deposition is defined by the Specific Absorption Rate (SAR), calculated as the RF power absorbed per unit of mass of an object (see p. 858-9 in [8]). This limits the radio-frequency power deposited in the patient, insuring a safe limit against the heating of the patient's tissue.

Movement artefact   The comfort of the patient inside the bore of an high field magnet is important, not only for the reduction of some physiological effects, but also for the quality of the images. As the resolution of the images can be increased with the field strength, movement artefacts causing blurring of the images may also arise when imaging very small voxels. Minimizing the patient head movement is performed in Nottingham with small pads that the subject places between their ears and the receiver coil. Specifically vacuum pillow provides a robust method to minimize the head movement of the subjects neck, and is used especially for high resolution scans, as well as long fMRI studies. Slow movement due to neck relaxation can be seen between successive images acquisition, and is normally corrected off-line via registrations algorithm. However movement during image acquisition is more difficult to correct and causes blurring and motion artefacts, as shown in fig. 1.6. As the amplitude of the movement is intrinsic to the subject, it can cause large variation in the final image quality of the scans and has thus to be minimized accordingly.
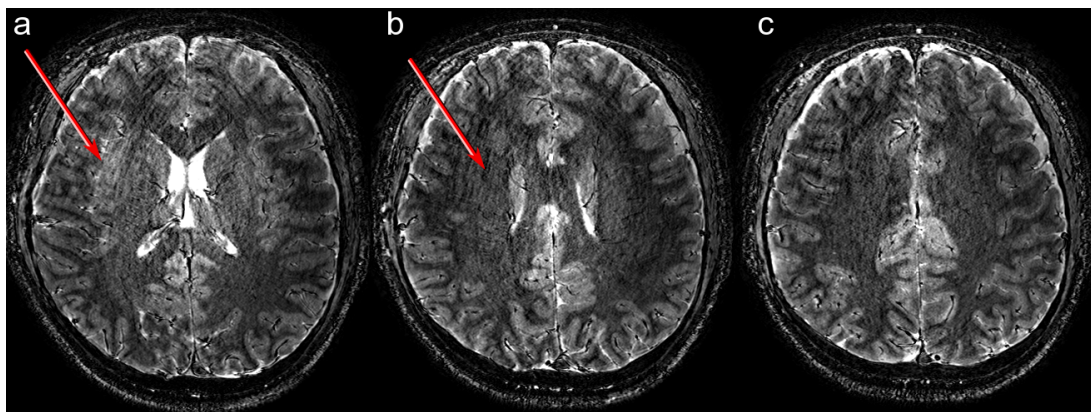
Figure 1.6: Movement artefacts inside a MRI of an healthy subject. Note the ringing inside of the brain in the image a, due to the skull edges producing multiple lines artefacts. It can produce blurring in the cortex (a) or artificial decrease in contrast (b). The image c does not show such a strong effect, due probably to a difference between the acquisition timing and the movement.

Movement of the brain inside the skull is rarely mentioned, but the cardiac pulsations as well as the inflow and outflow of the cerebro-spinal fluid are possible sources of minute contraction and ex-

pansion of neighbouring tissues, resulting in possible movement up to 0.15mm in the thalamus region [16]. While cardiac artefacts are not observed in imaging other than diffusion and perfusion studies, increase in resolution could suffer from this pulsation problem, ultimately affecting the optimal resolution achievable.

1.4.3   Chemical shift artefact

In a magnetic field, the difference in the resonant frequencies of different compounds gives rise to chemical shift artefacts. This has the effect of shifting the apparent position in the image of one set of spins relative to another, even if they originate from the same position in the sample. The most prominent chemical shift artefact is the water fat shift artefact, which manifests itself as a mis-registration of the signal from fatty tissues. For water and fat, the chemical shift difference is approximately 3.4 ppm, and as the frequency separation ($\sim$1013 Hz at 7 T) increases with the static magnetic field strength, this mis-registration is also most prominent at high field. In order to avoid excessive mis-registration of pixels containing fat, we need to have a pixel bandwidth which is large relative to the frequency offset of fat with respect to the water signal. The fat artefact can be eliminated by using fat suppression, such that a spectrally selective pulse excites only the protons in the fat prior to the imaging sequence so that when the image excitation pulse is applied the fat spins are already saturated and do not contribute to the image.

1.4.4   Radiation damping

The radiation damping (RD) is an effect occurring when the rotating transverse nuclear magnetization induces a current in the receiver coil strong enough to generate a rotating magnetic field in the sample, thus producing a torque on the magnetization. This effect is very low at standard magnetic field (*e.g.* 1.5T), but is known to disturb NMR experiments such as relaxation measurements [15] and two-dimensional spectroscopy [4] at high field. It has been shown to influence measurement of T_1 of the blood in a clinical 3T scanner [14], creating a small decrease of the effective T_1. It is shown in [19] that RD can also give rise to unexpected effects in Z-spectroscopy, the detection of magnetization exchange between water and macromolecules by measurement of the water magnetization as

a function of the frequency of low-power RF pre-irradiation. Although RD is an intrinsic physical phenomenon in all NMR experiments, the magnitude of the damping field depends on the Q value, the filling factor of the probe, and on the bulk magnetic moment of the sample, which depends on the static field strength as well as the quantity of spins present inside the coil. The Q factor is a figure of merit of the coil, and is the ratio between the energy provided for the RF pulse, with the energy loss by resistance. Reduce the Q of the coil to suppress RD would reduce the SNR. The method of choice to suppress RD is to suppress the transverse relaxation before the actual acquisition, for example by applying a small gradient before the imaging part. As gradients are generally used to encode the spins positions in MRI, it is rare to observe radiation damping effects in imaging experiments. However, as for certain imaging experiments (such as some presented in the following chapters), either inversion pulses or saturation pulses will be used to prepare the magnetization, and will necessitate the removal of radiation damping effects.

1.4.5 NMR properties of brain tissues

While the increase in Signal to Noise Ratio (SNR) is directly related to the increase in magnetic field strength, other NMR and imaging properties behave differently at high magnetic field. The lengthening of the T_1 values of the different brain tissues with increasing magnetic field strength is accompanied with a decrease in T_2 values and a dramatic increase in magnetic susceptibility effects. The increase relaxation time T_1 affects the recovery time necessary for the system to come back to equilibrium, prolonging the scanning time. This is however beneficiary to study the intake of contrast agent, either endogenous (Arterial Spin Labelling), or exogenous (Blood-Brain Barrier disruption). T_2 values in brain tissue decrease with increasing magnetic field strength. T_2^* values are also shortened with field strength, the additional relaxation term T_2' scaling with the field strength because of increased magnetic susceptibility effects, and thus becoming dominant in T_2^*-relaxation. The dramatic increase of T_2^* contrast with increasing magnetic field strength is the reason for the strong interest in T_2^* contrast applications at ultra high field. The increase in susceptibility provides additional sensitivity for functional imaging (increased BOLD effect) and new possibility for morphological imaging, as the increase in T_2^* contrast between the white and the grey matter [10] together with the increased resolution makes it possible to observe the cortex at a detail never seen before *in vivo*, for example

cortical substructures such as stria of myelin inside the cortical ribbon. The sensitivity of the phase of T_2^*-weighted images also increases with field strength due to the increased susceptibility-induced phase shifts, providing complementary information to the modulus images. It has been shown that the use of MR signal phase in gradient echo images can improve contrast in specific human brain structures such as veins and iron rich regions [9, 5], and also provides good contrast between grey and white matter [1].

Bibliography

[1] A. M. Abduljalil, P. Schmalbrock, V. Novak, and D. W. Chakeres. Enhanced gray and white matter contrast of phase susceptibility-weighted images in ultra-high-field magnetic resonance imaging. *J Magn Reson Imaging*, 18(3):284–290, Sep 2003.

[2] F. Bloch, W. Hansen, and M. Packard. Nuclear induction. *Physical review*, 70(7-8):460–474, 1946.

[3] N. Bloembergen, E. M. Purcell, and R. V. Pound. Relaxation effects in nuclear magnetic resonance absorption. *Phys. Rev.*, 73(7):679–712, Apr 1948.

[4] Chen, Mao, and Ye. Fractional-frequency peaks in two-pulse 2d experiments under strong radiation damping. *J Magn Reson A*, 123(1):126–130, Nov 1996.

[5] J. H. Duyn, P. van Gelderen, T.-Q. Li, J. A. de Zwart, A. P. Koretsky, and M. Fukunaga. High-field mri of brain cortical substructure based on signal phase. *Proc Natl Acad Sci U S A*, 104(28):11796–11801, Jul 2007.

[6] W. A. Edelstein, G. H. Glover, C. J. Hardy, and R. W. Redington. The intrinsic signal-to-noise ratio in nmr imaging. *Magn Reson Med*, 3(4):604–618, Aug 1986.

[7] K. Farahani, U. Sinha, S. Sinha, L. C. Chiu, and R. B. Lufkin. Effect of field strength on susceptibility artifacts in magnetic resonance imaging. *Comput Med Imaging Graph*, 14(6):409–413, 1990.

[8] E. Haacke, R. Brown, M. Thompson, and R. Venkatesan. *Magnetic resonance imaging: physical principles and sequence design*. New York: John Wiley & Sons, Inc, 1999.

[9] E. M. Haacke, N. Y. C. Cheng, M. J. House, Q. Liu, J. Neelavalli, R. J. Ogg, A. Khan, M. Ayaz, W. Kirsch, and A. Obenaus. Imaging iron stores in the brain using magnetic resonance imaging.

Magn Reson Imaging, 23(1):1–25, Jan 2005.

[10] E. M. Haacke, Y. Xu, Y.-C. N. Cheng, and J. R. Reichenbach. Susceptibility weighted imaging (swi). *Magn Reson Med*, 52(3):612–618, Sep 2004.

[11] E. L. Hahn. Spin echoes. *Phys. Rev.*, 80(4):580–594, Nov 1950.

[12] L. Hanson. Is quantum mechanics necessary for understanding magnetic resonance? *Concepts in Magnetic Resonance Part A*, 32(5):329–340, 2008.

[13] M. H. Levitt. *Spin Dynamics: Basics of Nuclear Magnetic Resonance*. John Wiley & Sons, 2001.

[14] H. Lu, C. Clingman, X. Golay, and P. C. M. van Zijl. Determining the longitudinal relaxation time (t1) of blood at 3.0 tesla. *Magn Reson Med*, 52(3):679–682, Sep 2004.

[15] Mao, Guo, and Ye. Nuclear-magnetic-resonance line-shape theory in the presence of radiation damping. *Phys Rev B Condens Matter*, 49(22):15702–15711, Jun 1994.

[16] M. Soellinger, A. K. Rutz, S. Kozerke, and P. Boesiger. 3d cine displacement-encoded mri of pulsatile brain motion. *Magn Reson Med*, 61(1):153–162, Jan 2009.

[17] I. Tkác, P. Andersen, G. Adriany, H. Merkle, K. Ugurbil, and R. Gruetter. In vivo 1h nmr spectroscopy of the human brain at 7 t. *Magn Reson Med*, 46(3):451–456, Sep 2001.

[18] J. T. Vaughan, M. Garwood, C. M. Collins, W. Liu, L. DelaBarre, G. Adriany, P. Andersen, H. Merkle, R. Goebel, M. B. Smith, and K. Ugurbil. 7t vs. 4t: Rf power, homogeneity, and signal-to-noise comparison in head images. *Magn Reson Med*, 46(1):24–30, Jul 2001.

[19] D. C. Williamson, J. Närväinen, P. L. Hubbard, R. A. Kauppinen, and G. A. Morris. Effects of radiation damping on z-spectra. *J Magn Reson*, 183(2):203–212, Dec 2006.

IMAGING WITH A MAGNETIC RESONANCE SCANNER

Since the early 1970's, the localization of the NMR signal has gained a lot from hardware improvement, such as the use of dedicated gradients coils or surface coils development, as well as algorithms for quicker signal acquisition or image reconstruction. This chapter describes how to form an MR image from a sequence of radio-frequency and gradient pulses while explaining the concept of k-space to then introduce some imaging techniques relevant to the work on this thesis. A complete overview of the hardware requirements and limitations of an MR system is then given, and the sources of artefacts arising in an MRI experiment are reviewed.

2.1 Image formation

NMR imaging was developed in the early 1970's. In 1973, Lauterbur proposed a field gradient to localize the NMR signal [5]. A linear gradient was applied at different angles to a sample and the projections were combined using a back-projection method to produce 2D images of the sample. At the same time Mansfield and Grannell [9] presented a method to determine spatial structures in solids based on NMR 'diffraction', using a sequence composed of multiple pulses and gradients. A year later, different selective excitation techniques were proposed by Mansfield's group [3], including slice selection in the exact form it is used today. One year later, Ernst published work on the first Fourier imaging method [4], using non-selective excitation and orthogonal linear gradients to generate

2D Fourier encoded images. These techniques are the heart of Magnetic Resonance Imaging (MRI) today, and are reviewed hereafter.

2.1.1   Signal localization

The early MR images were based on the projection reconstruction method used in X-ray CT scans nowadays. The spin density of a given slice is sampled in a multitude of directions (projections) and back projected to obtain a radial density image. However, the image is blurred when reconstructed in a Cartesian grid due to the sampling of measurements, but can be overcome using specific filters or via appropriate interpolation. An alternative technique called Fourier zeugmatography was proposed by Kumar, Welti and Ernst [4] and became so popular that it is a method used widely in MRI today. The Fourier technique requires a quadrature detection of the FID, providing the phase and the frequency of the signal necessary for a complete reconstruction.

2.1.1.1   Position encoding

To create an image, it is necessary to localise the source of the NMR signal. The image formation employed in MRI is done in the frequency space, also called k-space as presented in more details in 2.1.2. This is done by varying the resonant frequency linearly with position with the use of three orthogonal linear field gradient coils, G_x, G_y and G_z, designed to produce a linearly varying field along its respective axis which superimposes onto the main magnetic field B_0. The Larmor frequency of the spins at position (x, y, z) is then a function of the applied gradients at a given time:

$$\omega(x, y, z, t) = \gamma \left(B_0 + xG_x(t) + yG_y(t) + zG_z(t) \right) \tag{2.1}$$

The following sections introduce three different methods used for position encoding using additional magnetic gradients.

2.1. Image formation

2.1.1.2 Slice selection

Slice selection, also called selective excitation, is a method consisting of applying a gradient at the same time as the RF pulse used for excitation. An RF pulse alone would excite all the spins present inside the coil within a certain bandwidth, independent of their position. This is called a non-selective RF pulse and is often accomplished with a narrow, square pulse (of wide bandwidth). The bandwidth depends on the shape of the RF pulse used as well as its timing. If an RF pulse is applied in the presence of a field gradient, the gradient spatially isolates the effect of the pulse by selecting only a thin slab where the spins rotate at a frequency lying inside the bandwidth, the spins outside of this slab rotating either slower or faster than the frequency present in the RF pulse (as shown in fig. 2.1).
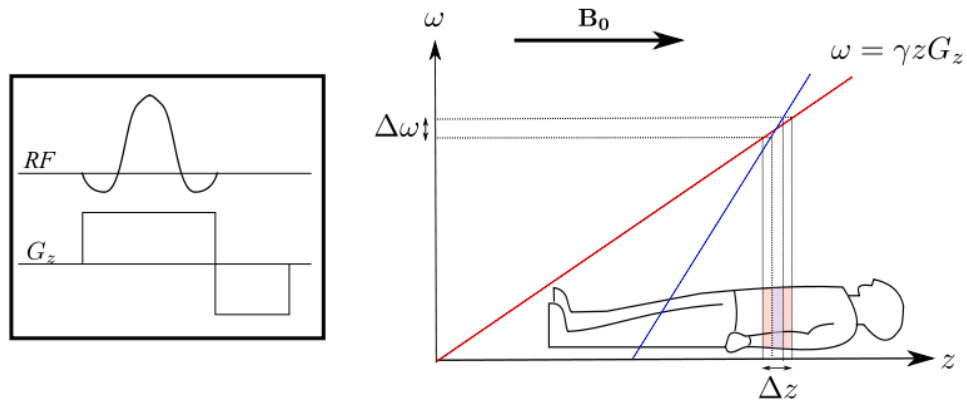
Figure 2.1: Illustration of selectively exciting spins in a slice of thickness Δz with a range of frequency $\delta\omega$ and a slice selection gradient of strength G_z. The steeper gradient (blue line) produces a thinner slice. Note the reverse slice gradient after the slice selection radio-frequency and gradient, required to refocus the phase shift created by the slice selection gradient.

RF pulses   The bandwidth (BW) of the radio-frequency pulse describes the range or thickness of frequencies that are excited by this pulse. One way to decrease a slice thickness is to decrease the BW of the pulse, making the region where the spins are resonating inside the gradient narrower, as presented in blue in fig. 2.1. Another way to change the excitation profile is to vary the RF carrier shape, also called the RF envelope. It can be demonstrated that this RF envelope is the exact Fourier transform of the slice profile, so that an infinite sinc pulse would create a perfect rectangular profile. As in practice the RF pulse is finite in time, a sinc pulse would often be limited to 3 or 5 lobes and

2.1. Image formation

filters are applied to improve the resulting slice profile.

Adiabatic pulses If the pulse timing is not an issue (*e.g.* for an inversion recovery experiment), the RF pulses used are often adiabatic because of their excellent excitation profiles when used in inhomogeneous B_1 fields. In fact, adiabatic pulses do not obey the relationship described in Eq. 1.9 between the angle and the B_1-field amplitude. Instead, the flip angle of an adiabatic pulse depends on how the amplitude and modulation frequency of B_1 varies during the pulse, but requires a longer time to produce the requested flip angle than hard pulses. Theoretically, as long as the B_1-field amplitude exceeds a minimum threshold, the resultant magnetization vector becomes insensitive to B_1-field variations, leading to a spatially uniform inversion of the magnetization.

2.1.1.3 Frequency encoding

For frequency encoding, the field gradient is used during the readout rather than during the excitation, influencing only those spins that have been excited by slice selection. The gradient can be applied in one, two or three directions, the precession frequency always being a function of the gradient axis:

$$\omega(\mathbf{r}) = \gamma \left(B_0 + \mathbf{G_r r} \right) \tag{2.2}$$

Without relaxation, measure of the signal S emanating from $\mathbf{r}$ at a time t is proportional to the proton density ρ (assuming complete rephasing after an RF pulse applied at $t = 0$):

$$S(\mathbf{r}, t) \propto \rho(r) e^{i \int_0^t \omega_L(\mathbf{r} t') dt'} \tag{2.3}$$

The signal is generally received from an extended region of the sample of volume V:

$$S(t) \propto \int_V \rho(r) e^{i \int_0^t \omega_L(\mathbf{r} t') dt'} dV \tag{2.4}$$

The frequency of the spins depends on the main magnetic field B_0 as well as on the evolution of

2.1. Image formation

the gradients over time. If the gradient is applied from a time $t = 0$ to $t = t'$, and the received signal demodulated to remove the ω_0 component, the signal is then:

$$S(t) \propto \int_V \rho(r) e^{i \int_0^t \mathbf{r}.G_r(t')dt'} dV \tag{2.5}$$

The space represented by the phase evolution is known as k-space (2.1.2), and defined as the reciprocal gradient space vector:

$$\mathbf{k}(t) = \gamma \int_0^t \mathbf{G_r}(\mathbf{t'})dt' \tag{2.6}$$

The signal reduces then to a 3D Fourier Transform expression of the spin density:

$$S(t) \propto \int_V \rho(r) e^{i\mathbf{r}.k(t)} dV \tag{2.7}$$

This means that the information about the spin density of an object can be obtained directly from the inverse Fourier Transform of the received signal. This concept forms the basis of modern imaging techniques in MRI.

2.1.1.4   Phase encoding

The concept of the phase encoding is to create a linear spatial variation of the phase of the magnetization to localize the NMR signal orthogonally to the frequency encoding direction. It employs a short-lived pulse of field gradient, set between the RF pulse and the acquisition. A specific phase dependant on the position is introduced to the spins in the y-direction by applying a phase encoding gradient $\mathbf{G}(t') = G_y\hat{\mathbf{y}}$ for a time $t' = 0$ to $t' = t_1$ after the excitation pulse and before the readout gradient, $\mathbf{G}(t') = G_x\hat{\mathbf{x}}$, where $\hat{\mathbf{x}}$ is a unit vector along x. The signal from spins experiencing such gradients is acquired during the application of the readout gradient, during the time $t' = t_1$ to $t' = t_2$, and is given by

$$S(t) \propto \int \int \int \rho(\mathbf{r}) e^{-i\Phi_y - i\gamma x G_x t} dx dy dz \tag{2.8}$$

where $\Phi_y = \gamma y G_y t_1$ is the amount of phase introduced to the signal due to G_y. Varying either the duration or strength of the gradient enables encoding of the spins in the y-direction, while typically the x-direction is encoded via the readout gradient, and the z-direction encoded via slice selection. The next section reviews how this can be understood in the k-space.

2.1.2   k-space concept

The concept of k-space was introduced in 1983 [6] as a way of visualizing the trajectories of the spins phase under the influence of field gradients. k-space can be consider as the Fourier space (k_x, k_y, k_z) in which the signal is acquired, before being Fourier transformed into Cartesian image space (x,y,z). k-space represents the spatial frequency distribution of the MR image. Low spatial frequencies (coarse image structures) appear close to the origin while higher spatial frequencies (edges and fine detail) appear at the outer edges of k-space.
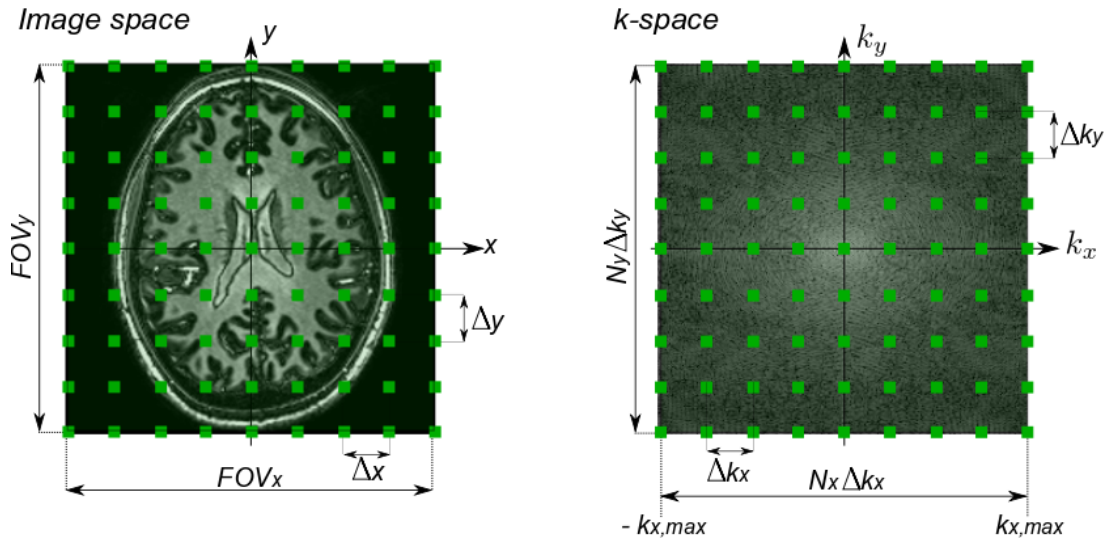
Figure 2.2: The relationship between image space (left) and k-space (right).

Applying field gradients in the correct way in the imaging plane encodes the spatial positions of signals as frequencies and phases (section 2.1.1), as described in the fig. 2.2. Immediately after excitation, the sampling position is at the centre of k-space and the position at a time, t, after excitation is proportional to the integrated gradient at that time. So, signal acquired in the presence of a constant x-gradient samples k-space along a line in the k_x-direction. Therefore, during frequency encoding,

data points are recorded at regular intervals as k-space is swept, while during phase encoding the location in k-space is altered without sampling the signal, resulting in instantaneous jumps in the sampled trajectory, as presented in fig. 2.2. To sample an image, fully, all four quadrants of k-space must be covered by the readout trajectory, although theoretically only half of the k-space is necessary (the other half being exactly the complex conjugate).

Although k-space trajectories are continuous, the signal is sampled only at discrete intervals along a path. The spacing of the measurements made in k-space determines the field-of-view (FOV) of the resulting image, the further from the centre of k-space, the greater the resolution of the reconstructed image:

$$\Delta k_{x,y} = \frac{1}{FOV_{x,y}} \tag{2.9}$$

2.1.2.1 How to produce an image out of k-space

Once the raw data matrix sampling in the k-space is acquired, reconstruction is achieved via Fourier Transform (FT). Applying a 2D FT to the quadrature data composing the k-space produces a complex image, with a real and a imaginary part, or magnitude and a phase image, the magnitude representing the spin density function. For a 3D volume, the proton density is defined as:

$$\rho(x, y, z) = \int \int \int S(k_x, k_y, k_z) e^{-i(k_x x + k_y y + k_z z)} dx dy dz \tag{2.10}$$

The acquisition of the signal, however, is not instantaneous, and relaxation of the signal between the different phase encoding points influences the measured k-space signal. 2D, as well as 3D techniques are used to obtain the k-space signal distribution, the advantage of 3D techniques being thinner slices with better profile, but requiring longer acquisition. Averaging similar acquisitions in the Fourier space gives better SNR per unit time generally.

2.1.2.2 Acceleration of the k-space sampling

k**-space sampling strategies** Different techniques can be used to speed up the acquisition of k-space, for example by acquiring only half of k-space, hence the name 'half Fourier'. As said in 2.1.2, the full k-space is composed by the complex representation of the signal, as well as its complex conjugate. By acquiring only half (or two-thirds, or *etc.*) of the k-space, no contrast information is lost and the image can be reconstructed similarly to the full Fourier technique (part of the phase information can be lost, and can be a problem to correct susceptibility artefacts). However a lost of SNR in the image of approximately 30 % for half the k-space makes the gain of acquisition time not always required, and increases the sensitivity of the sequence to artefacts. It is also possible to acquired only a reduced k-space matrix, reconstructing a larger image by using zero-filling. The advantage is a better image quality (smoothing), but without adding new information into the final image. The Gibbs artefact phenomenon, arising from truncation of signal at the edge of k-space, can be reduced to improve the image quality via windowing the k-space data by applying specific filters onto the signal data (more details in [1], as well as in section 5.3.3.4).

Parallel imaging Recently, algorithms based on the reconstruction of images acquired via multicoil arrays boosted the time efficiency of MRI acquisition. Developed first to improve the SNR, it became clear that it would produce a gain in scanning time, if designed appropriately. Parallel imaging requires the use of multiple decoupled receiver coils, each with a separate pre-amplifier and digitizer. Each coil has a sensitivity map similar to a surface coil, which, when combined with the other coils, produces an increased signal, and so increased SNR. As the data collected from each coil are overlapping, it is possible to use a field of view smaller than the actual volume to image, and still retrieve all the data. The acceleration factor R defines the distance increase between the phase-encoding k-space lines, while keeping the maximal extent covered in k-space (spatial resolution) fixed. In this case, part of the object outside of the FOV creates signal that wraps back into the image after Fourier Transform. The SENSE technique (short for SENSitivity Encoding as described in [11]), is the parallel technique used in the Nottingham Philips 7T scanner. The key to signal separation is that the superposition occurs differently in each coil, depending on the local sensitivity of the coil. The reconstruction technique uses weights constructed from the sensitivity maps to unaliase the images,

higher reduction factors R speeding up the acquisition, but also increasing the subsequent noise in the images. Compared to the early days of MRI, the reconstruction process using Fast Fourier Transform algorithms are nearly instantaneous, but required a dedicated array of processors different from the scanning console to perform without slowing down the scanning process.

2.2   Gradient Echo versus Spin Echo Imaging
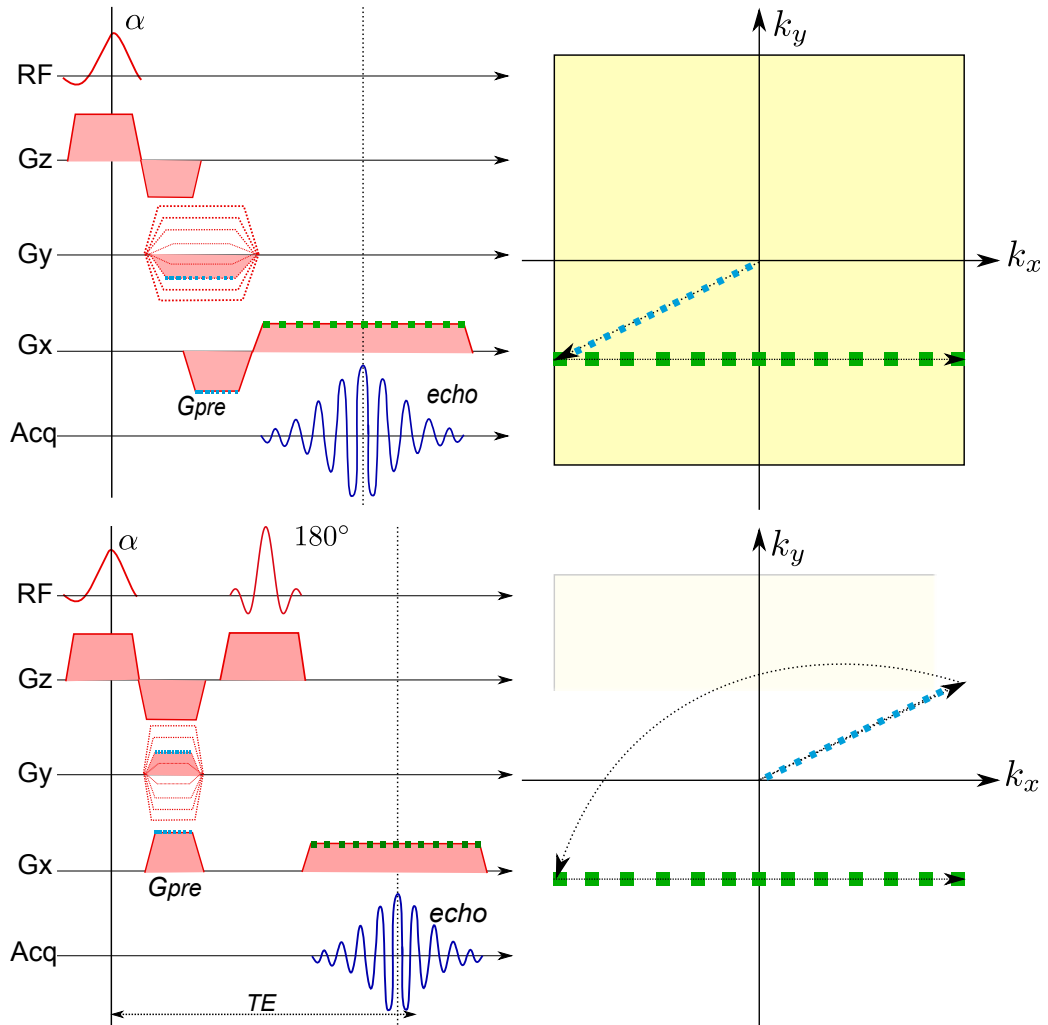
Figure 2.3: Schematic description of Gradient echo acquisition (top) versus Spin echo (bottom). The diagrams on the left describe the evolution of the radiofrequency pulses and the gradients during the acquisition of one echo (either gradient echo or spin echo), while the right part illustrate how the pulses and gradients are translated into the k-space formalism. Blue dots represent the phase encoding, while the green dots represent the acquisition readout, corresponding to the acquisition of one line of k-space.

2.2. Gradient Echo versus Spin Echo Imaging

MR imaging sequences are generally based either on a Spin Echo (SE) or a Gradient Echo (GE) sequence, described in section 1.2.2 and outlined in fig. 2.3. During the slice selection performed by the gradient G_z, an excitation pulse of angle α is applied. After an evolution time which can be varied to change the contrast of the image, k-space is traversed using gradients applied along the x- and y-directions to ensure that sampling starts at the appropriate point in k-space. Two orthogonal gradients (G_{pre} and G_{phase}) are applied along G_x and G_y, considering the slice is oriented along those axis. Their combined effect is to cause a phase evolution that moves the spins system in k_x and k_y direction along the blue dotted line in k-space. The variable phase encoding gradient moves the sampling position in the k_y-axis whereas the purpose of the pre-phasing gradient is to prepare the transverse magnetization so that an echo can be acquired at a later time.

For the gradient echo, the negative pre-phasing gradient lobe causes a traversal of k-space to the extreme left of the sampled area and the readout gradient of opposite polarity is applied while data are acquired at points along the k-space line represented by green dots in fig. 2.3. As described in the chapter 1, the readout gradient reverses the dephasing effects of the pre-phasing gradient and the peak of a gradient recalled echo occurs when the area under the two gradients lobes are equal. For the spin echo protocol, the positive pre-phasing gradient lobe causes a traversal of k-space to the extreme right of the sampled area and a refocusing pulse of $180°$ which negates the phase of the spins is applied before the readout. The effect of the refocusing pulse is shown by the dotted line in fig. 2.3. Then a gradient G_x is applied (green dots), with the same polarity as G_{pre}, in order to record the echo. The time from the excitation pulse to the peak of the spin or gradient echo is called the echo time, TE. The system is then allowed to relax to equilibrium before the sequence is repeated with different phase encoding steps (variation of the amplitude of G_{phase}) in order to fully sample the k-space. The time between two excitation pulses is called the repetition time, TR.

As mentioned in 1.2.2, conventional gradient echo imaging yields images which show $T_2^\star$ contrast, whereas the refocusing RF pulse eliminates T_2' effects, producing a true T_2 contrast in the image. T_2-weighted images are also less sensitive to local B_0-field variation due to the multiple refocusing pulses, reducing through-plane dephasing artefacts related to macroscopic susceptibility effects. However, the additional refocusing pulse in SE imaging makes spin echo sequences more difficult to implement since imperfect pulses introduce errors on the refocusing slice profile and affect the

magnetization of adjacent slices. The specific absorption rate (SAR) also imposes a limit on the implementation of SE sequences because of the energy deposited from the multiple refocusing RF pulses. This is a problem at high field and may result in increased acquisition time or reduce coverage. Advantage of $T_2^\star$-weighted imaging at high field is that it suffers less from artefacts related to inhomogeneous RF excitation fields and requires a relatively low RF power. Images can however be prone to large signal void artefacts in the inferior frontal and inferio-lateral temporal lobes produced by the susceptibility differences between tissue and other air-containing structures. Small field gradients arising from the heterogeneous magnetic susceptibility of tissue can also cause distortions in the image.

2.3 Fast Imaging acquisition techniques

2.3.1 Turbo Field Echo imaging

GRE acquisitions can be fast due to the lack of a spin echo refocusing pulse, providing also the advantage of reduced SAR. A small angle is generally used, leaving a large component of the longitudinal magnetization unaffected by the RF pulse, while an appreciable amount of transverse magnetization is created. The signal is recorded and the remaining transverse magnetization is spoiled before the next excitation pulse, ensuring the only contrast remaining in the image is defined by the T_1 recovery. The excitation pulse reduces the longitudinal magnetization $M_z(t)$, while the relaxation process recovered it by a similar amount before the next excitation pulse. A short period for recovery of M_z can be used and thus a short repetition time (TR).

If the magnetization in the imaging slice (which may have been previously prepared by an inversion or a magnetization transfer pulse) experiences a series of identical excitation pulses with low flip angle evenly spaced in time by TR, the longitudinal magnetization, M_z, will reach a dynamic equilibrium after a sufficient number of excitation pulses. This process depends on the repetition time (TR) used as well as the T_1 of the tissue of interest, and the flip angle α of the readout. Assuming perfect spoiling of the transverse magnetization before each RF pulse, the signal obtained with a

spoiled GRE is then defined as:

$$S_{spoil} = M_0 \; \frac{sin\alpha \; \left(1 - exp(-\frac{TR}{T_1})\right)}{1 - cos\alpha \; exp(-\frac{TR}{T_1})} \; exp(-\frac{TE}{T_2^*}) \tag{2.11}$$

The angle that maximises the signal S_{spoil} for a given TR is defined as the Ernst angle, α_E, which verifies: $cos\left(\alpha_E\right) = exp(-TR/T_1)$. For strong T_2^*-weighting image, the TE is made relatively long (approximately 20 ms at 7 T), with the TR relatively low compared to the T_1 and a relatively low flip angle to prevent T_1-weighting. Gradient or RF spoiling is used to remove transverse coherences, nulling the transverse magnetization M_{xy} before the next excitations.

A variety of names exists for those spoiled GRE pulse sequences including Fast Low-Angle Shot (FLASH), spoiled gradient echo (SPGR), and T_1 fast field echo (T_1-FFE), depending on the manufacturer. If a large number of FFE acquisitions are acquired at very short TR during one recovery, it is possible to encode a 3D-volume in a small amount of time. For instance Magnetization Prepared Rapid Gradient Echo (MPRAGE [10]) uses an inversion pulse as a preparation of the magnetization before using a train of spoiled GRE sequence (as FLASH for example) to acquire the full volume, and is described in more details in 3.1.3.3.

2.3.2 Turbo Spin Echo imaging

While a standard spin echo sequence records a single line of k-space per excitation pulse, the Turbo Spin echo (TSE), also called Fast Spin echo (FSE) or Rapid Acquisition with Refocused Echo (RARE) used only one excitation pulse and a chain of spin echoes to record many lines of k-space. The TSE sequence is similar in concept with the EPI sequence (described in 2.3.3), with multiple refocusing $180°$ pulses used after the excitation pulse to continually refocus the transverse magnetization, creating a train of echoes, as presented in fig. 2.4. Each echo, however, has a different amount of phase encoding as well as a different amplitude due to the intrinsic T_2 decay of the transverse magnetization. The number of refocusing pulses applied after the excitation pulse is called the echo train length (ETL), it is also known as the 'turbo factor' since this provides the factor by which the total scan time can be reduced compared to a conventional spin echo sequence.
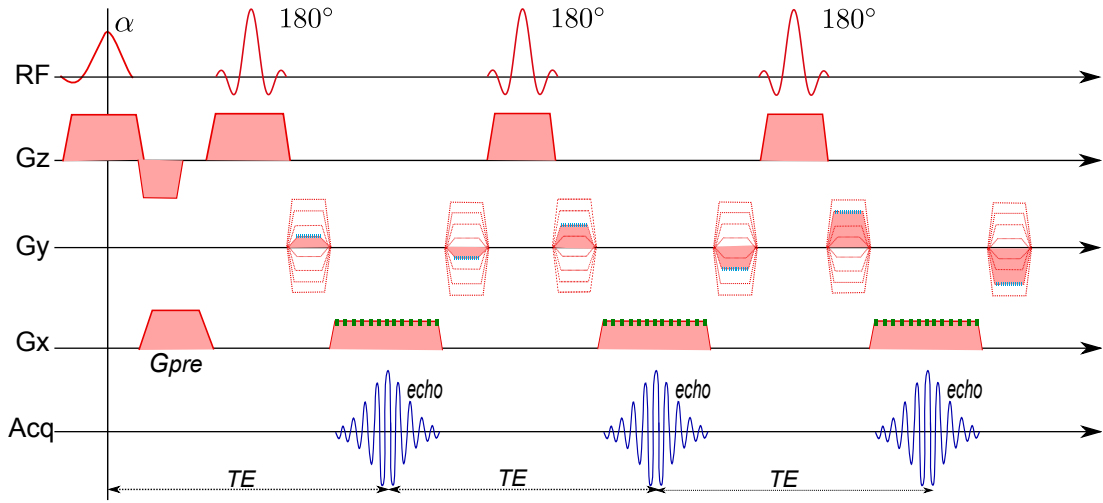
Figure 2.4: Schematic description of Turbo Spin Echo acquisition. The diagram describes the evolution of the radio-frequency pulses and the gradients during the acquisition of one echo train, with the blue and green dots illustrating how the pulses and gradients are translated into the k-space formalism from fig. 2.3. Blue dots represent the phase encoding, while the green dots represent the acquisition readout, corresponding to the acquisition of one line of k-space.

2.3.3 Echo Planar Imaging

Echo Planar Imaging (EPI), proposed in 1977 by Mansfield [7], is a much faster imaging modality where all lines in k-space are efficiently sampled after a single excitation (a single 'shot') rather than via multiple RF excitations. The imaging sequence with the k-space trajectory is shown in fig. 2.5. After the excitation pulse, the negative lobes of the phase encoding (G_y) and frequency encoding (G_x) gradients cause a phase evolution that moves the spins system to the periphery of k-space (as shown by the dashed blue line). The frequency encoding (readout) gradient is then rapidly switched between maximum positive and maximum negative amplitude, repeatedly refocussing the transverse magnetization to yield a train of gradient echoes while sweeping across k_x in alternate directions. Between switching, a small 'blip' is applied to the phase encoding gradient, incrementing the k_y position in k-space (solid blue lines). Alternating k-space lines (echoes) are traversed (sampled) in opposite directions of the readout gradient, therefore every other line has to be time-reversed before Fourier Transformation is applied to generate an image. EPI is the most commonly used dynamic sequence, for example in fMRI studies, due to the high temporal resolution it offers, which allows measurements to be made on a physiological time scale. EPI is good for quantification study as it uses so few RF pulses that their effects on the magnetization are easier to model, as presented in chapter 3 and 4.

2.3. Fast Imaging acquisition techniques
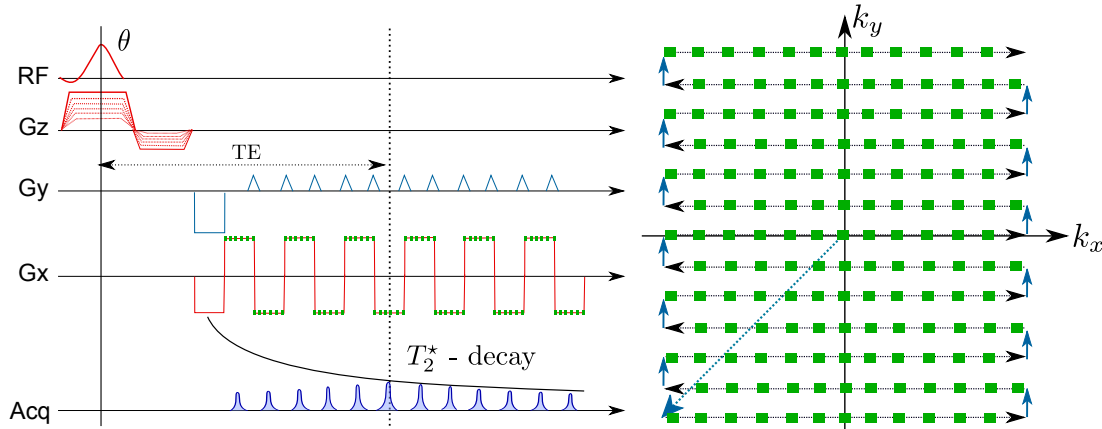
Figure 2.5: Schematic diagram of the Echo Planar Imaging sequence and k-space trajectory. The repeatedly reversed readout gradient and blipped phase encoding gradient forms a series of echoes so that all of k-space is sampled after a single excitation.

Artefacts in EPI   While EPI has the advantage of being a very fast imaging method, there are also drawbacks to the sequence. Inhomogeneities of the B_0 field due to poor shimming and susceptibility effects influence the evolution of the phase during the echo train, affecting the EPI more severely than conventional sequences. Local field inhomogeneities result in significant geometric distortions in the phase-encode direction, as it is the slowest sampled direction. A phase variation due to chemical shift also accumulates in the phase encode direction, which can cause substantial displacements of fat signals. EPI data suffers from signal drop-out in areas where local field inhomogeneities cause through-slice dephasing of signal and therefore reduce echo amplitudes. Imperfections in gradient coils or eddy currents cause a slight offset between lines collected in the positive and negative direction, leading to a Nyquist ghosting artefact in the reconstructed image. This appears as a lower intensity ghost of the image shifted by half the field of view in the phase encoding direction.

Resolution   The resolution of EP images can be increased with high field strength magnets (see [8]) but the implementation of high spatial resolution EPI gives rise to a number of challenges at 7T. In EPI, the acquisition time for a given spatial resolution is proportional to the field of view (FOV) in the phase encoding direction and thus to the number of k-space lines acquired. The shortening of T_2 and $T_2^\star$ relaxation times at 7T poses a limit on the number of k-space lines that can be acquired after excitation as it is not possible to sample the entire k-space with a long echo train length and retain a good TE. High resolution raises heavy demands on the gradients and due to the use of high slew rates

can cause peripheral nerve stimulation (PNS) in the subject. Increasing spatial resolution generally requires an increase in the data acquisition time, and consequently a reduction of the pixel bandwidth in the phase encoding direction. Field inhomogeneities and susceptibility effects increase with field strength and so do artefacts in EPI that occur as a result of the very low effective bandwidth in the phase encoding direction. To increase the resolution without sacrificing the contrast (similar TR and TE), segmented EPI can be used. Instead of a single shot that covers the complete k-space, the latter is acquired via two or three segments, relaxing the demand on the hardware but also increasing the chance of artefact due to movement. Partial Fourier sampling or parallel imaging techniques enable the echo train length to be shortened while maintaining the same resolution (and same FOV) at the expense of reducing the available SNR. The use of multiple coils allows the number of phase encoding steps to be reduced while maintaining the same k-space sampling area. In this way, the acquisition time is reduced compared with the conventional EPI method, and this also reduces the cumulative effect of field inhomogeneity, reducing geometric distortions.

2.4 Instrumentation

To be able to produce an image of a sample, an MR scanner is composed of a multitude of components, the main magnet producing the static magnetic field, the gradient coils encoding spatially the NMR signal, the RF system exciting and receiving the NMR signal, the console where the physicist and/or the clinician command the scanner and receive the data, and all the in-between necessary electronics. This section provides a description of these components.

2.4.1 Main magnet

In order to produce enough signal/polarization out of the spins in a human body, a large magnetic field is necessary. A magnetic field can be produced via a permanent magnet, however the resulting magnetic field cannot reach a strength higher than 0.3 Tesla. Another way to produce a magnetic field is to induce a current inside a solenoid or a pair of loops (or more), the induced field depending on the intensity of the current inside the wires as well as the number and arrangement

of the loops. An efficient way to run high current is to use superconducting wires, *e.g.* made of niobium-titanium (Nb_3Ti), which lose all resistance to current flow at temperatures lower than $9.5°K$. To produce such a low temperature, a bath of liquid helium (boiling at $4.2°K$) is used to keep the wires superconductor, restricting the need for a strong electric current to installation only, *i.e.* during the built up of the magnetic field. The Nb_3Ti wires/helium mix was immersed historically in another bath of liquid nitrogen (boiling at $77°K$) to reduce thermal loses. Nowadays, cryo-coolers are used to pump out the heat of the system as low as $70°K$ based on the Stirling engine. This overcomes the need to use Nitrogen and subsequent reducing the running cost of a superconducting magnet. Active or passive shield also surround the magnet in order to reduce the fringe of the magnetic field at the edge of the magnet. Active shielding can be used to reduce spatially the magnetic field outside the bore, but also has the consequence of reducing the field inside the bore. The Nottingham 7T system is passively shielded with a total of 200 tonnes of iron.

2.4.2 Shim coils

A superconducting magnet generally produces an homogeneous magnetic field with deviations of about ±100 ppm, which would be unusable for imaging purposes. Shimming the magnet reduces the inhomogeneities by up to two orders of magnitude. This is done at the installation of the magnet by passive shimming: *i.e.* additions of small pieces of iron inside the magnet bore to shape the field as desired. The position of the irons pieces is done with the help of a computer, which repeatedly computes the position of new pieces of irons until the field is considered homogeneous. Active shielding is achieved by adjusting the current flowing inside additional coils, also placed inside the magnet bore, until the magnetic field is considered homogeneous. Shim coils may be superconducting and/or room-temperature resistive coils of wire. The later technique has the advantage to be possible without hardware changes, repeatable at will, even with a patient inside. A combination of the two is generally used for high magnetic field magnets to ensure that the generated magnetic field is homogeneous enough for imaging purposes.

2.4.3 Gradient coils

Gradient coils are generally placed inside the shim coils and deliberately alter the magnetic field when energized in order to localise the NMR signal. An MRI system has typically three orthogonal gradient coils, replacing the early use of the shim coil to alter B_0 [4]. Due to high current necessary to produce the localisation gradients ($\sim$ 600 A), the coils are generally water-cooled to prevent over-heating. Gradient coils installed in the Nottingham 7T Philips scanner produce a field gradient of 40 mT/m using a slew rate 200 mT/m/ms. Due to high Peripheral Nerve Stimulation (PNS) issues it was necessary to reduce the gradient strength to 30 mT/m and the slew rate to 100 mT/m/ms. The large, rapidly switched gradients results in eddy currents in any conducting surface close to the coils, particularly the inner part of the cryo-shields very close to the gradient coils. The changing magnetic fields created by the gradient coil induce electric potentials inside the nearby metal, producing eddy-currents. If the metal is forming a closed loop, an additional magnetic field opposed to the source field is created. One way to remove this field is to shield the gradients, a method initially presented by Turner and Bowley **??**, so that no reflective field is produce inside the bore of the magnet. Another way to overcome this, one way is to modify the gradient shape initially put in the gradient coil so that the final gradient sensed by the sample (due to the coils and the eddy currents) is actually the original one. Another method developed by Bowtell and Mansfield [2] consists of actively cancelling the eddy currents (active magnetic screening) by designing a coil to apply an opposite field to the unwanted one in the region of the scanner housing, but not in the bore.

2.4.4 Waveform controller

The waveform controller controls the MR system during an experiment. A pulse sequence is downloaded from the master computer at the start of a scan. The waveform controller then generates the required gradient waveforms, which are passed to the gradient amplifiers and then to the coils, sets the frequency generated by the RF synthesizer and produces the RF pulse envelope. It also gates the digitizer during reception.

2.4.5 RF transmission and reception of the NMR signal

The RF system, also known as the RF chain, is responsible for generating the oscillating B_1 field used to excite the sample and for reading back the NMR signal it produces. The RF signal is generated by the spectrometer. An adjustable frequency synthesizer produces the pure radio frequency signal ω_0, which is then mixed with a pulse envelope (for example a $sinc$ function) and passed to the RF power amplifier. The required peak RF power level is high, the Nottingham 7T system being equipped with a 4kW amplifier. However, a typical imaging sequence consists of a small number of short RF pulses, so the average transmitted power is much lower. The RF probe then converts the electrical signal from the power amplifier into a homogeneous oscillating magnetic field inside the sample. The probe, in combination with the power amplifier, must be capable of generating a 15 to 20μT B_1 field inside the sample. Following excitation, the system switches to receive mode. The receive probe detects the weak rotating magnetic field generated by the sample due to the NMR effect and converts it back to an electrical signal via Faraday induction. The same probe may be used for both transmission and reception. However, because the transmit signal ($\sim$ kV) is much larger than the receive signal ($\sim$ μV), the pre-amplifier must be protected from the transmit system. A TR (Transmit/Receive) switch is used to isolate the pre-amplifier during RF transmission. The pre-amplifier is placed physically close to the probe to reduce SNR loss in the connecting cable. The amplified signal is then fed back to the spectrometer outside the shielded room. The spectrometer splits the received signal and mixes it with a reference signal at 0° and 90° to generate real and imaginary channels at a lower intermediate frequency. Both channels are then low-pass filtered and digitised. The sampled data is then passed to the main computer for reconstruction. Modern systems often sample the intermediate or radio frequency signal directly, and perform quadrature detection and low pass filtering digitally.

Transmit and receive coils RF coils are used to excite the spins in a sample and to detect the resulting MR signal. The transmit coil is generally large, *e.g.* the volume coil, in order to produce a homogeneous RF field over the entire field of view to image. In order to use a volume coil the target anatomy must fit totally within the coil. In contrast, the receiver coil is generally positioned close to the surface of the anatomy to be imaged to optimise the quality of the received signal. To image specific anatomy (knee, shoulder, spine, *etc.*) surface coils have been developed to sit right

at the surface anatomy. These coils cannot be used as transmit coils but provide extremely high SNR at their vicinity, with the penalty of having high non-uniformity. It is also now common for MR systems to have multiple independent receive channels for use in parallel imaging. The coil used in the Nottingham 7T Philips scanner is a NOVA head coil with one volume transmit coil and 16 independent receive channels. This platform was used both for transmission (volume coil) and reception (16 channel coil) for all the remaining of this thesis. Coils with multiple transmission channels are being developed that will potentially achieve uniform RF excitation and increased sensitivity, and thus time efficiency, for high-field MRI.

2.5 Safety aspects

The safety and comfort of the subject is important at all field strengths, but physiological aspects have been under scrutiny as they scale with magnetic field strength. Particularly, the gradient switching necessary for fast imaging experiments causes noise over the discomfort limit of 99 dB, making the use of ear plugs compulsory. Dizziness and nausea have been reported, but are transient, and can be reduced by moving slowly the patient through the fringe of the magnetic field (at the edges of the magnet), as well as reducing the movement of the patient inside the magnet to the strict minimum. Metallic taste, particularly while speaking inside the magnet, has been reported, but will go away outside of the scanner. Specific studys reporting all these effects have been carried out in diverse sites, with no severe or long term side effects reported so far.

The attractive force of a magnetic field on anything ferromagnetic can turn ordinary objects into potentially lethal projectiles. The force of attraction is dependent on the strength of the static field, the strength of the spatial gradient, the mass of the object, its shape and its magnetic susceptibility. The danger posed by the attraction of ferromagnetic objects, ought to be reduced by limiting the possibility of such objects coming within the stray field of the magnet. This is achieved by ensuring that all scanner rooms are only accessible through security doors and by providing lockers for items which should be left outside, such as keys, watches, mobile phones *etc*. Subjects who are particularly at risk are those with metallic or electronically activated implants, such as cardiac pacemakers. Magnetic field related translation and torque on implants may cause a hazard to these subjects.

The major party of the RF power transmitted to the sample is transformed into heat within the patient tissue as a result of resistive losses. The dosimetric term used to describe the absorption of RF radiation is the specific absorption rate (SAR), a mass normalized rate at which RF power is coupled to biologic tissue and typically indicated in units of watts per kilogram (W/kg), as already mentioned in section 1.4.2. However, special care is necessary with the use of additional hardware positioned close to the subject (such as surface coil), as cables presented in the RF field can create skin burn.

Bibliography

[1] M. Bernstein, K. King, X. Zhou, and W. Fong. *Handbook of MRI pulse sequences*, volume 32. Academic Press New York, 2005.

[2] R. Bowtell and P. Mansfield. Gradient coil design using active magnetic screening. *Magn Reson Med*, 17(1):15–9; discussion 19–21, Jan 1991.

[3] A. Garroway, P. Grannell, and P. Mansfield. Image formation in nmr by a selective irradiative process. *Journal of Physics C: Solid State Physics*, 7:L457–L462, 1974.

[4] A. Kumar, D. Welti, and R. Ernst. Nmr fourier zeugmatography. *Journal of Magnetic Resonance (1969)*, 18(1):69–83, April 1975.

[5] P. Lauterbur. Image formation by induced local interactions: examples employing nuclear magnetic resonance. *Nature*, 242(5394):190–191, 1973.

[6] S. Ljunggren. A simple graphical representation of fourier-based imaging methods. *J. Magn. Reson*, 54(2):338–343, 1983.

[7] P. Mansfield. Multi-planar image formation using nmr spin echoes. *J Phys C*, 10 (6):L55–L58, 1977.

[8] P. Mansfield, R. Coxon, and P. Glover. Echo-planar imaging of the brain at 3.0 t: first normal volunteer results. *J Comput Assist Tomogr*, 18(3):339–343, 1994.

[9] P. Mansfield and P. K. Grannell. Nmr 'diffraction' in solids? *Journal of Physics C: Solid State Physics*, 6(22):L422, 1973.

[10] J. P. Mugler and J. R. Brookeman. Three-dimensional magnetization-prepared rapid gradient-echo imaging (3d mp rage). *Magn Reson Med*, 15(1):152–157, Jul 1990.

[11] K. P. Pruessmann, M. Weiger, M. B. Scheidegger, and P. Boesiger. Sense: sensitivity encoding for fast mri. *Magn Reson Med*, 42(5):952–962, Nov 1999.

LONGITUDINAL RELAXATION TIME T_1 AT 7T

The contrast in anatomical images of brain tissue generally arises from proton density, T_1 and T_2 variation between different tissue types and regions (e.g., white matter vs grey matter, cortex vs subcortical nuclei). T_1-weighted images are thus a familiar contrast in clinical MRI. In those images, the signal is generally inversely related to the longitudinal relaxation time (T_1) in a non-linear manner, other factors such as the exact radio frequency field, the sensitivity profile of the receiver coil, the receiver gain and the competing effects of different relaxation times will also affect the contrast and signal. This makes the relaxation time a more reliable marker of tissue state than MRI signal intensities alone, as described in details in [36]. Longitudinal relaxation time measurements are presented in this chapter and provide an improved method for studying disease progression and characterizing normal tissues type for instance in studies of factors affecting brain development, with adequate sensitivity and accuracy. While numerous techniques are described in the literature on how to measure the T_1 of human brain *in vivo*, few managed to get a decent coverage in a clinical acquisition time at high spatial resolution. The aim of the principal study presented was to investigate methods of mapping the water proton longitudinal relaxation time (T_1) at 7T at high spatial resolution using the MPRAGE sequence, and to compare values of grey and white matter T_1 measured at field strengths of 1.5T, 3T and 7T. Comparison has been made with two other sequences, the IR-EPI, considered as our gold standard, and the IR-TSE, a spin-echo based sequence. The described technique has been applied in a number of studies, such as the measurement of the evolution of the relaxation time with age,

or measurement of the T_1 alteration inside and around MS lesions at high resolution. Furthermore, knowledge of the tissue relaxation time can be important for sequence optimization, i.e. providing maximum image contrast, optimizing contrast agent dose, and for other quantitative applications such as perfusion measurements. Optimization and quantification of the proposed method will be discussed here.

3.1   Longitudinal relaxation time T_1

The longitudinal relaxation time is a measure of the time necessary to the excited system to return to the thermal equilibrium. This time gives information about the interactions between the spins of interest and the lattice and is typically in the range 0.5 to 5 seconds. Some methods to quantify the time T_1 are reviewed hereafter.

3.1.1   Why is it important to measure T_1?

As stated in the chapter 1, T_1 is related to macromolecular concentration, water binding and water content. As the level of molecular complexity increases and/or the binding of the water is increased, the spins tend to relax more rapidly than in a free water environment. Changes in the internal structure of pathologic brain tissue can be highlighted by mapping the T_1 of those tissues. If a tissue looses its organization such as during inflammation, the intra and inter-cellular water environments change, and thus respond differently to the relaxation process. For example, inflammatory acute MS lesions lead to an increase in T_1 [4]. Conversely, T_1 is reduced at the rim of active MS lesions by the presence of cellular debris which constitute extra-relaxation centres in the fluid. Other changes, such as myelination of developing brain [31], decrease of myelination due to aging [40] or inter-individual variation in the white matter tracts [9] can benefit from T_1 quantification.

T_1 values depend on the main magnetic field. As the field increases it was originally expected that the relaxation times would get longer, and that the values obtained from different tissues would converge toward a single value [23]. This would predict a lower contrast in the brain at higher magnetic fields, making it particularly important to monitor changes in T_1 with field strength. In this

chapter, it is showed that this contrast is not diminished with higher field strength, and that no convergence of the T_1 could be predicted.

3.1.2 Review of Longitudinal Relaxation measurement techniques

As the field strength increases, the resolution can be increased as well, and details inside tissues can be picked up due to changes in relaxation time. Mapping the T_1 inside the brain can thus provide measure of tissue micro-structure. The challenge is then to provide enough sensitivity to T_1 relaxation, as well as high resolution images with good Signal to Noise Ratio (SNR) in a reasonable imaging time. Mapping T_1 requires image encoding to occur simultaneously with T_1 measurement. Several encoding options are available but only methods with strong T_1-weighting in the image and relatively easy modelling will be reviewed. In addition, many methods of measuring T_1 are sensitive to RF pulse amplitude errors arising from errors in pre-scan procedure, non ideal slice profile and transmit non uniformity. Field inhomogeneities (both B_0 and B_1) alter the recorded signal, which can lead to errors in the measured T_1 if not corrected for or accounted for during the quantification process. Requirements of a measurement protocol include: good accuracy and precision; short measurement time; high spatial resolution; good spatial coverage; low image geometric distortion. The optimum method will depend on the application and hence the relative importance of these requirements. The model chosen to fit the data is also important and will be discussed in a later paragraph.

3.1.2.1 Basic principles of longitudinal relaxation time measurement

T_1 measurement requires the recovery of the magnetization in the longitudinal direction to be monitored, but this cannot be measured directly. Instead the magnetization must be flipped into the transverse plane to be measured. By recording the recovery of the longitudinal magnetization at different times following a perturbation, it is possible to measure T_1. This means that at least two pulses are present in the T_1 measurement protocols, an excitation pulse to perturb the system and a readout pulse to measure the state of the system at a given time τ. It is also possible to use the readout RF pulse as an excitation for the rest of the sequence, thus varying only the time between two excitations can provide informations on the underlying T_1 (as described in the next paragraph). The

measurement of the longitudinal relaxation time via NMR imaging, as described by Bakker [3], can be done by acquiring series of saturation recovery and inversion recovery sequences, and recovering the quantities by solving the corresponding model equations. The precision of pulses used for saturation, inversion and imaging is of the greatest importance to the quality of the results.

3.1.2.2 Saturation-Recovery sequence and T_1 measurement

The simplest way to measure T_1 is by Saturation-Recovery (SR), as depicted in fig. 3.1. A 90° RF pulse is applied to flip the magnetization into the transverse plane (Saturation). After a variable time τ, the magnetization recovers to a certain level (Recovery). Another excitation pulse is then applied to flip back this magnetization into the $x-y$ plane to record its amplitude. By varying the time τ, the recovery of the longitudinal magnetization can be sampled. For short τ, the spin system is saturated and the amplitude of the measured signal is low, whereas for longer τ the signal increases approaching M_0, as shown on the fig. 3.2. In order to let the magnetization recover its equilibrium M_0 before the next measurement, the time TD must be long compared to the measured T_1. The evolution of M_z is described by the following equation:

$$M_z\left(\tau\right) = M_0 \left(1 - exp\left(-\frac{\tau}{T_1}\right)\right) \tag{3.1}$$

This technique, with some variations (as the amplitude of the flip angle), has been used for different studies [25, 10, 35]. One of the main disadvantage of this method is the actual saturation pulse performance, which is critical for a robust measurement. The other main disadvantage is the relatively low dynamic range in the recovery data, and a low contrast obtained in the images with a
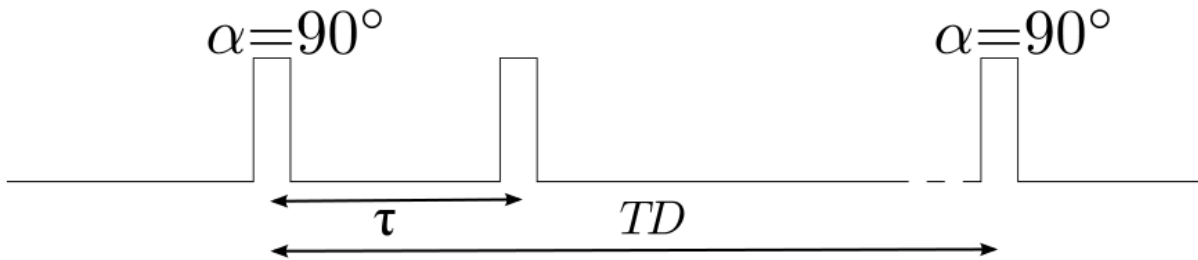

Figure 3.1: Sequence diagram of a simple Saturation-Recovery experiment.

3.1. Longitudinal relaxation time T_1
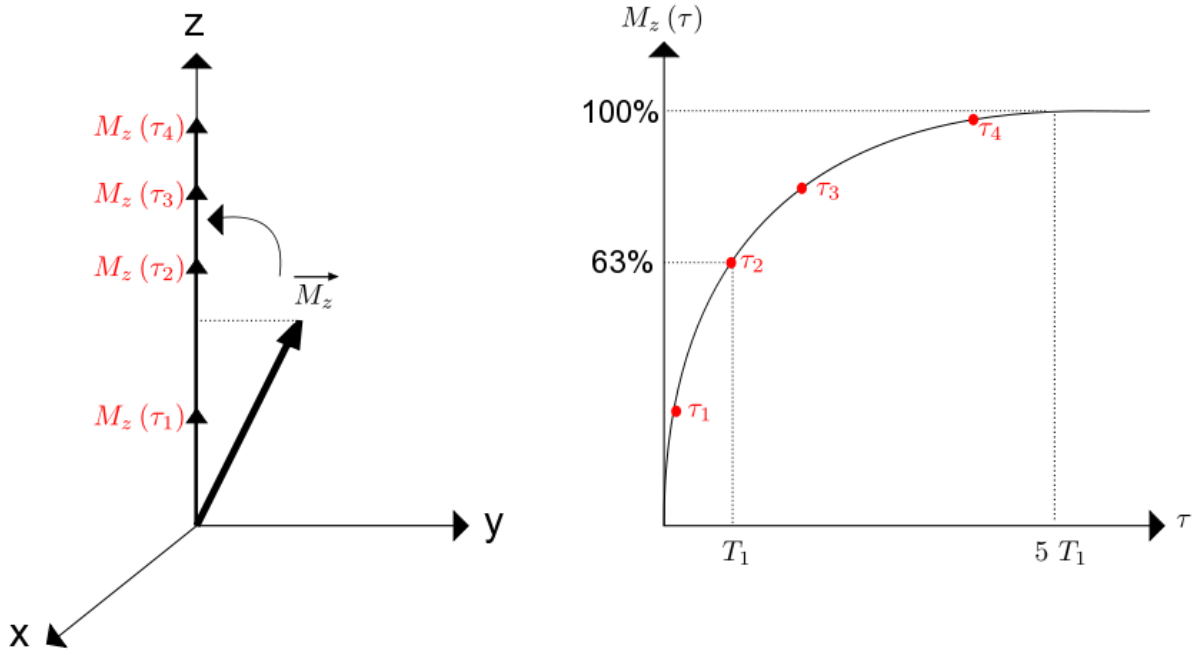
Figure 3.2: Recovery of the magnetization along the longitudinal axis after a 90 degree RF pulse.

short τ. This can be translated in the estimated T_1 as a loss of precision, as the SNR of the estimated T_1 is directly dependent on the ratio of the signal dynamic range, *DR*, to image noise standard deviation [18]. It also creates images dominated by proton density contrast of the region of interest. If the RF pulse is applied at flip angle lower than 90°, the recorded signal does not need to recover fully to be measured again. The resulting steady-state of the signal can be modelled and images acquired at a variety of flip angles can be used to measure relaxation times [30]. To produce this steady-state, also called dynamic equilibrium, identical flip angles (α) are evenly spaced in time by TR and the recorded signal is dependant on the T_1 via the following relation:

$$S = S_0 \ sin\alpha \ \frac{\left(1 - exp\left(-\frac{TR}{T_1}\right)\right)}{1 - cos\alpha \ exp\left(-\frac{TR}{T_1}\right)} \tag{3.2}$$

with S_0 the signal observable after the system is perturbed from equilibrium by a 90° pulse. Varying the repetition time TR can also give information about the time necessary for the magnetization to recover between each excitation. Parker *et al.* [30] used a two point method to fit the T_1 by acquiring the same set of data twice, with two different TRs. The acquisition was performed with a multi-slice 2D gradient echo sequence, and inhomogeneities due to non-uniformity in the slice

selection profile as well as in the RF field were corrected for.

Another method based on the Driven Equilibrium Single Pulse Observation of T_1, or DESPOT, was originally described by Christensen et al. [7], and derives the longitudinal relaxation time from a multi-angle acquisition dataset. The method derives T_1 from a series of two or more spoiled gradient recalled echo (SPGR or spoiled FLASH) with a constant TR and an increasing flip angle, the contrary (constant flip angle and increasing TR) being also possible. This method thus relies on a good knowledge of the transmit/receive field B_1, and makes its application at high field more difficult. Deoni combined both of these approach (varying TR and varying flip angle) to measure the longitudinal relaxation time in the brain [12] at 1.5T without B_1 correction. He then showed [11] that it is possible to acquire a whole brain in ten minutes at 3T with a resolution of 1 mm isotropic, correcting for field inhomogeneities.

3.1.2.3 Inversion-Recovery sequence

The Inversion-Recovery sequence, considered to be the gold standard, uses a nominal 180° inversion pulse to invert the magnetization in the longitudinal plane. After this inversion, the magnetization recovers following an exponential curve. After a variable time TI called the inversion time, the magnetization is flipped via a flip angle θ into the transverse plane in order to be read. For a small TI, the signal will be large but negative. For a longer time TI, the signal will increased to pass by zero and to grow again. After a long ($TI \gg T_1$) wait time, the system is back to equilibrium, with the signal at its maximum. The IR sequence can be repeated for different TI: in this way the recovery curve is sampled for each TI. The evolution of the magnetization is thus described by the following expression:

$$M_z = M_0 \, sin\alpha \, \left(1 - (1 - cos\theta) \, exp\left(-\frac{TI}{T_1}\right)\right) \qquad (3.3)$$

where θ is the amplitude of the inversion pulse (nominally 180°), α the amplitude of the readout pulse, M_0 the longitudinal relaxation time at equilibrium and TI the inversion time, as shown in the fig. 3.3. This sequence is more precise for measuring the T_1 due to the large dynamic range of signal intensity, but still requires a good knowledge on the inversion pulse angle θ. For this purpose,

3.1. Longitudinal relaxation time T_1
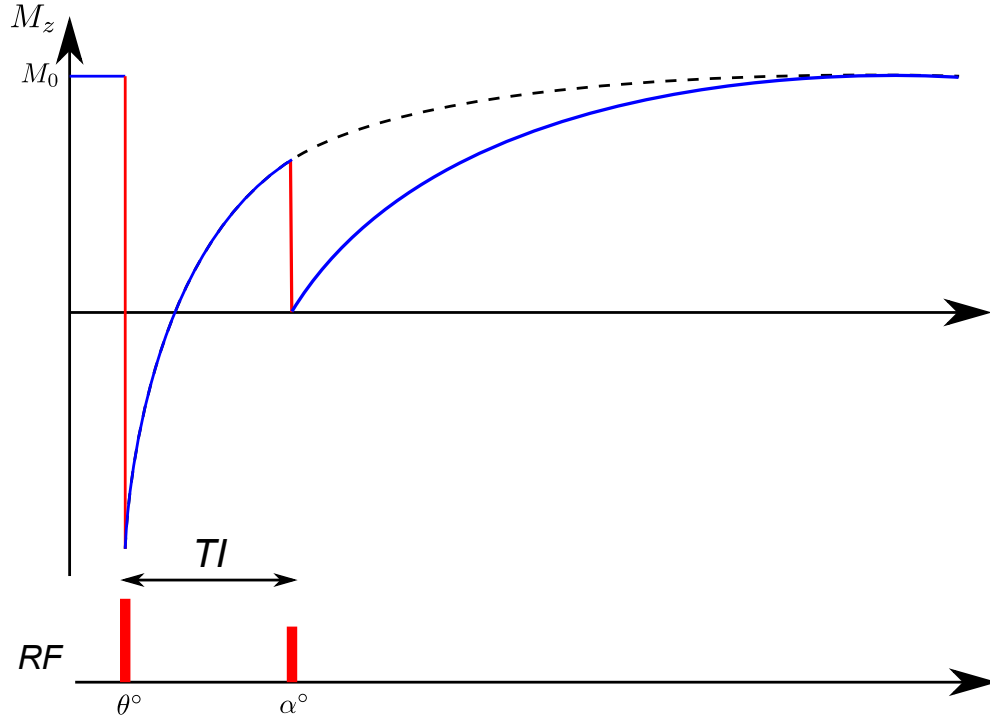
Figure 3.3: Signal and pulse sequence during a Inversion Recovery sequence, the labels corresponding to the equation 3.3, with the angle α being here a 90 degree RF pulse.

adiabatic pulses are used to perform the inversion evenly throughout the region of interest inside the sample, independently of the local B_1 field as described in [16]. A B_1 map can also assess the inhomogeneities on the RF pulses (α) and thus correct it in equation 3.3. Note that after the inversion, any imaging sequence can be use to record the recovering magnetization, as long as the evolution of the magnetization is not affected by the readout process. Sequences such as Echo Planar Imaging or a simple Gradient Echo (GE) readout can be applied as imaging sequence, due to their short acquisition time compared to the measured T_1. However the GE is too long in practice, as after the acquisition of one echo, *i.e.* one line of k-space, one has to wait $5\,T_1$ before the next shot, to have the same initial magnetization (as seen in 3.3).

Quicker GE sequences have been developed where the repetition time TR can be shorter than $5\,T_1$, as with the FastIR introduced by Canet [5] and further optimized by Gupta [17]. The timing of the FIR sequence can be summarized as $[180°, \tau, 90°, (\Delta - \tau)]$, as shown in fig. 3.4. This Fast Inversion Recovery method takes into account the waiting time W (equivalent to TD) between successive measurements, with the time $\Delta = \tau + W$ kept constant, and a minimal value for W greater or equal

than $\sim 3\ T_2^*$. For an optimum value of $\Delta = 2\ T_B$, T_B being the upper limit of the expected T_1, the FIR method needs 11 measurements to reach the same precision as the IR method (*i.e.* for $W = \infty$) provides with 8 measurements, but with a substantial gain in the overall scanning time.
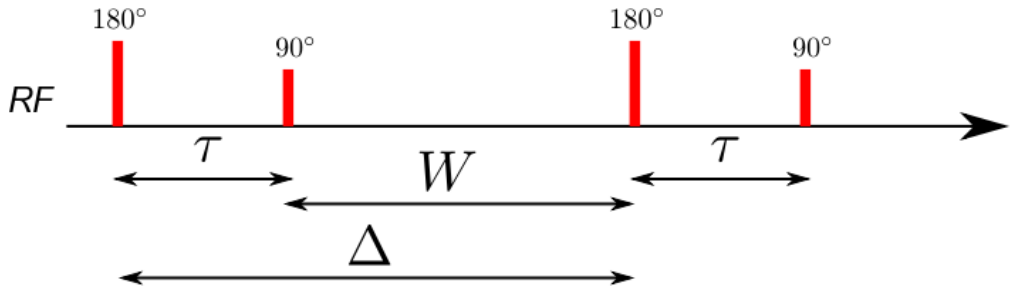

Figure 3.4: Pulse sequence during a Fast Inversion Recovery sequence.

Other methods rely on repeatedly sampling the longitudinal relaxation time with a set of small flip angles during each of the repetition period TR. This is based on the Look-Locker sequence [24, 21] and offers the possibility to sample the T_1 from a single inversion recovery experiment. This required a complete spoiling of the remaining transverse magnetization between two different RF pulses. This has been used in different studies, both in 2D and 3D versions [19, 35], but suffers from a high dependency of estimated T_1 on the flip angle α. It also required the establishment of a steady-state, with an equally spaced sampling period TR. However, it can be used for dynamic contrast uptake studies [22], which make it an ideal tool to observe the uptake of contrast agents inside the blood for example. Other methods based on the Look-Looker sequence have been recently implemented, such as the TAPIR technique introduced by Shah *et al.* [34]. This particular method provides the possibility to acquire a multitude of points to sample the recovery curve. This is achieved by using several very low flip angle to sample continually the recovery curve, leading to an effective longitudinal relaxation time T_1^* shorter that the real T_1, as each flip angle reduces the available longitudinal magnetization for the next pulse. Relation between T_1^* and T_1 can be derived from the dynamic equilibrium state and the sequence timing, and the real T_1 recovered.

To reduce the overall scanning time, Deichmann *et al.* [10] used a pre-saturation module before the actual Inversion-Recovery sequence, destroying the magnetization of the previous acquisitions and providing a constant magnetization for the IR module. Between the pre-saturation and the inversion pulse, a constant time Δt is provided for the magnetization to recover, the recovery being dependant

only on the T_1. This has the advantage to reduce the TR, since the longitudinal magnetization does not need to return to equilibrium before the next acquisition. This technique does not necessitate a precise radio-frequency, as the model of the evolution of the magnetization is independent of the pulse efficiency. However this results in a loss of dynamic contrast range if Δt is too short, reducing the precision of the T_1 measurement.

Finally, another method presented in [43] uses a constant relaxation period TD after the sampling of the recovery, while the repetition time TR and the inversion time TI are variables. Its advantages are the robustness to RF inhomogeneities as well as a two fold decrease in sensitivity to noise in the T_1 measurement. Another advantage of this technique is the relative insensitivity of the measurement to the repetition time, independently of the dynamic range of the signal. However it only has been used for low abundance species, as selected carbons of sucrose [43], with no applications in humans. The main reason might be because the technique necessitates a period between the two measurements similar or superior to the estimated T_1 value, making the acquisition slightly long. This method also had been investigated by Gupta *et al.* [17], but did not found any improvement in efficiency compared to the FIR method.

For most of the sequences presented in this paragraph, the repetition time still has to be long compared to T_1. To make the acquisition time shorter, one strategy consists of interleaving acquisitions, more favourable to 2D imaging. Selective inversion and acquisition is performed normally, with the idle time for a given slice location used to perform another slice inversion or acquisition. For 3D imaging, the use of multiple slabs with interleaved acquisition can also speed up the acquisition. In the following, more sophisticated sequences are used in order to sample the magnetization more efficiently.

3.1.3   Possible readout schemes to map the T_1

Many versions of the standard Inversion Recovery methods are present in the literature, with the main variation being the readout used for the acquisition of the image. For instance techniques such as FSE, RARE, EPI or GRASE provide multiple samples of the transverse magnetization and fill several k-space lines with one excitation pulse. An hybrid T_1-mapping technique based on the Look

and Looker has been presented and takes advantage of the evolution of the T_1 through the k-space [38], by modelling the magnetization evolution during the acquisition of the k-space. Two modified Turbo-FLASH acquisitions are necessary, one T_2^*-weighted (*i.e.* a normal Turbo-FLASH acquisition), and one T_1-weighted (*i.e.* a Turbo-FLASH immediately preceded by an inversion pulse). While the first set of data maps the complex evolution of the magnetization inside the k-space, the second gives information about the T_1 recovery. A modified 2D Fourier transform is used to compute the T_1 map. Acquisition time can be less than 3 seconds, making it appropriate for dynamic T_1 mapping, such as tracking injection of a contrast agent [26].

Another possibility is to collect multiple lines of k-space using multiple readout pulses after each Inversion-Recovery period. In this case each k-space data will have a different TI. The desired TI is then usually defined by the acquisition of the centre of the k-space, as the T_1-weighted contrast is predominantly determined by the longitudinal magnetization at that time. This method is used for the IR Turbo Spin Echo sequence and consists of the acquisition of multiple spin echo after a single inversion pulse. It will be compared to the MPRAGE sequence, an IR Turbo Gradient Echo introduced by [27] and further described in section 3.1.3.3, somewhat similar but based on multiple gradient echoes. Using faster readout such as EPI makes sure that no relaxation happen during the readout, and will be considered here as our gold standard.

3.1.3.1 IR-EPI as a gold standard

The fastest way to acquire an image is by using an EPI sequence, i.e. an Echo Planar Imaging sequence (described in 2.3.3). This method is particularly attractive for measuring relaxation times for two main reasons: 1) it involves a minimal number of RF pulses, so opportunities for introducing systematic errors are reduced 2) as the whole image is acquired in a very short time (few *ms*), it is possible to use a long wait time (TD), simplifying modelling and further reducing the sensitivity to pulse errors, and reducing movement artefacts within the image readout. Measurement of T_1 with an IR-EPI sequence provides a reliable and relatively quick technique to measure T_1 in the brain of healthy subjects, and has been used extensively for T_1 measurement in MRI [29, 14, 8]. While the spatial resolution of the EPI images cannot be made very high, it provides a gold standard to refer to. T_1 measurement can be precise, if it is ensured that there is no pre-saturation, so that the

3.1. Longitudinal relaxation time T_1
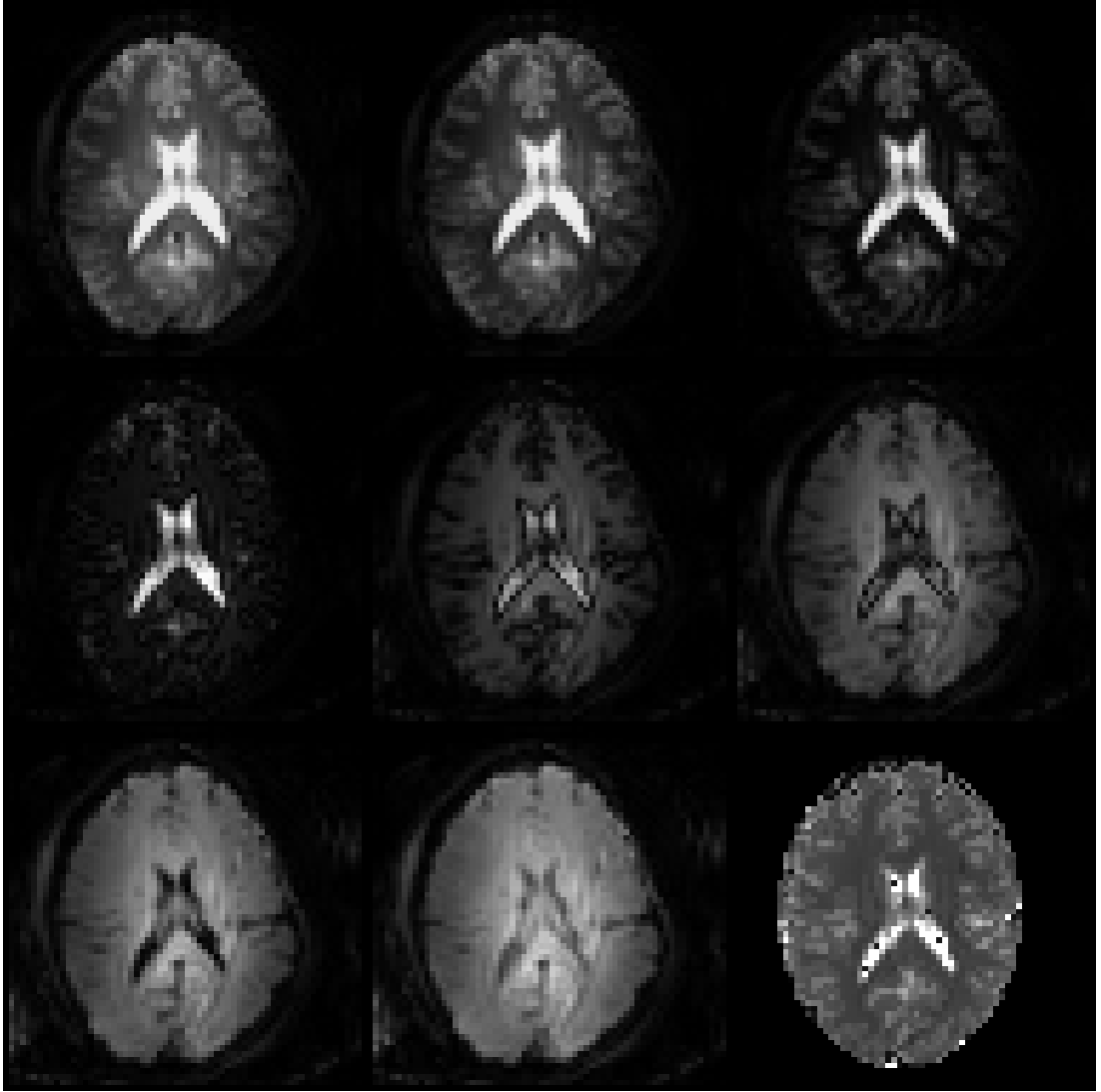
Figure 3.5: Set of 8 axial slices of an healthy subject at 7T with an IR-EPI sequence, together with the corresponding T_1 map (last image).

magnetization recovers completely between each inversion of the magnetization. Several samples of the recovery curve are necessary for the T_1 to be measured precisely, this number depending also of the noise level in the images. The timing at which each sample is taken is also important and can be optimized before performing the experiment, as described in [39] and further discussed in the section 3.2.2. Fig. 3.5 shows a set of eight images acquired at various inversion times with an EPI readout. Using the equation 3.3, a pixel-by-pixel fitting process can be used to create a T_1 map from the eight acquired images.

3.1.3.2 Inversion-Recovery Turbo Spin Echo sequence
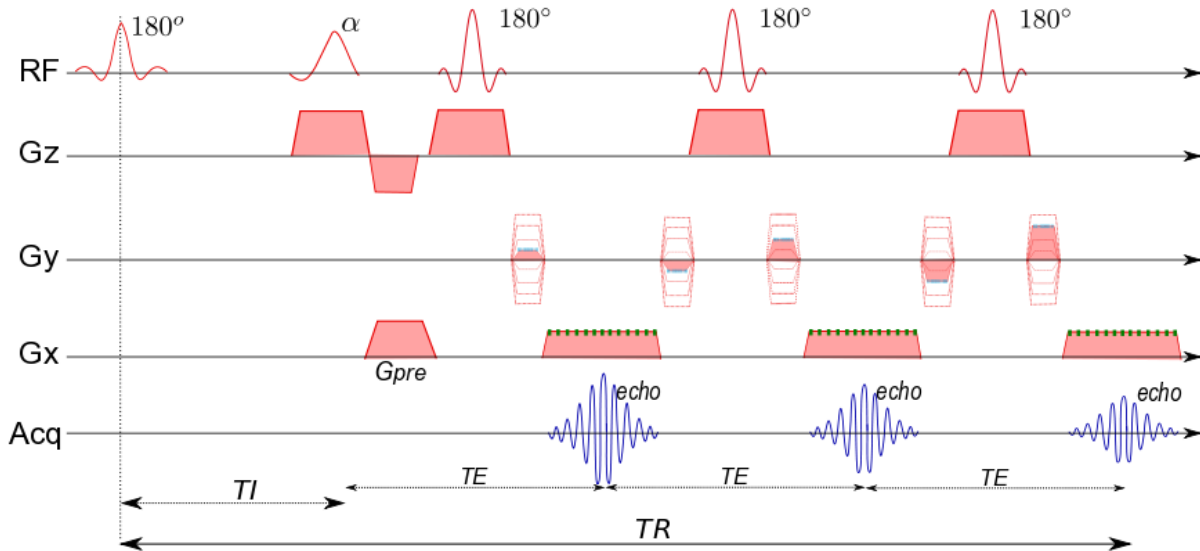
Figure 3.6: Schematic description of IR-Turbo Spin echo acquisition for single slice imaging. The diagram describes the evolution of the radio-frequency pulses and the gradients during the acquisition of one echo train after an inversion pulse and a recovery period TI, the repetition time TR being much longer than the acquisition time, providing possibility to interleaved imaging.

While a standard Inversion Recovery Spin echo sequence records a single line of k-space per excitation pulse, the IR Turbo Spin echo (IR-TSE) uses only one excitation pulse and a chain of spin echoes to record many lines of k-space. The TSE sequence, also called Fast Spin echo (FSE) or Rapid Acquisition with Refocused Echo (RARE), is similar in concept to the EPI sequence (described in 2.3.3), but with multiple refocusing 180° pulses used after the excitation pulse to continually refocus the transverse magnetization and create a train of echoes, as presented in fig. 2.4. Each echo, however, has a different amount of phase encoding as well as a different amplitude due to the intrinsic T_2 decay of the transverse magnetization. Applying an inversion pulse before the TSE block determines primarily a T_1-weighting inside the image, even with a long train. This makes this protocol applicable clinically, but not without artefacts. The interleave of slice acquisition during the different recovery time increases significantly the speed of the imaging process, possibly creating crosstalk when the slice gap is too small. The slice selection can also create off-resonance saturation in the neighbouring slices, altering the true T_1 contrast in the final image. 3D IR-TSE techniques exist and could overcome some of these issues, but necessitate a large number of refocusing pulses, highly increasing the power deposited in the subject. The associated scanning time becomes longer, especially at high field.

3.1. Longitudinal relaxation time T_1

3.1.3.3 The MPRAGE sequence for T_1 mapping?

MPRAGE sequence description The MPRAGE sequence introduced by [27], also called IR-TFE on Philips scanners, is a 3D imaging technique with a T_1-contrast driven by both the flip angle of the inversion pulse (normally a 180° adiabatic pulse) and the flip angle of the excitation pulse α.
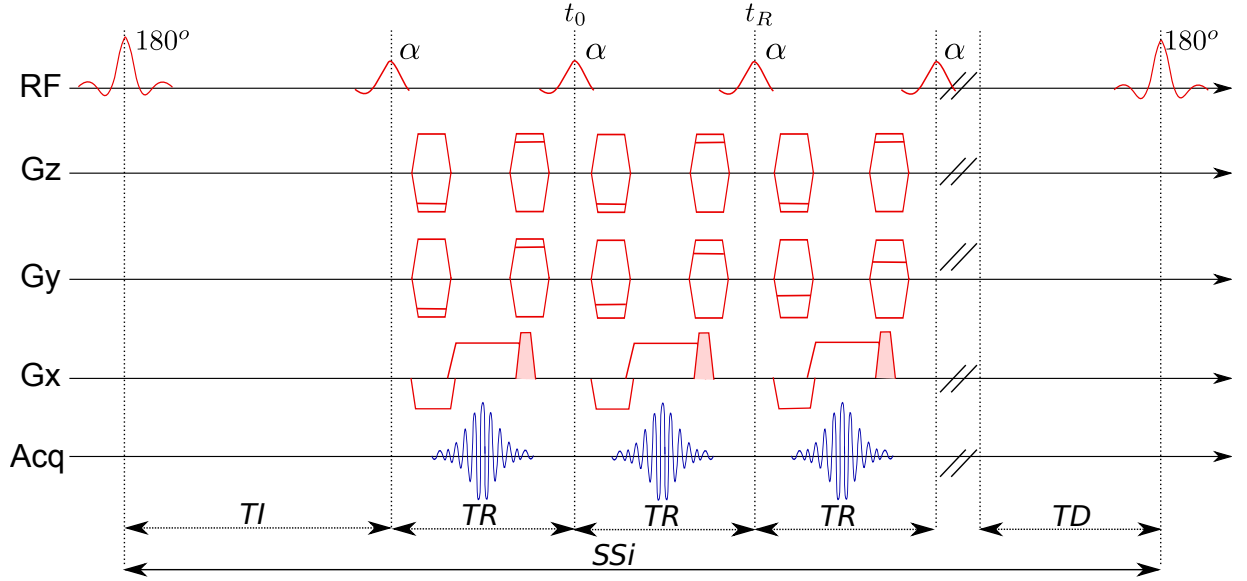
Figure 3.7: Schematic diagram of the 3D TFE-FFE sequence, or MPRAGE sequence with spoiler gradients at the end of each TR.

The pulse sequence depicted in 3.7 is based on the inversion recovery pulse sequence, with the time delay between the inversion and the excitation pulse known as the inversion time (TI). After the time delay TI, the TFE-FFE (Philips terminology) is played out, with its own parameters. TR is the repetition time between the excitation RF pulses of angle α while TE is the echo time of the FFE readout. The number of FFE pulses inside the train is called the TFE factor, while the delay between the end of the train and the next inversion pulse is called the delay time TD. If n is the number of excitation pulses in the train, named the TFE factor on Philips scanners, then the Shot to Shot interval (SSi), *i.e.* , the time from one inversion pulse to the next one, is given by $TI + nTR + TD$. The intrinsic readout method used here is a T_1-FFE pulse sequence, also called incoherent gradient echo (RF spoiled), where the residual transverse magnetization is spoiled using a phase cycling scheme. This is used instead of gradient spoiling to make the available TR shorter. This scheme is a standard protocol used for neuroanatomy purposes, as it gives an exquisite visual contrast

3.1. Longitudinal relaxation time T_1

(see fig. 3.8) between the white matter, the grey matter and the CSF, the three main constituents of the brain tissues. However the transformation of this sequence into a quantitative imaging facility is not straightforward, as discussed in the next section.
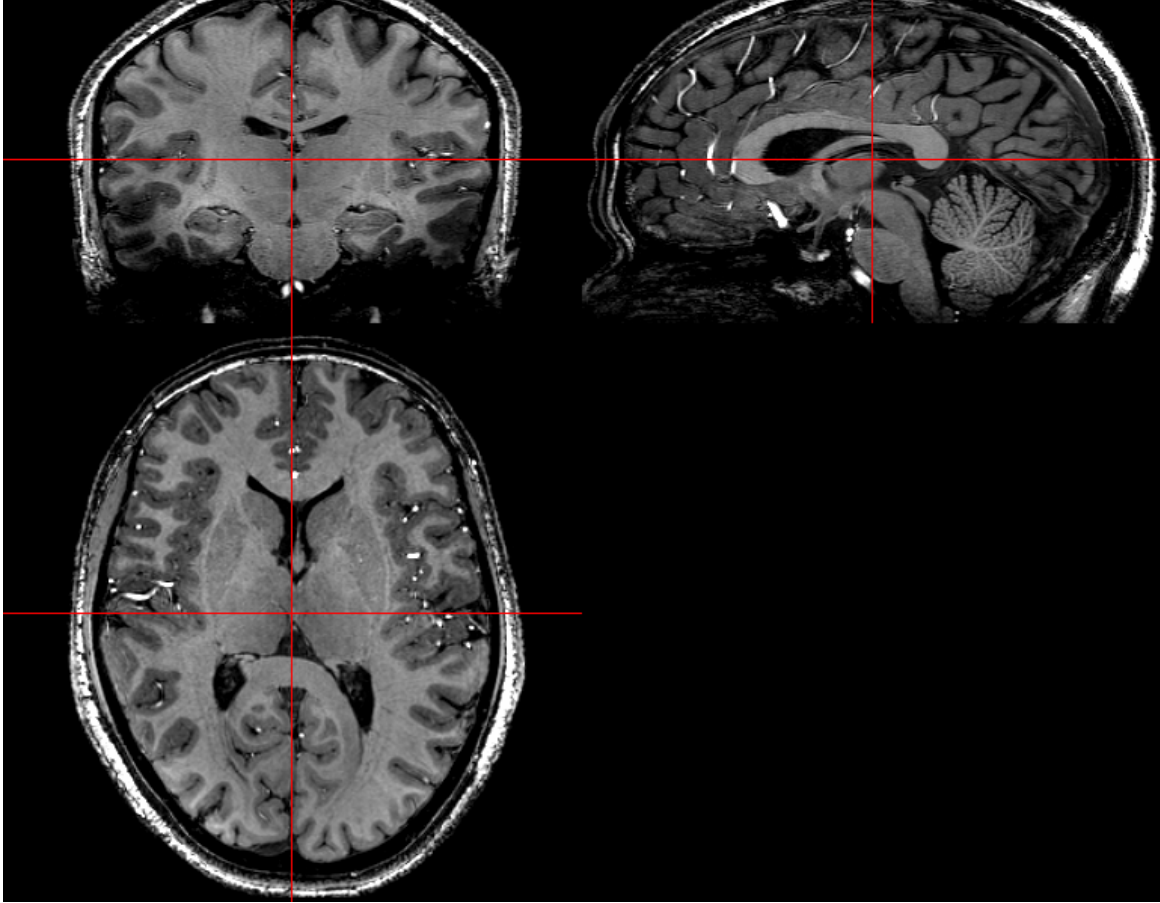
Figure 3.8: Image acquired with the 3D TFE-FFE sequence (MPRAGE) over the whole brain at a resolution of 0.5 mm isotropic.

The image in 3.8 was acquired with a TI of 1051 ms, a TR of 15 ms and a TFE factor of 148. The overall scanning time was 10 min and 8 sec, for a total FOV of 192mm x 130mm x 164mm. The MPRAGE sequence displays a contrast weighted by the T_1 of the tissues, as does the SPECIAL sequence [13], both GRE imaging methods. The SPECIAL sequence differs from the MPRAGE one by the absence of recovery time TD between the end of the acquisition and the next inversion, and was shown to produce similar contrast with shorter acquisition time. However the dynamic range of signal intensity is largely reduced, making the acquisition of contrast reversal and null signal impossible.

Why choose the MPRAGE sequence for T_1 mapping? One particular target of this study was to map the relaxation times inside the brain by avoiding partial volume effects as much as possible. For this, high resolution images with as little distortion as possible was necessary. As lots of studies are using an anatomical T_1-weighted MPRAGE scan for high resolution imaging and for segmentation purpose, the choice of this sequence for mapping the T_1 was tempting. Moreover, this sequence has a good coverage due to its 3D nature, with possibility of isotropic resolution with reasonable SNR, advantageous for reducing the partial volume effect into the T_1 measurements. By using an already widely used sequence, and changing only one parameter (the inversion time) to perform the acquisitions, T_1-weighted can be used for anatomical imaging as well as T_1 mapping. Moreover, as shown in the chapter 5, the MPRAGE sequence can also be used to perform other measurements, this versatility facilitating the scanning process as the planning and the registration procedure.

3.2 Use of MPRAGE for high resolution quantitative imaging

The challenge of obtaining high resolution images for T_1 mapping rely on the timing of the sequence, short enough to be applicable clinically, but long enough to get the highest dynamic range necessary to have reliable T_1 measure.

3.2.1 Modelling the acquisition protocol

The quality of the maps not only depends on the images quality, but also on the exactitude of the model. Specific description of the model, later used for the fitting, is presented here.

3.2.1.1 Preparation of the TFE acquisition

Contrary to other imaging sequences, image data are acquired during the approach to steady state in a MPRAGE protocol. The longitudinal magnetization is inverted via an adiabatic pulse, before relaxation occurs during the time TI. Sampling then proceeds in a low to high spatial frequencies: this scheme is chosen to optimize the T_1 contrast in the image, the tissue contrast being mainly determined by the value of the longitudinal magnetization when the central k-space lines are acquired. For a spin

ensemble with longitudinal relaxation time T_1, the equilibrium longitudinal magnetization is driven into a steady-state via preparation cycles. Simulation shows that repeating the sequence described in fig. 3.9 three to four times (depending on T_1) leads the magnetization after the inversion pulse to reach a constant value M_I. This step is implemented inside the scanner via preparation cycles so that the acquired signal is acquired at a steady-state.

3.2.1.2 Model description
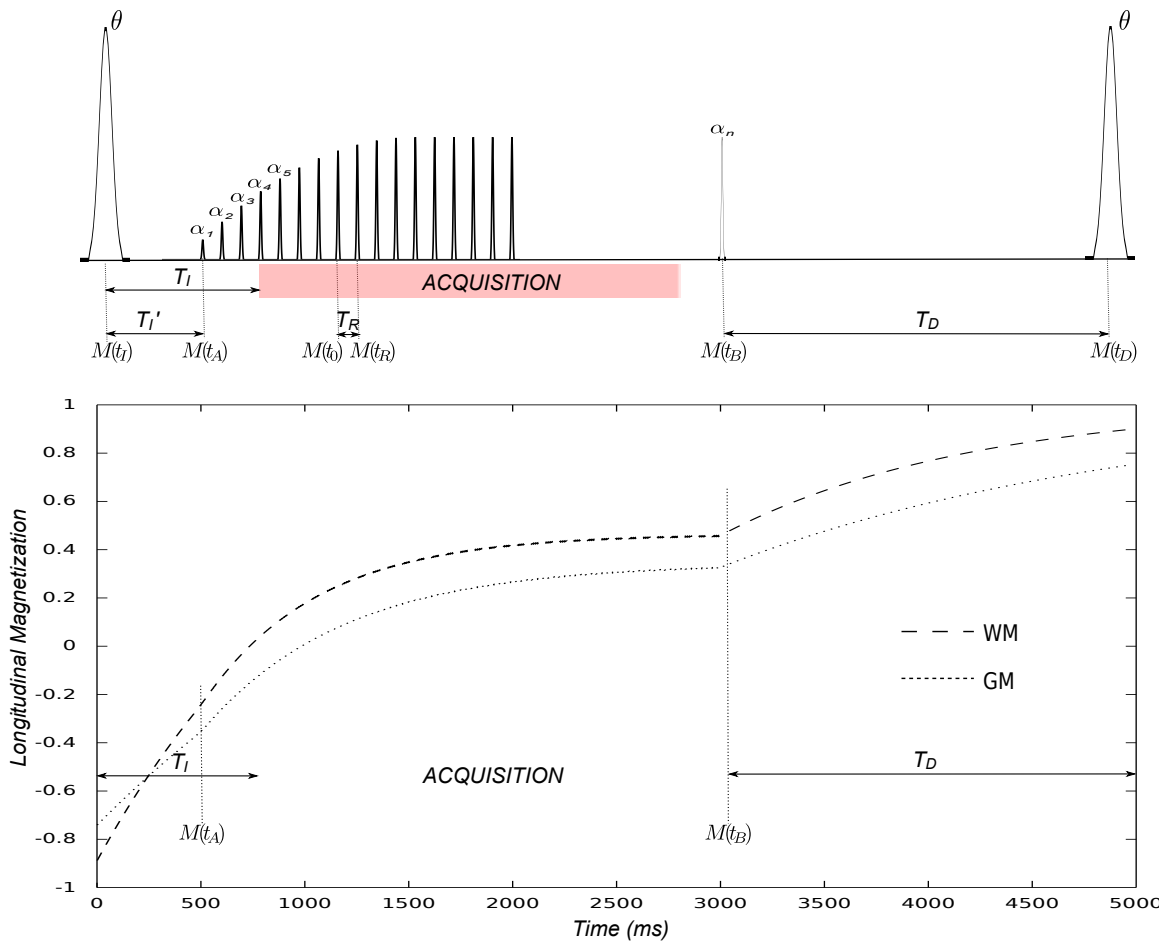
Figure 3.9: Schematic diagram of the ramping of the readout pulse during the 3D TFE-FFE sequence, together with the evolution of the magnetization during the acquisition.

Once the details of the imaging sequence are completely known, the evolution of the signal can be modelled. Assuming that the spoiling is perfect, we can ignore the evolution of transverse magnetization for the modelling. Each excitation pulse converts the available longitudinal magnetization

into transverse magnetization, which produces a signal that can be recorded using a GRE. The present concern is to determine the longitudinal magnetization before each RF pulse during the sequence. After the inversion, the available longitudinal magnetization M_I relaxes during the time TI'. Between the time TI' and the time TI, the defined Inversion Time, a ramping pulse train is played to give a smooth evolution of the magnetization through the k-space. The exact effect of this ramp will be examined in chapter 5, but the general effect of this ramp is to provide a better imaging quality (Point Spread Function sharper). The start-up consists of a series of RF pulses with variable flip angles, ramping up to the nominal value, but without gradient readout. Data are acquired after the first third of the ramp. In the Philips implementation, the initial sweep consists of the rise of the flip angle from 0 to the nominal value in a quadratic manner, as presented in fig. 3.9. The duration of the ramp is defined automatically (generally 20 pulses) or manually in the Philips software. The number N_{ramp} entered corresponds to the number of pulses applied before the start of the first acquisition readout, *i.e.* :

$$TI = TI' + N_{ramp}TR \qquad (3.4)$$

However, the ramping does not reach its maximum flip angle α_n at the time TI, the total of ramping RF pulses being $M_{ramp} = 3 * N_{ramp}$. The flip angle for each pulse during the ramping period is then defined by:

$$\alpha_i = \alpha_n \left(1 - \left(\frac{M_{ramp} - i}{M_{ramp}} \right)^2 \right) \qquad (3.5)$$

The longitudinal magnetization at a time TR after each excitation pulse (either during the ramping or after) can be calculated recursively from the time t_0 (the time immediately after the pulse) to the time t_R via:

$$M(t_R) = \rho \left(1 - e^{-\frac{t_R}{T_1}} \right) + M(t_0) \cos(\alpha) e^{-\frac{t_R}{T_1}}, \qquad (3.6)$$

with the time t_0, t_R and TR defined as: $TR = t_R - t_0$, as defined in fig. 3.7. At the end of the acquisition segment (*i.e.* at the time t_B), the longitudinal magnetization recovers during the recovery

period t_D to:

$$M(t_D) = \rho \left(1 - e^{-\frac{t_D}{T_1}}\right) + M(t_B)e^{-\frac{t_D}{T_1}}, \tag{3.7}$$

where $M(t_B)$ is the longitudinal magnetization at the end of the acquisition segment, i.e. after the nth excitation pulse. After t_D there is an inversion of flip angle θ followed by a delay t_I (equivalent to TI') so that the longitudinal magnetization directly before the acquisition block has the value $M(t_A)$ equal to:

$$M(t_A) = \rho \left(1 - e^{-\frac{t_I}{T_1}}\right) + M_I \cos(\theta)e^{-\frac{t_I}{T_1}} \tag{3.8}$$

By numerically simulating the evolution of the longitudinal magnetization using equations 3.6, 3.7 and 3.8 one can see that the steady state is reached after a few cycles for M_I. Using this steady-state value as the starting point in equation 3.6, the signal intensity at the beginning of each acquisition segment is kept the same, and can be used for the following step, namely the fitting procedure. The analytical expression corresponding to the succession of these RF pulses on the longitudinal magnetization can be obtained by assuming the equilibrium expression:

$$M(t_D) = -M(t_I) \tag{3.9}$$

However the exact solution is becoming too complex as the number of FFE readouts becomes larger, and a simplified solution cannot be found easily. Algebraic computation was performed via the Maple software package [6] and simplification done. The obtained expression was still impracticable, explaining the choice of numerical simulation for the present case.

3.2.2 Protocol design and optimization

The MPRAGE sequence is a 3D slab-selective sequence, necessitating several volume acquisitions with different TIs to measure the T_1 in tissues. The choice of pulse spacing is thus as important as the number of measurements in the minimization of experimental uncertainties or the reduction

of experimental running times. If the model does not introduce bias in the estimation process, errors on T_1 measurement can come from instrumental errors, such as noise. The goal of this protocol is to provide a T_1 map of the tissues in a clinically feasible time, thus a compromise between scan time and SNR has to be found. From the model described in 3.2.1, three parameters are unknown, namely M_0, T_1 and the flip angle θ. The number of measurements has to be optimized to measure accurately these three parameters, or at least the parameter T_1. As shown by Weiss and Ferretti [39] with a three parameter estimation in an IR experiment, the inversion time of the different measurements has to be spaced quadratically to optimized the estimation of T_1. In the following, errors due to noise are minimized for a fixed scanning time with the minimization of the covariance matrix and with a Monte-Carlo simulation method, both numerical methods due to the complexity of the analytical expression of the measured signal.

3.2.2.1   Numerical evaluation

The first experimental parameters for the acquisition are derived from the MPRAGE sequence and are TR = 11ms, TE = 6.7ms, flip angle of the FFE readout β = 8°. The SSi is 5 sec, for a total acquisition time per TFE train of 2.7 sec, letting a maximal inversion time of 2.1 sec. The reconstructed matrix size was 256x256x20, for a voxel size of 0.86x0.86x1.5 mm^3. Based on [39], data were acquired using eight inversion times of 160, 190, 285, 441, 680, 1050, 1619 and 2100ms in a random order, giving a total scanning time per inversion time of 1min40s. Optimization of the sequence was based on these parameters, as those provide a good image quality, a parameter not taken into account in the present optimization.

The steady-state signal in each MPRAGE image was calculated as a function of M_0 and T_1, using a stepwise model that takes into account all the RF pulses in the sequence, all the recovery periods, and the approach to steady-state from equilibrium, as described in the paragraph 3.2.1. However since the inversion pulse is phase modulated, the exact flip angle of the adiabatic inversion pulse can not be predicted from the RF map and so is included as a free parameter in the fitting process. Using this numerical approach, in combination with the B_1 map, the steady-state signal in the MPRAGE sequence can be calculated as a function of T_1, M_0 and the flip angle of the inversion pulse. While the magnetization is constantly evolving during the sequence (shown in fig. 3.9), the contrast is strongly

65
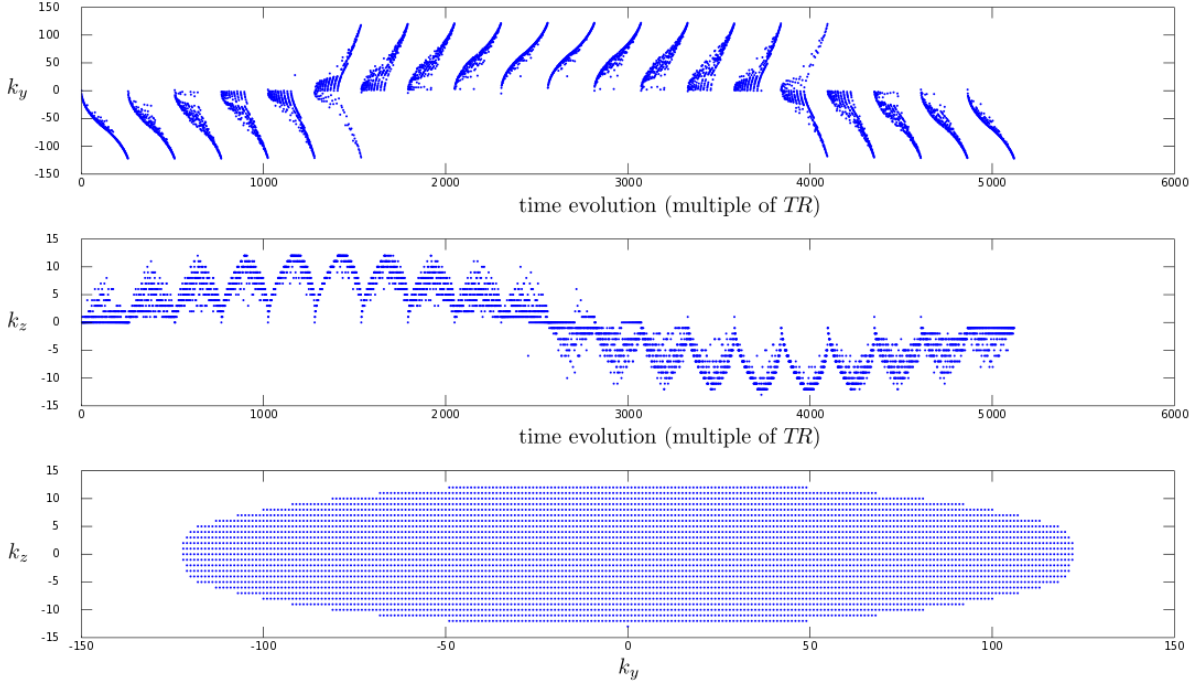
Figure 3.10: Visualization of the k-space trajectory in the different planes. The top graph represents the k_y-axis acquisition function of the time (one point in the x-axis is equivalent to one TR). The middle presents the same data, but for the k_z-axis. Note that the recovery period t_I and t_D are not represented. The lower graph presents the overall k_y-k_z space, each blue dot representing one acquisition in the k_x axis (*i.e.* the readout axis)

defined by the center of the k-space, acquired during the ramp up from zero to the nominal value of the RF pulses (eq. 3.5). Each train of turbo excitation pulses (one per inversion pulse, twenty represented in fig. 3.10) is sampling the k-space in a centric phase encoding manner, with a spiral ordering of phase encoding lines through the second and third dimensions of k-space. At the start of each train, the magnetization is sampled around the middle of the k_x-k_y plane (close to the coordinates $(0-0)$ in fig. 3.10), before the acquisition of the periphery of the k-space.

3.2.2.2 Optimization via covariance matrix

The statistical error introduced by noise in the data can be reduced to provide a robust measurement, either with an elevated number of measures, or with a wise choice of measurement parameters. Theoretical optimization of the acquisition parameters is performed here based on the minimization of the random error as a function of T_1. Analytical expression of the signal is not straightforward,

as shown in 3.2.1, but numerical methods based on the Bloch equations can be easily implemented to estimate and quantify the error due to the quantification process. Calculating and comparing the covariance matrix based on a raw SNR in S_0 of 1% can be done in a stepwise fashion, using the chain and product rules for differentiation. The covariance matrix is then used to optimize the sequence for the maximum SNR in the fitted T_1, for the resolution and coverage used experimentally, and for a total imaging time of 15 min. The optimization is assuming a target T_1 of 1.6 s and a raw SNR in S_0 of 1%. Results show that the optimal number of acquisitions in term of SNR in the fitted T_1 is five for a SSi of 9s, but with a flip angle of 62°. This flip angle is however too high practically for two reasons: (1) the Specific Absorption Rate (SAR) induced by the quick repetition of the flip angle in the train is over the limit fixed by the International Electrotechnical Commission (IEC) standard; (2) the resulting image created with those high RF pulses during a TFE train will suffer a lot of blurring effects, due to a poor PSF. Fine optimization has thus to be perform to optimize both the quality of the T_1 measurement together with the quality of the image, and could be done with the simulator described in the chapter 5. For the following of the study, the quality of the individual images is preferred over the robustness of the measurements, and optimization of the inversion times is done assuming a flip angle α of 8°.

Optimization of the protocol could also be done recursively via Monte-Carlo (MC) simulation, another method of estimating the variance of the measurement and described in3.2.3.2. But in our case the MC simulation was only performed to validate the robustness of the results, as it is a rather slow method, especially if used for recursive algorithms. Results obtained from the minimization of the standard deviation of the measurement of T_1 via covariance matrix are presented in the fig. 3.11. For any of the protocol parameters, the error increases with an increasing T_1, mainly due to the fixed scanning time that reduces the Dynamic Range of the signal for high values of T_1. Without considering the quality of the images and using a flip angle of 62°, the error can be very low for a large range of T_1. However using the highest flip angle available (42°), the blur in the image due to poor PSF was too important to be usable. With a longer SSi (*i.e.* 9s) the error increases slightly, but stays relatively constant for T_1 values up to 2s. With the experimental protocol, the T_1 values have an standard deviation of less that 2ms for values up to 2s, which is lower than 0.1% of error on the measured T_1.
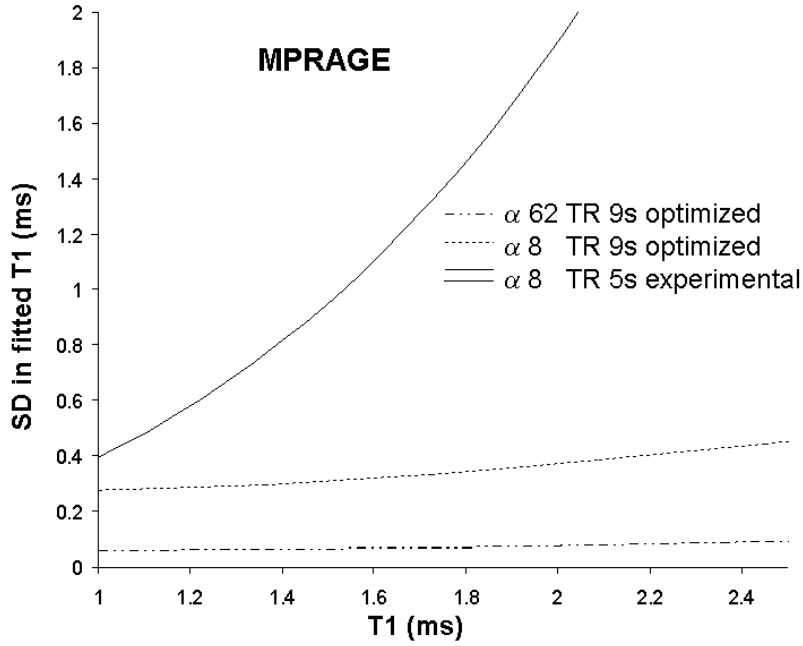
Figure 3.11: Error analysis and optimization of the MPRAGE sequence. The graph plots the random error in T_1 assuming a SNR of 1 %, for the pulse sequence used here (Experimental) and the optimized pulse sequence (optimized for the resolution and coverage used experimentally, and for a total imaging time of 15 minutes).

3.2.3 Fitting procedure

The signal extracted from the images is first polarity restored on a voxel-by-voxel basis (to correct for the effect of the inversion pulse on the sign of the longitudinal magnetization) using the phase information to detect where the sign of the signal is changing [15]. The fitting of the model to the data is then done with a least-squared cost function, together with a downhill simplex search algorithm.

3.2.3.1 Fitting algorithm

The chosen algorithm to compute the search of the solution is the downhill simplex method created by Nelder & Mead [28]. It consists of a numerical method for the non-linear optimization of a many-unconstrained problem. The method uses a simplex, which is a polytope, *i.e.* a geometric shape with $N + 1$ vertices in N-dimensions (*e.g.* a segment in 1D, a triangle in 2D, a 3-face pyramid in 3D, *etc.*). This simplex is progressively displaced on the solution ensemble in direction of the

solution. Three operations are possible on this simplex, depending on the evaluation on each of its vertices on the cost function: the reflection, the expansion and the contraction. This algorithm is not fully robust but has the advantage to find easily the solution without requiring the derivative of the objective function. More complex search algorithms can be used to resolve this fitting problem, as the Levenberg-Marquardt algorithm, but generally require at least the computation of the first derivative of the signal. Finite-difference approximation of the derivative would be the best approach for this complex computation. A numerical derivative does required a trade-off for the scale of the perturbation, leading either to digit rounding errors, or to truncation errors. These errors could led the search algorithm to deviate dramatically from the minimum, leading to a possible meaningless result. More explanations can be found in [37], with an insight into automatic differentiation, a method which would provide a more robust derivative function Δf in a reasonable amount of time (maximum three time the cost of evaluating the function f), but is beyond the scope of this work.

3.2.3.2   Monte-Carlo evaluation of the fitting algorithm

To test the sensitivity of the results of the search algorithms to the noise in the data, a Monte-Carlo study is performed on the fitting algorithm with practical data (high SNR) and the addition of noise. The noise considered is a pink noise, added to the magnitude of the signal. Its amplitude is proportional to the maximum amplitude of the signal, *i.e.* the magnetization available at equilibrium (M_0).

Best search algorithm?   The fitting algorithm written for this purpose is based on the algorithm in the book "Numerical Recipes in C" [32], which enables a fast and accurate fitting algorithm for the present purpose, but might be outperformed, particularly in robustness, compared to other more specific optimization algorithms. To compare this algorithm to others using the same language, the following java library "Optimization Algorithm Toolkit" (`http://optalgtoolkit.sourceforge.net`) created by Jason Brownlee is used. Addition of noise gives the possibility to evaluate the robustness of the search algorithms in realistic conditions, but also requires repetition of the fitting experiment. The results presented hereafter uses this library to test different optimization algorithms under specific functions.
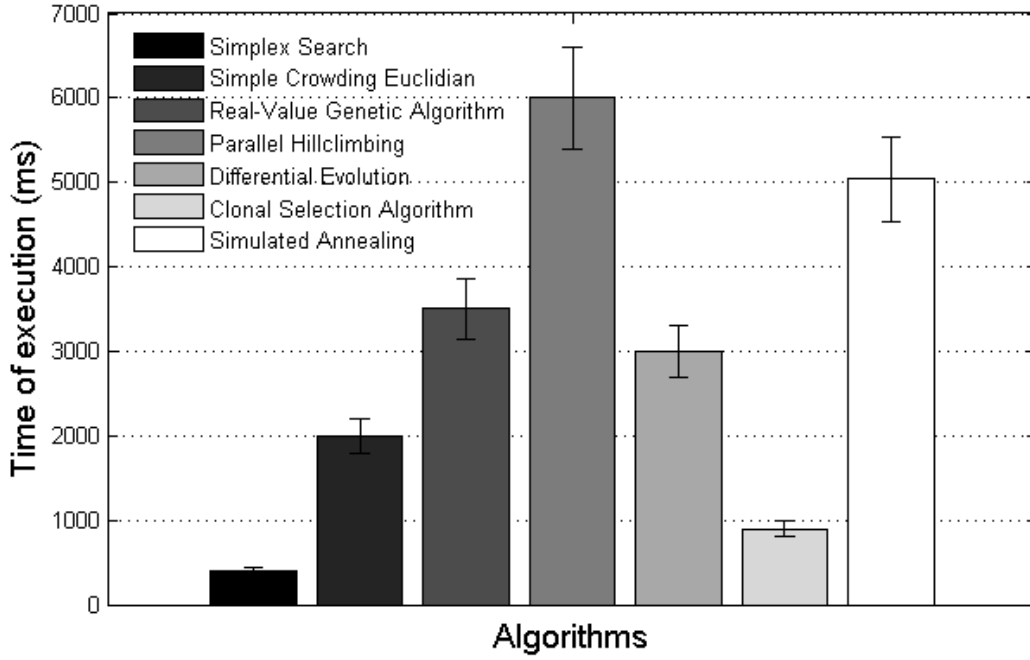
Figure 3.12: Evaluation of the speed of different optimization algorithms tested on simulated MPRAGE signals (0.1% of additional noise). The stop condition of the optimization was set to achieve a given precision. 5,000 repetitions of the fitting were performed for each search algorithm.

The performance of an algorithm can be assessed by different features, such as speed, accuracy, number of iterations (somehow related to speed), but also complexity, robustness to local minima and to initial conditions to cite a few. While the local minima problem did not occur in our data set, it is worth mentioning it for completeness, as it is a recurrent problem, especially for noisy data. This study mostly focused on the number of iterations, as the evaluation of the signal is the dominant source of computational time. A computational comparison (results in fig. 3.12) showed that the downhill simplex algorithm is the quickest to converge, as it does not require a large number of iterations to find the minima. Other algorithms, based on random search, are generally slower to converge to the solution, and are thus not adapted to this particular problem. However, search algorithms are very tunable, and the result of the search, as well as its computation, is highly dependent of the starting parameters. Optimization of the other algorithms for the specific application (*e.g.* Simulated Annealing, Tabu Search or Genetic Algorithm to cite a few) could give a better results, but are beyond the focus of this work. By fixing the end of the search with a non-evolutionary stopping condition, the different algorithms are compared for accuracy, speed and robustness to the given problem (here the optimal set of parameters describing a recovery curve acquired/simulated with a MPRAGE sequence).

3.2. Use of MPRAGE for high resolution quantitative imaging

Fig. 3.12 shows that the downhill simplex method is the quickest to converge to the answer.

Robustness to noise The search algorithm of choice is the downhill simplex algorithm, and the added noise is white and gaussian. A series of eight *TI* measurements is simulated, considering a volume with a longitudinal magnetization M_0=8,000,000 and a T_1 of 1200 ms. The inversion is considered nearly perfect (99%) and the parameters used for the acquisition are the same as in the study. Additional noise is added to the signal, with the standard deviation defined beforehand. Levels of 0.005%, 0.01%, 0.03%, 0.05%, 0.08%, 0.1%, 0.3%, 0.5%, 0.8%, 1%, 3% and 5% of noise are added to the simulated signal, and 50,000 repetitions are fitted for each level of noise. The mean, median and standard deviation is computed out of the fitted results for the three parameters of interest, number of evaluation and best score, and are presented in fig. 3.13.
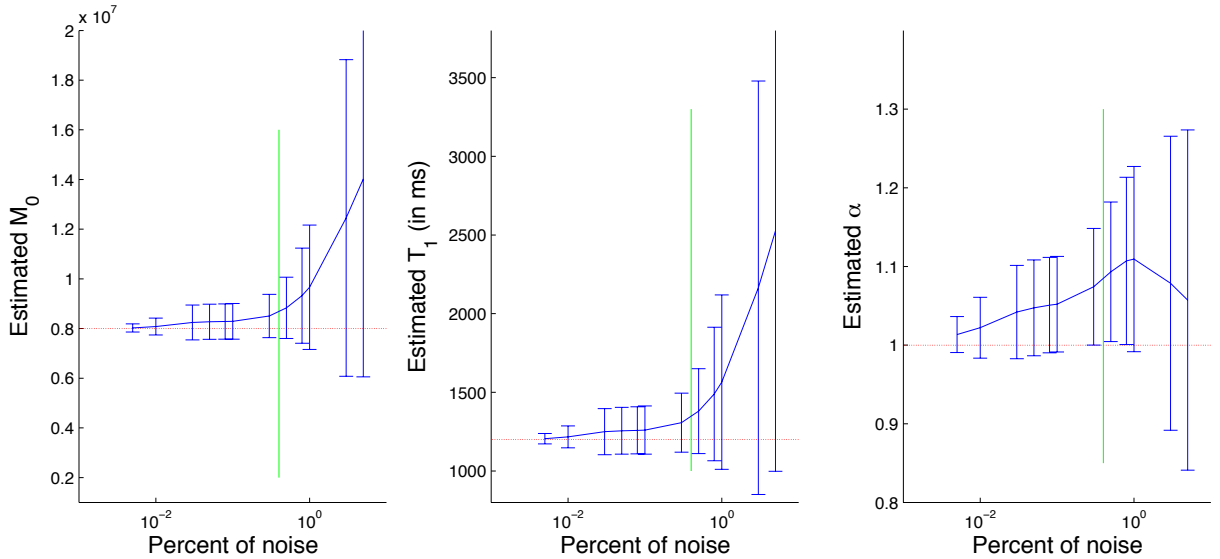
Figure 3.13: Variation of the average fitting results depending on the noise added, with the standard deviation represented by the error bars. The green line represents the real SNR present in the acquired images.

As the noise level increases, the random error on the fitted parameters increases, as expected. One surprising result is that the fitting results globally increase with the noise level, indicating a bias of the fitting by the noise. While the results all have the answer (represented as a red line) in their confidence range, the parameters results move away from the true result as the noise increases. However, the level of noise in the collected images is small (SNR around 250 with a standard deviation of the background noise being around 0.05% of the fitting results for M_0, as expressed in fig. 3.13).

71

It give us an error on the measured T_1 of less than 50 ms for a T_1 of 1200 ms (4% error). Comparing these results to results obtained via the DESPOT-HIFI method presented in [11], the error here is smaller, as for a noise level of 0.01%, the variance and error is below 1%, while the DESPOT-HIFI method has a variance below 2% for the same level of noise. The scanning time was somehow similar, with 10 minutes for the DESPOT-HIFI method compared to 15 minutes for the MPRAGE method, but our field-of-view was somehow smaller (30mm compared to a whole brain coverage) and the number of data points larger (8 compared to 2).

3.2.4 Variability with/without the B_1 map

Another source of error comes from the B_1 assumed in the fitting, defined here as the B_1^{fit}. Even if the RF amplitude is measured via the acquisition of the B_1 map for each subject, the acquisition is not simultaneous, and can be subject to errors as well.
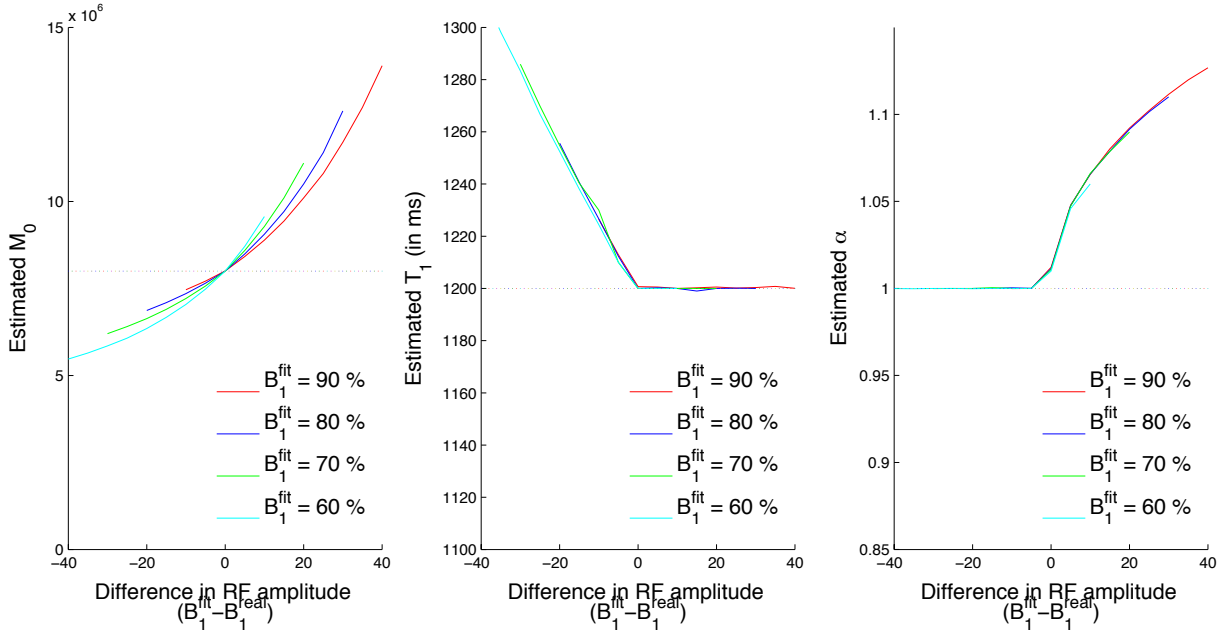
Figure 3.14: Variation of the fitted results with the fitted RF amplitude B_1^{fit} plotted as a difference between the fitted amplitude B_1^{fit} and the real RF amplitude (B_1^{real})

The influence of the B_1 on the fitting algorithm was assessed by simulating the signal with an amplitude B_1^{real} and then fitting the signal with a different B_1^{fit} amplitude, reproducing an eventual error on the acquired B_1 map. Fig. 3.14 plots the fitted parameters against the difference between

real and fitted flip angle. The results show an interesting behaviour: if B_1^{fit} is lower or equal to the B_1^{real}, the T_1 obtained from the fitting decreases, but if the B_1^{fit} increases higher than B_1^{real}, the fitted T_1 is correct. The case $B_1^{fit}=B_1^{real}$ returns initial parameters value (shown by the dotted line) as expected. The results for the parameter M_0 show a linear correlation with the B_1^{real}, with increase of M_0 as B_1^{fit} increases. The most interesting result is for the parameter α, which is inversely correlated to T_1 result, somehow expected as T_1 and α are anti-correlated in the model. In fact, if the B_1^{fit} is higher or equal to the B_1^{real}, the α obtained from the fitting decreases. But when $B_1^{fit} < B_1^{real}$, the fitted parameter α is correct and constant throughout the decrease of B_1^{fit}. It means that looking at the results of the parameter α could give a clue as to the goodness of the fit. More importantly, setting a high B_1^{fit} assures a good measure of T_1. Unless the B_1 map can be obtained as a certainty measure of the RF amplitude, the use of a high B_1^{fit} provides a robust answer for the measurement of the T_1, if this parameter is the only quantity of interest. The dependence of the fitted parameters, specifically between T_1 and α, shows that relaxation effects occurring between the excitation RF pulses are correlated with the amplitude of the RF pulses, the parameter α compensating for increase inM_0 for $B_1^{fit} > B_1^{real}$, while T_1 compensates M_0 for $B_1^{fit} < B_1^{real}$.

3.3   Crossfield T_1 mapping studies

While MRI enables high-resolution images to be used as an essential tool in both clinical and research environments, especially in the neurological area, limitations come with the interpretation of the specificity of the contrast itself. Looking at the inherent properties of the tissues directly, such as the relaxation times for example, provides a differentiation assessment with a good repeatability. The studies presented hereafter are focused on measuring T_1 in the brain of healthy volunteers at different field strength, as accurately as possible.

3.3.1 T_1 mapping validation study

The aim of the study presented hereafter was to investigate mapping of the water proton longitudinal relaxation time (T_1) at 7T at high spatial resolution using the MPRAGE sequence, and to

compare values of grey and white matter T_1 measured at field strengths of 1.5T, 3T and 7T. Comparison has been made with two other sequences, the IR-EPI, considered as our gold standard, and the IR-TSE, a spin-echo based sequence.

3.3.1.1 Phantom experiment

To validate both the model used to simulate the acquired signal and the image quality obtained from the MPRAGE sequence, validation with phantoms is performed and compared with other quantification methods. A calibration study was performed on two spherical phantoms, each divided into four quadrants, filled with saline solution containing varying concentrations of 0.5-4% wt/wt agar and 0.038-0.4% v/v gadolinium (0.5M Magnevist, Schering) to give a range of T_1 and T_2 relaxation times. This design is chosen to minimize the effects of B_1 and B_0 inhomogeneities at high field. The phantoms were scanned on Philips Achieva 1.5, 3, and 7T MRI scanners using the IR-EPI, IR-TSE and MPRAGE sequences described above, as well as in [41]. As the B_1 field is known to be more inhomogeneous as the field strength increases, additional B_1 maps were acquired at the same location as the series of MPRAGE for correction purposes at high field. The flip angles of the RF readout pulses can be calculated from B_1 maps obtained at 3T and 7T, with preliminary experiments showing that the flip angle calibration from the scanner is good across the field of view at 1.5T. This B_1 map is based on the double repetition time technique, acquiring the same volume twice with a different repetition time, and producing the B_1 map as explained in [42]. Fig. 3.15 shows the T_1 values obtained from the multi-slices IR-TSE and the MPRAGE images plotted against the values obtained using IR-EPI.

It can be seen that in the phantom the results from all the sequences are very similar (r^2 ranging from 0.97 for MPRAGE at 1.5T to 0.99 for IR-TSE at 1.5T), although there is some scattering for longer T_1 values for both sequences at all field strengths. Comparison of the MPRAGE and IR-EPI results obtained from the experiments carried out on the phantom shows that the sequences give no significant systematic errors up to 2000 ms. The errors at longer relaxation time may be due to random noise which was expected to be greater at lower field and have a greater effect at longer T_1, or due to through-plane motion, such as slow flow into or across the volume slice due to vibration in the long T_1 segment of the phantom, which is also the most weakly gelled. This scatter could also be due to a

3.3. Crossfield T_1 mapping studies
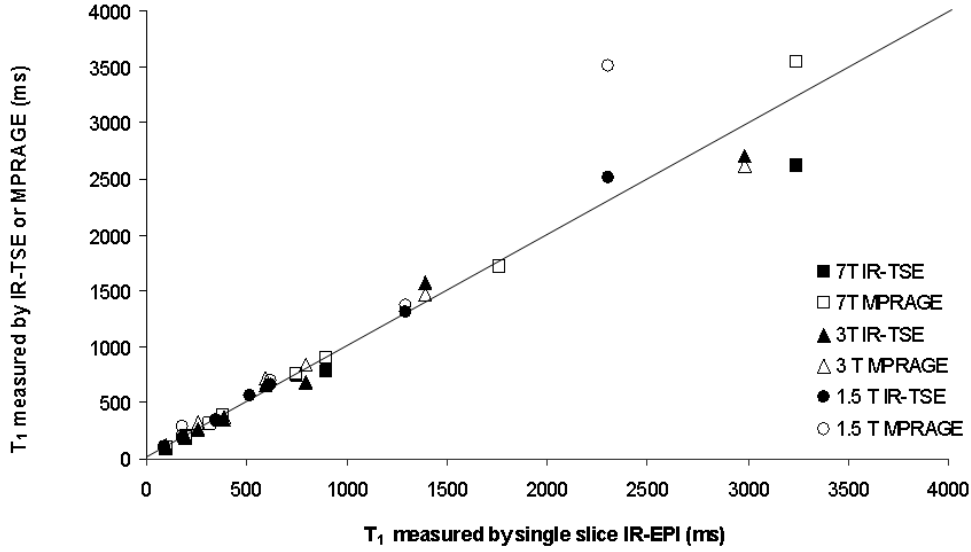
Figure 3.15: Calibration of IR-TSE and MPRAGE data to the assumed gold-standard IR-EPI results obtained in phantoms (data from [41])

short inversion repetition time, which saturate most the spins with longer T_1. The recovery is thus not complete, leading to more errors in the fitted values due to a smaller dynamic range. A trade-off thus occurs between improving the precision of T_1 measures of tissues with longer T_1 (as the grey matter or the CSF), or having a shorter imaging protocol, with the choice depending on the application.

3.3.1.2 Measure repeatability

To assess the reproducibility of the T_1 measurement protocol described above, one subject was scanned several time (N=5) on the 7T scanner. The scans were performed on five different occasions (*i.e.* five different days), with the planning and shimming positioned as close as possible to the same location. Once all the images were acquired, rigid-body image registration was performed using the FLIRT linear registration algorithm from the FSL platform (FMRIB, Oxford UK). Because of the variation of contrast with inversion time, the cost function used was based on maximization of the mutual information. To compute the image entropies necessary for the mutual information algorithm, a low number of bins in the histogram (100 maximum) was used to assure the success of the registration for all inversion time. The white matter was segmented from the brain on an additional T_1-weighted scan via the SPM software (http://www.fil.ion.ucl.ac.uk/spm).

The final interpolation was performed with a sinc kernel for the modulus images, and the nearest neighbour method for the phase images (in order to keep the phase fringe as close as the reality). Histograms analysis was used in order to assess the repeatability of the measure. To evaluate the effect of addition of the B_1 field map, the RF mapping was either obtained from the measurement, or a default value was used. No significant difference could be observed between the different days. Looking at specific regions inside the white matter (N=8), no significant difference could be seen either, both in the mean T_1 (μ=1204±34 ms) and in the variance inside each measure (σ=64±9 ms). The histogram 3.16 shows good overlap of the measures produced at different days, and proves the good confidence on the reproducibility of the T_1 quantity.

3.3.2 In-vivo crossfield study

This experiment was approved by the local ethics committee. Four healthy subjects (aged 24, 39, 40 and 43 years; sex: m, m, m, and f) were scanned at 1.5, 3, and 7T using the MPRAGE, IR-TSE and IR-EPI sequences described above. After registering the acquired images as described in the paragraph 3.3.1.2, T_1 maps were created for each subject and then T_1 was measured from these maps in two regions of cortical grey matter and four regions of cortical white matter, the putamen and caudate head (3.17). The size of the regions of interest were typically 75 voxels for white matter, 20
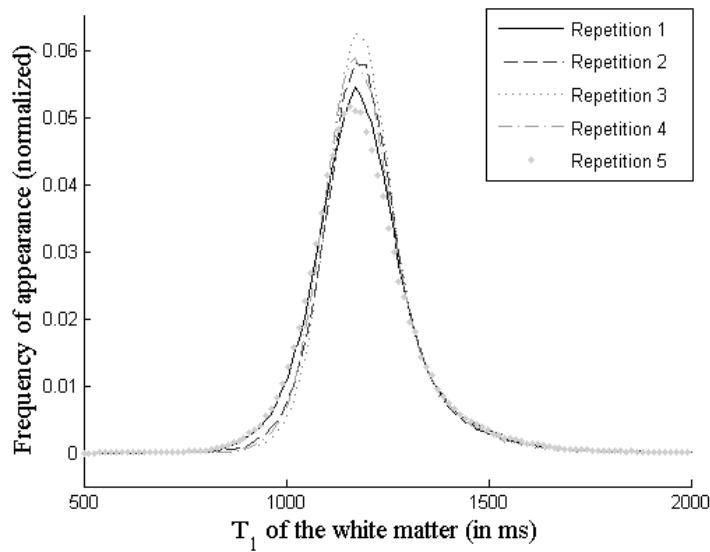
Figure 3.16: Histograms of the diverse repetitions of the measurement of the T_1 of the white matter inside an healthy subject.

voxels for cortical grey matter, 90 voxels for the caudate head and 100 voxels for the putamen.
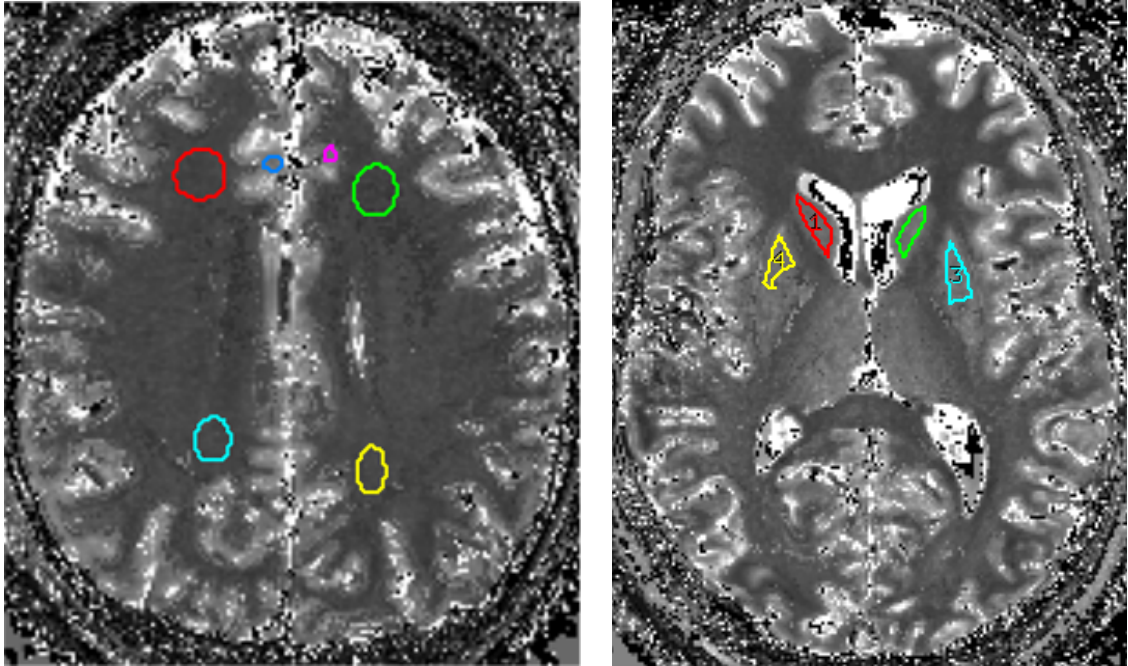
Figure 3.17: Regions of Interest drawn on the T_1 map from the MPRAGE sequence
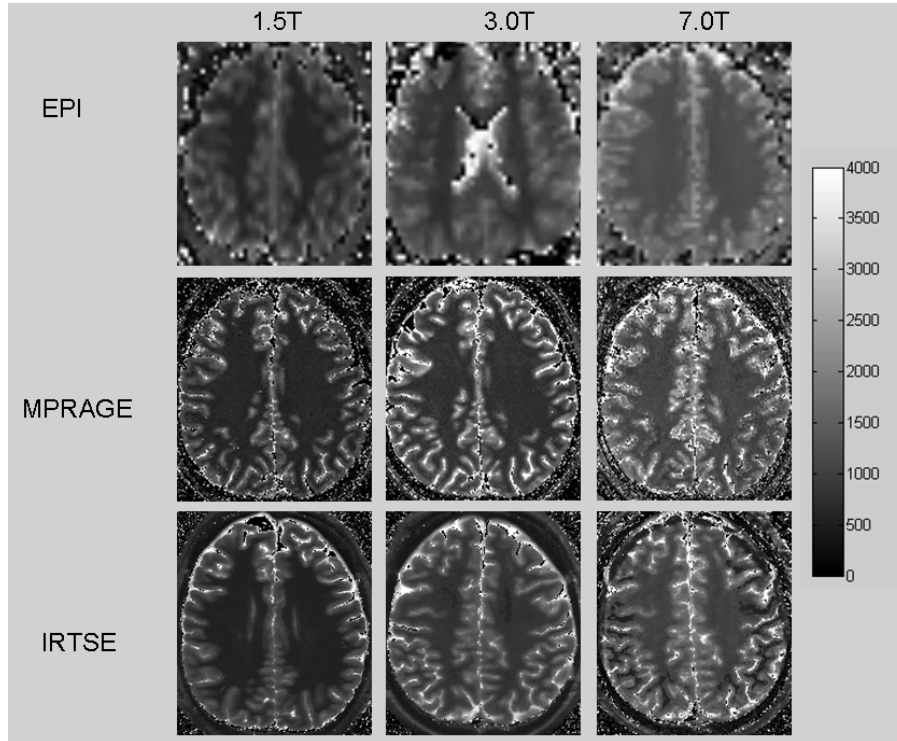
Figure 3.18: Map obtained on one subject at the three different field strengths.

This study compares T_1 measurements at 1.5, 3 and 7 T in cortical grey matter, white matter,

the putamen and caudate head. The MPRAGE results reported here are very similar to those reported previously at 7 T [33], although the T_1 values are slightly lower in grey matter. This could be because of the larger 1.5 x 1.5 x 5 mm^3 voxel size used by Rooney et al, which may have led to some partial voluming with CSF in GM. However a difference was also observed in white matter where partial volume effects (due to CSF in the Virchow Robin spaces) are expected to be less significant, and also the EPI images (which were acquired at much coarser resolution) did not measure longer T_1s than the MPRAGE sequence.
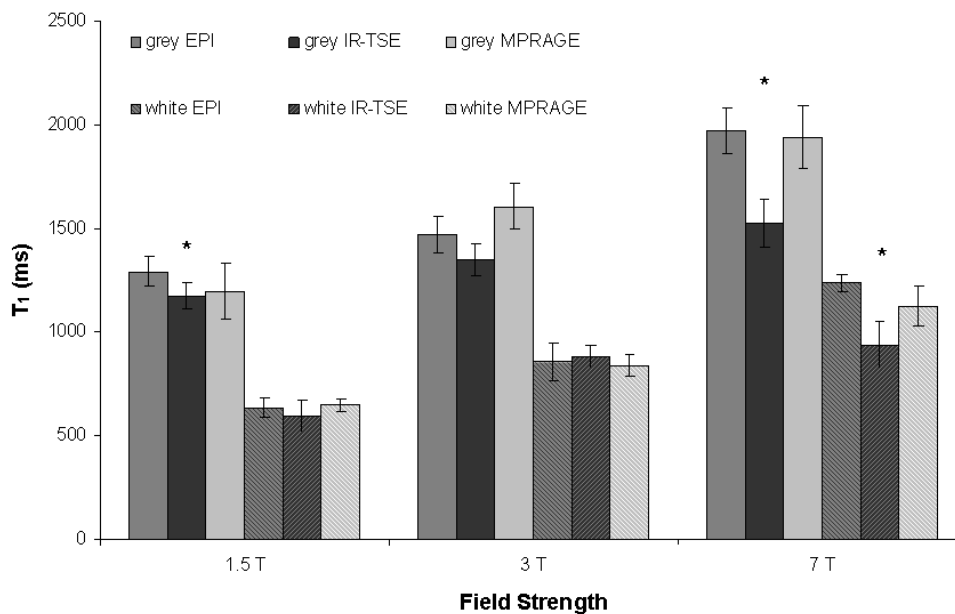
Figure 3.19: Values obtained for the four subjects at the three different field strengths (figure from [41]).

Results from fig. 3.18 and 3.19 demonstrate that the distribution of T_1 values among different tissues in the brain, including the difference between cortical grey matter and the surrounding superficial white matter, increases with magnetic field strength. Thus high resolution T_1-weighted images can be obtained at high fields, as well as high-resolution T_1 maps 3.17.

3.3.3 Other applications

From the reassuring fact that the T_1 contrast is still large at high field, and that it can discriminate with high efficiency between different tissues, other more specific questions can be asked. Specific applications, in the domain of neuroscience and for clinical pilot studies, are performed on the Nottingham 7T Philips scanner and are presented here.

3.3.3.1 Neuro-plasticity study of the cortico-spinal tract

Some high-resolution T_2^*-weighted images obtained at 7T show a tremendous contrast inside the white matter tracts as well as in the region of the deep nuclei, where lower field scanners only show homogeneous white or grey matter. One can assume that the T_1 can also be different, depending on the different amount of myelin present inside those tracts for example. The corticospinal tract (CST), which is part of the motor system, is visible with MRI because of the presence of large neural fibres, which endows it with particular MRI properties on structural MR images. Furthermore, at the behavioural level, both the anatomy and function of the CST are expected to differ in relation to handedness. The aim of the present study was to verify if hemispheric asymmetries in MRI properties of the CST and behaviour (Handedness) are related. Results from Hervé [20] partly present in fig. 3.20 showed that significant difference of T_1 could be seen in the CST between right-handed subjects (N=10) and left-handed subjects (N=11). However, the difference was the least significant (p=0.005) compared to either T_2 or MTR (p<0.001).
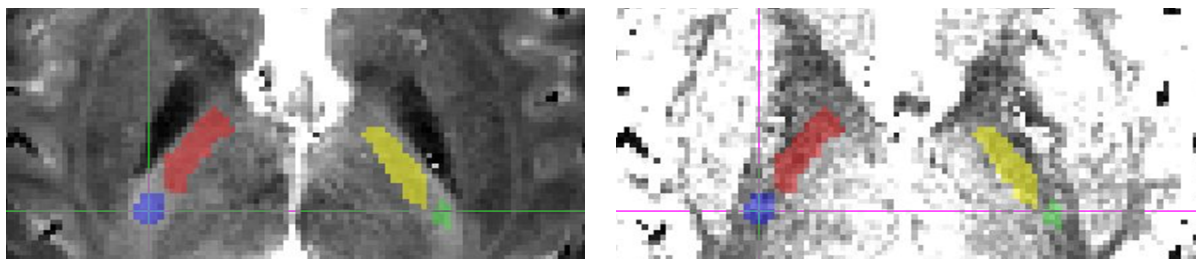
Figure 3.20: Regions of Interest drawn on the T_2^*-weighted image and the corresponding regions on the T_1 map from the MPRAGE sequence. The blue and green dots represent respectively the left and the right CST, while the red and yellow patches represent the Internal Capsule.

3.3.3.2 Assessment of the white matter integrity in Clinically Isolated Syndrome patients

The same quantitative T_1 measurement method has also been applied to study the use of 7T in assessing multiple sclerosis. T_1 was used to compare the White Matter (WM) in healthy controls with Normal Appearing WM (NAWM) in MS patients, as explained in [2]. Fourteen MS patients were recruited from Nottingham University Hospital (7 males and 7 females). Seventeen age and sex matched healthy volunteers were also recruited, and both groups were consented according to local ethics. More details about the image acquisition and processing can be found in [1], but a brief overview is given here. The scan protocol included a 3D MPRAGE sequence and a 2D multi-slice FLAIR sequence, both at an isotropic resolution of 0.6 mm.
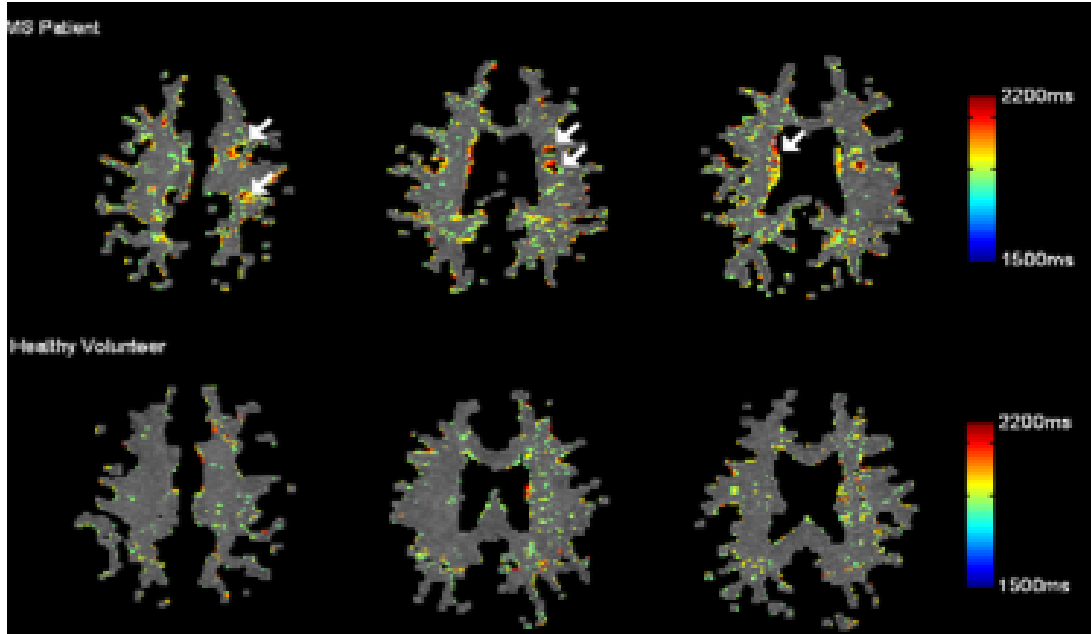
Figure 3.21: Spatial distribution of high T_1 values. It is noticeable, for the MS patient (top images), that areas of high T_1 appear as a 'halo' around the location of the MS lesion. In these images the MS lesions themselves appear black since they were not included in the WM mask. Also notice that high T_1 is apparent close to the ventricles.

T_1 maps were derived using data acquired with the modified version of the MPRAGE sequence presented in this chapter. The imaging parameters were modified to give a 200x170x73 mm^3 FOV using a 1.25 mm isotropic voxel size. The other parameters are TE=3.2 ms, TR=6.9 ms, TFE shots=16, 58 slices, SENSE factor=2. Seven separate TIs were used with values 150, 300, 500, 800, 1200, 1800 and 2500 ms. The total scan time was 2 minutes per TI. The MPRAGE scan was used to segment the

NAWM using FSL (FMRIB, Oxford UK), the lesions being excluded by their low contrast compared to the WM. Histogram analysis shows an increase in the Full Width Half Maximum (FWHM) of the WM peak of the CIS patients compared to the controls. A slight increase in the mode of the peak was also observed, but was not significant. Fig. 3.21 shows the distribution of the high T_1 values inside the white matter of a CIS patient (top), and a control subject. Although the segmentation algorithm removed the apparent lesions due to low contrast compared to the NAWM, the neighbourhood of both the lesions and the ventricles appears to have higher T_1 pixels. This shows that the extent of the lesions is somehow slightly larger than what can be detected on normal images. However, the recent study presented in [2] shows that the MTR measure is more sensitive to detect abnormalities in the NAWM than the T_1.

3.4 Conclusion

Results presented inside this chapter showed that the measure of the longitudinal relaxation time is realisable *in vivo* at a high resolution. Effects of inhomogeneities have been shown to be minimal in the fitting robustness and in the results. Quantitative imaging is a definite improvement over simple anatomical imaging, especially at high field, as it provides a specific and reliable marker of tissue, giving a stronger differentiation between tissue (*i.e.* pathological, plasticity, ...) far more powerful than with a single image modality. High field does increase the SNR in the fitted T_1 whilst maintaining good T_1 dispersion (separation). The increased SNR was used in this study to increase the resolution, in the same time as to decrease the scanning time, giving enough SNR in the image to produce robust T_1 map. The method and algorithm present here is actually used for different studies running in the SPMMRC, such as evolution of the T_1 with age [40], and the effect of premature delivery on brain development in the near future.

Bibliography

[1] A. Al-Radaideh, M. Brookes, O. Mougin, E. C. Tallentyre, N. Evangelou, S.-Y. Lim, A. Pitiot, C. Constantinescu, P. Morgan, P. Morris, and P. Gowland. High resolution white matter t1

mapping in multiple sclerosis at 7t. In *Proceeding of the 17th ISMRM meeting, Honolulu*, 2009.

[2] A. Al-Radaideh, O. Mougin, S.-Y. Lim, C. Tench, C. Constantinescu, and P. Gowland. Multi-modal high resolution magnetization transfer and t1 mapping in nawm of patients with cis. In *Proceeding of the 18th ISMRM meeting, Stockholm*, 2010.

[3] C. J. Bakker and J. Vriend. Multi-exponential water proton spin-lattice relaxation in biological tissues and its implications for quantitative nmr imaging. *Phys Med Biol*, 29(5):509–518, May 1984.

[4] W. Brück, A. Bitsch, H. Kolenda, Y. Brück, M. Stiefel, and H. Lassmann. Inflammatory central nervous system demyelination: correlation of magnetic resonance imaging findings with lesion pathology. *Ann Neurol*, 42(5):783–793, Nov 1997.

[5] D. Canet, G. Levy, and I. Peat. Time saving in'ic spin-lattice relaxation measurements by inversion-recovery. *J Magn Res*, 18:199–204, 1975.

[6] B. Char, K. Geddes, and G. Gonnet. The maple symbolic computation system. *SIGSAM Bull.*, 17(3-4):31–42, 1983.

[7] K. Christensen, D. Grant, E. Schulman, and C. Walling. Optimal determination of relaxation times of fourier transform nuclear magnetic resonance. determination of spin-lattice relaxation times in chemically polarized species. *The Journal of Physical Chemistry*, 78(19):1971–1977, 1974.

[8] S. Clare and P. Jezzard. Rapid t1 mapping using multislice echo planar imaging. *Magn Reson Med*, 45(4):630–634, Apr 2001.

[9] E. Cox, P.-Y. Herve, P. Wright, A. Loftipur, O. Mougin, S. Pritchard, T. Paus, and P. Gowland. Variations in t2, t2* and t1 between white matter tracts at 7t. In *Proceeding of the 17th ISMRM meeting, Honolulu*, 2009.

[10] R. Deichmann, D. Hahn, and A. Haase. Fast t1 mapping on a whole-body scanner. *Magn Reson Med*, 42(1):206–209, Jul 1999.

[11] S. C. L. Deoni. High-resolution t1 mapping of the brain at 3t with driven equilibrium single pulse observation of t1 with high-speed incorporation of rf field inhomogeneities (despot1-hifi). *J Magn Reson Imaging*, 26(4):1106–1111, Oct 2007.

[12] S. C. L. Deoni, B. K. Rutt, and T. M. Peters. Rapid combined t1 and t2 mapping using gradient recalled acquisition in the steady state. *Magn Reson Med*, 49(3):515–526, Mar 2003.

[13] T. K. Foo, A. M. Sawyer, W. H. Faulkner, and D. G. Mills. Inversion in the steady state: contrast optimization and reduced imaging time with fast three-dimensional inversion-recovery-prepared gre pulse sequences. *Radiology*, 191(1):85–90, Apr 1994.

[14] P. Gowland and P. Mansfield. Accurate measurement of t1 in vivo in less than 3 seconds using echo-planar imaging. *Magn Reson Med*, 30(3):351–354, Sep 1993.

[15] P. A. Gowland and M. O. Leach. A simple method for the restoration of signal polarity in multi-image inversion recovery sequences for measuring t1. *Magn Reson Med*, 18(1):224–231, Mar 1991.

[16] P. A. Gowland, M. O. Leach, and J. C. Sharp. The use of an improved inversion pulse with the spin-echo/ inversion-recovery sequence to give increased accuracy and reduced imaging time for t1 measurements. *Magn Reson Med*, 12(2):261–267, Nov 1989.

[17] R. Gupta, J. Ferretti, E. Becker, and G. Weiss. A modified fast inversion-recovery technique for spin-lattice relaxation measurements. *J Magn Reson*, 38:447–452, 1980.

[18] E. Haacke, R. Brown, M. Thompson, and R. Venkatesan. *Magnetic resonance imaging: physical principles and sequence design*. New York: John Wiley & Sons, Inc, 1999.

[19] E. Henderson, G. McKinnon, T. Y. Lee, and B. K. Rutt. A fast 3d look-locker method for volumetric t1 mapping. *Magn Reson Imaging*, 17(8):1163–1171, Oct 1999.

[20] P.-Y. Herve, E. Cox, A. Loftipur, O. Mougin, S. Wharton, R. W. Bowtell, T. Paus, and P. Gowland. Assessing the corticospinal tract with multimodal quantitative mri. In *Proceeding of the 18th ISMRM meeting, Stockholm*, 2010.

[21] R. Kaptein, K. Dijkstra, and C. Tarr. A single-scan fourier transform method for measuring spin-lattice relaxation times. *J Magn Reson*, 24:295–300, 1976.

[22] M. Karlsson and B. Nordell. Analysis of the look-locker t1 mapping sequence in dynamic contrast uptake studies: simulation and in vivo validation. *Magn Reson Imaging*, 18(8):947–954, Oct 2000.

[23] S. H. Koenig, R. D. Brown, M. Spiller, and N. Lundbom. Relaxometry of brain: why white matter appears bright in mri. *Magn Reson Med*, 14(3):482–495, Jun 1990.

[24] D. C. Look and D. R. Locker. Time saving in measurement of nmr and epr relaxation times. *Review of Scientific Instruments*, 41(2):250–251, 1970.

[25] J. L. Markley, W. J. Horsley, and M. P. Klein. Spin-lattice relaxation measurements in slowly

BIBLIOGRAPHY

relaxing complex spectra. *The Journal of Chemical Physics*, 55(7):3604–3605, 1971.

[26] C. A. McKenzie, F. S. Prato, R. E. Thornhill, and D. J. Drost. T(1) fast acquisition relaxation mapping (t(1)-farm): optimized data acquisition. *Magn Reson Imaging*, 18(2):129–138, Feb 2000.

[27] J. P. Mugler and J. R. Brookeman. Three-dimensional magnetization-prepared rapid gradient-echo imaging (3d mp rage). *Magn Reson Med*, 15(1):152–157, Jul 1990.

[28] J. A. Nelder and R. Mead. A simplex method for function minimization. *The Computer Journal*, 3:308–313, 1965.

[29] R. J. Ordidge, P. Gibbs, B. Chapman, M. K. Stehling, and P. Mansfield. High-speed multislice t1 mapping using inversion-recovery echo-planar imaging. *Magn Reson Med*, 16(2):238–245, Nov 1990.

[30] G. J. Parker, G. J. Barker, and P. S. Tofts. Accurate multislice gradient echo t1 measurement in the presence of non-ideal rf pulse shape and rf field nonuniformity. *Magn Reson Med*, 45(5):838–845, May 2001.

[31] T. Paus, D. L. Collins, A. C. Evans, G. Leonard, B. Pike, and A. Zijdenbos. Maturation of white matter in the human brain: a review of magnetic resonance studies. *Brain Res Bull*, 54(3):255–266, Feb 2001.

[32] W. Press, S. Teukolsky, W. Vetterling, and B. Flannery. *Numerical recipes in C*. Cambridge Univ. Press Cambridge MA, USA, 1992.

[33] W. D. Rooney, G. Johnson, X. Li, E. R. Cohen, S.-G. Kim, K. Ugurbil, and C. S. Springer. Magnetic field and tissue dependencies of human brain longitudinal 1h2o relaxation in vivo. *Magn Reson Med*, 57(2):308–318, Feb 2007.

[34] N. J. Shah, M. Zaitsev, S. Steinhoff, and K. Zilles. A new method for fast multislice t(1) mapping. *Neuroimage*, 14(5):1175–1185, Nov 2001.

[35] S. Steinhoff, M. Zaitsev, K. Zilles, and N. J. Shah. Fast t(1) mapping with volume coverage. *Magn Reson Med*, 46(1):131–140, Jul 2001.

[36] P. Tofts. *Quantitative MRI of the brain : measuring changes caused by disease*. Wiley, 2003.

[37] J. Tolsma and P. Barton. On computational differentiation. *Computers and Chemical Engineering*, 22(4-5):475–490, 1998.

[38] C. Y. Tong and F. S. Prato. A novel fast t1-mapping method. *J Magn Reson Imaging*, 4(5):701–

708, 1994.

[39] G. H. Weiss and J. A. Ferretti. Optimal design of relaxation time experiments. *Progress in Nuclear Magnetic Resonance Spectroscopy*, 20(4):317 – 335, 1988.

[40] P. Wright, O. Mougin, S. Pritchard, E. Cox, and P. Gowland. Age and gender variation in t1 measurements of white and grey matter structures within the human brain at 7t. In *Proceeding of the 18th ISMRM meeting, Stockholm*, 2010.

[41] P. J. Wright, O. E. Mougin, J. J. Totman, A. M. Peters, M. J. Brookes, R. Coxon, P. E. Morris, M. Clemence, S. T. Francis, R. W. Bowtell, and P. A. Gowland. Water proton t1 measurements in brain tissue at 7, 3, and 1.5 t using ir-epi, ir-tse, and mprage: results and optimization. *MAGMA*, 21(1-2):121–130, Mar 2008.

[42] V. L. Yarnykh. Actual flip-angle imaging in the pulsed steady state: a method for rapid three-dimensional mapping of the transmitted radiofrequency field. *Magn Reson Med*, 57(1):192–200, Jan 2007.

[43] H. Zhao, W. M. Westler, and J. L. Markley. Precise determination of t1 relaxation values by a method in which pairs of nonequilibrium magnetizations are measured across a constant relaxation period. *Journal of Magnetic Resonance, Series A*, 112(2):139 – 143, 1995.

CHEMICAL EXCHANGE AND SATURATION TRANSFER AT 7T

The Magnetic Resonance Imaging (MRI) signal is dominated by protons in water molecules, but this signal is strongly influenced by the interaction between these protons and neighbouring protons situated in other molecules, including proteins, macromolecules, *e.g.* fatty acids or other lipids. Protons in water are relatively free to diffuse inside the tissue, experiencing different environments and having the possibility to interchange with labile protons of certain groups (-OH, -SH, -NH) situated on larger molecules, or exchange their magnetization via dipole-dipole interaction (see fig. 4.1). A properly designed experiment can highlight and even measure those interactions. This is known as Magnetization Transfer (MT) experiment, which studies the transfer of saturated magnetization associated with macromolecules to the free water where it can be recorded, as well as Chemical Exchange Saturation Transfer (CEST), which allows study of chemical exchange of protons between different molecules groups. Investigation of these effects at high field strength will be discussed in this chapter, with a presentation of a method to measure the z-spectrum (MT effects) and to observe the z-spectrum asymmetry (CEST effect) *in vivo* at 7 T, within SAR limits. It also presents a 3 compartment model that has been used to measure chemical exchange and magnetization transfer parameters from the z-spectrum data.
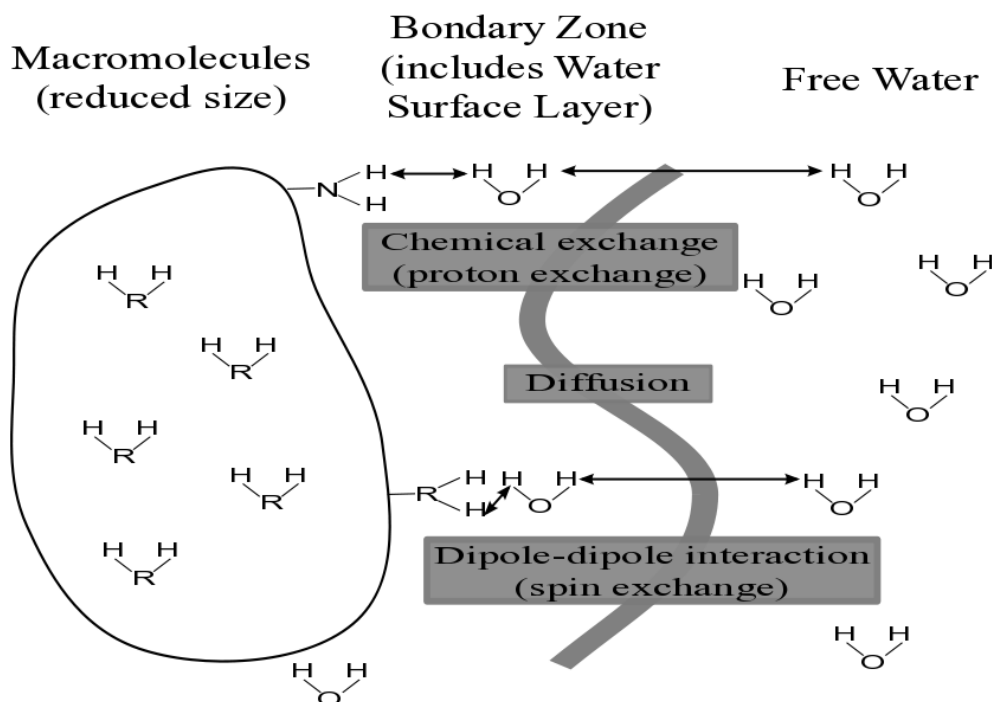
Figure 4.1: Possible exchange of magnetization between the bound protons (left) and the bulk protons (right).

4.1 Introduction

MT has been used for a long time in Nuclear Magnetic Resonance [11]. In a typical MT experiment, radio-frequency (RF) irradiation is applied to the sample to saturate protons resonating at a different frequency (off resonance) to that of free water. Some of the saturated protons then exchange or transfer their magnetization with protons situated in the free pool where the effect on the water signal is then monitored. If the frequency of the irradiation is altered, then the variation in the MT effect with the resonant frequency of the protons associated with other molecules can be explored. This can be represented via the z-spectrum (also known as MT spectrum or CEST spectrum), a graph giving the MT effect as a function of irradiation frequency.

First, saturation of protons resonating at a certain frequency offset compared to the water frequency is applied. This energy is then gradually exchanged with the water protons via different magnetization transfer processes. The resultant water signal is used to study solutes and macromolecules present in the sample, as presented in fig. 4.1, indirectly via the water signal allowing their relative

4.1. Introduction

concentrations and exchange rates with the water to be estimated. Depending on the strength of the RF irradiation as well as the range of frequencies (tens to hundreds of ppm for MT, few ppm for CEST), the observed z-spectra will reveal magnetization transfer effects, chemical exchange saturation transfer effects, or both, as represented on fig. 4.2.
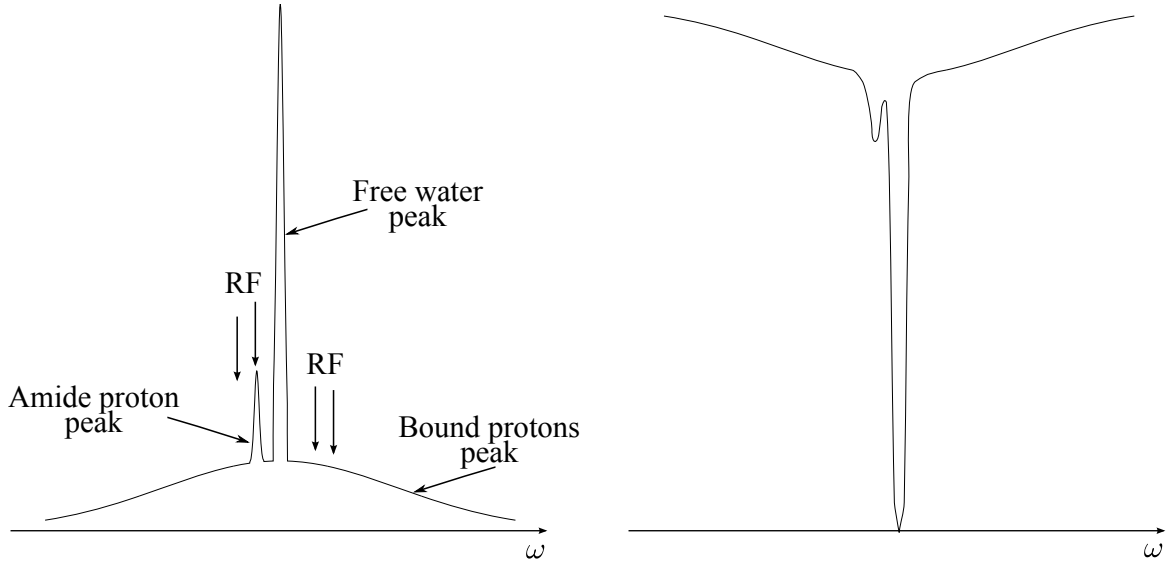
Figure 4.2: Diagram of spectrum of water proton in biological tissue (left), with the free protons, the bound protons and the amide protons represented. The corresponding Z-spectrum is also presented (right). The free and amide protons have a sharp, narrow lineshape compared to the bound protons. Saturation pulses have a non-negligible bandwidth and can induce direct saturation of the free water peak, if positioned too close. This is known as RF bleeding, or direct effect.

The shape of the z-spectrum depends on characteristics of the exchange of nuclear magnetization between protons of solutes, macromolecules and their hydration layer, and free water, via inter and intra-molecular dipole-dipole interactions, spin exchange or molecular exchange [62, 7, 14, 57]. Via exploration of the z-spectrum, the multiple mechanisms occurring during a magnetization transfer experiment can be highlighted, but cannot be observed separately. Exchange of magnetization also influences the observed relaxation times, as the bulk water relaxation parameters (T_1, T_2, chemical shift), reflecting in part the exchange rates and ratio of the hydrated macromolecules.

The phenomena can be distinguished via the inherent properties of the molecules studied. It can be observed that large macromolecules such as proteins or lipids embedded inside the cell membrane have a very short T_2 and wide overall MT effect, while small proteins at the surface of the bilayer, responsible for the CEST effect, have a longer T_2, seen sharper on the Z-spectrum. The presence of a

large bound proton pool inside the cerebral white matter makes Magnetization Transfer Imaging the ideal modality to probe myelination, both in healthy subjects and patients. This modality is routinely used clinically to look at diseases affecting the cerebral white matter [3], especially patients with Multiple Sclerosis, a demyelinating disease [29].

While MT imaging is of great interest both for understanding the disease and planning treatments, the acquisition suffers at low field strength from either poor contrast to noise ratio, or low resolution. Standard MT imaging sequences do not run on high field systems, due to excessive power deposition, beyond the Specific Absorption Rate (SAR) limit. Another problem, specially with high field systems, is the field inhomogeneity, which is a major concern for the saturation part of the experiment. Overcoming this can provide great imaging possibilities of the white matter, especially its myelin content.

4.2 Magnetization Transfer and Chemical Exchange Saturation Transfer

Magnetization transfer, and particularly chemical exchange, are sources of contrast highlighting the interaction between macromolecules inside a volume of interest and the surrounding water. The following will focus on the nature of these interactions, how exactly they can be measured, and the advantages and inconveniences of high magnetic field.

4.2.1 Origin of the magnetization transfer

The concentration of specific cells components, such as proteins, lipids and other macromolecules constituting the tissue, together with their chemical environment, alters the amount of magnetization transfer contrast available. Chemical exchange and magnetization transfer occur frequently during a NMR experiment, even when not wanted. Sources of exchange and transfer of magnetization are discussed in more details in the following sections.

4.2. Magnetization Transfer and Chemical Exchange Saturation Transfer

4.2.1.1 Macromolecules and hydration layer
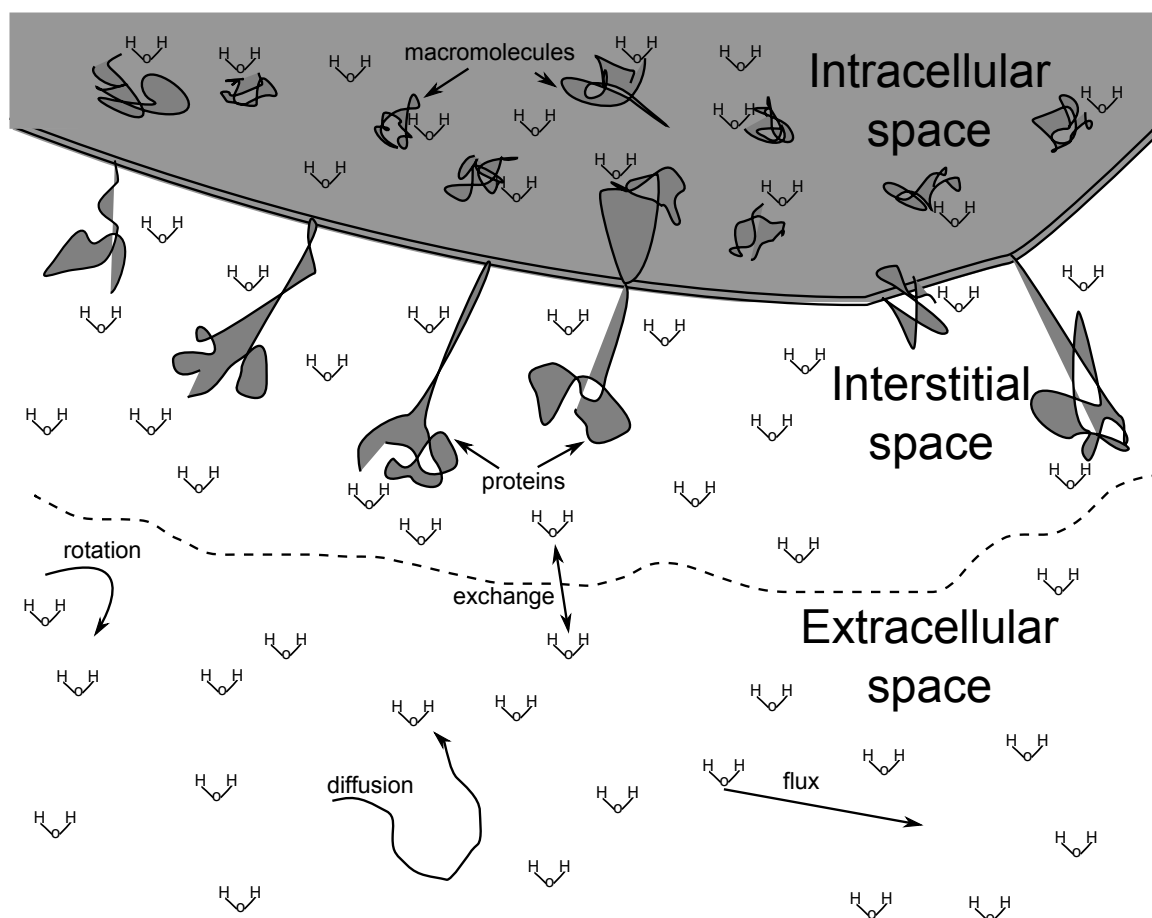
Figure 4.3: Diagram of water proton presence in biological tissue. Rotation, diffusion, external flux as well as magnetization exchange and chemical exchange are depicted.

The transfer of magnetization can occur via two paths: transfer of magnetization and transfer of protons. Several studies have tried to measure effects of dipole-dipole interaction in order to quantify the hydration layer surrounding proteins and other macromolecules. The general relaxation phenomena used by spectroscopists to look at three-dimensional structure of macromolecules is the Nuclear Overhauser Effect (NOE). The NOE is equivalent to dipolar cross-relaxation through space between two nuclear spins sufficiently close to each other. The intra-molecular or inter-molecular interaction between the nuclear magnetic dipole moments induces measurable magnetization transfer between the nuclei [41], the NOE dropping very fast with the distance ($1/r^6$). Recent studies [23, 36] have looked at the close hydration of proteins to map their structural changes, providing insight of their dynamic and function. Previous to this, hydration of protein has been extensively examined,

particularly with Nuclear Magnetic Relaxation Dispersion (NMRD) data (see [27, 67, 26]), as well as with temperature-dependent data [5], $T_{1\rho}$ experiments [4], or via high-resolution NMR spectroscopy using NOE [41]. These studies demonstrated the presence of different sites on the protein, each with specific properties (lifetime or rotational correlation time, position, density on the surface), with each site described via a single Lorentzian distribution [26]. These sites are also subject to proton transfer, with the exchange rate being specific to each particular site, but also influenced by local pH. In fact the presence of ions, such as H^+ and $(NH_3)^+$ for the positive interfacial charges, and OH^- and $(COO)^-$ for the negative charges, influences the chemical exchange of protons with the bulk water, either from protons situated in the macromolecular phase or in the hydration phase [25]. While no exact link between phantom experiments and *in vivo* experiments can be demonstrated yet, the hydration of macromolecules influences the MR signal in a way that can be predicted (see [26, 41, 15]). This exchange, and rate of exchange, thus influences the imaged water signal.

4.2.1.2 Slow, intermediate and fast chemical exchange rate
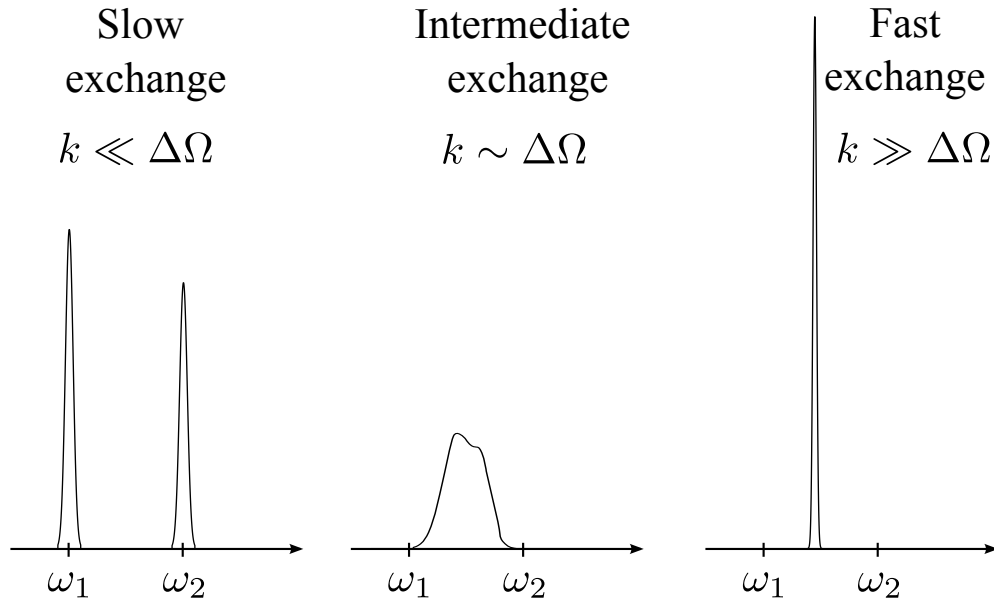

Figure 4.4: Schematic representation of NMR spectrum for an asymmetric two-site exchange process, depending on the frequency of the exchange. A low rate is presented on the left, with two distinctive peaks, and a high rate is presented on the right, where only one peak is detectable.

Before discussing chemical exchange in more detail, it is useful to examine the different cases

in which a nucleus exchanges between two sites resonating at different offset frequencies Ω_1 and Ω_2 at a constant rate k. Three cases can be distinguished [35, 30] and are presented in fig. 4.4: If the frequency difference $\Delta\Omega$ is much greater than the exchange rate k, then the system is said to be in slow exchange (it is rather misleading, as the exchange is extremely fast, only the probability of the transition is low). In this case, two distinct resonance lines can be observed in the spectra. In the case k is larger than $\Delta\Omega$, fast exchange happens, reducing the lines to one sharp resonance line, mainly due to the motional narrowing effect [60, 26]. In the intermediate case, also called coalescence case, the resonant line broaden extensively, making the detection of the two peaks more difficult, as shown in fig. 4.4. Thus the study of the evolution of the line-shape due to exchange after saturation reveals the system properties, and is generally used to study systems in, or close to, the intermediate exchange where the apparent T_2 dispersion in the sample can provide information about the exchange rate constant k [34]. For the slow chemical exchange, the saturation transfer method described first by Forsen [11]) is generally used, whereas for fast exchange, a spin lock experiment measuring a relaxation time called $T_{1\rho}$ is used to map the evolution of the $T_{1\rho}$ as a function of the locking RF field strength as well as the exchange rate [22]. In fact, the locking field applied after the excitation pulse attenuates the effect of chemical exchange together with the effect of dipolar relaxation, making the exchange rate easier to quantify with the use of standard readout imaging sequence. It is clear that these water exchange phenomena perturb the contrast in Magnetic Resonance Imaging [41, 26], but a full picture is still to come.

4.2.1.3 Molecules responsible for the exchange

It has been established that the measured relaxation time in tissue is dominated by the interaction of water with proteins at specific inter-facial sites, representing less than 1 % of the protein-water interface [27]. It means that when bound to a few specific sites in the protein or the lipid bilayer, the magnetic moment of the water protons behaves similarly to the moment of the protons from the macromolecule. This can only happen if the lifetime of the bound water is on the order of 1 μs or more. In comparison, at neutral pH, the lifetime of a proton on a water molecule is on the order of 0.4 ms [28], but is a strong function of the concentration of H^+ and OH^- ions. The size and rotational motion of the protein influences the exchange properties, with small proteins producing

more possible proton exchangeable sites (due to easy access to the protons), while the larger proteins generate wider hydration layers, giving higher probability of magnetization exchange via dipole-dipole interaction. Exchange of hydroxyl and amides protons, such as the ones on NH and OH groups, have been generally disregarded when considering magnetization transfer, as the exchange effect was considered minimal compared to NOE interactions effects between hydration layer and macromolecules. However NOE interactions decrease quickly with distance and are much weaker than the exchange of hydroxyl protons [42], mostly situated on OH and NH groups of different amino acids side chains. Liepinsh and Otting [31] have proposed that the number of exchangeable protons from OH and NH groups is reflected in the contrast of MR images dependent on the magnetization transfer between biomolecules and water. Since then, the interest in amide protons has increased, with spectroscopy methods such as water exchange (WEX) experiments or imaging experiments as amide proton transfer (APT) imaging [69].

4.2.2 Review of quantitative Magnetization Transfer experiments

Different methods can be used to quantify the amount of transfer of magnetization between two pools of protons. They all require saturation of one of the pools, followed by a transfer of the magnetization between the two pools. The magnetization of the volume of interest is then acquired with a readout at the water proton frequency. The Magnetization Transfer Contrast (MTC, [62]) technique requires the acquisition of two images, one proton weighted image (M_0) and the same one with irradiation of the bound pool (M_s). The ratio image (M_s/M_0) shows that the free water component is in exchange in tissue with a relatively immobile component. However this ratio is not directly correlated to the amount of macromolecules present in the tissues, as the exchange rate and relaxation time of the specific species also influence the final MTC. A more quantitative approach requires acquiring Magnetization Transfer Ratio maps (described in details in 5) with different saturation schemes, and then deriving quantities such as the amount of spins inside the compartments, the exchange rate between them, *etc*. The next section reviews possible ways to measure those quantities.

4.2. Magnetization Transfer and Chemical Exchange Saturation Transfer

4.2.2.1   Saturation efficiency for MT quantification

Since its inception in MRI [62, 2], studies have suggested that the MTC depends on the physical environment of the macromolecules, their correlation time as well as the saturation scheme. In recent years, several methods have been developed to measure these different MT parameters, both in tissue-like phantoms (generally composed of Bovine Serum Albumin (BSA) or agar gel), as well as in human tissue *in vivo*. On-resonance and off-resonance RF irradiation can be applied to probe the transfer of magnetization. Common problems related to the saturation are: (1) it takes a lot of power to make the saturation efficient (power efficiency); (2) it takes time to assure that all spins from the targeted pool are saturated (time efficiency).

Power efficiency versus time efficiency   Saturation can be applied on-resonance (*i.e.* on the free pool) via binomial pulses, assuming that the line width of the free spins is infinitely narrow. The saturated free spins exchange with the bound protons, the excitation readout giving directly the amount of spins exchanged. Another saturation technique consists of saturating the bound pool via off-resonance RF pulses, and then measuring the reduced signal on the free pool (on-resonance). The off-resonance saturation can also be achieved via a continuous wave (CW) but requires additional hardware not generally available in clinical settings. The efficiency of the methods can be resumed as follows [20, 13]. The time efficiency of the saturation is best with binomial pulses (around one millisecond), with the off-resonance soft pulses intermediate (around one second for 20 sinc pulses with a 50ms TR), and the CW the worst (more than five seconds). With respect to the power efficiency, the CW is the best, followed by the soft pulses, the binomial pulses being the worst. In conclusion, Hua and Hurst [20] give these practical considerations when choosing between these three techniques: (a) the hardware modifications necessary to implement CW in clinical scanners, (b) experimental difficulties in properly implementing the binomial-pulse approach, and (c) mediocre power/time efficiency for soft shaped pulses. As at 7T a major concern is the RF power deposition, the CW seems impracticable at ultra high field (UHF). The experimental difficulties (due to RF inhomogeneities) in implementing binomial pulses in UHF systems would make the direct effect even harder to deal with. The reasonable choice is thus soft pulses applied off resonance, where the poor time efficiency is balanced by the high sensitivity at high field. Another advantage is the possibility to choose the frequency at which the

saturation is applied, *e.g.* to target specific solutes or to explore the entire spectrum of frequency. For these principal reasons, and due to the constraints of both power deposition (SAR limit) and flexibility of parametrization, the majority of *in vivo* studies use off-resonance pulsed saturation.

In the following paragraphs, techniques to highlight either phenomena used to quantify exchange of magnetization are presented. The optimal design of even a simple MT ratio (MTR) clinical acquisition would benefit from the knowledge of the intrinsic MT parameters (concentration and relaxation times of different species, pH, exchange times). Those parameters may also provide new information about tissues composition.

4.2.2.2 Magnetization Transfer quantification

Magnetization transfer appeared as a new source of contrast in MRI in the late 80's, but has long been known by spectroscopists, who used this phenomenon to enhance signal of specific species by cross-relaxation. Quantification studies [10, 18] of MT contrast in an MRI scanner were carried out to shed more light on the phenomenon *in vivo*.

Continuous wave saturation Quantification of the proton exchange inside a rabbit kidney *in vivo* is described in [10], based on variation of both the strength and the length of the saturation B_1 field, while keeping the offset resonance constant. B_1^2 irradiation strength varied between 0 and $2\,e^{-10}$Tesla^2 for a time up to $10\,s$. A study performed by Henkelman *et al.* [18] presented a refinement where the evolution of the magnetization exchange depended both on the irradiation strength and the offset frequency. Agar gel phantoms of different concentrations was used to show that the MT effect is dependent on the agar concentration, and described the effect of direct saturation competing with the MT effect. Both models were derived from the steady-state saturation condition, as the CW was used long enough (several seconds) for both quantitative studies to assure a constant exchange of magnetization between the two pools before the end of the CW saturation.

4.2. Magnetization Transfer and Chemical Exchange Saturation Transfer

In vivo **quantification via steady-state saturation** More recently, Sled and Pike [49] managed to quantify MT in human brain *in vivo*. The sequence, a spoiled gradient echo, was developed to acquire images at reasonable resolution (2 mm in plane for a slice thickness of 7 mm) for a series of saturation parameters, namely frequency offset and power deposition. The total acquisition time for the series of 60 images was 35 min on a 1.5T scanner. Results shown on agar gel compared well with the ones of Henkelman [18], and *in vivo* results from two subjects showed good similarities. The main difference between the last study presented with the previous ones was the saturation process. In [49], the steady state was not obtained via CW but built up by the imaging sequence. A 6 seconds dummy period was played before the imaging sequence to put the system into steady state, and the saturation was maintained by an additional off-resonance soft pulse before each readout sequence, as presented in fig. 4.5. Yarnykh [64] then presented a similar protocol, called Z-spectroscopy, but simplified the model with only a three parameter approximated analytical model. Results showed that no quantitative difference could be seen between pulsed and CW quantification methods.
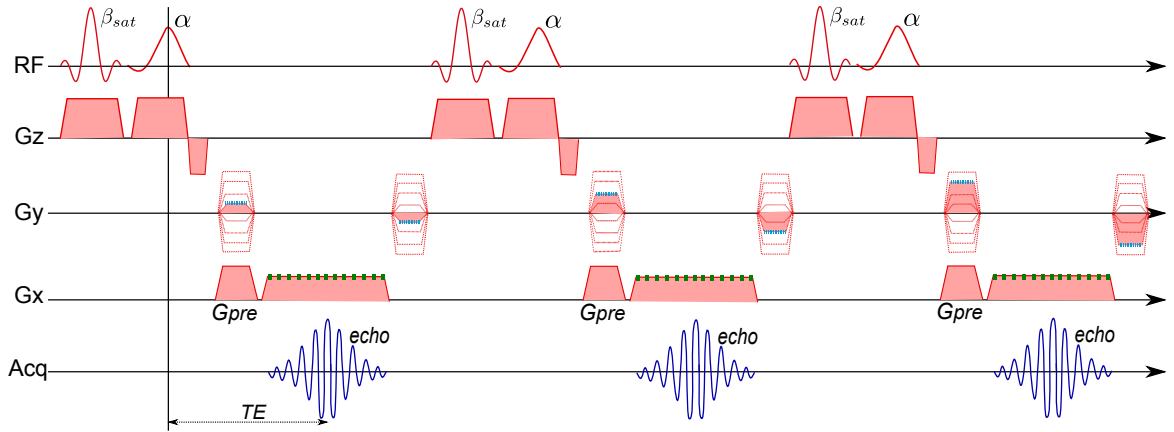
Figure 4.5: Diagram of a MT-GRE pulse sequence, with the saturation pulse β_{sat} occurring before each excitation pulse α.

Quantification during approach to steady-state saturation Both theoretical work [32, 16] and practical work [17, 55] have been used to present the saturation during the approach to steady-state, but the complexity of a time-varying solution to the modified Bloch equations makes it a less appealing method. Techniques described in [55] as well as in [13] combined a train of pulsed off-resonance irradiation to partially saturate the bound pool, directly followed by a single shot acquisition (for example an EPI readout). No steady-state is reached by this method, making the model more com-

plicated, but in no way less efficient as demonstrated in [13]. Moreover, study of the approach to steady-state is possible, potentially richer than a steady-state quantification, as the dynamic of the transfer can be probed as well. The main difficulty is the establishment of a realistic modelling of the saturation and its effects on the magnetization.

4.2.2.3 Chemical exchange quantification

Chemical Exchange dependent Saturation Transfer (CEST) imaging is a particular type of MT experiment, focused on measuring chemical exchange between solutes and free water spins on a frequency range close to the water resonance, resulting in an increase of several orders of magnitude in sensitivity for metabolites over direct detection methods [14]. On fig. 4.1 and 4.3, the chemical exchange is provided by exchange of protons between the hydration layer (from water trapped inside macromolecules as membranes, proteins or myelin, or protons at the surface of small proteins) and the free water. The chemical exchange effect depends on proton concentration (pH) and thus provides a method of measuring pH *in vivo* [69, 70] particularly in ischaemic strokes [53]. CEST is also being used to study endogenous molecules, in particular amide protons in proteins at +3.5 ppm from water (Amide Proton Transfer, APT imaging), peptides and other polymers, and has proved useful in imaging tumours [69, 24]. CEST occurs when saturation is applied at the exact frequency of the solute protons, and therefore is usually detected by examining asymmetries in the z-spectrum to balance the effects of direct saturation of the water peak on the z-spectrum. CEST is also being used to design novel contrast agents for MRI, including both diamagnetic and paramagnetic agents, the latter being used to increase the chemical shift between the species to ensure they are in slow exchange [58, 70]. These have the potential to make MRI a molecular imaging modality. Quantification of CEST effects can provide relatively direct information about molecular motion and molecular exchange, and could potentially help to understand the hydration of proteins as well as quantification of metabolites concentration *in vivo* with use of external agents (LipoCEST, PARACEST [1]), facilitated with high magnetic field systems. However, these effects are strongly dependent on pulse sequence design, as well as the concentrations and relaxation times of the molecules involved in magnetization transfer, relaxation times of bulk water and pH. CEST requires that the two pools of protons are sufficiently separated in frequency to be in slow (*i.e.* infrequent) exchange as explained in section 4.2.1.2, and that

the exchange rate must be fast enough to be detectable before the saturated magnetization recovers with T_1 ($k > T_1^{-1}$) [30]. Therefore it is expected that CEST will particularly benefit from increased field strength since the chemical shift between the pools and the T_1 of water will both increase with field strength.

Quantitative MT methods have been applied in the brain to probe the amount of the principal component of the white matter, myelin. However myelin composes only half of the dry white matter weight, meaning other macromolecules and cells can influence the movement of water as well. Before using the MT quantification clinically, a review of the composition and role of the myelin in the brain is necessary.

4.2.3 Myelin and white matter

Myelin is a major component of the white matter of the Central Nervous System, and is essential for the normal functioning of nerve fibres. Once formed, myelin sheaths have a relatively long-term metabolic stability, with a higher turnover rate for newly synthesized myelin in the adult [56]. Quantifying the amount of myelin *in vivo* in the white matter would provide a great opportunity to study both the maturation of the fibre tracks in the brain, as well as deterioration due to age or disease.

4.2.3.1 Cellular composition of the white matter

The human brain is composed of around 80 % of water, the remainder consisting of many more complex molecules, mostly lipid and proteins. The contrast obtained in MRI is hugely dependent on the environment of this water, since the water molecules hydrate, and thus interact with, most macromolecules composing cells such as vessels walls, neurons or white matter tracks, but also with proteins such as haemoglobin, myelin or even lipid complexes necessary for energy storage or membrane constitution. However, the voxel size obtained via an MR imaging session is generally several hundreds of microns to few millimetres, containing millions of cells (one averaged cell being $1\,\mu\mathrm{m}^3$). The principal constituent of the white matter is the myelin, essential for normal functioning of the nerve fibres composed by axons. These axons are extensions of the neurons, transmitting signal be-
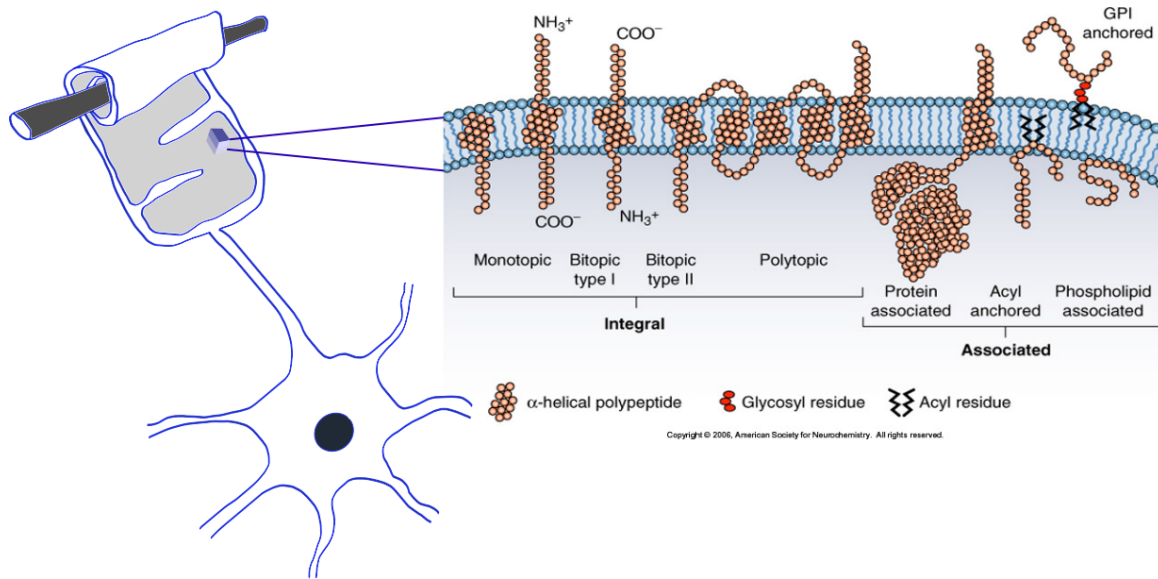
Figure 4.6: Diagram showing the axon being rolled in the myelin sheath, together with representation of the chemistry of the cell membrane of the oligodendrocyte producing the myelin. Adapted from Basic Neurochemistry [48]

tween neuronal cells bodies situated inside grey matter. Axons are microscopic in diameter (typically around 1μm), but may be up to a meter in length (*e.g.* the sciatic nerve). In the brain, neurons are frequently myelinated, providing a better electrical signal conduction rate, or reducing its required diameter (*e.g.* for the same conduction efficiency of 25 m/s, a unmyelinated squid axon of 500 μm requires 5000 times as much energy and occupy 1500 times as much space as a 12 μm diameter myelinated nerve in a frog!). Axons in the brain are enveloped into myelin sheaths, extensions of the plasma membrane of oligodendrocytes, as seen on fig. 4.6. One layer of the myelin sheath measures approximately 160-180 Å in width, one axon having up to 100 layers wrapped around its body. The total of the myelin sheaths composes about 50% of the total dry weight of the white matter, this volume being determined by the number of axons, their calibre and the thickness of the sheaths. The g-ratio, a ratio between the axon diameter and fibre diameter (sum of axon diameter and myelin sheath thickness), proved to be relatively stable ($\sim$0.6 [45]) across the brain, and has proven useful for studying the maturation of the brain [44]. This maturation is possible via production of myelin from oligodendroglial cell, producing up to three times its own weight of myelin per day. One oligodendrocyte can be responsible for the production and maintenance of up to 40 nerve fibres, the ratio between body surface membrane and myelin membrane being estimated to 1/620 in the case of oligodendrocytes (most data from [56]).

4.2.3.2   Molecular view of the white matter

Looking closer at the structure of the myelin sheath, one discovers that the membrane is formed by a series of lipid bilayers, scattered with proteins (fig. 4.6). The lipid elements of the membrane are phospholipids, glycolipids and cholesterol. The common feature of these lipids is that they are amphipathic, meaning that the lipids have both hydrophobic and hydrophilic regions. This property enables the lipids to form stable aggregation like in a micelle, where the hydrophobic regions joined to a virtual point, leaving the hydrophilic regions in direct contact with water (see 4.7). Another stable structure, the bilayer form, exists as a sheath in which the hydrophobic regions of the lipids are protected from the water, while the hydrophilic regions are immersed in water. The membrane structure composing the myelin sheath is highly stable due to the presence of very long chain of saturated fatty acids. This bilayer lipid structure allows for interactions of amphipathic proteins with the membrane, the hydrophobic end of these proteins traversing the layer and being held by the hydrophobic core of the layer, while the hydrophilic region is protruding to the outer side of the membrane (see 4.7). The myelin sheaths contain also a large number of enzymes, playing an active role in myelin synthesis and repair.
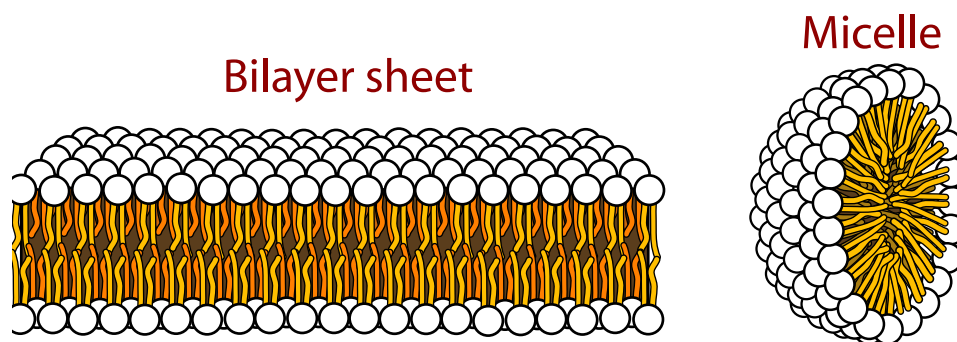
Figure 4.7: Diagram showing the micelle structure and the bilayer structure, the bilayer being similar to the membrane structure of a cell

In addition, peripheral proteins are bound to the hydrophilic regions of specific integral proteins. The close correlation between position of water inside or around myelin sheaths with its movement restriction provides a good indirect myelin quantification [59]. On T_1-weighted images, regions with myelin appear brighter, indicating a decrease in the observed T_1 probably due to restricted motion of water molecules bound to the myelin sheath.

4.2.3.3 Quantification of the myelin

Recent studies have been focused on retrieving distinctive water pools via multi-component T_2 analysis. MacKay [33] described a model taking into account water environment (either a myelin pool, a pool containing the intra and extra cellular water, or a free water pool composed mainly by the CSF). Each of these pools is assumed to have different exchanging rates and different relaxation times, the observed relaxation time T_2 inside one voxel having a multi-exponential behaviour reflecting each of the pools. The myelin water is assumed to have a short T_2 ($\sim$20 ms) due to its compartmentalisation in myelin membranes, while the intra- and extra-cellular water have a longer T_2 ($\sim$80 ms) , the cerebro-spinal fluid having a T_2 of $\sim$2 s [59]. Diffusion of the water within the myelin sheath is slow enough so that no significant exchange between the different pools could occur. However this model did not look at the source of the exchange, *i.e.* the macromolecules generating the fast or slow exchange. Stanisz *et al.* [50] looked at the relationship between the T_2 and the MT of the bovine optic nerve, modelling each voxel as a two-tissue compartments, each with a semi-solid pool and a liquid pool. The MT effect originating from the myelin water was found to be nine times larger than that of intra/intercellular water, indicating that the MT characteristics observed for white matter are mainly related to myelin. Looking from another perspective, histology experiments indicate that MT effects in the white matter can be linked to myelin amount [38, 46]. The specific myelin proteins (MBP) were stained via chemical reactions in order to get a density map of the quantity of interest at a very fine detail, correlating with the MR data. However, histological processing of tissues enabling the observation of very thin layers of tissue (in the order of μm) requires strong chemical alteration (fixation). This involves protein cross-linking which will have large effects on the hydration layer [47]. Therefore MR studies of fixated tissues can be misleading. It does not alter the fact that the amount of myelin measured with MRI and with histology was strongly correlated in the white matter of post-mortem tissues from patients suffering from Multiple Sclerosis [46], a demyelinating disease.

4.2.4 CEST, MT and high field

Studies of chemical exchange and magnetization transfer have been performed extensively during the last two decades. However, MT experiments did not benefit massively from the rise of high

4.2. Magnetization Transfer and Chemical Exchange Saturation Transfer

field scanners, the main reason being the power deposition limit. Some experiments have been performed at field strengths of 7 Tesla and above on purposed-built phantoms and rats, but not in humans *in vivo*. As demonstrated in the previous paragraph, CEST effects are expected to increase with field strength, together with an increase of sensitivity due to better spectral resolution. By varying both the irradiation power and the frequency offset, both MT and CEST can be probed, if optimized accordingly. Therefore a more thorough understanding of the full z-spectrum at 7 T should highlight the different exchanging process, possibly providing a biomarker for myelin. The following list details the main problems of magnetization transfer scanning *in vivo* at high magnetic field strengths.

- **Increased SAR** As MT experiments require a high irradiation power to partially or completely saturate the bound pool, it becomes a major concern for high field MT experiments not to reach the SAR limits. The MT-GRE imaging sequence, *i.e.* one saturation pulse before each excitation pulse, used in a common Magnetization Transfer imaging experiment, is imposible to apply at 7T due to its high power deposition. Duvvuri *et al.* [9] have shown that a clinical MT sequence could be used at 4T in a standard system, generating an increase of MTR compared to lower field (1.5T). It was also shown that similar MT effects could be obtained at 4T with a decrease of 20% of B_1 compared to 1.5T.

- **Increased B_0 inhomogeneity** The homogeneity of the main magnetic field affects the effective frequency of the saturation. A change of one ppm (corresponding to 300Hz at 7T) leads to noticeable changes in the measured MTR, depending on the frequency saturated as described with a z-spectrum (fig. 4.2). The offset resonance dispersion can be reduced with a higher order shimming, together with post-processing correction.

- **Increased B_1 inhomogeneity** The effective saturation depends on the homogeneity of the transmit B_1 field, in a similar manner that variation in the receiver field affects the image contrast, with the power delivered at a specific location dependent on the B_1^+ field. Measure of the amount of protons exchanging, together with their rate, is based on the power delivered to the sample, making the local variation of the transmit B_1 a problem to account for. Additional care is thus necessary when correcting for inhomogeneities (both during acquisition and post-processing) and will be described later on.

- **Increased SNR** Higher field strength provides an increase in SNR. However the increase of longitudinal relaxation time with field strength decreases the amount of SNR per unit time. In [9], the major improvement at 4T was found in the MT signal-difference-to-noise (SDNR) in all tissues as a consequence of the higher SNR compared to 1.5T, with similar results being reported by Cercignani [8] at a field strength of 3T.

- **Increased spectral separation** The Larmor frequency increases linearly with the field strength, directly providing a better spectral resolution in Hz at 7T compared to 3T for example. Compounds in the spectra are easier to separate (*e.g.* the glutamate and glutamine peaks) , and APT is no exception. This reduces dramatically the overlap between the CEST peak and the direct water saturation peak, providing the possibility to detect solely the CEST effect at 7T.

- **Increased linewidth** The increase in resonance frequency widens the linewidth of the water (in Hz), due to motional narrowing of the water protons dependent on the magnetic field strength. The direct saturation effect, due to saturation of the water directly and thus not related to MT, is expected to decrease (in ppm), but depends also on the precision of the shimming.

- **Increased T_1/MT effect** The MT effects proved to be greater at high field, probably due to the lengthened T_1. Small readout flip angle were used in both these studies ($12°$ in [9] versus $5°$ in [8]), while higher contrast could be obtained with higher flip angles, but would have resulted in a complex interaction between MT effects and T_1 recovery. Henkelman *et al.* [19] also observed no change of exchange rate between 0.6T and 1.5T in agar gel phantoms, the increased in MTR being solely attributed to the increase in T_1.

4.3   Modelling the pulsed MT experiment

The aim of the present study, described in [39], was to measure the full z-spectrum during the approach to steady state *in vivo* at 3 T and 7 T using an MT prepared gradient echo EPI sequence to reduce SAR [69, 55], and to investigate the possibility of using a 3 compartment model to quantify various MT and CEST parameters in phantoms and *in vivo* at 7 T. To allow the quantification of both MT and CEST, a more specific model than the conventional two-pool model was necessary. Instead of

using only two pools (one for the bulk water and one for the bound water), a third pool was included, as discussed below. The Bloch equations modified by Mc Connell [34] were used in a pulse by pulse numerical simulation to model the chemical exchange occurring between the different pools.

4.3.1 Three compartment model

The model assumes three interacting pools of protons which are (i) the free water magnetization describing the water diffusing freely in the intra or intercellular space (free pool, M_f), (ii) the macromolecular protons and protons associated with macromolecules via the hydration layer of large proteins (bound pool, M_b), and (iii) a pool of protons in small proteins in chemical exchange with the free pool (exchanging pool, M_c). Modified Bloch equations can be used to describe the evolution of different pools of protons, assuming each of the pools has a single transverse relaxation time T_2. The macromolecular associated pool is not in this category but this can be dealt with by adding a line-shape function (generally a Super Lorentzian lineshape for *in vivo* tissues [37, 49]), assuming that the macromolecules have a symmetric spectrum [57]. Ceckler *et al.* [6] have previously proposed a three pool model to describe interaction between magnetization of bulk water, macromolecular protons and the hydration layer associated with macromolecules via physical exchange and dipolar coupling. They showed that under reasonable conditions this three pool model reduces to a two pool (bulk water and macromolecular/hydration layer protons) model. Here we use this result to assume that the bulk water/ hydration layer/ macromolecule system can be described by a two model system, but let the third pool describe chemical exchange with the protons in a small solute protein. We used the model of Woessner *et al.* [61] to describe the evolution of magnetization in a three pool model:

$$\frac{dM(t, \omega_{rf})}{dt} = A(t, \omega_{rf}).M(t, \omega_{rf}) + B.M_0 \tag{4.1}$$

4.3. Modelling the pulsed MT experiment

where

$$
M(t,\omega_{rf}) = \begin{pmatrix} M_x^f(t,\omega_{rf}) \\ M_y^f(t,\omega_{rf}) \\ M_z^f(t,\omega_{rf}) \\ M_x^b(t,\omega_{rf}) \\ M_y^b(t,\omega_{rf}) \\ M_z^b(t,\omega_{rf}) \\ M_x^c(t,\omega_{rf}) \\ M_y^c(t,\omega_{rf}) \\ M_z^c(t,\omega_{rf}) \end{pmatrix}, M_0 = \begin{pmatrix} 0 \\ 0 \\ M_0^f \\ 0 \\ 0 \\ M_0^b \\ 0 \\ 0 \\ M_0^c \end{pmatrix}, B = \begin{pmatrix} 0 & 0 & 0 & 0 & 0 & 0 & 0 & 0 & 0 \\ 0 & 0 & 0 & 0 & 0 & 0 & 0 & 0 & 0 \\ 0 & 0 & \frac{1}{T_1^f} & 0 & 0 & 0 & 0 & 0 & 0 \\ 0 & 0 & 0 & 0 & 0 & 0 & 0 & 0 & 0 \\ 0 & 0 & 0 & 0 & 0 & 0 & 0 & 0 & 0 \\ 0 & 0 & 0 & 0 & 0 & \frac{1}{T_1^b} & 0 & 0 & 0 \\ 0 & 0 & 0 & 0 & 0 & 0 & 0 & 0 & 0 \\ 0 & 0 & 0 & 0 & 0 & 0 & 0 & 0 & 0 \\ 0 & 0 & 0 & 0 & 0 & 0 & 0 & 0 & \frac{1}{T_1^c} \end{pmatrix}
$$

$$\text{(4.2)}$$

and

$$
A(t,\omega_{rf}) = \begin{pmatrix} -\frac{1}{T_2^f}-k_f & -2\pi\Delta_f & 0 & k_{bf} & 0 & 0 & k_{cf} & 0 & 0 \\ 2\pi\Delta_f & -\frac{1}{T_2^f}-k_f & -\omega_1(t,\omega_{rf}) & 0 & k_{bf} & 0 & 0 & k_{cf} & 0 \\ 0 & -\omega_1(t,\omega_{rf}) & -\frac{1}{T_1^f}-k_f & 0 & 0 & k_{bf} & 0 & 0 & k_{cf} \\ k_{fb} & 0 & 0 & -\frac{1}{T_2^b}-k_{bf} & -2\pi\Delta_b & 0 & 0 & 0 & 0 \\ 0 & k_{fb} & 0 & 2\pi\Delta_b & -\frac{1}{T_2^b}-k_{bf} & -\omega_1(t,\omega_{rf}) & 0 & 0 & 0 \\ 0 & 0 & k_{fb} & 0 & -\omega_1(t,\omega_{rf}) & -\frac{1}{T_1^b}-k_{bf}-R_b(\omega_{rf}) & 0 & 0 & 0 \\ k_{fc} & 0 & 0 & 0 & 0 & 0 & -\frac{1}{T_2^c}-k_{cf} & -2\pi\Delta_c & 0 \\ 0 & k_{fc} & 0 & 0 & 0 & 0 & -2\pi\Delta_c & -\frac{1}{T_2^c}-k_{cf} & -\omega_1(t,\omega_{rf}) \\ 0 & 0 & k_{fc} & 0 & 0 & 0 & 0 & \omega_1(t,\omega_{rf}) & -\frac{1}{T_1^c}-k_{cf} \end{pmatrix}
$$

$$\text{(4.3)}$$

In these vectors and matrices, the free pool is indicated by the superscript f, the bound pool is indicated by the superscript b and the exchanging pool is indicated by the superscript c. (M_x^i, M_y^i, M_z^i) are the components of the magnetization for each pool ($i= f$, b or c), M_0^i is the equilibrium magnetization for each pool, and T_1^i and T_2^i are the longitudinal and transverse relaxation times of each pool. Δ_i represents the difference in frequency between the applied saturation pulse of amplitude $\omega_1(t)$ and frequency ω_{rf}, and the chemical shift of the corresponding pool δ_i. k_{bf} and k_{cf} are the exchange rates of the bound pool and the exchange pool with the free water reservoir, and k_{fb} and k_{fc} are the exchange rates of the free water with the bound pool and the exchange pool, the relation between

4.3. Modelling the pulsed MT experiment

these being:

$$k_{ij} = \frac{M_0^j}{M_0^i} k_{ji} \tag{4.4}$$

k_f represents the total exchange rate between the free water and the other pools, and is the sum of the exchange rate k_{fb} and k_{fc}. The relaxation times are related by:

$$\frac{1}{T_1^{obs}} = \frac{1}{T_1^f} + \frac{M_0^b}{M_0^f} \frac{1}{T_1^b} + \frac{M_0^c}{M_0^f} \frac{1}{T_1^c} \tag{4.5}$$

and

$$\frac{1}{T_2^{obs}} = \frac{1}{T_2^f} + \frac{M_0^c}{M_0^f} k_{cf} + \frac{M_0^b}{M_0^f} k_{bf} \tag{4.6}$$

where T_1^{obs} and T_2^{obs} are the measured relaxation times for the bulk sample, while T_1^f and T_2^f are the computed relaxation times for the free water pool based on the equations 4.5 and 4.6. The term $R_b(\omega_{rf})$ present in the matrix 4.3 describes the lineshape of the bound pool, which was chosen to be Super Lorentzian [49]. To study the approach of the system to steady-state, no simple analytical solution to the system of differential equations above exists. Instead an Ordinary Differential Equation (ODE) solver was implemented to compute the evolution of the magnetization of the different pools during the approach to saturation, using a 4th order Runge-Kutta algorithm with a 10 μs interval. A pulse by pulse numerical simulation was implemented, with the resulting value of M_z^f used to plot the z-spectrum.

4.3.2 Sequence description

A schematic of the pulse sequence is shown in fig. 4.8. Either a CW SAT or a PULSED SAT scan (as indicated in the figure, and following the discussion in 4.2.2.1) is acquired, along with an additional NO SAT scan. Both the CW and PULSED acquisitions were simulated but only the PULSED acquisition was used experimentally. The off-resonance saturation scheme used PULSED SAT (fig. 4.8) which consisted of a train of up to N=20 off-resonance pulses (Gaussian-windowed,

4.3. Modelling the pulsed MT experiment
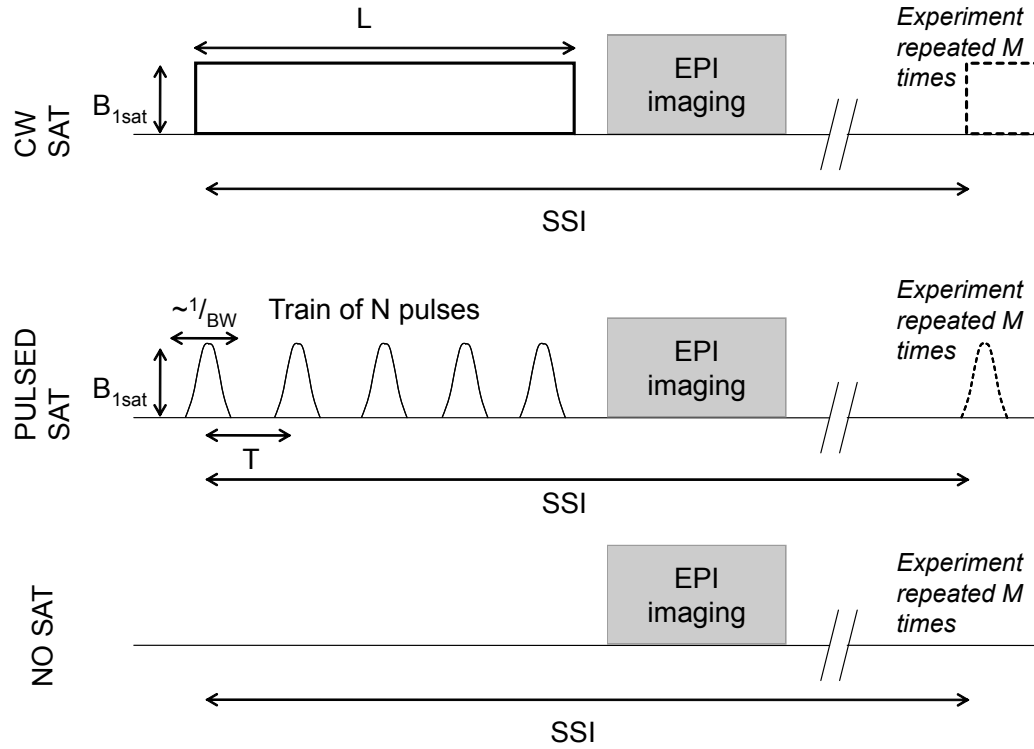
Figure 4.8: Schematic diagram of the pulse sequence used in simulations and experiments. Either a CW or PULSED saturation acquisition was followed by a NO SAT acquisition. The CW acquisition was only simulated and not used in experiments. The imaging module was either gradient echo EPI or turbo-field echo.

sinc shaped pulses) with amplitude B_1^{sat} and a delay of T=55 ms between each pulse. The pulse train was followed by a spoiler gradient in the slice direction to destroy any transverse magnetization. The amplitude and duration of the spoiler was chosen after a series of experiments, looking at the resultant signal in an agar phantom without excitation pulse. A gradient of 33 mT/m strength applied during 14.6 ms left no significant signal and is the gradient used hereafter. To allow the full z-spectrum to be acquired *in vivo* in a reasonable imaging time an EPI readout was applied after the PULSED SAT preparation pulses (MT-EPI). The EPI readout was single shot, TR/TE=10000/16 ms, BW of 2.8 kHz for an isotropic resolution of 2x2x2mm^3. A shot-to-shot interval (SSI) of 10 s was left between each acquisition to allow the longitudinal magnetization of the different pools to relax back to equilibrium before the next saturation train was applied. The frequency offset of the saturation pulses was varied from -10 to +10 kHz logarithmically, allowing the z-spectrum to be measured at 24 points in less than 5 min.

4.3.3 Simulations

Since only a pulsed experiment could be implemented experimentally without hardware modification, the model described above was used to simulate the effect of experimental parameters on the z-spectrum and in particular to compare the effect of pulsed and CW off resonance saturation. The parameters used in the simulations are given in table 4.1 unless otherwise stated.

	Free pool	Bound pool	CEST pool
$T_1(s)$	1	1	1
T_2	40 ms	10 μs	0.5 ms
M_0	-	10 % of M_0^f	7 % of M_0^f
R	-	35 Hz	15 Hz
Chemical shift	0 Hz	0 Hz	1000 Hz

Table 4.1: Table of the different parameters values used in the simulation, if not stated otherwise.

Pulsed versus CW irradiation schemes were compared by varying the amplitude and effective length of the off resonance irradiation. For CW irradiation, varying amplitudes of B_{1sat}= 0.95, 3.75 and 7.6 μ T at a length of 1 s and varying lengths L= 275, 550, 1100 and 2750 ms at an amplitude of 3.79 μ T were investigated. For pulsed varying amplitudes of B_{1sat}= 0.95, 3.75 and 7.6 μ T and varying train lengths of N=5, 10, 20, and 50 pulses of bandwidth (BW) 200 Hz and with period (T) 55 ms were investigated. The length and amplitude of the CW irradiation and the number and period of the RF pulses were matched to give the same integrated power and/or total saturation length as for the pulsed case. For pulsed irradiation the time between the off-resonance pulses (T=30-100 ms) for N=20 pulses, and the bandwidth of the pulses (BW=200-400 Hz) were also varied, adjusting the amplitude to keep the integrated power of the off resonance irradiation constant in this case. To observe the approach to steady-state of the pulsed train, simulation of the magnetization evolving during the saturation and the exchange was recorded. As shown in [55] and in fig. 4.9, evolution of the magnetization tends to stabilize and reach a steady-state, the timing depending principally on the T used for the saturation pulses. As this time T gets longer, the steady-state occurs with less pulses, but at the expense of a weaker saturation value (55% with a 30 ms TR compared to 28% with a 100 ms TR, all other parameters being the same) as well as a longer saturation time (1.2 s with T=30 ms versus 2.3 s with T=100 ms).

4.3. Modelling the pulsed MT experiment
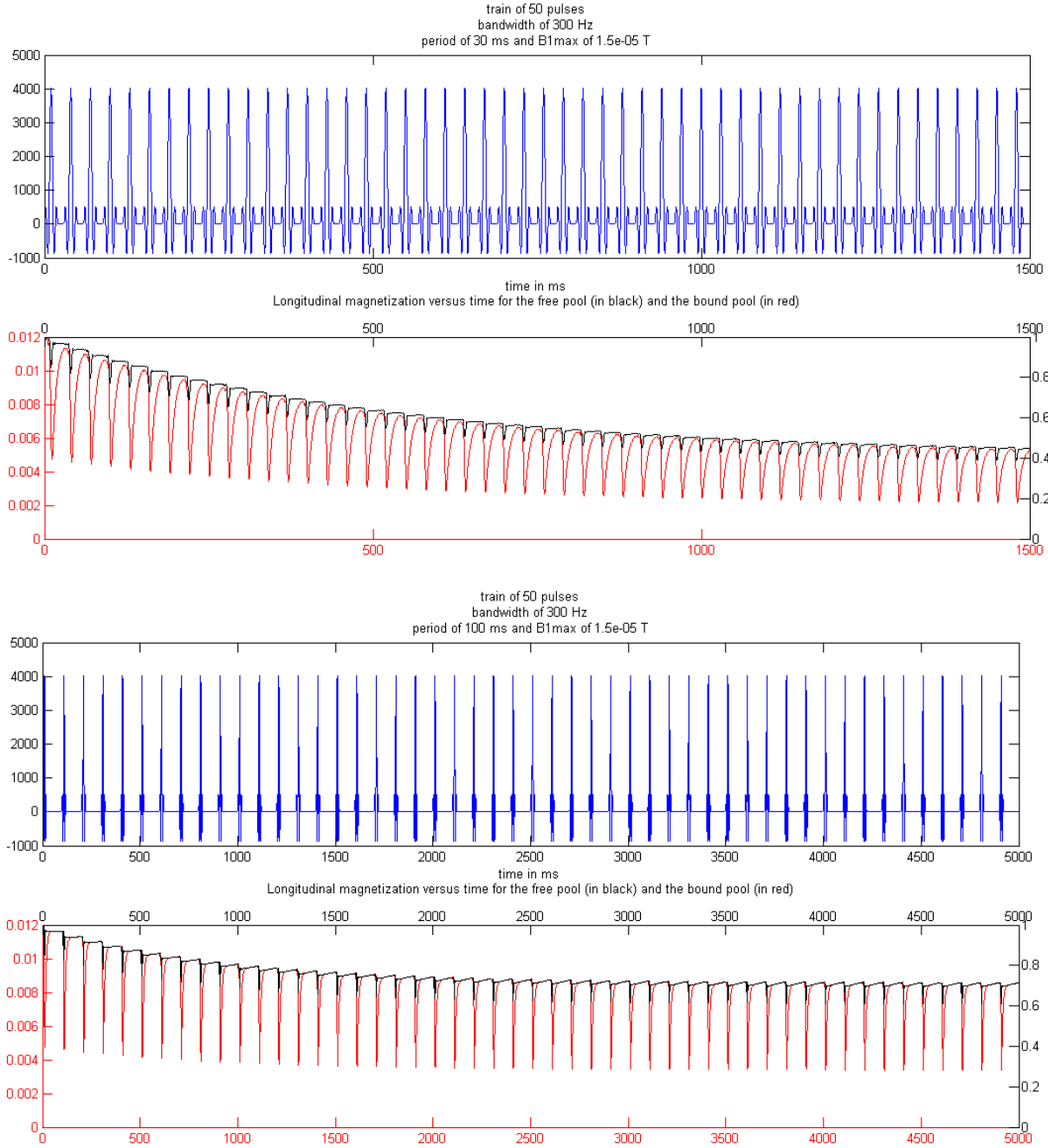
Figure 4.9: Simulation of a train of 50 off-resonance pulses with a bandwidth of 300 Hz and a varying period of 30 ms and 100 ms.

Simulated z-spectra are presented in fig. 4.10 and 4.11. Fig. 4.10 compares the effect of different CW and pulsed MT saturation schemes on the z-spectrum (fig.4.10 b, c, e and f) and spectral asymmetry at a single offset frequency of 3.5 ppm (MT_{asym} which is effectively APT contrast) (fig.4.10 a and d). Fig. 4.10 a simulates the effect of CW and pulsed saturation amplitude on MT_{asym},
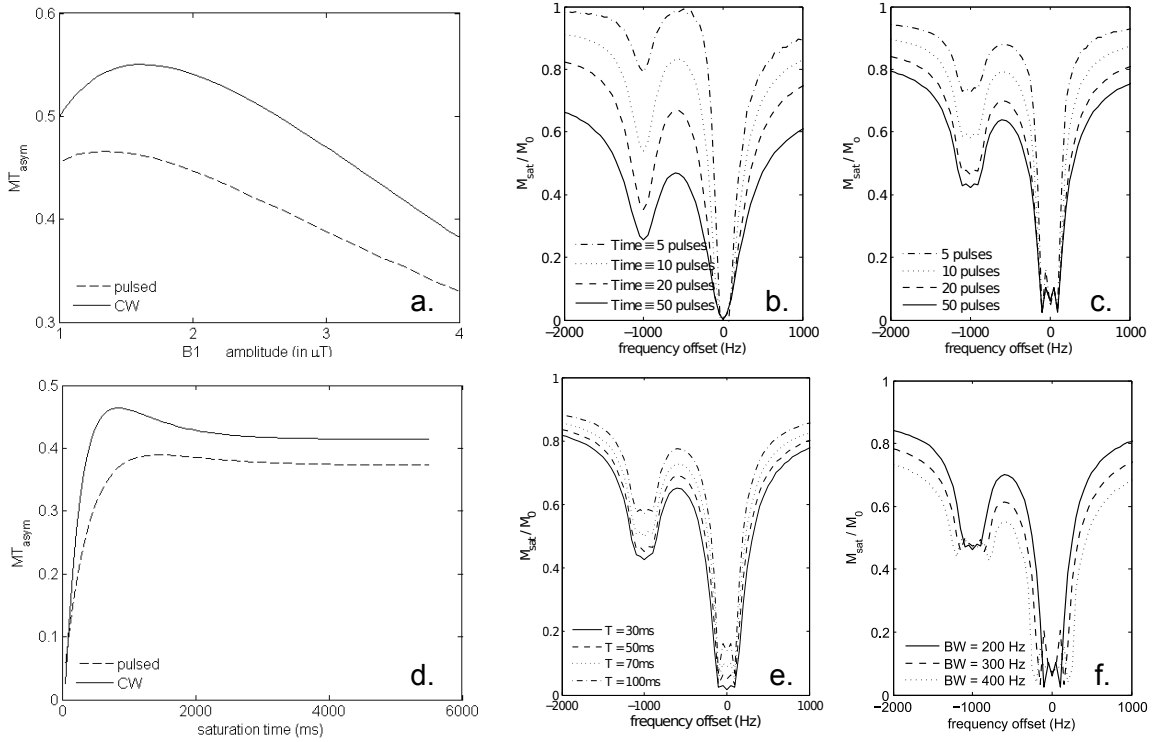
Figure 4.10: Simulations of the effect of saturation sequence on spectral asymmetry at 3.5 ppm (a, d) and the full z-spectra (b, c, e, f). (a) compares the effect of the saturation amplitude on APT contrast for pulsed and CW saturation, with the B_1 amplitude varied in CW to keep the RF power constant compared to pulsed saturation. This figure also compares the effect of the duration of (b) CW and (c) pulsed saturation on the z-spectrum (T between pulses=50 ms), and on the (d) MT_{asym}, as well as the effect of pulse separation (e) and bandwidth (f).

with the integrated saturation power matched between the CW and pulsed experiments and total saturation length of 1 s (made up of 20 pulses with T=50 ms for pulsed irradiation). Fig. 4.10 b and c compare the effect of changing the length of CW saturation or number of saturation pulses on the z-spectrum. For the CW spectra (b) the total length of the saturation and integrated RF power were matched to those for the pulsed saturation (c) which had bandwidth = 200 Hz, T= 55 ms. Fig. 4.10 e and f demonstrate the effect of pulse interval and bandwidth for pulsed saturation on the z-spectrum.

Fig. 4.10 shows that similar spectral definition can be obtained with CW and pulsed saturation except for a small amount of ringing on the pulsed z-spectrum close to resonance. Fig. 4.10 also shows that as expected [54] there is an optimum B_1 amplitude for good spectral definition in the CEST peak and good MT contrast, since at low B_1 amplitude there is little saturation to exchange

to the water peak, whereas at high B_1 amplitude, when the irradiation power is comparable to the frequency difference between the water protons and the amide protons, the direct suppression of the water peak overwhelms the CEST and MT effects, the z-spectrum asymmetry being lost. A similar effect happens with increasing length of CW saturation or pulse train. Fig. 4.10 e shows that as the period T between the pulses increases, off-resonance saturation decreases together with the line widths, suggesting that changing T may provide additional information for probing both the exchange rate and transverse relaxation rate of the diverse pools thanks to the extra dynamic introduced by the period T. Longer T will reduce the effective saturation power, but will provide more exchange time for the pools, depending on the T_2 of the species of interest. Fig. 4.10 f also shows that as the bandwidth of the pulses decreases (adjusting the amplitude to keep the power of the off resonance irradiation constant) then the spectral definition increases, as is expected.
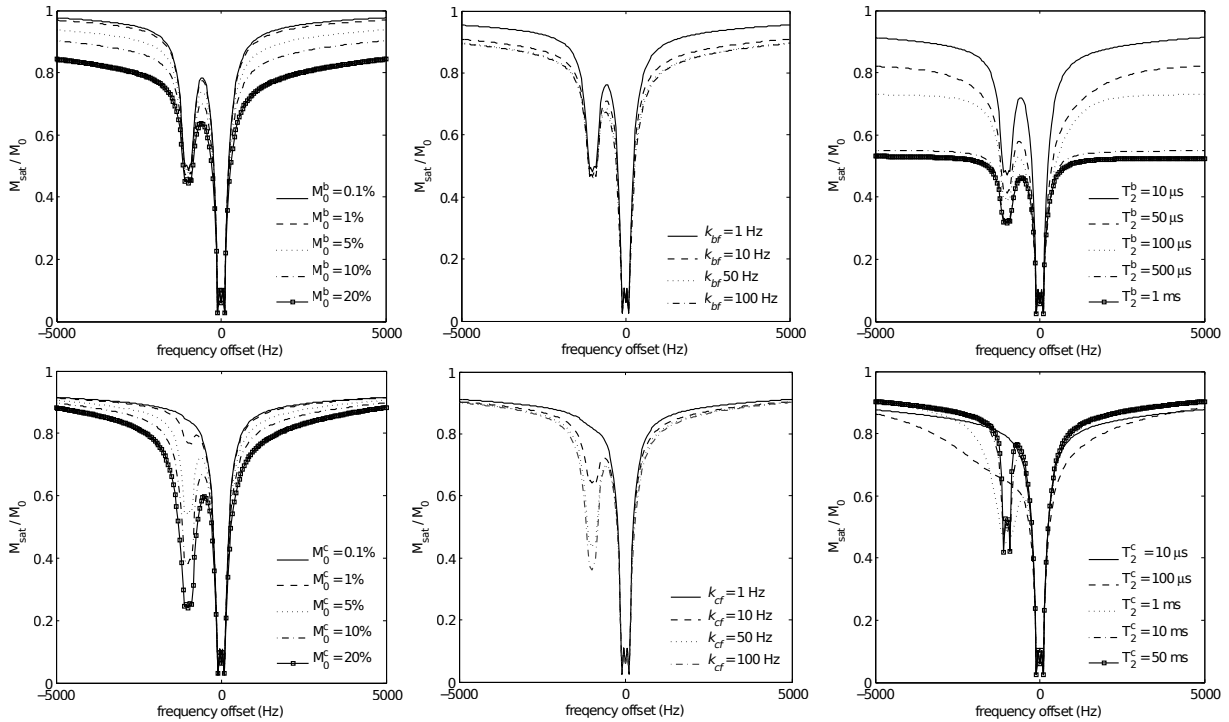
Figure 4.11: Simulation of Z-spectra for the variation of different physical parameters of the macro-molecular pool (top) and the CEST pool (below).The parameters are respectively the size of the pool (M_0^i, left), the exchange rate (k_i, middle) and the transverse relaxation times (T_2^i, right).

The model was also used to simulate the effect of varying M_0^i, transverse relaxation times (T_2^i) and exchange rate (k_i) for both the bound and exchanging pools on the z-spectrum. As shown on fig. 4.11, both the exchange rate and the proportion of protons of the exchanging pool are preponderant

in the detection of the CEST peak compared to the MT effect. This information was used in selecting the initial values for the fitting algorithm. Moreover, those preliminary results were used to create the first set of phantoms and compare the results to the simulations, as described below.

The different simulations shown above demonstrate that pulsed saturation produces similar effects that CW saturation, making it possible to observe the CEST effect without hardware modification, and with safe SAR values for *in vivo* applications. Possibility of tuning the pulse train is high, providing a large search space to probe the CEST effect.

4.3.4   Validation with phantoms

Phantoms were prepared from a gel composed of varying concentrations of agarose and creatine (Sigma-Aldrich). Three solutions of different viscosity were prepared by adding 1, 2 and 3 g of agarose (molecular weight of 306 g/mol) to a solution of 100 ml of distilled water (0.6-1.8 mM for protons). The solution was heated to the boiling point, and then cooled to 40°C. Creatine solution (molecular weight of 149 g/mol) was then added to give concentrations of 75 mM to 125 mM (0.675-1.125 mM for protons). The solution was then transferred to small plastic spheres (external diameter 19 mm) before being brought back to room temperature slowly to solidify. The spherical geometry was chosen to minimize susceptibility artefacts. Z-spectra were acquired using the EPI readout sequence described above. These phantoms were used to investigate the effect of different pulse sequence parameters and the concentrations of bound and exchanging protons on the z-spectra experimentally. In particular, adding creatine inside the agar gel shows the CEST effect directly at ~1.9 ppm, where the labile amine protons of creatine exchange with the surrounding water, and can be seen on fig. 4.12 at the frequency of 560 Hz. It is particularly pronounced with a saturation bandwidth of 110 Hz, as the simulation (fig.4.10 f) already showed.

4.3.4.1   Exchange of creatine protons

Fig. 4.12 shows experimental z-spectra obtained from the phantoms. The exchange peaks swap side of the water peak between this phantom and the *in vivo* data since the peak relates to creatine for the phantom and amides for the simulation. Fig. 4.12 a shows the effect of increasing the number of
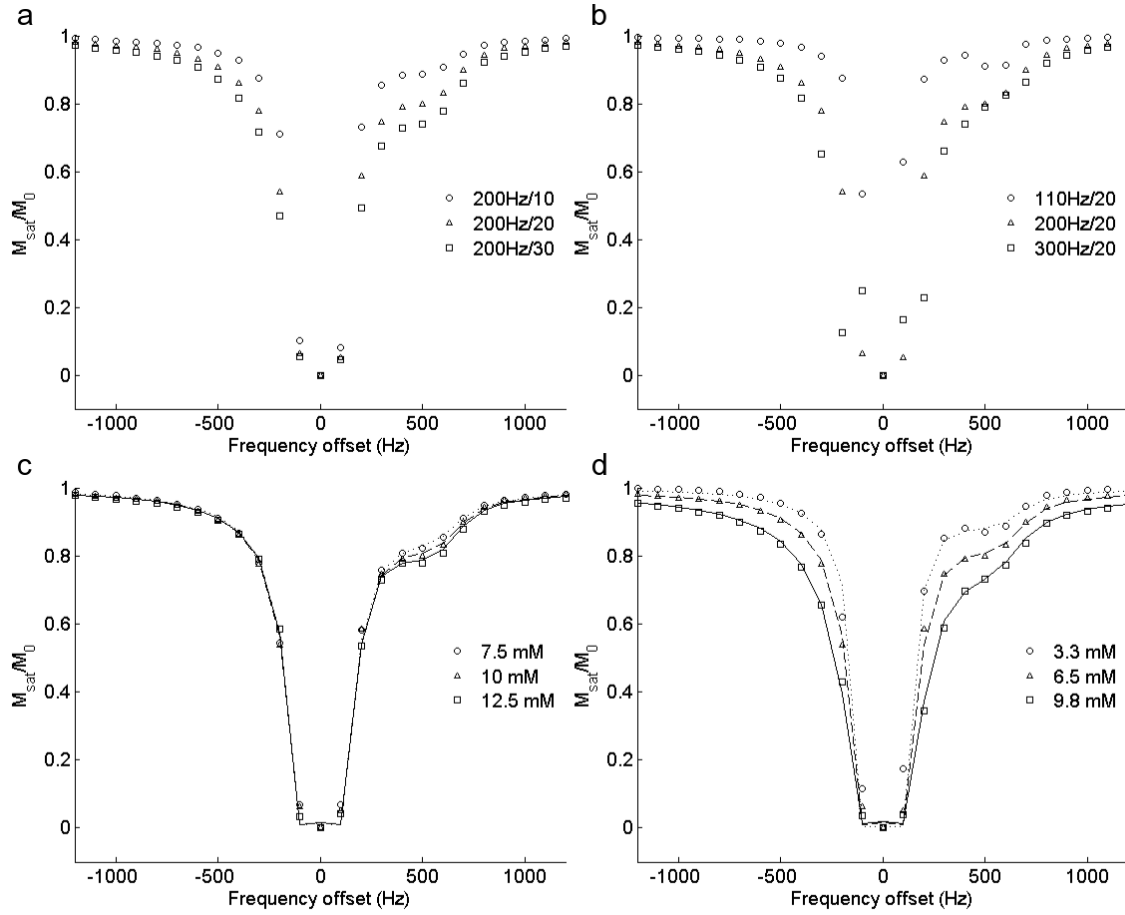
Figure 4.12: Experimental results showing the effect of changing (a) the number (bandwidth = 200 Hz) and (b) the bandwidth of the saturation pulses (number of pulses = 20 and B_{1sat} = 3.79 μT for both figures) on the z-spectra from 2 % agarose and 100 mM creatine phantom. Experimental results (dots) superimposed with fit results (lines) showing the effect of changing the concentration of (c) creatine and (d) agar on the MT spectrum with 30 saturation pulses at low bandwidth 200 Hz.

off-resonance pulses and can be compared to fig. 4.10 c (bandwidth of 200 Hz and B_{1sat} of 3.79 μT for both figures). Fig. 4.12 b shows the effect of changing pulse bandwidth, comparable to results in fig. 4.10 f (number of pulses = 20 and B_{1sat} of 3.79 μT for both figures). Fig. 4.12 c shows that with increasing concentration of creatine an increase in the amplitude of a peak in the z-spectrum at $\sim$1.9 ppm was observed. Fig. 4.12 d shows that increasing the concentration of the agar macromolecule gives an increasingly strong MT effect across a broad bandwidth. In fact, the more macromolecular protons per unit volume in a tissue, the higher the magnetization transfer (as demonstrated in [25] with polymer gels).

114

4.3.4.2 B_1 and B_0 artifacts

(a) Normalized saturated images obtained after offset saturation from -400 Hz (top left) to +400 Hz (bottom right), with the top right figure indicating the ROIs used in c.

(b) B_0 map (in Hz) acquired at the same location.

(c) Corresponding z-spectra from various ROIs indicated in a.

Figure 4.13: Images presenting the artefacts observed at low offset frequency (from -400 Hz to 400 Hz). Corresponding B_0 map (in Hz) and Z-spectra for selected small ROI.

4.3. Modelling the pulsed MT experiment

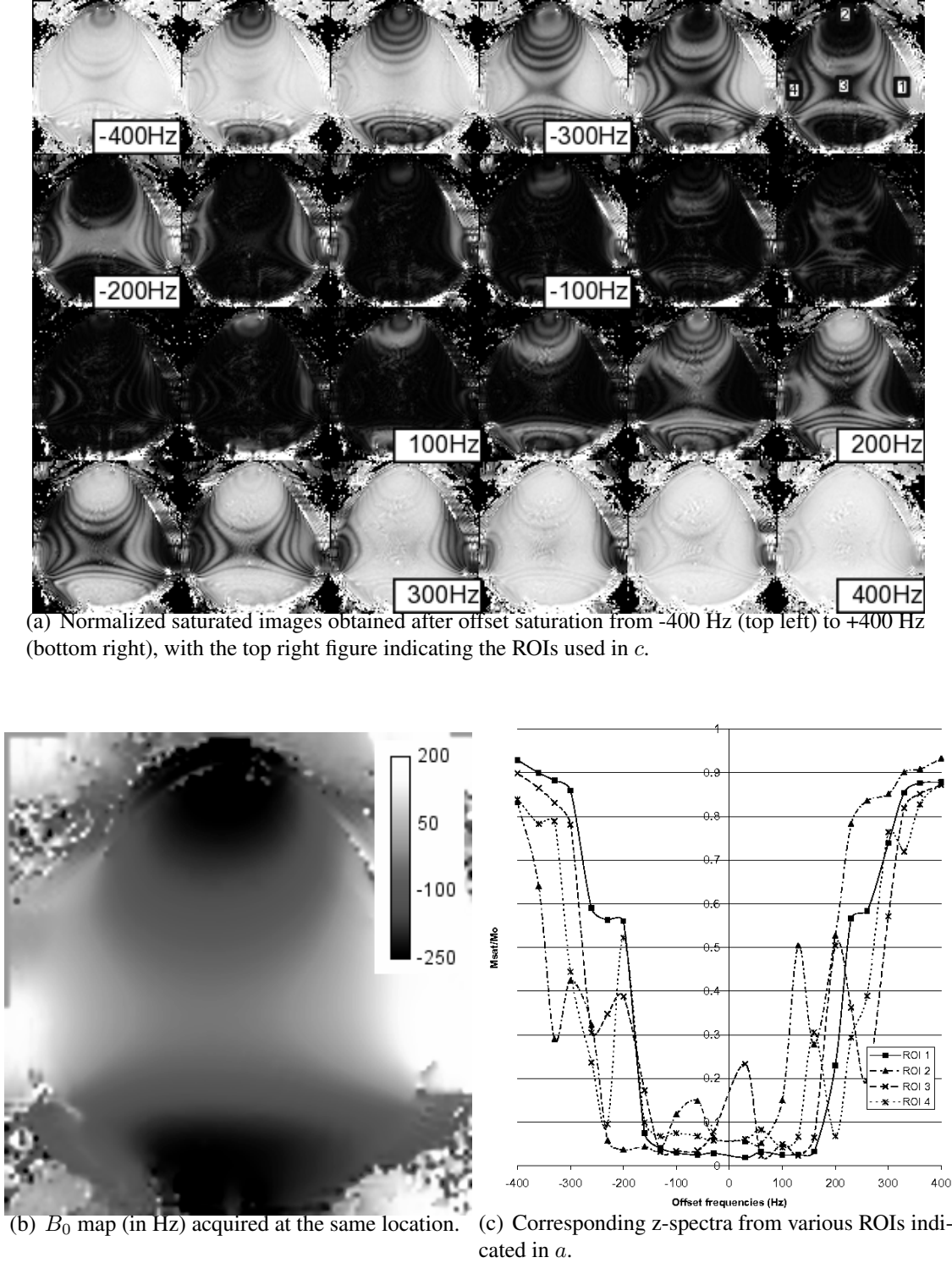In order to see how the z-spectrum is influenced by B_0 and B_1 inhomogeneities, examples at low frequency offset acquired on a simple agar gel phantom, of the size of a human brain, are presented here. On fig. 4.13, images acquired with a saturation train of 20 pulses of bandwidth of 400 Hz are presented (fig. 4.13 a). The corresponding Z-spectra for small specific regions of interest are presented (fig. 4.13 c). For completion, the actual B_0 map is presented in Hertz (fig. 4.13 b). The specific pattern observed in a can be retrieved easily in the B_0 map, indicating that these artefacts at low offset frequencies are created by the inhomogeneities of the main magnetic field. This can be diminished by a more powerful shimming procedure, but will still be present *in vivo* in certain regions (especially near the sinuses). Effect of B_1 inhomogeneities can be seen at higher offset frequencies, where the phantom saturation does not appear homogeneous, the smaller saturation contrast corresponding with lower value in the B_1 map (not shown).

4.3.5 Preliminary experiments *in vivo*

Several parameters influence the saturation and the exchange of magnetization recorded via the z-spectrum, and their extent should be probed before acquiring the data set necessary for quantification. The number of saturation pulses, as well as offset resonance, are among those.

The influence of the number of pulses, their bandwidth and the offset frequency at 1.5 T shown on fig. 4.14 can be related to the simulated results presented on fig. 4.11. As the number of pulses increases, more power is deposed into the volume of interest, the spins becoming more and more saturated, especially those in the white matter. Comparing the results acquired at 1.5 T (fig. 4.14) and 7 T (fig. 4.15), the difference due to field inhomogeneities is clear at higher magnetic field. In fact the contrast in the white matter is independent of position at 1.5 T, while inhomogeneities are evident on the images acquired at 7 T. Moreover, the saturation is less efficient at 7 T compared to 1.5 T if one compares the rows representing the variation of pulses number (third row on fig. 4.14 and second row on fig. 4.15). Artefacts due to B_0 inhomogeneities can be seen in the fig. 4.16 at low offset frequency (highlighted with arrows), as previously shown in the phantom (fig. 4.13). Looking closer to low offset frequency in a region known for its difficulty to be well shimmed (Red Nuclei (RN) and Substantia Nigra (SN)), ringing artefacts due mainly to inhomogeneous static field is visible on fig. 4.16, and shows similarities to the artefacts seen on fig. 4.13. The correction of B_0 inhomogeneities
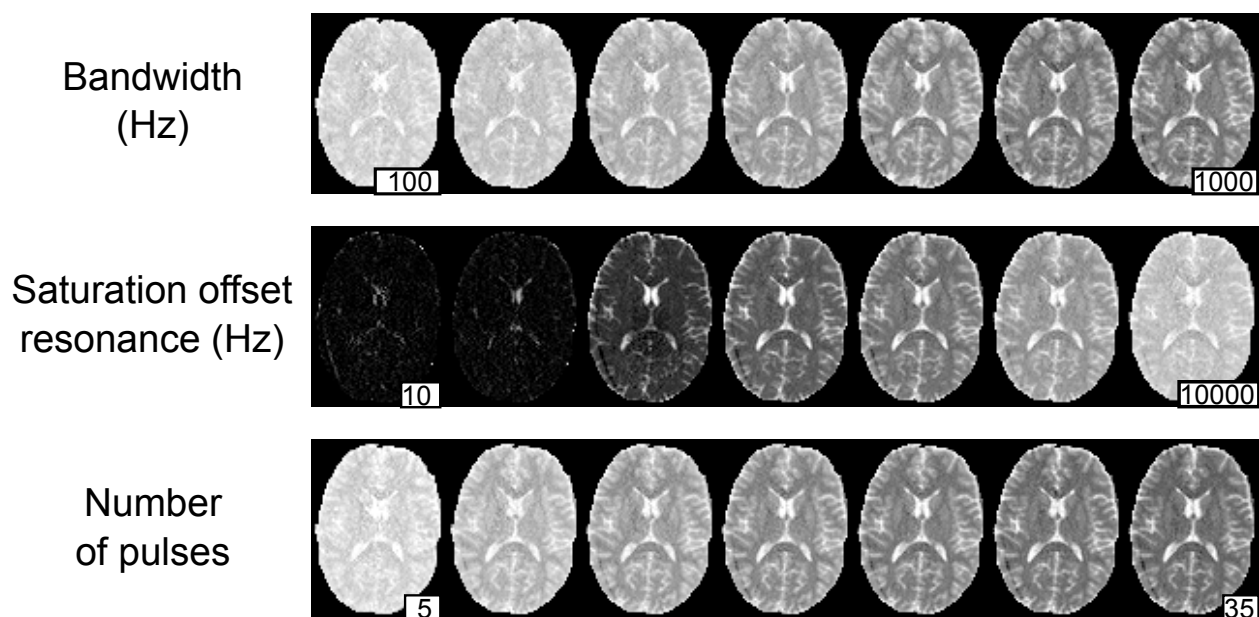
Figure 4.14: Normalized saturated images acquired at 1.5T on a healthy volunteer. First row represents a variation of the bandwidth of the pulses (from 100 Hz to 1 kHz). Second row represents variation of the offset resonance of the saturation (from 10 Hz to 10 kHz). The last row shows variation of the number of pulses, from 5 pulse to 35 pulses. The defaults parameters were 20 pulses, a bandwidth of 200 Hz, an offset frequency of 1 kHz and a period T of 50 ms, apart from the first row where the period between pulses was changed in order to match the bandwidth.
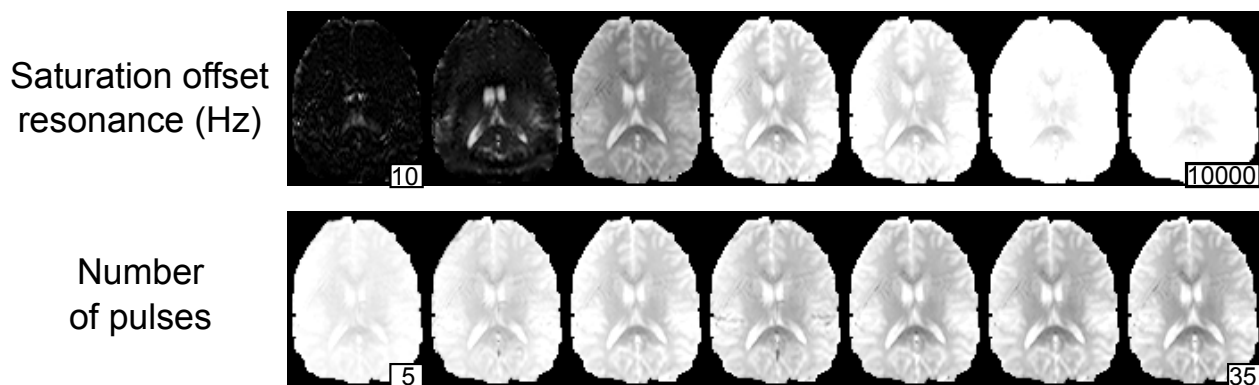
Figure 4.15: Normalised saturated images acquired at 7 T on a healthy volunteer. First row represents variation of the offset resonance of the saturation (from 10 Hz to 10 kHz). The second row shows variation of the number of pulses, from 5 pulse to 35 pulses. The default parameters were 20 pulses, a bandwidth of 200 Hz and an offset frequency of 1 kHz.

is thus compulsory at high field if one wants to observe a Chemical Exchange effect between water

and a compound having a relatively long T_2, such as amides, compared to the macromolecular pool.
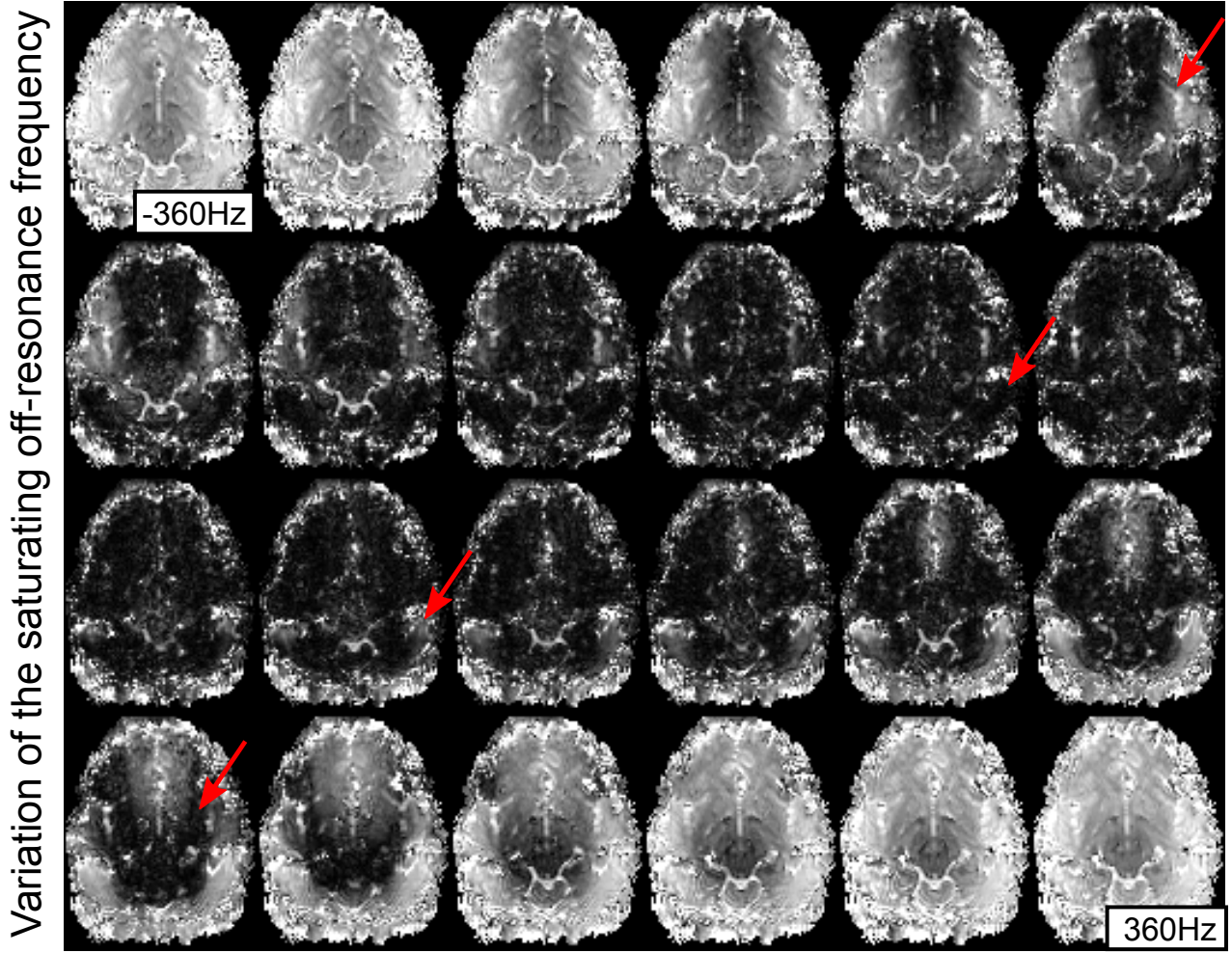
Figure 4.16: Normalised saturation images acquired at the level of the Red Nuclei (RN) for low offset resonance (from -360 Hz (top left) to +360 Hz (bottom right), with a bandwidth of 200 Hz). The arrows indicates regions where the contrast observed at a positive offset frequency is inverted at the opposite frequency.

Default parameters at 7 T (20 pulses, bandwidth of 200 Hz and offset frequency of 1 kHz) showed the best contrast available, and the range of contrast variation was acceptable from 10 pulses to 25 pulses, with offset resonance between 300 Hz to 10 kHz, for a bandwidth between 100 Hz and 400 Hz. A larger bandwidth could create more contrast, but as shown via the simulations, would result in a decrease of the CEST effects. From this series of experiments, the following parameters were chosen. Five different spectra were acquired with the bandwidth/amplitude/number of saturation pulses given by 110 Hz/2.1 μT/20 pulses, 200 Hz/3.8 μT/20 pulses, 300 Hz/7.6 μT/20 pulses, 200 Hz/3.8 μT/10 pulses and 200 Hz/3.8 μT /15 pulses.

4.4 Quantification of magnetization exchange

Preliminary results showed that Z-spectra could reveal additional information compared to a normal magnetization transfer imaging experiment, both for phantom and *in vivo* study. Quantification of the different MT effects can be done via simulation and fitting of the 3 pool model described earlier.

4.4.1 Phantom data analysis

Acquisition of Z-spectra on phantoms with different concentration of Agar and Creatine were used to validate the quantification process, as the concentration of the different species was known from preparation. Furthermore the shimming procedure of the scanner is not optimized for small objects, thus the field correction could also be optimized via these experiments.

4.4.1.1 Field inhomogeneity correction

The creatine peak, similar to the amide peak *in vivo*, has a width on the order of the B_0 variations, and can thus be overwhelmed by inhomogeneities. B_0 maps were thus automatically acquired for each session at the same location, and correction was made via the following procedure. A two stage interpolation was used on the spectrum, from which the exact frequency of the saturation could be deduced. After shifting on a pixel by pixel basis the frequency of each z-spectrum according to the acquired B_0 map, the first interpolation gave an average of the exact frequency of the water (*i.e.* where the z-spectra was the lowest in average). All the z-spectra were then shifted by the same amount to centre them on the average water frequency. To obtain the z-spectra values at the same offset frequency, a second interpolation was performed. Correction for B_1 inhomogeneities was done by reducing the amount of saturation according to the B_1 map. Previous studies have also used a B_0 and B_1 map to make a similar correction but based on correcting the model rather than the data [52]. The described approach corrects just the data, and can be applied only with a reasonable number of data in the z-spectrum.

4.4. Quantification of magnetization exchange

4.4.1.2 Fitting procedure

The model described above was fitted to phantom z-spectrum 7 T data for M_0^b, M_0^c, k_{bf} and k_{cf}, using a Levenberg-Marquardt algorithm. T_1^c = 1 s and T_1^b = 1 s were assumed since it has previously been shown that the z-spectrum shows low sensitivity to these parameters [55] and hence T_1^f was determined from equation 4.5. T_2^c and T_2^b to be used in the model were found from the literature [6, 61] and then initial values used in simulations and fits are given in table 4.1. The B_{1sat} amplitude in the fit was determined using the B_{1sat} amplitude set by the scanner, scaled according to the B_1 map. The lines superimposed on fig. 4.12c and d show the result of fitting the model to the data (average R^2 of 0.995). Fig. 4.17 shows the model parameters resulting from fitting the z-spectra of the phantoms to the 3 pool-model at 7 T. It can be seen that there was a linear correlation between M_0^b and agar concentration (R^2 of 0.938). There was also good correlation between M_0^c and creatine concentration for a given agar concentration (R^2 of 0.9959) but the fitted value of M_0^c also depended on agar concentration. Additionally, a crude Monte Carlo simulation was used to assess the robustness of the fitting procedure. Noise sampled from a Gaussian distribution of width determined by the experimental SNR (0.5 % of the reference signal) was added to simulated data, before fitting it. This was only repeated 150 times since the computation time required for one fit was approximately 2½hours. Results showed that 0.5% noise in the data resulted in less than 10% standard deviation in the fitted parameters, except for M_0^c where the standard deviation reached 12%.

4.4.2 *In vivo* cross-field study

Approval of the ethics committee was obtained to scan healthy subjects at different field strengths (namely 1.5 T, 3 T and 7 T) in order to explore the effects of MT at high field. Four healthy subjects (aged 27 ± 3 years, 1 female, 3 males) were scanned at the different field strengths after giving their consent. Since the EPI acquisition used to acquire the Z-spectra was single slice, subjects were particularly asked to keep still and were immobilized by padding. Relaxation time measurement data (T_1^{obs}, T_2^{obs}) were acquired using the same EPI readout, but prepared with either a hyperbolic secant inversion pulse at variable inversion times for the T_1 map, or with spin echo at variable echo times for the T_2 map. Similarly the echo time of the basic EPI sequence was varied to produce phase images
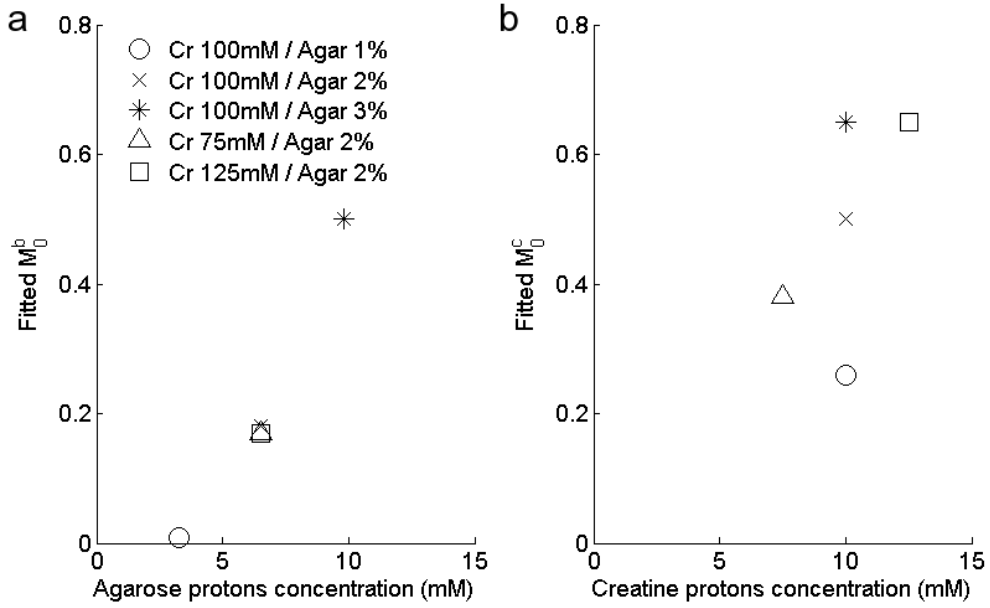
Figure 4.17: Fitted value of (a) M_0^b plotted against molar concentration of protons bound to agar, and (b) M_0^c against molar concentration of protons in creatine, for experimental phantom data.

which were unwrapped and fitted to produce a B_0 map and the flip angle of the EPI readout pulse was varied to produce a B_1 map. Z-spectra were calculated by averaging the signal in regions of interest of approximately 25 pixels, drawn in two regions of frontal lobe white matter, the corpus callosum, and grey matter (indicated on fig. 4.18A). MT-TFE images were also acquired on these subjects at 7 T.

4.4.2.1 Data analysis

For the MT-EPI data, after registration, MT ratio (MTR) maps were calculated by dividing the difference between the NO SAT signal and the off-resonance PULSED SAT signal by the NO SAT signal. The data were then used to produce z-spectra on a voxel by voxel basis, which had to be corrected for the effects of B_0 inhomogeneities and eddy currents, with the method explained in 4.4.1.1. The model described above was then fitted to the *in vivo* z-spectra acquired at 7T, for M_0^b, M_0^c, k_{bf} and k_{cf}, using a Levenberg-Marquardt algorithm. Spectra were fitted for individual subjects and also averaged over all subjects. $T_1^c = 1$ s and $T_1^b = 1$ s were assumed since it has previously been shown that the z-spectrum shows low sensitivity to these parameters [55]; T_1^f was determined from equation 4.5. T_2^c and T_2^b to be used in the model were found from the literature [6, 61] and then initial
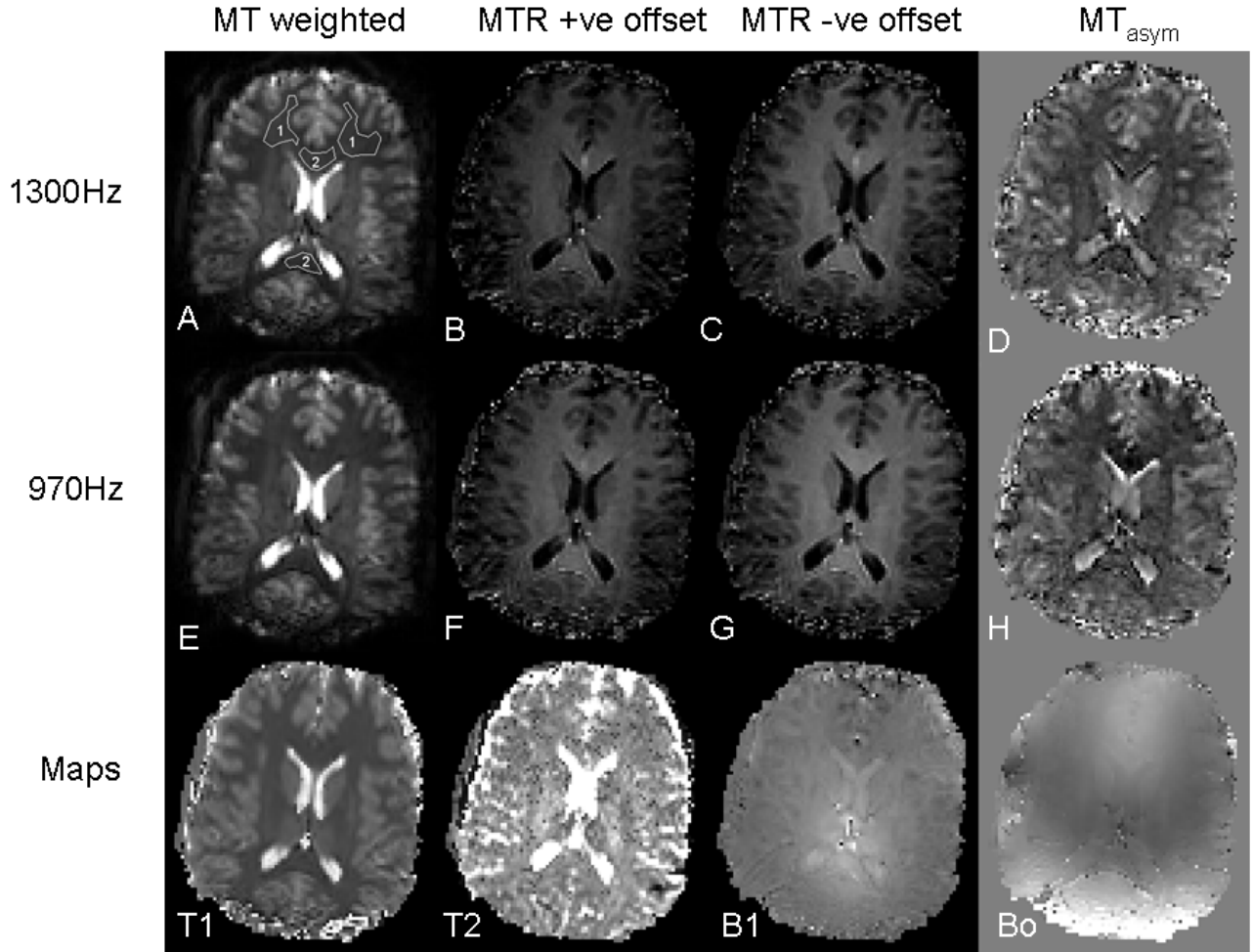
Figure 4.18: Raw MT images acquired using MT-EPI with saturation offsets of 1300 Hz (A) and 970 Hz (E), together with MTR maps calculated for a positive offset (B: 1300 and F 970 Hz) and negative offset (C: -1300 and G -970 Hz) for a saturation with 20 pulses of bandwidth 300 Hz. D and H are the corresponding MT_{asym} maps. T_1, T_2, B_1 and B_0 maps are added for the same subject scanned at 7 T (reproduced from [39]).

values used in simulations and fits are given in table 4.1. The B_{1sat} amplitude in the fit was scaled according to the B_1 map.

4.4.2.2 Z-spectra quantification

Z-spectra for the different ROIs were processed and fitted on a subject by subject basis, but the average z-spectra of all four subjects was also fitted. The averaged z-spectrum is shown in fig. 4.19, with the results of the 2 and 3 compartment fits presented in fig. 4.20. Fig. 4.19 a and b show the
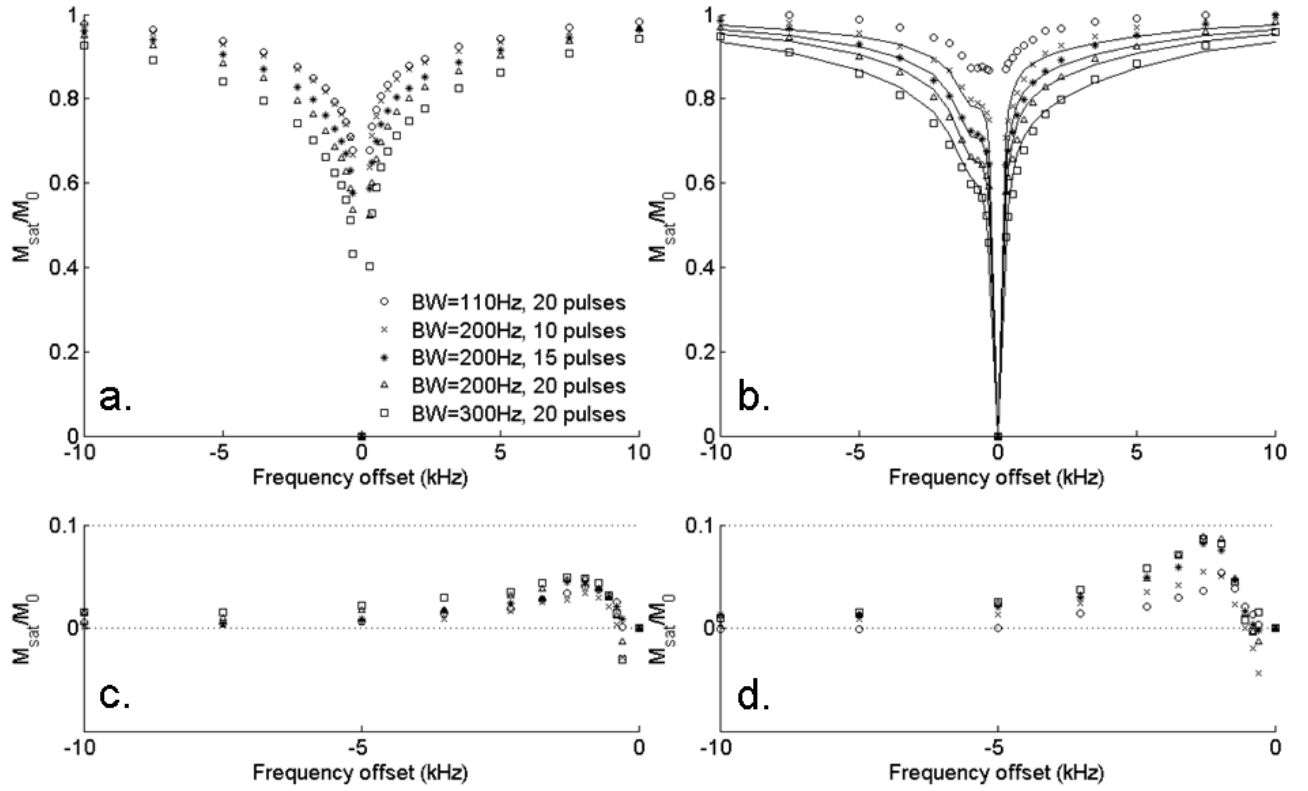
Figure 4.19: Z-spectra (a and b) and corresponding asymmetry spectra (c and d) acquired at 7 T (a, c) and 3 T (b, d) for various pulsed saturation sequences as shown in the legend. The data were taken from two ROI in the frontal white matter and averaged over 4 healthy subjects. The results of fitting the 3 compartment model to the 7 T data are also shown (b).

corresponding z-spectra, at 3 and 7 T, averaged over all subjects. Whereas the asymmetry can be seen at both field strengths, a distinct peak at 3.5 ppm (450 Hz at 3T vs 1050 Hz at 7 T) is only visible at 7 T. Fig. 4.19 c and d show the resulting asymmetry spectra and demonstrate the increase in z-spectrum asymmetry with field strength. The spectral asymmetry around 3.5 ppm is increased by 50 % (p-value of 0.00013 with a Student t-test) at 7 T compared to 3 T, and the APT peak is more distinct. The solid lines for the 7 T data on fig. 4.19 b shows the result of fitting the 3-compartment model to the averaged data. The data acquired for pulses with a bandwidth of 110 Hz were not included in the fit due to their significant deviation from the fitted line. This was probably because the low bandwidth pulses were very long and close in length to the period of the pulses (T), giving a very high duty cycle which may have led to drift in the amplifier output.

Fig. 4.20 shows the model parameters resulting from fitting the z-spectra to the 3-pool model at 7 T, both in an individual manner (subject by subject fit) and in an averaged manner. There is
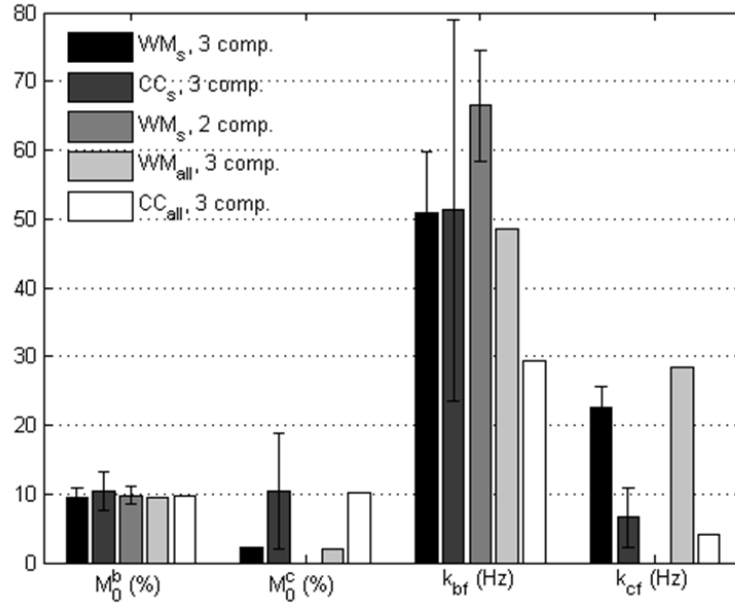
Figure 4.20: Fitted values of M_0^b, M_0^b, k_{fb} and k_{fc} for different white matter regions (White Matter and Corpus Callosum), for a 3 compartment model as well as a two compartment model, on a subject by subject basis (s) and for z-spectra averaged over all subjects (all).

reasonable agreement between the results obtained by fitting to the spectra created by averaging the spectra from all subjects, and by fitting the spectra from each subject individually and then averaging the fitted parameters. Fig. 4.20 also shows the results of fitting the 2-pool and 3-pool model on an individual subject basis for WM data. The R^2 obtained with the 3 pool model was 0.96 ± 0.01, compared to a R^2 of 0.86 ± 0.02 for the two pool model. The F ratio between the two fits was 114, suggesting that the extra parameters modelled true variation in the data. The results also show a significant increase in the value of M_0^c in the corpus callosum compared to the rest of the white matter, together with a decrease in the exchange rate k_{cf}. It can be noted on fig. 4.20 that the error bar are particularly important for the corpus callosum quantification, this region being extremely close to the ventricles, possibly corrupting the z-spectra.

4.5 Discussion

A discussion concerning this chapter can be found in [39], but an overview is given here.

4.5. Discussion

Improvement via simulation   Initial simulations were used to investigate the effect of pulse sequence parameters on the z-spectra, in particular comparing the effects of pulsed and CW saturation. Similar spectral definition was obtained in both cases (fig. 4.10) confirming previous results [20]. This model could be used to extend the work of [54] who considered CW irradiation and a two compartment model of free and exchanging protons, to choose pulse irradiation parameters to optimize separately CEST contrast in MT_{asym} weighted images, and signal to noise ratio in measured CEST parameters from z-spectra. It will be discussed in the next chapter.

Inhomogeneity correction   Field inhomogeneities can cause artifacts in MT asymmetry studies, as shown by fig. 4.13. Here the use of a two stage interpolation over the spectrum based on a B_0 field map was used to address this problem. Previous studies have also used a B_0 and B_1 map to make a similar correction but based on correcting the model rather than the data [52]. Better characterization of the z-spectrum will allow experiments to be designed to reduce sensitivity to field inhomogeneities whilst maintaining sensitivity to CEST effects, for instance by increasing the bandwidth of the off resonance saturation pulses (fig.4.10 f). Improvement in the transmit homogeneity of the RF field, as well as in the shimming procedure, would also help reducing inhomogeneities seen around the cortex compared to the corpus callosum.

Phantom results   The creatine/agar solution is a good experimental model for an *in vivo* CEST experiment [52]. The molar fraction of the creatine protons and macromolecule protons in the phantoms were of the same order. However the MT effect of the macromolecule protons is considerably greater and of broader spectral width than the creatine protons (fig. 4.12). This could either be because the hydration layer around the macromolecule effectively amplifies its effect on the z-spectrum or because of more frequent exchange between the water and the protons associated with macromolecules than between the water and the chemically exchanging protons. Fig. 4.17 a shows an excellent correlation between the fitted values of M_0^b and the molar fraction of agarose protons in the phantoms. However the line does not pass through the intercept suggesting that there is a threshold of agar concentration below which no MT effect is detectable. A similar dependence of magnetization transfer phenomena on crosslinking has been shown previously in other gel systems [25]. Furthermore it is possible that the pH of the gels change with increasing agar concentration, changing the rate of exchange [12]. Fig.

125

4.5. Discussion

4.17 b also shows excellent correlation between the fitted values of M_0^c and the molar fraction of amide protons in the phantoms, but the fitted value of M_0^c depends on the amplitude of the bound water peak. This could be due to an error in the choice of the line shape of the macromolecule or exchanging pool, or it could be because the creatine protons will also exchange with the macromolecules, so that the macromolecules buffer their effect on the water protons. A more complete set of phantoms with a controlled pH could be used to further investigate these phenomena.

The model used here assumed that the creatine protons had a single T_2, whereas the bound pool line was described by a Super Lorentzian. It is likely that the creatine protons cannot be represented by a single T_2. However, the peak in the spectrum of the amine group is sharp enough to assume Lorentzian dispersion. According to the literature [51], the T_2 of the macromolecular protons is independent to field strength and around 10 μs, with the T_2^c of the amine protons lying between T_2^{obs} and T_2^b. The T_2^c that gave the optimum fit to the data here was shorter than the literature ([52] reported a T_2^c of 8 ms for creatine protons, and mentioned that inhomogeneity broaden the CEST peak, creating an artificially larger peak), and with a slower exchange rate (742 Hz in [52]) (a longer T_2^c with a higher exchange rate k_{cf} gave a CEST peak that was too pronounced). The difference may be because the results from the literature were acquired at higher field with phantom and better shimming.

***In vivo* z-spectra**   The MT-EPI sequence produced z-spectra that showed a clear asymmetry *in vivo* at both 7 and 3 T. The difference in contrast at low offset frequency between positive and negative side of the spectrum has been previously observed at 3 T and has been explained by chemical exchange with protons in small proteins, particularly amides at 3.5 ppm (APT). An asymmetry in the underlying macromolecule spectrum has been observed in the brain at 3 T [21], so that the z-spectrum is elevated at large positive frequency offsets (-40 ppm), as opposed to the APT effect at small negative frequency offsets (3.5 ppm). No such effect was observed in the z-spectra presented here at either 3 T or 7 T. It is not clear whether this is because in this work any underlying asymmetry in the bound pool spectrum is overwhelmed by the CEST peak although this seems unlikely since similar results were seen in 7 and 3 T z-spectra. It seems unlikely that this effect was due to systematic variation in output power with frequency offset since there is no evidence of underlying asymmetry in either direction in phantom or CSF spectra. Furthermore this work used a similar platform (Philips) to the work presented previously which showed asymmetry in the underlying bound pool spectrum at 3 T.

126

4.5. Discussion

A review of other works suggest that this asymmetry in the bound pool spectrum has been observed in some other studies [69], although not all [68]. This suggests the effect may depend on the exact experiment, the sensitivity being also function of the exchanging species probed. Previous results seem to be independent of whether pulsed or CW irradiation were used, but the integrated power used here was lower than in [21] and the larger interval between the pulses used here (T=55 ms) may have interacted with exchange rates to change line broadening (fig. 4.10). A method for separating out the effect of macromolecular protons from exchanging protons has been suggested, based on their different T_2s, and phase cycling of the saturation pulses [40] that may help to elucidate the origin of this discrepancy. The increased sensitivity to APT at 7 T made it possible to fit a 3 compartment model to the data, and opens up the possibility of quantitative CEST imaging *in vivo*. The 7 T data could be fitted to the 3 compartment model, both on an individual basis or averaged over all subjects to improve SNR (fig. 4.19, and 4.20) (more discussion about the lineshape choice in [39]). Similarly to the results obtained with the creatine phantoms, the amide protons may have a longer T_2^c, somehow underestimate due to the large inhomogeneities widening the peaks [52].

Fig. 4.19, and 4.20 clearly shows a difference in the amplitude of the amide CEST (Amide Proton Transfer, APT) peak between the corpus callosum and the rest of the white matter. The APT signal has previously been associated to proteins and peptides. The corpus callosum is known to be highly myelinated, and cell membrane and in particularly myelin sheaths contain amides for instance within sphingomyelin. Yarnykh and Yuan [65] previously noted that the bound pool fraction varied between white matter regions, although they were assuming a two compartment model and associated the change in exchange rate with water bound to myelin, and they only studied one side of the z-spectrum (probably for positive off resonance pulses). Sun et al [52] also mentioned a change in APT contrast in the corpus callosum of rats compared to the rest of the white matter, but then excluded it from further analysis. If the hypothesis linking APT contrast to myelination can be proved in post mortem data (using quantitative myelin staining) then this would open up the possibility of using APT to quantify myelination. However amide protons are not present only in the myelin, and this method will probably lack specificity. The difference in APT contrast between CC and surrounding white matter can also be explained by change in pH or/and temperature (the corpus callosum being a slow perfused area). Amide Proton Transfer imaging (APT) has been shown to have many potential applications in clinical imaging. Recently it has been shown that the APT contrast provides good

127

contrast between tumour and oedema [24], and that the APT effect depends on the grade of a tumor [68]. Furthermore the APT rate is pH dependent [58] and so has been used to detect changes in pH in ischemia [52]. There are many other solutes at low frequency offsets such as glycogen at about + 1.2 ppm and glucose at about + 2.2 ppm, but there was no sign of these metabolites in this data. The indications from this study and those in the literature are that APT contrast is sensitive to myelination, so that ultra-high field, high resolution imaging of APT and MT is likely to provide a new marker of demyelination [43].

Relevance to phase shift between grey and white matter Phase imaging and susceptibility weighted imaging (SWI) suggest that there is a phase shift of about 3 Hz between grey and white matter at 7 T (with the white matter resonating at lower frequency). The origin of this field shift remains a matter of debate, although it is frequently attributed to susceptibility differences due to possible differences in iron concentration between grey and white matter. An alternative explanation is that the shift in the water peak in white matter is due to exchange with protons at lower frequencies [66]. The work described here suggests that in white mater there is a large (8 %) proton pool at about 3.5 ppm lower frequency in relatively slow exchange with the water peak. Assuming that the exchange rate is 200 Hz (higher than measured here) and that there is no similar exchange process in grey matter, then the shift in the bulk water resonance in white matter compared to grey matter would be of the order of 2 Hz [30], which is lower than observed. However more importantly as the field increases the exchange regime effectively becomes slower, so this shift would decrease with increasing field strength (in contrast to the single peak observed in fast exchange whose width would increase with increasing field strength). The available literature suggests that the frequency shift between grey and white matter increases linearly with field strength [66, 63] which is expected for a magnetic susceptibility difference if the magnetization is not saturated. This suggests that the phase shift between white matter and grey matter is not due to slow chemical exchange with amide protons. However phase images show considerable contrast between white matter tracts, and the field dependence of white matter contrast in phase imaging should be explored further to rule out exchange contributions.

4.6 Conclusion

Magnetization transfer is an important source of contrast in Magnetic Resonance Imaging which is sensitive to the concentration of macromolecules and other solutes present in the tissue. Magnetization transfer effects can be visualized in Magnetization Transfer Ratio images, or quantified via the z-spectrum. This chapter presented methods of measuring the z-spectrum and maps of z-spectrum asymmetry in vivo at 7T, within SAR limits. It also presented a 3 compartment model that has been used to measure chemical exchange and magnetization transfer parameters from the z-spectrum data. The peak in the z-spectrum associated with chemical exchange between amide and water protons (Amide proton transfer, APT, effects) is much more apparent at 7T than 3T. Furthermore at 7T quantitative APT results varied between the corpus callosum and other white matter structures, suggesting that quantitative APT imaging is specific to change in myelination, pH or even temperature. Pulse by pulse numerical simulation of the sequence was used in fitting parameters of interest, but also proved useful in improving the efficiency of quantification. While the proposed experiment could resolve the exchange rate and the amount of protons in each pool, a better design of the experiment is possible, with for example variation of another parameter, the time between the saturation pulses present in the train. Phantoms provided a good tool for validation, but additional experiments would improve the robustness of the quantification process, especially concerning the exchange rate measurement. The reasonable imaging time permits this protocol to be run in patients, which could produce new insight into detection and pathological quantification of demyelinating diseases in particular. The results also suggest that chemical exchange is not responsible for the phase shift observed in susceptibility weighted images between grey matter and white matter. The next chapter focused on producing high resolution MTR images at 7T based on the results (both from quantification and simulation) present in this chapter, and presents first clinical applications of MTR at 7T.

Bibliography

[1] S. Aime, M. Botta, V. Mainero, and E. Terreno. Separation of intra- and extracellular lactate nmr signals using a lanthanide shift reagent. *Magn Reson Med*, 47(1):10–13, Jan 2002.

[2] R. S. Balaban and T. L. Ceckler. Magnetization transfer contrast in magnetic resonance imaging.

Magn Reson Q, 8(2):116–137, Jun 1992.

[3] A. J. Barkovich. Magnetic resonance techniques in the assessment of myelin and myelination. *J Inherit Metab Dis*, 28(3):311–343, 2005.

[4] A. Bax and D. Davis. Practical aspects of two-dimensional transverse noe spectroscopy. *J. Magn. Reson*, 63(1):207–213, 1985.

[5] R. G. Bryant. The dynamics of water-protein interactions. *Annu Rev Biophys Biomol Struct*, 25:29–53, 1996.

[6] T. Ceckler, J. Maneval, and B. Melkowits. Modeling magnetization transfer using a three-pool model and physically meaningful constraints on the fitting parameters. *J Magn Reson*, 151(1):9–27, Jul 2001.

[7] T. L. Ceckler, S. D. Wolff, V. Yip, S. A. Simon, and R. S. Balaban. Dynamic and chemical factors affecting water proton relaxation by macromolecules. *Journal of Magnetic Resonance (1969)*, 98(3):637 – 645, 1992.

[8] M. Cercignani, M. R. Symms, M. Ron, and G. J. Barker. 3d mtr measurement: from 1.5 t to 3.0 t. *Neuroimage*, 31(1):181–186, May 2006.

[9] U. Duvvuri, D. A. Roberts, J. S. Leigh, and L. Bolinger. Magnetization transfer imaging of the brain: A quantitative comparison of results obtained at 1.5 and 4.0 t. *J Magn Reson Imaging*, 10(4):527–532, Oct 1999.

[10] J. Eng, T. L. Ceckler, and R. S. Balaban. Quantitative 1h magnetization transfer imaging in vivo. *Magn Reson Med*, 17(2):304–314, Feb 1991.

[11] S. Forsén and R. Hoffman. Study of moderately rapid chemical exchange reactions by means of nuclear magnetic double resonance. *The Journal of Chemical Physics*, 39:2892, 1963.

[12] D. F. Gochberg, R. P. Kennan, M. J. Maryanski, and J. C. Gore. The role of specific side groups and ph in magnetization transfer in polymers. *J Magn Reson*, 131(2):191–198, Apr 1998.

[13] S. J. Graham and R. M. Henkelman. Understanding pulsed magnetization transfer. *J Magn Reson Imaging*, 7(5):903–912, 1997.

[14] V. Guivel-Scharen, T. Sinnwell, S. D. Wolff, and R. S. Balaban. Detection of proton chemical exchange between metabolites and water in biological tissues. *J Magn Reson*, 133(1):36–45, Jul 1998.

[15] M. Helgstrand, T. Härd, and P. Allard. Simulations of nmr pulse sequences during equilibrium

and non-equilibrium chemical exchange. *J Biomol NMR*, 18(1):49–63, Sep 2000.

[16] G. Helms, H. Dathe, and G. Hagberg. Pulsed saturation of the standard two-pool model for magnetization transfer. part ii: The transition to steady state. *Concepts in Magnetic Resonance*, (1), 2004.

[17] G. Helms and A. Piringer. Dynamic evaluation of magnetization transfer (mt) in human brain: the approach to steady state after pulsed saturation. In *Book of Abstracts, 6th Annual Meeting of the Intl Society for Magnetic Resonance in Medicine. Berkeley CA: ISMRM*, volume 2192, 1998.

[18] R. M. Henkelman, X. Huang, Q. S. Xiang, G. J. Stanisz, S. D. Swanson, and M. J. Bronskill. Quantitative interpretation of magnetization transfer. *Magn Reson Med*, 29(6):759–766, Jun 1993.

[19] R. M. Henkelman, G. J. Stanisz, and S. J. Graham. Magnetization transfer in mri: a review. *NMR Biomed*, 14(2):57–64, Apr 2001.

[20] J. Hua and G. C. Hurst. Analysis of on- and off-resonance magnetization transfer techniques. *J Magn Reson Imaging*, 5(1):113–120, 1995.

[21] J. Hua, C. K. Jones, J. Blakeley, S. A. Smith, P. C. M. van Zijl, and J. Zhou. Quantitative description of the asymmetry in magnetization transfer effects around the water resonance in the human brain. *Magn Reson Med*, 58(4):786–793, Oct 2007.

[22] R. Ishima and D. A. Torchia. Estimating the time scale of chemical exchange of proteins from measurements of transverse relaxation rates in solution. *J Biomol NMR*, 14(4):369–372, Aug 1999.

[23] R. Ishima and D. A. Torchia. Protein dynamics from nmr. *Nat Struct Biol*, 7(9):740–743, Sep 2000.

[24] C. K. Jones, M. J. Schlosser, P. C. M. van Zijl, M. G. Pomper, X. Golay, and J. Zhou. Amide proton transfer imaging of human brain tumors at 3t. *Magn Reson Med*, 56(3):585–592, Sep 2006.

[25] R. P. Kennan, K. A. Richardson, J. Zhong, M. J. Maryanski, and J. C. Gore. The effects of cross-link density and chemical exchange on magnetization transfer in polyacrylamide gels. *J Magn Reson B*, 110(3):267–277, Mar 1996.

[26] S. H. Koenig. Classes of hydration sites at protein-water interfaces: the source of contrast in

magnetic resonance imaging. *Biophys J*, 69(2):593–603, Aug 1995.

[27] S. H. Koenig and R. D. Brown. A molecular theory of relaxation and magnetization transfer: application to cross-linked bsa, a model for tissue. *Magn Reson Med*, 30(6):685–695, Dec 1993.

[28] W. Lamb, D. Brown, and J. Jonas. Temperature and density dependence of the proton lifetime in liquid water. *The Journal of Physical Chemistry*, 85(25):3883–3887, 1981.

[29] H. Lassmann, W. Brück, and C. F. Lucchinetti. The immunopathology of multiple sclerosis: an overview. *Brain Pathol*, 17(2):210–218, Apr 2007.

[30] M. H. Levitt. *Spin Dynamics: Basics of Nuclear Magnetic Resonance*. John Wiley & Sons, 2001.

[31] E. Liepinsh and G. Otting. Proton exchange rates from amino acid side chains–implications for image contrast. *Magn Reson Med*, 35(1):30–42, Jan 1996.

[32] J. Listerud. Off-resonance pulsed magnetization transfer in clinical mr imaging: optimization by an analysis of transients. *Magn Reson Med*, 37(5):693–705, May 1997.

[33] A. MacKay, K. Whittall, J. Adler, D. Li, D. Paty, and D. Graeb. In vivo visualization of myelin water in brain by magnetic resonance. *Magn Reson Med*, 31(6):673–677, Jun 1994.

[34] H. McConnell. Reaction rates by nuclear magnetic resonance. *The Journal of Chemical Physics*, 28:430, 1958.

[35] A. McLaughlin, J. Leigh, et al. Relaxation times in systems with chemical exchange: approximate solutions for the nondilute case. *Journal of Magnetic Resonance (1969)*, 9(2):296–304, 1973.

[36] A. Mittermaier and L. E. Kay. New tools provide new insights in nmr studies of protein dynamics. *Science*, 312(5771):224–228, Apr 2006.

[37] C. Morrison and R. M. Henkelman. A model for magnetization transfer in tissues. *Magn Reson Med*, 33(4):475–482, Apr 1995.

[38] J. P. Mottershead, K. Schmierer, M. Clemence, J. S. Thornton, F. Scaravilli, G. J. Barker, P. S. Tofts, J. Newcombe, M. L. Cuzner, R. J. Ordidge, W. I. McDonald, and D. H. Miller. High field mri correlates of myelin content and axonal density in multiple sclerosis–a post-mortem study of the spinal cord. *J Neurol*, 250(11):1293–1301, Nov 2003.

[39] O. E. Mougin, R. C. Coxon, A. Pitiot, and P. A. Gowland. Magnetization transfer phenomenon in the human brain at 7 t. *Neuroimage*, 49(1):272–281, Jan 2010.

BIBLIOGRAPHY

[40] M. J. Närväinen, P. L. Hubbard, R. A. Kauppinen, and G. A. Morris. A method for t2-selective saturation to cancel out macromolecular magnetization transfer in z-spectroscopy. In *Proceeding of the International Society of Magnetic Resonance in Medicine, 15th Annual Meeting, Berlin*, 2007.

[41] G. Otting and E. Liepinsh. Protein hydration viewed by high-resolution nmr spectroscopy: implications for magnetic resonance image contrast. *Accounts of Chemical Research*, 28(4):171–177, 1995.

[42] G. Otting, E. Liepinsh, and K. Wüthrich. Protein hydration in aqueous solution. *Science*, 254(5034):974–980, Nov 1991.

[43] X. Ou, S.-W. Sun, H.-F. Liang, S.-K. Song, and D. F. Gochberg. Quantitative magnetization transfer measured pool-size ratio reflects optic nerve myelin content in ex vivo mice. *Magn Reson Med*, 61(2):364–371, Feb 2009.

[44] T. Paus and R. Toro. Could sex differences in white matter be explained by g ratio? *Front Neuroanat*, 3:14, 2009.

[45] W. A. H. Rushton. A theory of the effects of fibre size in medullated nerve. *J Physiol*, 115(1):101–122, Sep 1951.

[46] K. Schmierer, F. Scaravilli, D. R. Altmann, G. J. Barker, and D. H. Miller. Magnetization transfer ratio and myelin in postmortem multiple sclerosis brain. *Ann Neurol*, 56(3):407–415, Sep 2004.

[47] K. Schmierer, C. A. M. Wheeler-Kingshott, D. J. Tozer, P. A. Boulby, H. G. Parkes, T. A. Yousry, F. Scaravilli, G. J. Barker, P. S. Tofts, and D. H. Miller. Quantitative magnetic resonance of postmortem multiple sclerosis brain before and after fixation. *Magn Reson Med*, 59(2):268–277, Feb 2008.

[48] G. Siegel, R. Albers, S. Brady, and D. Price. *Basic neurochemistry: molecular, cellular, and medical aspects*. Academic Press, 2006.

[49] J. G. Sled and G. B. Pike. Quantitative imaging of magnetization transfer exchange and relaxation properties in vivo using mri. *Magn Reson Med*, 46(5):923–931, Nov 2001.

[50] G. J. Stanisz, A. Kecojevic, M. J. Bronskill, and R. M. Henkelman. Characterizing white matter with magnetization transfer and t(2). *Magn Reson Med*, 42(6):1128–1136, Dec 1999.

[51] G. J. Stanisz, E. E. Odrobina, J. Pun, M. Escaravage, S. J. Graham, M. J. Bronskill, and R. M.

Henkelman. T1, t2 relaxation and magnetization transfer in tissue at 3t. *Magn Reson Med*, 54(3):507–512, Sep 2005.

[52] P. Z. Sun, C. T. Farrar, and A. G. Sorensen. Correction for artifacts induced by b(0) and b(1) field inhomogeneities in ph-sensitive chemical exchange saturation transfer (cest) imaging. *Magn Reson Med*, 58(6):1207–1215, Dec 2007.

[53] P. Z. Sun, Y. Murata, J. Lu, X. Wang, E. H. Lo, and A. G. Sorensen. Relaxation-compensated fast multislice amide proton transfer (apt) imaging of acute ischemic stroke. *Magn Reson Med*, 59(5):1175–1182, May 2008.

[54] P. Z. Sun, P. C. M. van Zijl, and J. Zhou. Optimization of the irradiation power in chemical exchange dependent saturation transfer experiments. *J Magn Reson*, 175(2):193–200, Aug 2005.

[55] D. J. Tyler and P. A. Gowland. Rapid quantitation of magnetization transfer using pulsed off-resonance irradiation and echo planar imaging. *Magn Reson Med*, 53(1):103–109, Jan 2005.

[56] M. Van Der Knaap and J. Valk. *Magnetic resonance of myelination and myelin disorders*. Springer, 2005.

[57] P. C. M. van Zijl, J. Zhou, N. Mori, J.-F. Payen, D. Wilson, and S. Mori. Mechanism of magnetization transfer during on-resonance water saturation. a new approach to detect mobile proteins, peptides, and lipids. *Magn Reson Med*, 49(3):440–449, Mar 2003.

[58] K. M. Ward, A. H. Aletras, and R. S. Balaban. A new class of contrast agents for mri based on proton chemical exchange dependent saturation transfer (cest). *Journal of Magnetic Resonance*, 143(1):79 – 87, 2000.

[59] K. P. Whittall, A. L. MacKay, D. A. Graeb, R. A. Nugent, D. K. Li, and D. W. Paty. In vivo measurement of t2 distributions and water contents in normal human brain. *Magn Reson Med*, 37(1):34–43, Jan 1997.

[60] D. Woessner. Brownian motion and its effects in nmr chemical exchange and relaxation in liquids. *Concepts in Magnetic Resonance*, 8(6):397–421, 1996.

[61] D. E. Woessner, S. Zhang, M. E. Merritt, and A. D. Sherry. Numerical solution of the bloch equations provides insights into the optimum design of paracest agents for mri. *Magn Reson Med*, 53(4):790–799, Apr 2005.

[62] S. D. Wolff and R. S. Balaban. Magnetization transfer contrast (mtc) and tissue water proton relaxation in vivo. *Magn Reson Med*, 10(1):135–144, Apr 1989.

BIBLIOGRAPHY

[63] B. Yao, T.-Q. Li, P. van Gelderen, K. Shmueli, J. A. de Zwart, and J. H. Duyn. Susceptibility contrast in high field mri of human brain as a function of tissue iron content. *Neuroimage*, 44(4):1259–1266, Feb 2009.

[64] V. L. Yarnykh. Pulsed z-spectroscopic imaging of cross-relaxation parameters in tissues for human mri: theory and clinical applications. *Magn Reson Med*, 47(5):929–939, May 2002.

[65] V. L. Yarnykh and C. Yuan. Cross-relaxation imaging reveals detailed anatomy of white matter fiber tracts in the human brain. *Neuroimage*, 23(1):409–424, Sep 2004.

[66] K. Zhong, J. Leupold, D. von Elverfeldt, and O. Speck. The molecular basis for gray and white matter contrast in phase imaging. *Neuroimage*, 40(4):1561–1566, May 2008.

[67] D. Zhou and R. G. Bryant. Magnetization transfer, cross-relaxation, and chemical exchange in rotationally immobilized protein gels. *Magn Reson Med*, 32(6):725–732, Dec 1994.

[68] J. Zhou, J. O. Blakeley, J. Hua, M. Kim, J. Laterra, M. G. Pomper, and P. C. M. van Zijl. Practical data acquisition method for human brain tumor amide proton transfer (apt) imaging. *Magn Reson Med*, 60(4):842–849, Oct 2008.

[69] J. Zhou, J.-F. Payen, D. A. Wilson, R. J. Traystman, and P. C. M. van Zijl. Using the amide proton signals of intracellular proteins and peptides to detect ph effects in mri. *Nat Med*, 9(8):1085–1090, Aug 2003.

[70] J. Zhou and P. C. van Zijl. Chemical exchange saturation transfer imaging and spectroscopy. *Progress in Nuclear Magnetic Resonance Spectroscopy*, 48(2-3):109 – 136, 2006.

HIGH RESOLUTION MAGNETIZATION TRANSFER AT 7T

As discussed previously, Magnetization Transfer (MT) experiments study the transfer of saturated magnetization associated with macromolecules to the free water where it is recorded [2]. During the last decade, MT has been widely used in clinical MRI, especially for neurological applications since demyelination, particularly in multiple sclerosis patients, can be observed via a loss of signal coming from myelin and other macromolecules [28, 31]. However applications of MT imaging are somewhat limited by the spatial resolution of the technique. This chapter will focus on the optimization of high resolution MT imaging at 7T.

5.1   Introduction

Chapter 4 focused on methods to quantify MT phenomenon, but the magnetization transfer ratio (MTR), which is the ratio of the water signal acquired with and without off resonance saturation at a single off-resonance frequency, is generally used clinically due to feasibility of making the measurement in clinically accessible imaging times. As first described by Wolff and Balaban [76], the restricted spins ^1H_r are selectively saturated with RF irradiation a few kHz off resonance from the bulk water protons ^1H_f. This is effective in saturating the broad ^1H_r component with little effect on the narrow ^1H_f signal (the linewidth of ^1H_f being minimum 10 Hz at 7T [67]).

5.1. Introduction

High resolution imaging is always attractive in MRI, and MTR is no exception, as it can provide indices of the myelin content of tissue, especially useful for clinical imaging. However MTR is a ratio between two images, reducing substantially the SNR in the final MTR maps. High field strength increases the sensitivity to the NMR signal, providing better resolution, quicker imaging time and/or higher SNR. However, high field MT images are difficult to achieve due to high RF power deposition (Specific Absorption Rate) induced by the saturation pulses. Duvvuri [17] demonstrated that MTR measurements were possible at 4T, despite power deposition (SAR considerations), making possible the acquisition of high resolution MTR maps with an acquisition matrix of 256x128x28 and a field-of-view of 24 cm. The acquisition time was however relatively long (13 min) due to long TR necessary to counter-balance limits imposed by the SAR.

This chapter aims to present a clinically acceptable method of producing high resolution MTR images with high sensitivity to myelination, within SAR limits. By using a MT-TFE sequence, corresponding to a IR-TFE sequence where the inversion module has been replaced by a MT saturation module, it is possible to overcome the SAR problem. As already mentioned in the chapter 3, the TFE module has a potentially complicated Point Spread Function (PSF). For this reason, a significant part of this chapter presents simulations needed to characterize the relationship between the MTR contrast, the achievable spatial resolution, the imaging time and the PSF for the MT-TFE sequence.

One way to investigate these relationships is to simulate in turn: 1) the MT effects during the saturation phase of the MT-TFE sequence; 2) the MT effects during the readout phase of the MT-TFE sequence; 3) the effects of the readout sequence PSF on the obtained images. Part of this chapter presents an MR simulator which produces realistic human brain T_1-weighted images for the popular 3D Magnetic-Prepared Rapid Gradient Echo sequence (3D MPRAGE) or IR-TFE (Philips terminology), as well as the MT-TFE acquisition used to produce the MTR maps. In this way the associated image contrast can be investigated, as well as effects of noise and averaging, partial volume effects and potential limit of spatial resolution. Realistic simulations were used to quantify effects of artefacts on the detectability of small objects, such as the stria of Gennari. Finally high resolution MTR maps were acquired both on healthy subject and MS patients to look closer to the amount of myelin present inside the cortex.

5.2 Magnetization Transfer in the white matter

Magnetization Transfer, via chemical exchange or dipole-dipole interaction, is a process occurring constantly during an NMR experiment, giving rise to some of the contrast observed in the different tissues of the brain. The amount of exchange is specific to tissue type, and more specifically to the proteins, lipids and other macromolecules constituting this tissue. The bound protons can be biologically as interesting as the free water protons, and in the white matter, are largely related to myelin (see chap. 4.2.3 for a detailed description of the myelin and its role in the brain). MT can thus give complementary information to the more conventional parameters such as the relaxation times T_1 or T_2.

5.2.1 Review of MT in MS

As soon as Magnetization Transfer Imaging (MTI) was introduced *in vivo*, it generated a strong interest from clinicians as a novel, and possibly more specific, alternative to traditional contrasts such as T_1, T_2, T_2^* or **PD**, with the first application being made in Experimental Allergic Encephalomyelitis (EAE) and Multiple Sclerosis (MS) patients [14], two conditions degrading the myelin of the white matter. Quantitative information about the condition of brain tissue can be obtained by estimating MT ratios (MTR, as described in 5.2.2.1), either voxel based and displayed as maps, or measured globally and displayed as MTR histograms.

Multiple Sclerosis is a disease primarily affecting the myelin present in the Central Nervous System (CNS), via an inflammatory process resulting in atrophy and lesions in various part of the brain. The disease is characterized by different stages, each one with specific frequency of appearance of the lesions, as well as their (dis/re)appearances. Inflammation of the demyelinating regions is the main marker of the disease, visible clearly on diverse MRI modalities. However MRI studies also revealed a much more widespread and global damage of the CNS, in particular in patients at late stage of the disease [34]. MT images are particularly sensitive to disease activity and can help to monitor the disease progression in MS, as the decrease in MTR values reflects principally demyelination and axonal loss.

5.2. Magnetization Transfer in the white matter

Pathology   MS is characterized by the formation of focal demyelinated plaques in the white matter, typically situated within the optic nerves, spinal cord, brainstem and the periventricular white matter of the cerebral hemispheres. Diverse clinical episodes occur, with the first acute episode affecting the CNS being classified as clinically isolated syndrome (CIS). If a second attack involving white matter abnormalities occurs, the patient is classified as having relapsing-remitting MS (RR-MS). New episodes occur at a rate generally under 1.5 a year, with recovery between episodes possibly being incomplete. Eventually, around 65% enter the secondary progressive phase (SPMS), with increased disability of the patient during the relapsing episode. Finally, there is a primary progressive form in 10-15% of the patients, with progressive disability from the onset (data from [71]). In all cases, the clinical course usually evolves over several decades. The sclerotic plaque formation is the last stage of a process involving inflammation, demyelinaion and remyelination, olygodendrocyte depletion and astrocytes, neurons and axon degeneration. The relationship between the different processes involving the formation of the plaques remain to be resolved. Overview of the pathology, aetiology and possible treatments are discussed in more detail in [34, 12].

MT in MS   Definite diagnosis has always been a problem in MS, with clinical criteria mimicking other diseases. MRI has established its value as a para-clinical test, with the possibility of assessing the dissemination of the plaques in space as well as in time, a formalisation of MRI criteria with clinical measures being originally described as the McDonald criteria [36]. Particularly for longitudinal studies, MTR is used in order to look at changes in structural integrity of the white matter, correlating strongly with axonal damage. In patients with MS, the MT effect falls drastically around and inside the WM lesions, corresponding to known changes in myelination from post mortem examinations [59]. Decreased MT effects are also seen in the Normal Appearing White Matter (NAWM) in MS, when T_1 or T_2-weighted images do not detect abnormalities. MT has been shown to be sensitive to demyelination and axonal loss, and to a lesser extent to inflammation or increase of free water [38]. When a number of imaging parameters are examined, whole brain MT has been shown to be an independent predictor of disability in MS, in addition to T_2 lesions [57]. It has also been shown that average WM lesion MTR correlates better with physical disability that the T_2 lesion volume [21].

5.2. Magnetization Transfer in the white matter

Detection power in clinical studies   The first clinical study [14] showed that the MTR values decreased in the demyelinating lesions, with the hope of observing a difference between acute and chronic lesions via MTI. In spite of that, they noted that inflammation with little or no apparent demyelination, observed in a EAE model produced on guinea pigs, created a substantial decrease in MTR. However, histological studies [41, 58] have shown that MTR relates to myelin content, even when taking into account the fixation effect [60]. However, the amount of myelin has not been shown to be directly correlated to the MTR. As recent studies have shown [62], the white matter displays regional variation in the measured MT, but were spatially different from what others have shown with a technique called myelin water imaging [75]. Another study measuring both the MT and the T_2 of myelin water founds correlation to some extent between these two measures [69]. The advance of demyelination inside and around lesions can thus not be followed solely via MTI, but MTI is able to provide important information about age of lesions, *i.e.* acute versus chronic lesions (see [28] for a complete description and review of MT in MS). Looking at the normal white matter, the reported MTR ranges from 16% to 60%, suggesting a wide range of effectiveness for clinical MT protocols. The important measure for clinical detection is the contrast between normal tissue and demyelinated lesions, and thus can be optimized via simulation, as suggested in [25]. In this work, Graham and Henkelman showed that if the MR parameters of MS White Matter (WM) lesions were assumed to be similar to Grey Matter (GM) then the maximum MTR contrast between Normal Appearing WM and WM lesions was obtained with a reduced saturating power.

Longitudinal follow-up studies   Many myelin disorders are related to changes in the build-up, organization and maintenance of the myelin and its membrane, making MT one of the favourite choices when studying white matter maturation or disorders. In particular, as the MTR values are considered to be quantitative, in the sense that they are reproducible and comparable amongst subjects (for the same sequence on the same scanner), following a subject with a MT protocol can provide useful information about small changes in the macromolecular content of the tissues, particularly the myelin. As explained in [56], MT MRI data can be post-processed to obtain metrics assessing the overall brain damage (via histograms analysis) which are sensitive enough to detect longitudinal changes in relatively short period of time, providing an additional predictor for evolution of Multiple Sclerosis. As summarized in [28], it is unlikely that MT effects alone reflect the complex pathology of MS

which combines demyelination, remyelination, axonal loss and inflammation, but it is accepted as an invaluable tool nowadays to monitor the advance of the disease, both at early stage of the disease and to response to treatment. One of the challenges posed by MT is the inter-institutional standardization of the protocols, in order to make it a powerful tool to monitor treatment response at a large scale.

5.2.1.1 Clinical relevance of MT beyond MS

Although mainly used for MS, MTR can also be used for other pathology, as well as for neuroscience related questions about the development and aging of the brain. During the developing of the paediatric brain, physiological age-related variation can be seen in MTR values [52, 70]. These changes are attributed to increased myelination associated with maturation of the brain. As axons grow in harmony with the brain, myelin produced by the olygodendrocytes wraps around the axons, leading to a local decrease in water content. Both the T_1 and the MTR are evolving during the maturation of the brain. It is important to be familiar with these age-dependent differences in MTR values, especially when looking at inborn errors of metabolism [4], generating abnormalities in the production or maintenance of the myelin. Ageing of the brain can also trigger minor changes in the chemical and cellular composition of the tissues, *e.g.* accumulation of iron in the deep nuclei especially during neuro-degenerative disorders, or the reduction of the MTR values, particularly in patients with Alzheimer Disease (AD), with the MTR values in the hippocampus correlating with neuropsychological parameters [27]. In general, ageing and neuro-degeneration lead to a weakening of cellular repair and compensatory mechanisms, which can lead to cell damage or cell death. Atrophy is thus generally observed during the ageing process, particularly in dementia. A comparison between volumetric changes and MTR values [53] shows that the volume change and the decrease in MTR was not correlated but shows complementary aspects of AD.

MT is a powerful tool, both for assessment of the normal evolution of the development of the brain throughout an healthy life, as well as detection and follow-up of abnormal variation, especially for patients suffering of myelin disorders. Characterization of the measure, its accuracy as well as its reproducibility is presented in the next section.

5.2.2 MTR: a semi-quantitative measure

Different methods have been used to acquire the amount of magnetization transfer between free (or bulk) protons ^1H_f and bound (or restricted) protons ^1H_r. They all require saturation of one of the pools, before acquiring the volume of interest with a normal readout. SAR considerations however limit the amount of saturation achievable, making lower SAR sequences a better choice, while reducing the MT sensitivity. Gradient Echo (GE) imaging sequences are thus preferred, as the excitation pulse flip angle can be kept low with no need for refocusing pulses. While this method reduces the available SNR compared to SE techniques, it also decreases the overall SAR. The aim of this section is to give an overview of the MTR measurement.

5.2.2.1 Basic method description

Initially, MT Contrast (MTC) was introduced by Wolff and Balaban [76] who measured the effect of cross-relaxation and chemical exchange due to saturation on the observed T_1. The measured MTC is a complex combination of cross-relaxation, chemical exchange and magnetization recovery happening during the saturation, and is reflected inside the MTR maps. A MT sequence is divided into two parts: 1) one image or volume is acquired without the saturation, giving a PD-weighted image M_0, 2) the second image M_{sat} is acquired with saturation, generally applied at 1-2kHz off-resonance on the bound pool. As the two images (or volumes) required for the computation of the ratio are acquired non-simultaneously, registration of the two volumes of interest (M_0 and M_{sat}) is necessary. MTR is then defined via the following:

$$MTR = \frac{M_0 - M_{sat}}{M_0} \tag{5.1}$$

where the magnetizations M_{sat} and M_0 depend on the imaging sequence. MTR is semi-quantitative, in the sense that the values depend on the exact pulse sequence used and does not give a direct measure of the magnetization transfer happening between the two pools.

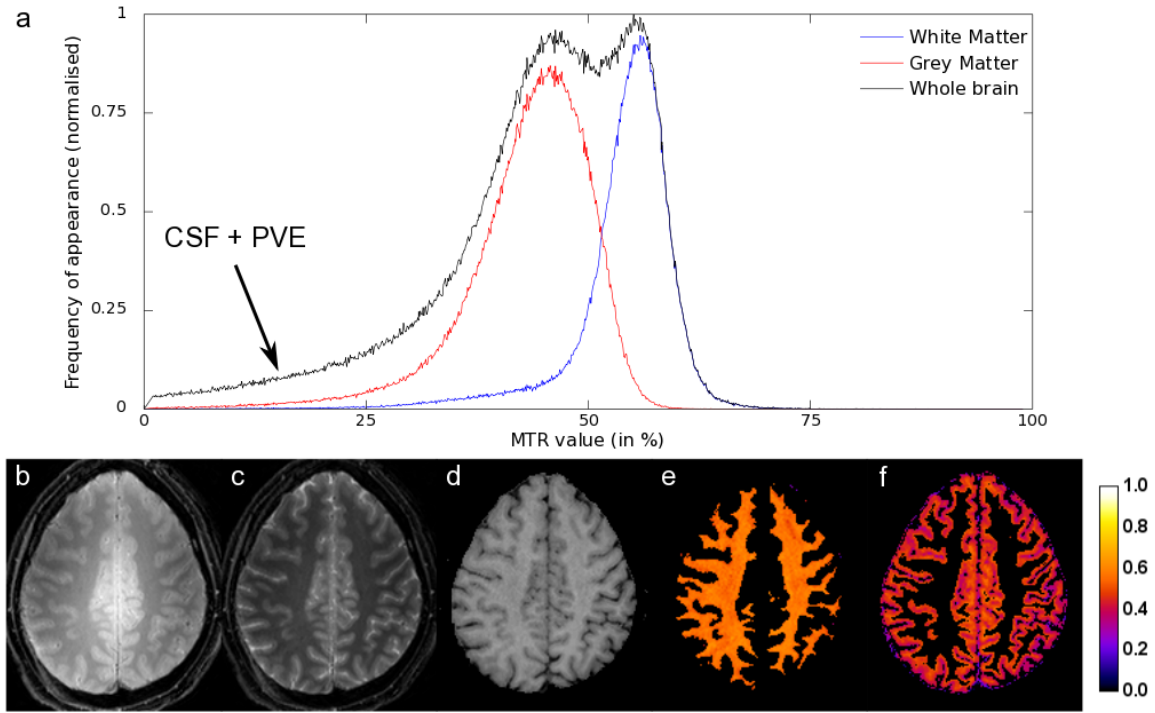## 5.2. Magnetization Transfer in the white matter

Figure 5.1: (*a*) MTR histogram of a healthy brain (FOV=210x210x100mm), with the color peak obtained respectively from the segmented white matter (blue: peak mode at 56%) and the segmented grey matter (red: peak mode at 43%). (*b*) Non-saturated image M_0, (*c*) saturated image M_{sat} and (*d*) corresponding MTR map from the same healthy subject. The brain volume was segmented with the SPM software (`http://www.fil.ion.ucl.ac.uk/spm`), and corresponding MTR map of (*e*) the white matter and (*f*) the grey matter were used to create the histogram. All images were acquired with the MT-TFE sequence (described in 5.2.5.1). The whole brain histogram shows both WM and GM peak as well as the Cerebro-Spinal Fluid (CSF), that has a very low MTR (< 5%) but appears wider due to Partial Volume Effects (PVE) with GM and WM.

5.2.2.2   MTR in the brain

Small regions of interest (ROI) have been used first to look at variation of MTR inside the brain, with the white matter having reproducible MTR values, with higher mean and lower standard deviation than the grey matter. Regional variations have been reported by Metha *et al.* [37] inside the white matter, with the corpus callossum having a higher MTR than the different lobes. Similarly, lower MTR value were reported in the subcortical U fibres, compared to either lobes or deep white matter regions, with no significant variations between the left and right hemisphere. ROIs have also been used to look at specific lesions or regions associated with particular symptoms, whereas MTR histograms can been used to look at more widespread diffuse tissue changes. Generally, a shift of

5.2. Magnetization Transfer in the white matter

MTR values to the left of the histogram reflects a decrease of macromolecules density, due to myelin or axonal loss. However the study of MTR histograms requires that the tissue of interest, generally the white matter, is segmented from other tissues (via image processing) before computing the histogram. Partial volume effects, particularly present at the white matter/ventricle border, can lead to abnormalities inside the histogram shape, influencing the overall results. Discarding MTR values below 5 or 10 % can reduce the problem, but should be done wisely. MTR map with their corresponding histogram is presented in fig. 5.1, and two peaks can be distinguished. The voxel size, and especially the slice thickness, are important when considering MTR histograms or MTR maps, as partial volume effects coming from vessels or CSF can mislead the interpretation. For fig. 5.1, no threshold was applied on the histogram, and the pixel size of the image was 1x1x1 mm. A large amount of pixels having a MTR value lower than 25% in the histogram of the whole brain of fig. 5.1 a are due to the CSF, creating partial voluming with adjacent white matter and grey matter tissues.

5.2.2.3   Robustness of the measure

While the magnetization transfer ratio is often considered quantitative and reproducible on a given scanner, in fact variation in the RF system can lead to difference in the measured MTR, posing problems for longitudinal or multi-centre studies. Generally, a quality assurance program is incorporated inside any longitudinal study to ensure stability of MT acquisition over time [28]. It means that any given clinical study should compare MTR values to healthy subject scanned on the same scanner during the same period. Age-matched subjects are also preferred, but the literature is contradictory on this matter (either with [22] or without [57] variation of MTR with age). However, imperfections of the scanner (inaccuracy and instability) in setting the flip angle is the strongest source of alteration of the MTR, with a lower amount of power applied during the saturation resulting in a lower MTR. It can widen the MTR histogram, but the effect can be diminished greatly by using the body coil for excitation, with a close multi-fitting array for reception, this setting giving the best reproducibility across centres [68]. Another possibility is to acquire a B_1 map of the subject during the same visit, and use it to correct the MTR images, by computing the actual power deposited for each voxel, and rearranging the MTR values in accordance (see [55] for more details, as well as in section 5.2.5.3).

5.2.3 Amide Proton Transfer imaging

Quantitative APT results, acquired at 7T and presented in chapter 4, varied between the corpus callosum and other white matter structures, suggesting that qualitative APT imaging could be used as a marker of myelination. Similarly to the MTR presenting the ratio of macromolecules inside the brain, the APT (short for Amide Proton Transfer) ratio can highlight the proportion of amide protons exchanging inside the brain tissues. In fact, taking into consideration the results presented in the chapter 4, the Amide Proton Transfer (APT) imaging protocol requires the acquisition of two images at the frequency $\delta = \pm 1050 \text{Hz}$ at 7T, one on each side of the water resonance. An APT map can be obtained by computing the ratio:

$$MTR_{asym} = \frac{M_{+\delta} - M_{-\delta}}{M_{+\delta}} \tag{5.2}$$

The ratio MTR_{asym} is directly related to the amount of exchangeable amide protons, a quantity possibly related to the pH, as demonstrated in [74], and used in clinical settings, for example to detect change of pH in ischemia [66] or to dissociate tumour to oedema [30]. In the case of APT imaging, the sensitivity to the B_0 and B_1 field is increased, as a shift in the frequency or a reduced flip angle during the saturation would result in a misleading contrast in both $M_{+\delta}$ and $M_{-\delta}$. Correction of the imaging artefacts can be performed after acquisition, as shown by Sun *et al.* [65]. However, it generally requires more than two images in order to recover the exact contrast for the nominal offset frequency. High-order shimming can also help reducing the variation of the B_0. The robustness of the APT sequence will be particularly examined in section 5.3.1.1 and 5.3.1.2. To be sensitive to the CEST contrast it is important to 1) put the saturation on the correct side of the water peak; 2) put the saturation at the CEST peak; 3) optimize the bandwidth of the saturation pulses to give the best CEST effect with minimal sensitivity to off-resonances.

5.2.4 MT effects during other imaging experiments

The saturation used clinically for inducing the magnetization transfer is mostly based on soft off-resonances pulses. Other studies focused in the general effects of off-resonance radio-frequency

pulses, as MT effects can confound some experiments, for instance causing systematic errors in the quantification of perfusion by arterial spin labelling [49, 24], and causing artefacts in multi-slice sequences [40]. This is because in these scanning experiments, irradiation must be applied at a variety of frequencies, which can be off-resonance from the water frequency when it is ultimately imaged. Alternatively MT effects can increase sensitivity in experiments such as angiography and contrast enhanced MRI, where it is used for background suppression. Angiography performed with MT-background suppression facilitates the detection of small veins [18]. Background suppression has also been applied together with the use of contrast agent (Gad) in order to enhance lesions contrast [19]. The effects of magnetization transfer in fMRI has also been investigated [64, 50, 83], as the high repetition of slice selection used during the fMRI experiment can cause off-resonance saturation in the neighbouring slices, thus altering or improving the image contrast due to inflow. It is for those reasons also that a quantitative measure of the MT phenomenon is important, as it can help to model and optimize a variety of the protocols described here.

5.2.5   MT and high field

High magnetic field increases the SNR in the acquired MR images, and also increases the chemical shift dispersion, as described in depth in chapter 4. This translates into a more robust measurement at a finer anatomical level, but as already mentioned in the previous chapter, the safety issues associated with the radiofrequency deposition energy into the patient, measured by the specific absorption rate (SAR) has limited the use of MT at 7 T so far. A detailed list of advantages and possible limitations is presented in the section 4.2.4. Overall, this suggests that MT-weighted images could reveal more details in a variety of pathology if performed at higher field. However, to correct the inhomogeneities of the transmit B_1^+ and the received B_1^- field, no hardware solutions are presently available. It is thus necessary to use additional scans, such as a B_1 map, which can be used to correct the measured MTR maps [55]. The following describes the pilot study performed at 7 T via a new designed imaging protocol based on the MT-TFE sequence.

5.2.5.1   Sequence description

The common Magnetization Transfer protocol used clinically is based on the MT-GRE sequence described in fig. 4.5, and consists of applying an off-resonance saturation pulse before each RF excitation pulse during the acquisition of the saturated image. This considerably increases the SAR, as explained in the section 4.2.2.2, and is the reason of the design of the MT-TFE sequence described here. The imaging readout module used in this MT-TFE sequence is a Turbo Field Echo readout (Philips terminology). PULSED saturation, as well as Continuous Wave saturation, were used in the simulation but only the PULSED saturation was used experimentally. A schematic of the pulse sequence used throughout this chapter is shown in fig. 5.2. A TFE scan is acquired, preceded by a pulse train saturation (indicated as PULSED SAT in fig. 5.2), along with an additional NO SAT TFE scan.
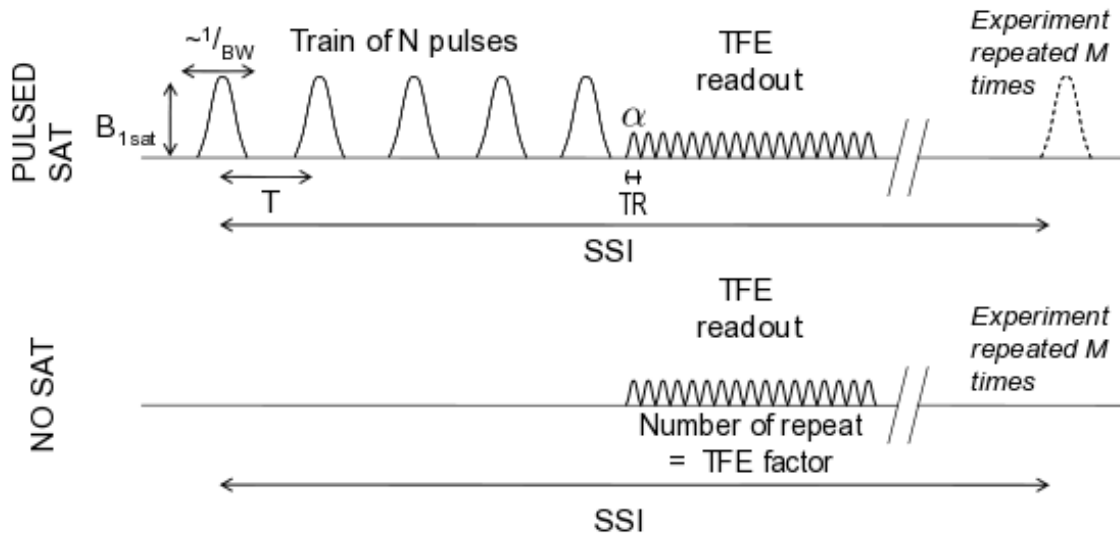

Figure 5.2: Schematic diagram of the pulse sequence used in simulations and experiments. A PULSED saturation acquisition was followed by a NO SAT acquisition. The imaging module was a turbo-field echo gradient echo.

PULSED SAT consists of a train of up to N=20 off-resonance pulses (Gaussian-windowed, sinc shaped pulses) with amplitude B_1^{sat}. The 20 MT preparations pulses (T=55ms, BW=300Hz, B_1=3.79μ T) were applied at $\pm$1050 Hz chosen to be sensitive to CEST effects observed in the spectra at 3.5ppm. The pulse train was followed by a spoiler gradient of strength of 33mT/m during 14.6 ms, as described in 4.3.2. The MT preparation pulses were followed by a Turbo-Field echo (TFE) readout

5.2. Magnetization Transfer in the white matter

(*TR/TE*=10/5.4 ms, flip angle= 8°, 0.86x0.86x1 mm^3). The TFE readout sampled k-space centre-out to maximize the MT contrast in the image, with a ramping of the first RF pulses, as already presented in section 3.2.1.2 and designed to ensure a smooth approach of the steady-state of the magnetization. A non-MT weighted image was also acquired before each sequence by applying the sequence with the off-resonance pulses replaced by a wait period and including the spoiler gradient and the readout to allow the normalization of the intensities.

5.2.5.2   First imaging results

The MT-TFE sequence described in section 5.2.5.1 was implemented for *in-vivo* applications, providing the first whole brain MTR imaging at a resolution of 1 mm isotropic showed in fig. 5.3. To obtain this in a reasonable imaging scan, two slabs were acquired in parallel, *i.e.* two TFE trains were
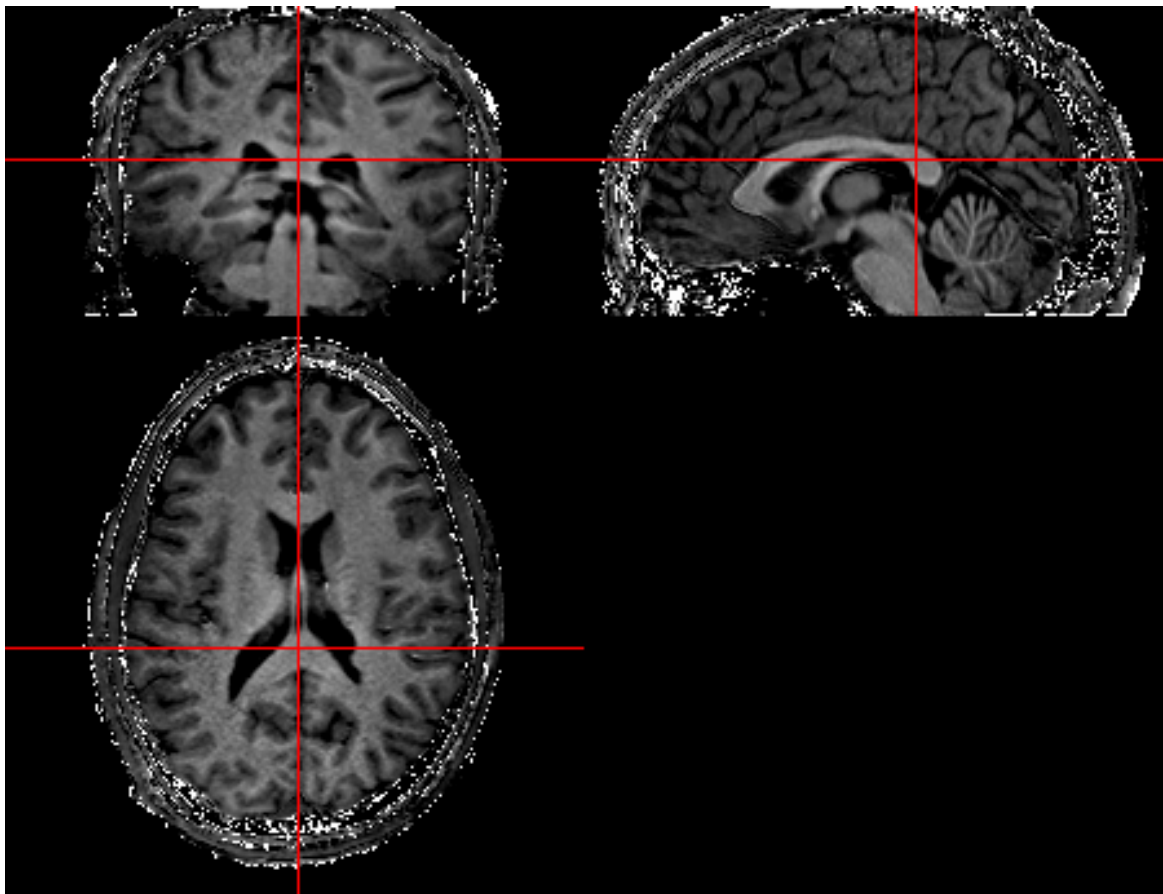

Figure 5.3: Volume MTR acquired at 1 mm^3 on a healthy subject. Acquisition time was 9min20s. A clear increase of contrast can be seen in the corpus callosum, as well as in the pons.

acquired at a different position inside one Shot-to-Shot interval (SSi). The total field of view was 210x180x120 mm, the two dynamics (with and without saturation) acquired over a total of 9 min and 20 s. Other acquisition parameters are TR/TE=10.2/5.8 ms, flip angle=8°, TFE factor=256, a SENSE factor of 1.5 and N=5 startup pulses.

The images presented in fig. 5.3 were the highest resolution MTR map of a whole brain acquired so far to our knowledge, and showed good delineation of the white matter with high detectability of the cortical ribbon through the whole brain, as well as a good visualisation of the pons and the cerebellum. Two modes were clearly seen on the volume histogram, with one at 20.2% representing the GM, and the other at 40.7% representing the WM. Regional MTR variation inside the white matter can be seen for the corpus callosum as well as the pons on fig. 5.3.

5.2.5.3 B_1 inhomogeneity correction

To provide an accurate and clinically useful MTR image, correction of the B_1 inhomogeneities was performed as described by Ropele *et al.* in [55]. This requires acquisition of an additional scan during the imaging experiment, *i.e.* a B_1 map which was acquired based on the double TR technique described in [79]. This map of the B_1 field produces information about the spatial variation of the power applied during the saturation, and can help to retrieve the actual MTR value that would have been observed if the power did not suffer alteration. As described in [55], a linear relationship was observed between the B_1 error and the corresponding MTR error. This relationship is subject dependent, and can be retrieved by fitting a straight line on the MTR values function of the B_1 error. Supposing that no static field error is present, the MTR values can be readjusted via this linear relationship. It is important to note that this was done only on the white matter, as the relationship between the grey matter MTR and the B_1 may not be defined by the same straight line. This method does not require a strong accuracy of the B_1 map, as error in this map would only affect the slope in the regression analysis. In the same manner a pixel with low MTR values (due to either pathology or imaging artefact) would only influence minimally the correction, supposing a large white matter volume as the brain. No mention was made of diffuse change in the white matter, but it is expected that lowering part of the white matter MTR values might affect the correction in an unpredictable way, if for example the white matter lesions are not excluded from the analysis. It is for this particular reason that it is

important to minimize the effects of the B_1 inhomogeneity on the acquisition, as presented in 5.3.1.2.

5.2.5.4 Reproducibility of the measure

To evaluate the reproducibility of the measured MTR over scans acquired at different visits of the subject, a reproducibility study was performed. It consisted of scanning the same subject (an healthy male of 28 years) over a period of two weeks with the same protocol and the same planning and orientation of the field-of-view. Scanning protocols were: one T_1-weighted volume (MPRAGE) used for inter-visit registration, one MT volume with and without the saturation train used to produce the MTR maps, and one B_1 map used for the saturation correction (as explained in 5.2.5.3). For each session, the MT images were registered to the T_1-weighting image, those images were also used to register the images from the diverse sessions. The histogram analysis is done without (a) and with (b) B_1 correction, and is shown in fig. 5.4.
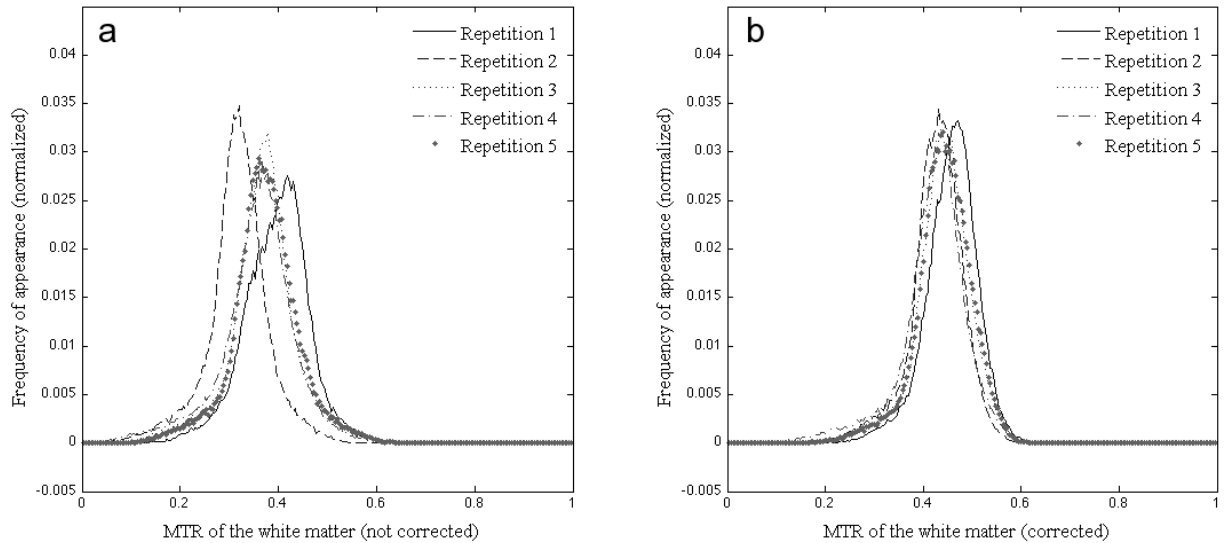

Figure 5.4: Histograms of the diverse repetitions of the measurement of the MT of the white matter inside an healthy subject, both (a) without and (b) with B_1 correction.

For the histogram analysis, the white matter was segmented based on the MPRAGE and extracted from the MTR maps. Normalisation of the height of each histogram was done separately, with the total number of pixels only considering the white matter volume. Analysis over the five repeats gave strong reproducibility, with the mode of the histogram being 0.44 ± 0.02, the height being 0.03 ± 0.001 and the full width at half maximum (FWHM) being 0.10 ± 0.004 [1]. Little variation

can be seen between the visits after the correction, while the dispersion of the peak position is clearly broader without correction.

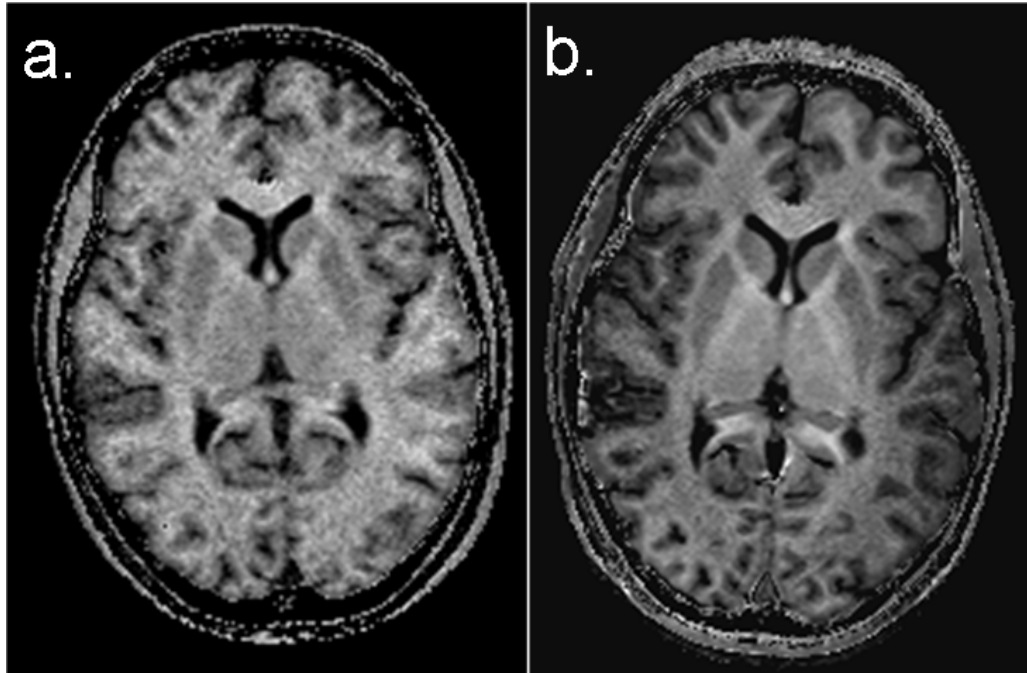### 5.2.5.5 High sensitivity via high field scanner

Figure 5.5: MTR maps formed from MT-TFE images acquired at (a) 3T and (b) 7T. Image resolution at 3T is $1\text{x}1\text{x}1\text{mm}^3$, while $0.86\text{x}0.86\text{x}1\text{mm}^3$ at 7T.

For high spatial resolution MT imaging, a smaller pixel size was reachable thanks to the high SNR available at 7T. Using both simulation and z-spectra results from chapter 4, a good saturation scheme was chosen to be a train of 20 pulses applied at an offset resonance of -1100Hz from the water resonance, with a bandwidth of 300Hz and a period between each pulse of 55 ms (as mentioned in the sections 5.3.1.1 and 5.3.1.2). A SSi of 10 s allows a long recovery time before the next saturation, all pools being thus able to recover equilibrium before the next saturation. The number of readout was chosen to cover the maximum volume per saturation, while letting enough time (typically 5 seconds) before the next saturation. Fig. 5.5 shows MT-TFE images acquired at 3 T and 7 T. A net increase in the contrast to noise ratio between white matter and grey matter tissue is observed at 7 T. Further increase via used of parallel imaging could be achieved, *i.e.* via SENSE, but the final CNR will mostly depend on the receiver gain and the acceleration used, and are beyond the scope of this study.

The aim of the present study is to produce high resolution MTR and MT asymmetry maps at 7T (using a novel MT prepared turbo field echo sequence, MT-TFE). The sensitivity increase with field strength facilitates the detection of variation with improved spatial resolution.

5.3   Modelling contrast and artefacts in MT experiment

For high resolution MT imaging, an alternative to the traditional saturation is to use the pulse train saturation described in the chapter 4. While this saturation works best for single-shot imaging, *i.e.* where a single pulse is used to readout the transverse magnetization for image encoding, it can also be implemented with longer readout sequences, as presented in the previous section. In fact, it is well known that the intensity in the image is carried mostly in the center of the k-space, and that the outer k-space encode the fine details of the image. Using this advantageous property, first the saturation pulse train is applied, reading out directly afterwards the center of the k-space, then multiple readout pulses are used to fill out the edge of the k-space, via a TFE-FFE sequence for example. In this way, the number of times the saturation pulse train is applied is reduced, while the images acquired are still heavily weighted by the offset resonance pulse train and the subsequent saturation transfer.

The saturation is determinant in the contrast obtained in the final image, but several parameters play a role in the quality of the acquisition, and can be separated in three different problems. Simulation is used to optimize the quality of the image via three separate analysis:

- The saturation part of the sequence, particularly at high field, is sensitive to inhomogeneities. Optimizing the parameters so that the obtained saturation is robust to standard acquisition set-up at 7T will be performed in the section 5.3.1.

- The acquisition of the signal, and particularly the timing and the chosen resolution, influences the final contrast and quality of the image. Attenuation of the contrast by the acquisition scheme will be evaluated and minimized in the section 5.3.2

- Finally, the encoding scheme of the k-space together with any post-processing applied on the signal before the display of the image influences the detection power of the sequence. Since the

PSF of the sequence presented in the next section is not trivial to derive analytically, a numerical simulator will be used to predict the quality of the final image, and is presented in the section 5.3.3.

To corroborate the validity of the MT-TFE protocol, the saturation scheme and the imaging sequence have been simulated numerically, and results compared similar scanning experiments on phantoms and *in vivo*. The simulation of the three-pool model, already covered in chapter 4, has been used to optimize the contrast between white and grey matter via the saturation of the magnetization during the approach to steady-state. A specific simulator has been designed to predict the influence of the imaging part, with its use being extendible to a variety of other applications. The goal of this section is to obtain a simple method of acquiring MTR imaging with minimization of the B_0 and B_1 inhomogeneities effects together with minimization of effect of image acquisition on the contrast (section 5.3.1), as well as maximization of the image resolution (section 5.3.3). As the white matter is highly myelinated compared to the grey matter, the optimization of the contrast between the white matter and the grey matter tissues can provide a useful protocol to detect demyelination, ultimately transferable to clinical trials.

5.3.1   Simulation of the contrast due to saturation in the non steady-state

The final contrast obtained in a MRI is a combination of many competing phenomena, but the preponderant contrast in the image is determined by the signal at the center of the k-space. Here the MPRAGE sequence was modified by replacing the inversion with a saturation scheme (MT-TFE or MTRAGE), and the k-space was then sampled in a low-high order fashion, as described in section 3.2.2.1.

The saturation part of the sequence described in 5.2.5.1 was the same as the pulsed train saturation used in chapter 4, and consisted of twenty RF pulses, applied at a specific off-resonance frequency, and generating exchange between the different pools present in the tissues. The three pools considered are the free pool of water protons (f), the protons bound on macromolecules (b) and the protons present on amide groups or CEST protons (c). The parameters used for the simulations

were obtained from the quantification present in the previous chapter and are: M_0^c=0.08, M_0^b=0.1, k_{fb}=50Hz and k_{fc}=20Hz for the white matter, and M_0^c=0.02, M_0^b=0.03, k_{fb}=50Hz and k_{fc}=15Hz for the grey matter. Evolution of the magnetization of the different pools, during both saturation and imaging readout was numerically simulated according to the model presented in 4.3.1. Fig. 5.6 presents the simulation results, taking account of the exchange in both the saturation and the imaging parts of the sequence.

The amount of M_0^f available at the end of the saturation strongly depends on the NMR parameters, the exchange rate and the proton density of the three different pools, as well as the number of saturation pulses used. These parameters, specific to each tissue type, have been assessed in different ways in the literature [63, 78, 42]. Only [42] has looked at CEST quantification, so although the values of these parameters obtained from the z-spectra quantification ([42] and chapter 4) have not been confirmed by other similar studies, these values are used here to investigate the MT effect, in healthy white and grey matter. Simulation of the contrast obtained in each tissue depending on the saturation
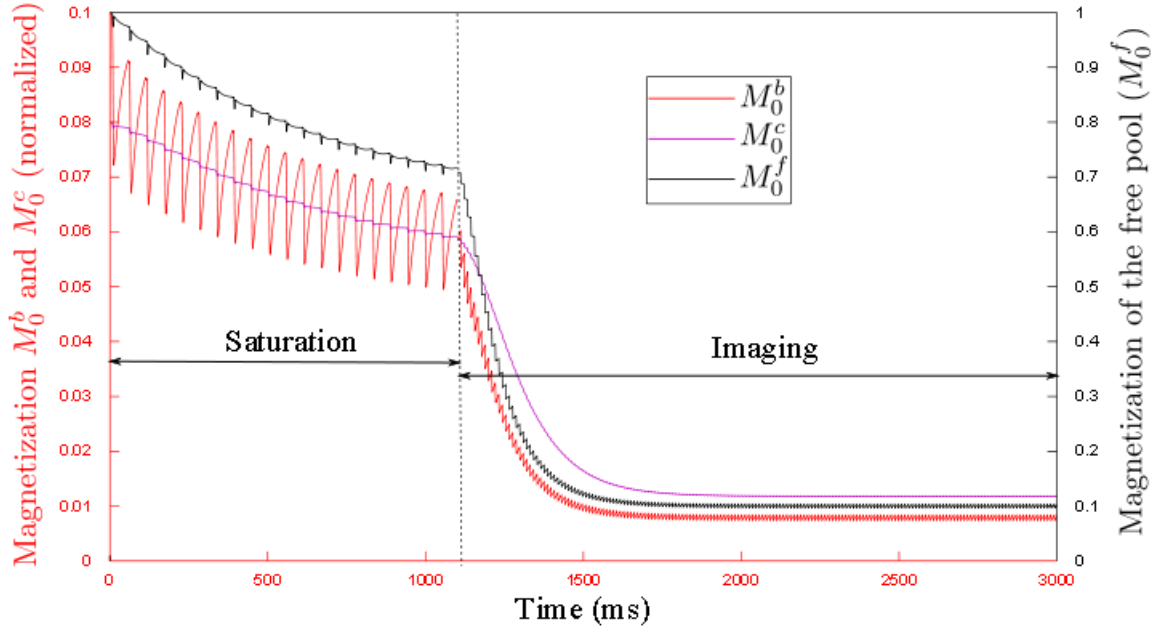

Figure 5.6: Effect of saturation and TFE acquisition on the magnetization of the different pools. Saturation is produced with a train of 20 pulses of bandwidth 200Hz, applied at +1050Hz off-resonance. The imaging part is a TFE train of 250 FFE readouts, each with an RF excitation pulse of 8 ° and a TR of 11ms. The bandwidth of the FFE excitation pulse is 11.3kHz, exciting all the pools during the imaging experiment, causing exchange throughout the imaging part.

scheme is then straightforward, and can give the optimum set of saturation parameters (bandwidth, number of pulses, time between pulse) to provide the best contrast for a given application.

Looking at fig. 5.7, the z-spectrum shows difference between the white and the grey matter mostly at the amide protons peak, with a maximum reaching 25% (fig. 5.7 c, d) for a relatively short saturation (*i.e.* around twenty pulses of 50 ms each, compared to a CW of 5 seconds required for the steady-state condition). It is interesting to note the differences in behaviour of steady-state sequences (*i.e.* long saturation via high power) and sequences such as the MT-TFE sequence which study the approach to the steady-state, possibly providing condition with better specific detection, such as for detection of MS lesions, particularly in the cortex (more details in 5.4.2.2). The approach to steady-state requires a smaller effective B_1 for the saturation, making it easier to implement at high field. However the inhomogeneities in both the main magnetic field and the B_1 field are stronger, and their effects are reviewed hereafter.
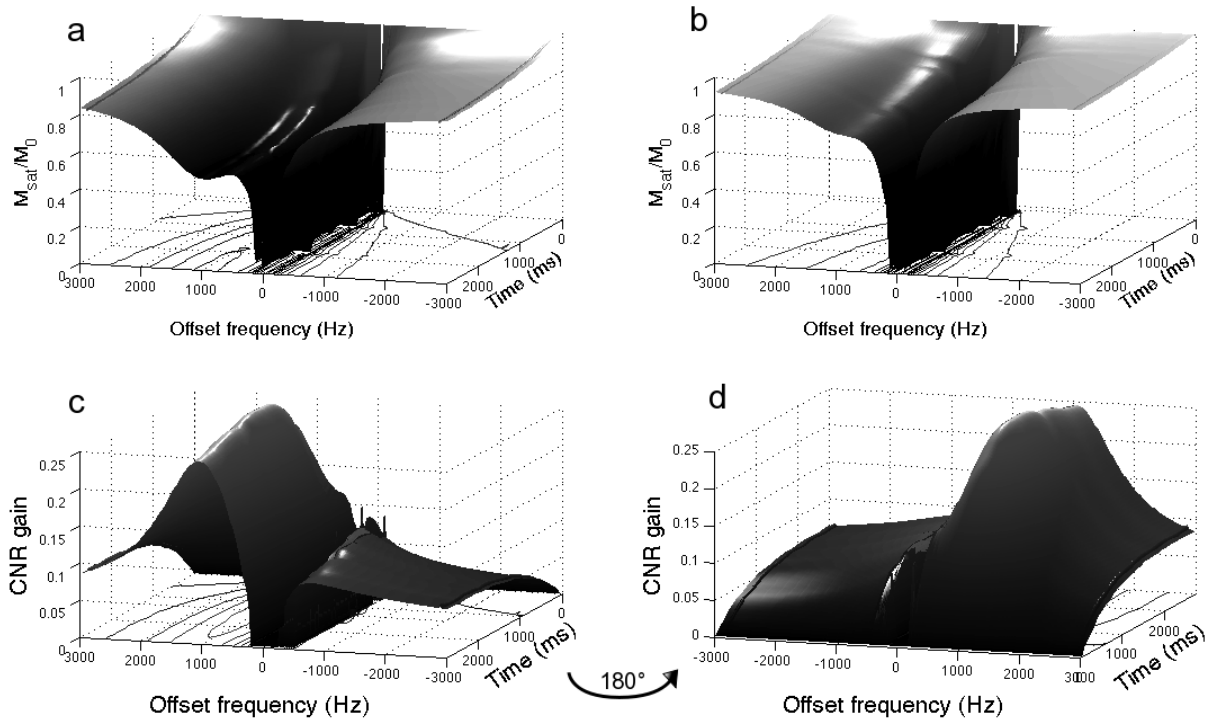

Figure 5.7: Effect of the saturation pulse on (a) WM and (b) GM. The 3D z-spectra represent the amplitude of the magnetization of the free pool left versus saturation time and emphasizes the exchange at specific frequencies happening before the acquisition readout. The maximum contrast appears for a limited saturation time (< 1 s), at the amide offset frequency (-1050 Hz), as shown by the bottom figure, which presents the difference between the WM z-spectrum and the GM z-spectrum (c and its flipped version d).

5.3. Modelling contrast and artefacts in MT experiment

5.3.1.1   Minimizing effects of B_0 inhomogeneity on MTR and APT

With perfect transmission and shimming, the effective longitudinal magnetization of the free water is 55.2% for the white matter, and 82.6% for the grey matter at the end of the saturation pulse train (N=20, off-resonance=-1050 Hz), the variation originating in the tissue specific properties (*i.e.* proton density, exchange rate, T_2). Field inhomogeneitites can cause artefacts in MTR and MT asymmetry studies, and this can be a particular problem at ultra-high field where susceptibility artefacts are more pronounced. A practical example of how the inhomogeneities influence the obtained contrast can be seen on the image 5.8, with a region known for difficulty in shimming and transmission of RF field, *i.e.* the temporal lobes. As it is difficult to discern the difference between effects due to B_0 and B_1 inhomogeneity, simulation was performed to provide insight into the minimization of these artefacts individually.
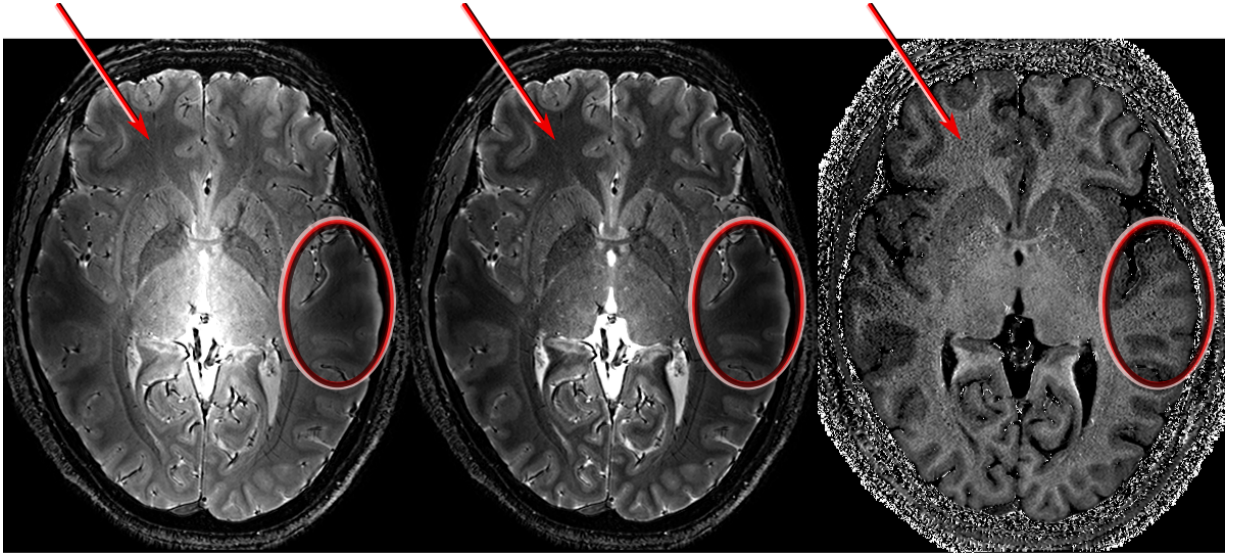

Figure 5.8: Effect of inhomogeneities coming from mediocre transmit field around the temporal lobes. M_0 (left) and M_{sat} (right) images acquired at 0.5 mm isotropic. The right image is the corresponding MTR map. Circles present the area of low signal in the temporal lobes, while the ROI used in the frontal lobes for comparison are pointed via arrows.

Z-spectra correction performed in chapter 4 was achieved via a shift of the spectrum based on a B_0 field map. Previous studies have also used a B_0 map to make similar corrections but based on correcting the model rather than the data [65]. Unfortunately both these approaches are too time-consuming for high resolution MT_{asym} weighted images created via MT-TFE images. A better characterization of the z-spectrum allows experiments to be designed to reduce sensitivity to inho-

mogeneities whilst maintaining sensitivity to CEST effects, for instance by increasing the bandwidth of the off-resonance saturation pulses. This approach is beneficial for both MTR and MT$_{asym}$ imaging studies, as described hereafter.

Effect of the variation of the main magnetic field on the resulting APT contrast is estimated via simulation of the longitudinal magnetization obtained after the saturation train. Different offsets of the main magnetic field (from -3 kHz to 3 kHz), as well as different bandwidths of the saturation pulses (from 150 Hz to 450 Hz), provides an overview of the robustness of APT imaging to B_0 inhomogeneities and is presented in fig. 5.9. The goal of this simulation is to find a reasonable range of frequency where the APT contrast differs little to the exact APT peak frequency. The simulation assumed a train of 20 RF pulses of varying bandwidth, but all applied at a different frequency from the APT peak. Parameters of WM tissue were assumed (M_0^c=0.08, M_0^b=0.1 k_{fb}=50 Hz and k_{fc}=20 Hz), and the exchangeable protons peak was set to -1050Hz compared to the water peak (described by a T_1 and T_2 of respectively 1,200 and 40 ms).
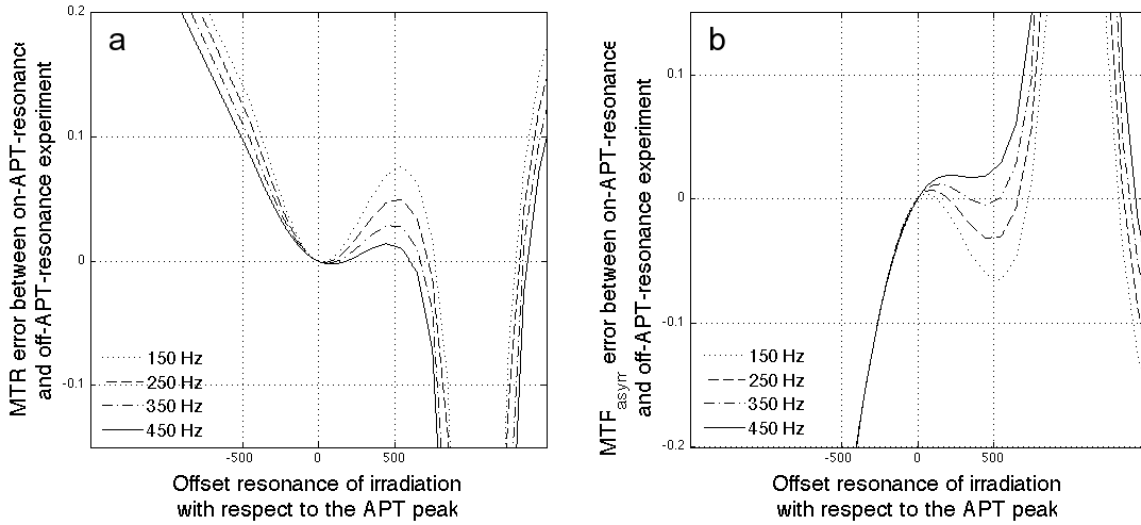

Figure 5.9: Difference in the APT signal amplitude (a) as well as in the asymmetry (b) as a function of the off-resonance frequency error for different saturation pulse bandwidth. Close to the exact frequency of the CEST peak, the difference is minimal. Depending on the bandwidth used, this difference in MTR can be lower than 5% for a BW of 450 Hz over a range of 500 Hz. For a bandwidth of 150 Hz, this difference of 5% is restricted to a range of 200 Hz. However, the error in MTR$_{asym}$ is larger for similar B_0 error, due to error in both side of the z-spectra.

For a small frequency error of the pulse train saturation, the difference in contrast at a single off-resonance (presented in fig. 5.9 a) is very low compared to the APT peak (similar for the MTR

contrast), but this error is dependant on the bandwidth used. In fact the saturation of the APT peak is nearly constant (less than 1% of variation) inside the bandwidth of 150Hz for the corresponding pulse bandwidth. For larger offset, the variation increases, exceeding 5% over a range of 300Hz. With a larger pulse bandwidth, however, the error on the CEST contrast stays small over a large frequency range, *e.g.* for a bandwidth of 350Hz the variation stays under 2% over a range of nearly 400Hz. As the range of frequency at 7T is generally below 300Hz inside the brain for a traditional shimming process, a bandwidth of 250Hz seems reasonable to keep the MTR error on the CEST measure below 5%. For asymmetry studies, the error is drastically larger for negative offset independently of the bandwidth used (presented in fig. 5.9 *b*). For positive offset however, the error is stabilizing at large bandwidth, reaching a plateau at 2% error over 400Hz for the bandwidth of 450Hz. While this behaviour is really interesting for MTR$_{asym}$ *in vivo* study at 7T, it is important to remember that using higher pulse bandwidth makes the measured signal more sensitive to MT, reducing the actual effect of APT contrast in the image. For this reason it is sensible to keep the bandwidth relatively low, while using a slightly lower offset frequency (950Hz instead of 1050Hz for example).

5.3.1.2 Effects of B_1 inhomogeneity on MTR

The effect of the receiver field B_1 is minimal on the ratio map MTR, as both the unsaturated image M_0 and the saturated image M_{sat} are affected in the same local manner. As shown in 5.3.1.2, the MTR is not affected by the local decrease of B_1, but the SNR is. Hardware improvements can reduce these effects, such as receiver coil with larger number of channels, or local surface coils for focal anatomical study. The major effect of B_1 inhomogeneity comes from the transmitted power to the sample during the saturation. It can be reduced by using hardware improvement such as multiple transmit coils, or by using adiabatic pulses (described in 2.1.1.2). However the goal of this section is to choose the sequence parameters that minimize sensitivity to B_1 inhomogeneity effects, both for saturation and imaging purposes, without hardware or pulse shape modification.

In vivo **estimation**   While the non-MT weighted image and the MT-weighted image clearly show reduction in the signal from the temporal lobes areas, the MTR map being a ratio is not too affected, as long as not in extreme conditions. From the data presented in fig. 5.8, an increase in noise could

be perceived in the MTR maps in the region of lower B_1 with a standard deviation reaching σ_{MTR} = 0.28 in the temporal lobes (circled areas), measured from the propagation of error equation. MTR contrast between white matter and grey matter was 12.6% in these regions. In comparison, the frontal lobes (showed by arrows) had lower standard deviation (σ_{MTR} = 0.15), and increased contrast (C_{MTR} = 16.9%).

Simulation validation The effect of B_1 inhomogeneity can be greatly reduced by choosing correctly the saturation parameters. Considering the frequency of -1050Hz with a pulse bandwidth (BW) of 300Hz, a 20% decrease in the transmitted power corresponds to a decrease in the contrast of 2.7% (0.438-0.411), while the same decrease of power with a 150Hz BW would create a contrast difference of only 1% (0.460-0.450). In the contra-lateral part (+1050Hz), the 300Hz BW creates a contrast difference of 9%, while the 150Hz BW only provides a contrast difference of 6%. This counteracts the robustness of large bandwidth saturation pulses proved for the B_0 inhomogeneity. The objective of this chapter is to define a robust protocol to both inhomogeneities, the amplitude and width of the CEST peak being just a parameter on the final image contrast. A BW of 200Hz will provide enough stability to the majority of frequency distribution inside the brain, while its amplitude would be influenced only slightly by B_1 inhomogeneity.

5.3.2   Contrast attenuation due to image acquisition

A large matrix size is required to reduce partial volume effects, especially for grey matter imaging. The increase in resolution generally leads to increase in acquisition time. There is thus a need to know how the imaging experiment influences the contrast during longer acquisition schemes. Tissue contrast is computed at a time t_{sat} equivalent to the end of the saturation scheme. While the imaging sequence used in the previous chapter was less than a hundred millisecond and involved only one RF pulse, the acquisition scheme presented in 5.2.5.1 is at least ten times longer than this. As the imaging acquisition is not instantaneous, longitudinal relaxation can occur at the same time-scale than the readout, although sampling of the center of k-space at first, where the overall contrast of the image is the strongest, minimizes the competition between acquisition and relaxation. However relaxation occurring during the acquisition changes the recorded magnetization from shot to shot, and can have

effects on the quality of the image due to apodization of the k-space signal. The contrast available at the start of the imaging acquisition is evolving during the acquisition. This evolution can be quantified theoretically, but can be quite laborious and arduous to obtain analytically. For these reasons, a numerical simulation of the sequence provides a great tool to optimize the quality of the image, together with the contrast.
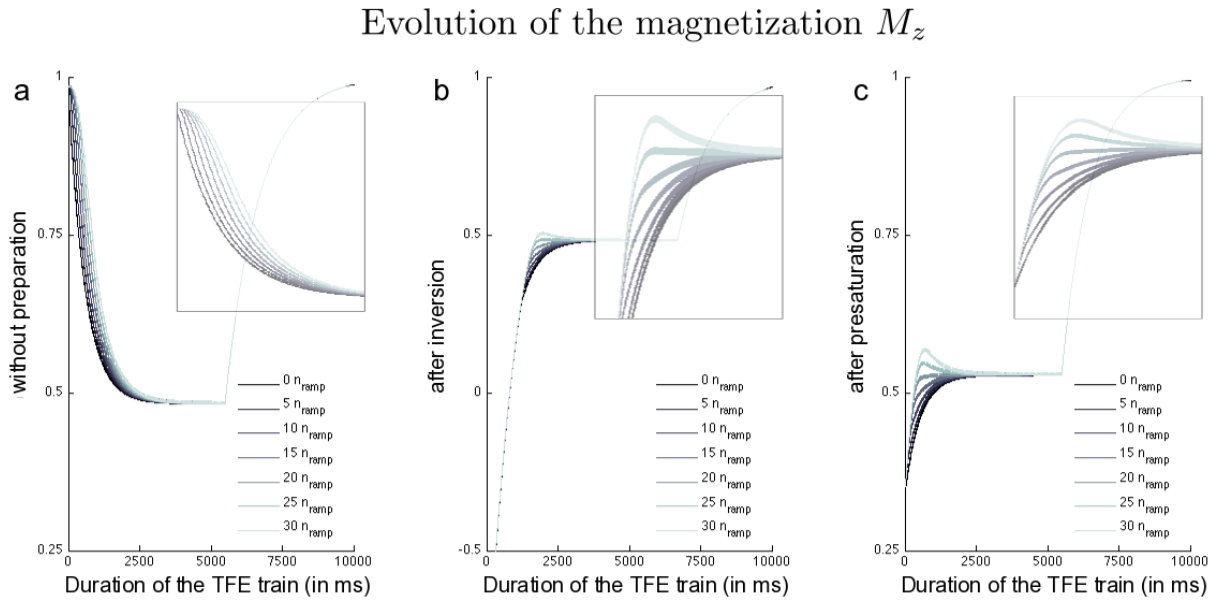

Figure 5.10: Effect of TFE startup ramp on the evolution of the magnetization during the TFE readout train. Fig. (a) represents the evolution of the magnetization without presaturation, while (b) represents magnetization following an inversion pulse and an inversion time of 1.2s. Fig. (c) represents the evolution of the magnetization during a TFE readout train after a saturation train. Inserts show zoomed versions of the graph, representing the startup ramp effect on the magnetization. Simulation is done for a T_1 of 1.2s, and an effective saturation of 60%, simulating the signal obtained from the white matter. Other parameters of the imaging sequence are a SSi of 10s, a TR of 11ms and a flip angle of $8°$.

Ramping of the RF pulses at the start of the TFE The acquisition of the image data during an MPRAGE (or MT-TFE) sequence is done in the approach to steady-state. This results in variation of the signal intensity as a function of spatial frequency (phase encoding step, as presented in fig. 5.10), thus applying a non-linear filter onto the k-space data. This can results in degradation of both the contrast and the image quality of the reconstructed image, but these effects can be reduced by shaping the evolution of the signal by variable flip angle [48], and apodization of the k-space via post-acquisition filtering. In the TFE sequence implemented on the Philips scanner, variations in k-

space signal are dealt with via both methods. As described already in the T_1 mapping chapter 3.2.1.2, a ramping of the excitation pulses at the start of the TFE acquisition reduces signal variations. A filter is applied on the k-space data before reconstruction, minimizing the variation of the signal during the different phase encoding periods.

As presented on fig. 5.10, the magnetization evolves non-linearly at the startup of the readout train, and is highly dependent on the imaging experiment (*i.e.* the available magnetization at the start of the acquisition). The ramp-up of the RF pulses is three time longer than $n_{ramp} \times TR$, with only the last two third of the RF pulses being used for the acquisition. To facilitate the visualization of the ramp on the magnetization M_z in fig. 5.10, all TFE trains start at the first RF pulse of the ramp. The variation of the signal at the start of the TFE readout (*i.e.* after $n_{ramp}TR$) can be minimized with 20 pulses in all the different cases, and is the default number set by Philips. While this ramping was modelled in 3.2.1 and is taken into account during the measurement of the relaxation time T_1, this ramping reduces substantially the contrast obtained in the final image after a saturation train. For this reason, a reduced number (n_{ramp}=5) of readout pulses were used prior to the start of the TFE train, producing a presaturation of 39% for n_{ramp}=5 compared to 46% for n_{ramp}=20. The rest of the readout was otherwise identical to the one presented in 3.2.2.1, with the k-space filled in a spiral fashion.

Contrast evolution with the TFE parameters Fig. 5.11 shows that measured MT effects are independent of the acquisition time increase of the TFE train for reasonable TFE train lengths (inferior to 600 pulses with a period of 11 ms). The available contrast for Magnetization Transfer Imaging is unchanged due to fixed Shot to shot interval (SSi). For the simulation, the longitudinal relaxation times were the following: $T_1^f = 1.2$s, $T_1^c = 1$s and $T_1^b = 1$s. Other imaging parameters are $TR = 11$ ms, SSi = 10 s and 5 start-up pulses. As the MTR is a ratio from two different images, it is necessary to observe the effects on both acquisitions (*i.e.* M_0 and M_{sat}). The simulation of the magnetization evolution during TFE acquisition trains of various durations is shown in fig. 5.11 a and b, the dotted lines showing the magnetization after saturation, and the continuous lines the magnetization without saturation (*i.e.* used to generate the image M_0). This simulation assumed that the exchange happened during the saturation only; a numerical simulation of both with and without exchange during the imaging sequence (not shown) proved that the exchange influences the magnetization recorded only very slightly. No variation was also obtained if the TR of the imaging sequence was increased (not
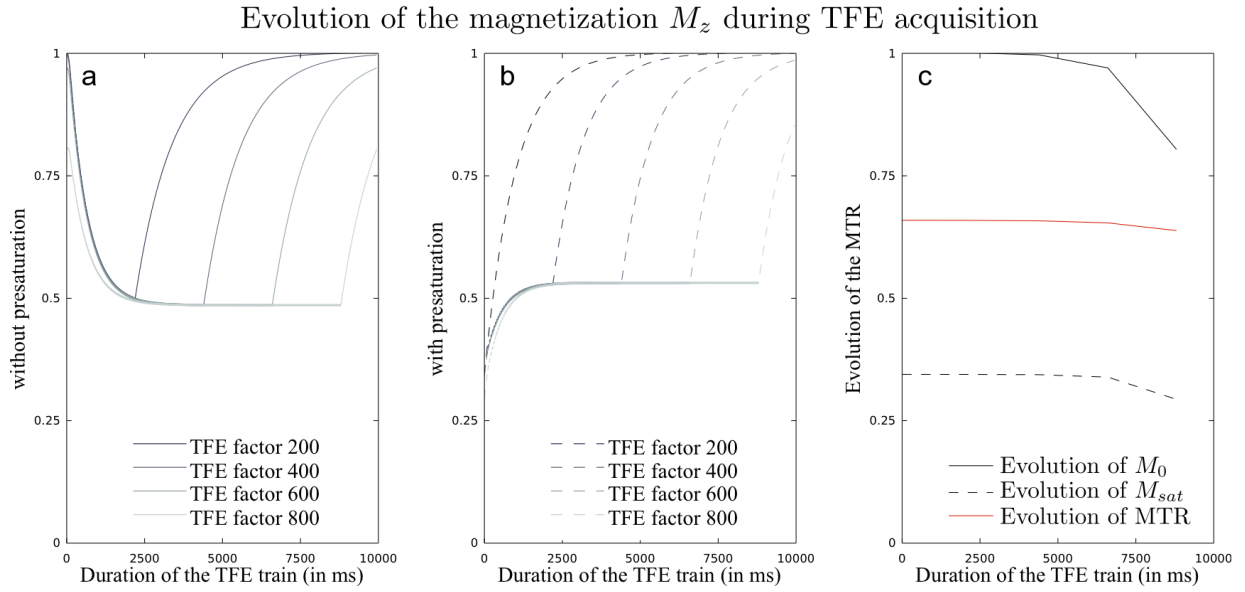
Figure 5.11: Effect of TFE duration on the available contrast for MTR. (a) Continuous lines represent the evolution of the magnetization without presaturation, while (b) represent the magnetization following a saturation. (c) The MTR does not change with TFE factor until it exceeds 600, allowing less than 4s for the magnetization to recover. Other parameters of the imaging sequence are a SSi of 10s, a TR of 11ms, a flip angle of 8° and a T_1 of 1.2s (the T_1 of the white matter at 7T).

shown). Therefore both the TR and TFE factor can be increased to obtain larger resolution/matrix size, without much change in the contrast of the final image. A reasonable delay time (the time between the end of one TFE train and the next saturation train) is however required for the longitudinal relaxation to come back close to equilibrium before the next saturation. If this time is set too small, the available magnetization at the next shot would be small, as visible with the case of a TFE factor of 900, leading to an artificial decrease in the measured signal as well as in the measured MTR.

While the simulation of the contrast alone can give important information for the optimization of the imaging sequence, other estimations such as measurement of the blurring via the Point Spread Function (PSF), the effect of noise on the final image, as well as the detectability performance, will benefit from the simulation of the whole image acquisition process, with the presence of encoding, readout and image reconstruction. This is the focus of the next section.

5.3.3 High resolution imaging with artefact minimization: a realistic simulator

The versatility of contrast obtained by MRI comes at the expense of operational simplicity: an imaging pulse sequence depends on optimizing an ever-increasing palette of possible sequence parameters to obtain the required type of contrast weighting in the image (*e.g.* in this case a MT-weighted image) and the desired image quality. As described in chapter 2, the process of forming an MR image involves applying a series of RF pulses of various amplitudes and shapes in concert with a series of time varying, spatial gradients of the static magnetic field along the three orthogonal axes. The purpose of this section is to simulate the MPRAGE sequence (in principle very similar to the MT-TFE sequence described earlier) since it exhibits a particularly complex relationship between the acquisition parameters and the Point Spread Function (PSF). The PSF is defined as the response of an imaging system to a single point source, and quantifies the blurring introduced by an imaging system. The PSF in MRI depends on the object, image acquisition technique and post-processing methods. While the PSF can be calculated analytically for any given imaging system, the complexity of the image formation in an MR scanner make the analytical solution difficult to obtain. It is possible to measure it directly on the scanner via a point or line source, but this result would only be valuable for a given set of relaxation times, and affected by noise. Measurements directly during the acquisition is possible *in vivo* [54], but requires a fast imaging technique as well as additional phase encoding gradients, and is highly susceptible to movement and flow. Simulating the acquisition of a small object (typically on the order of the voxel size) can be used to determine the sequence parameters that would optimize the sharpness of the PSF. It can also provide the PSF for arbitrary shape as well as more realistic 3D objects (such as a segmented brain). The following section presents an MR simulator [45] that can be used both as a validation tool for image processing algorithms, and as a sequence optimizer for high resolution, quantitative MRI.

5.3.3.1 Review of MR simulator

Since an MR scan is very expensive, and MR phantoms are of limited relevance, over the years a number of MR simulators have been developed to be used as learning tools, for sequence optimization

or for validation of image analysis methods. For instance, Hanson [26] described an educational simulator aimed at familiarizing students with the different scanning parameters and teaching them how to obtain different image contrasts. Mekle et al [39] used a simulator to optimize image quality whilst decreasing the acquisition time. Others ([5] and [15]) have used a simulator to increase the robustness of the acquisition process to artefacts from effects such as inhomogeneities of the main magnetic field, patient movement or blood flow. Finally, in the absence of *in vivo* ground truth and geometrically non trivial MR phantoms, simulators have been used to quantify the accuracy and robustness of image analysis algorithms (tissue classification, cortical thickness computation, *etc.*) to MR acquisition parameters and artefacts [33][61].

Simulation of the 3D MPRAGE sequence [47] has been used for quantitative MRI [77] and novel, acquisition based methods of image segmentation [51]. Although initially developed for the MPRAGE sequence, the same simulator could be used for a different sequence simply by definition of its pulse sequence and associated k-space trajectory (see [5]). The object to be imaged is modelled as a collection of isochromats. These consist of small imaginary volumes containing an ensemble of spins which resonate at the same frequency. In turn, each voxel contains a number of distinct isochromats with distinct resonance frequencies.

5.3.3.2 Description of a realistic simulator

The approach presented here estimates the magnetization vector of each isochromat throughout the MR pulse sequence. At each time step, the simulation takes into account the appropriate RF pulse and solves the Bloch equations. The MR signal in each voxel is then computed by vector summation of the signal of the isochromats it contains.

Let $M(r,t) = [M_x(r,t), M_y(r,t), M_z(r,t)]^T$ be the magnetization of an isochromat r at the time point t. Evolution of its magnetization is approximated by applying a series of operators, where each operator models the influence on the magnetization of the various components of a particular time step of the pulse sequence. It gives:

$$M(r, t + \delta t) = R_{grad}(t)R_{inh}(t)R_{relax}(t)R_{RF}(t)M(r,t) \qquad (5.3)$$

5.3. Modelling contrast and artefacts in MT experiment

$R_{grad}(t)$ is the operator corresponding to the application of gradient $G(t)$ where $\beta = \gamma \mathbf{r} G(t) \delta t$ relates $G(t)$ to the angle β around the z-axis, for each position. $R_{inh}(t)$ is the operator corresponding to B_0 field inhomogeneities where $\phi = \gamma \, \Delta B(r) \, \delta t$ relates the inhomogeneities $\Delta B(r)$ during the time δt to the angle ϕ around the z-axis. $R_{relax}(t)$ describes the magnetization relaxation and is most conveniently described by a 4D matrix acting on the magnetization vector with an additional term corresponding to the equilibrium magnetization $[M_x, M_y, M_z, M_0]$:

$$
R_{relax} = \begin{pmatrix} e^{\frac{-\Delta t}{T_2(\mathbf{r})}} & 0 & 0 & 0 \\ 0 & e^{\frac{-\Delta t}{T_2(\mathbf{r})}} & 0 & 0 \\ 0 & 0 & e^{\frac{-\Delta t}{T_1(\mathbf{r})}} & \left(1 - e^{\frac{-\Delta t}{T_1(\mathbf{r})}}\right) \\ 0 & 0 & 0 & 1 \end{pmatrix} \tag{5.4}
$$

$R_{RF}(t)$ is the operator describing the effect of an RF pulse tipping the magnetization by an angle α about the x-axis, applied instantaneously at time t. Due to B_1 field inhomogeneities, the tip angle α generally depends on the position of the isochromat, and could therefore be controlled by an a priori RF map, if available. Note that the relaxation times (T_1 and T_2) also depend on the isochromat position and can be given by a priori T_1 and T_2 maps. More details about the theory can be found in [6, 72].

5.3.3.3   Parallel implementation and versatility

The virtual object to be imaged (e.g. a synthetic shape, a brain or any other part of the body) has to be discretized into a number of isochromats, where each isochromat is defined by a proton density, a set of relaxation times and a frequency offset. T_1, T_2 and proton density maps can be imported directly. Each isochromat is positioned at the center of the voxel, representing an ensemble of spins distributed equally inside the pixel (a random distribution of the position of each isochromat being also possible). A segmented tissue map can also be provided, with each tissue being assigned appropriate values of T_1, T_2 and proton density.

At the initialisation stage, the user can specify the different parameters of the sequence, such as the sequence timings and the size of the output image. The coherence of the parameters, such as

the timing parameters or the resolution, is verified before creating the entities of the pulse sequence. Isochromats are placed in a matrix according to the input maps and their frequency offset are drawn from a Lorentzian distribution to model local field inhomogeneity. Field maps of inhomogeneities in the static and RF field can be introduced at this stage to modulate the effect of R_{RF} and R_{inh}. Any relevant scanner preparation steps, such as driving the magnetization to a steady state, are taken into account by applying the appropriate combination of R_{RF} and R_{relax} to the magnetization on an isochromat by isochromat basis. Then the acquisition can start. For each isochromat independently, the magnetization is obtained time point by time point by applying the above operators according to the pulse sequence. Rather than simulating a random phase encoding gradient order, the k-space phase encoding scheme can be read directly from our scanner software (Philips .list file). Thus, each point in time during the acquisition corresponds to a different point in k-space and the transverse magnetization (M_x and M_y) from all isochromats can be summed together to give the complex MR signal in k-space. This simulation of the k-space MRI data lends itself to data parallelism, as each isochromat can be simulated separately. Once all the isochromats have been processed, k-space is reconstructed simply by summing the contribution of all the different isochromats. In practice, the MR signal is contaminated by thermal noise so complex white noise with a specified variance is added to the complex data, before performing any post-processing. The signal can be filtered and/or zero-padded in k-space, as is generally performed on an MRI scanner to minimize effects such as Gibbs ringing. A fast Fourier Transform based on the FFTW algorithm is computed to create the simulated image. Additionally, the k-space data are saved to allow the effects of different noise distributions and processing algorithms to be analysed without having to simulate the whole acquisition again.

5.3.3.4 Validation of simulation: assessment of the PSF

The validity of the simulator was tested via different experiments, including simulation of objects with sharp, unrealistic shapes as well as realistic cortex shape obtained from segmented brain. The sequence implemented on the simulator is based on the TFE sequence, with evaluation of first inversion recovery imaging (MPRAGE), as well as saturation transfer (MT-TFE). Implementation of the code to run on a array of processors gave the possibility to simulate realistic 3D brain images in a reasonable time. The following paragraphs review the different experiments performed, together with

the evaluation of the designed sequence in specific conditions.

Ellipsoid simulation The simulation of a simple ellipsoid (radius 15 mm in plane and 30 mm in the z-direction) containing only one type of tissue was performed. The sequence implemented was a simple TFE FFE protocol, with a TR of 10 ms, a flip angle of $8°$ and a T_1 of 1.2 s. The initial volume was 1 $a.u$, while the reconstructed volume was 1.003 $a.u$ (measured via histogram analysis, with a threshold of the lower part of the histogram at 1% of the maximum signal, removing contribution of the noise). Increasing the reconstructed matrix size via zero-padding (by a factor of 1.5 and 2) actually increased the error (respectively 1.004 $a.u$ and 1.008 $a.u$).
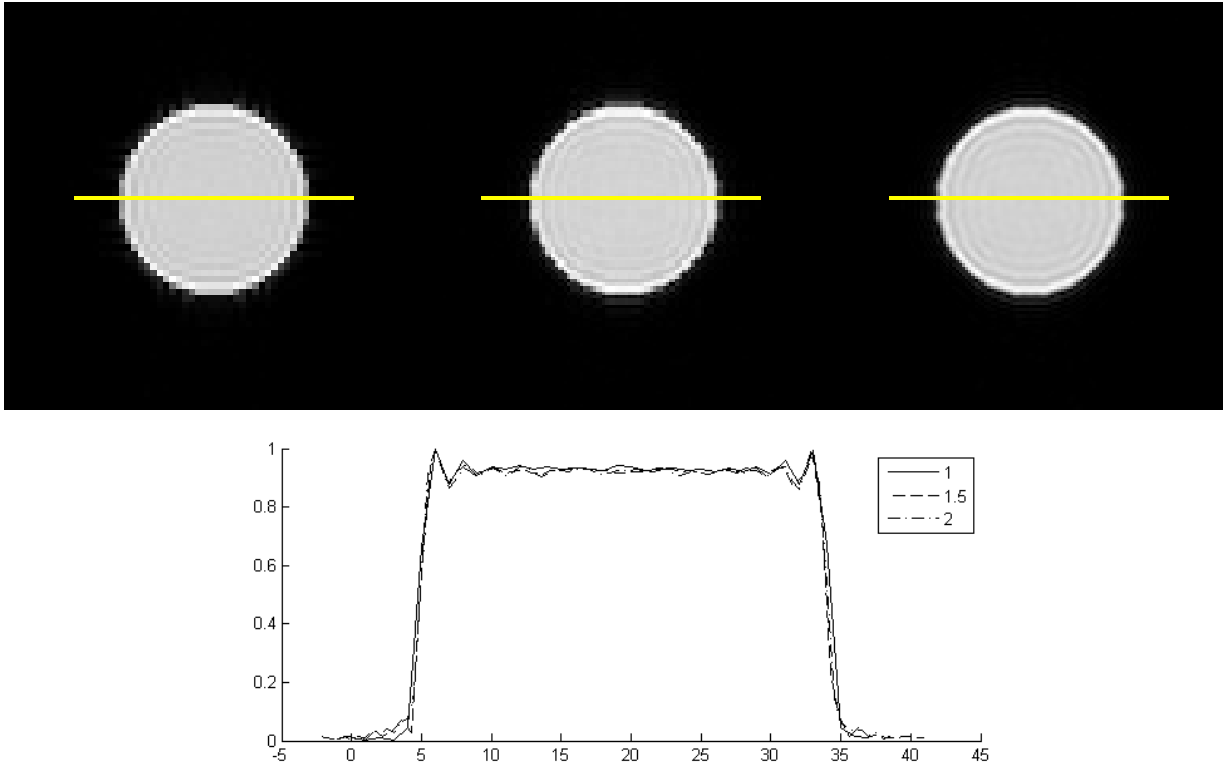

Figure 5.12: Reconstructed images after simulation of an ellipsoid with a matrix size increase of factor 1, 1.5 and 2. Profiles corresponding to the yellow line are represented in the bottom row.

From the reconstructed image, characteristic Gibbs ringing artefacts can be seen on 5.12 due to the sharpness of the transition at the edge of the sphere. The acquisition process generates a sampled version of the object and encodes it in the k-space (or Fourier domain). The most common sampling scheme used in MRI nowadays is the rectilinear k-space sampling, where the sampling frequency in the direction i (Δk_i) is related to the dimension of the image function (W_i, *i.e.* the field of view in the

i direction) by:

$$\Delta k_i = \frac{1}{W_i} \qquad (5.5)$$

The Shannon theorem states that a band-limited function can be reconstructed perfectly from its sampled values taken uniformly at an interval not exceeding the reciprocal of twice the signal bandwidth. For smooth transitions in the image, *i.e.* with finite frequency, the image can be considered as band-limited. However, sharp transitions, such as the one between the skull and the air, or here the edge of the sphere, are not support-limited and result in a loss of information in the frequency domain. The reconstruction is thus incomplete and the Gibbs phenomenon manifests itself in the reconstructed image as spurious ringing around the sharp edges. While the intensity of the ringing is independent of the number of data points used, the frequency of the ringing increases with the number of data points used in the reconstruction, to a point where the ringing covers a too short distance to be noticeable. An alternative to reduce the ringing artefacts (as the reconstructed matrix cannot generally be extended at will) is to filter the measured data before the reconstruction algorithm is applied. Specific filters used by Philips were implemented, with window function similar to the popular Hamming function. The windowing approach can suppress effectively the Gibbs ringing, but at the expense of degrading the resolution. Zero-padding of the signal before reconstruction does not reduce the ringing artefact amplitude, as shown in fig. 5.12. However it does improve the apparent image quality due to the increase of pixel and the reduction of sharp edges. It is for this reason that zero-padding can be used in clinical settings, as this can improve the apparent spatial resolution [16]. Moreover this is constantly used in MRI in order to extend the data length to the nearest power of two, as this accelerates considerably the reconstruction time by Fast Fourier Transform.

Realistic phantoms simulation   To validate the simulator implementation, a comparison between acquired images and simulated ones was performed with the MPRAGE sequence. In fact, the encoding order of the k-space has a strong influence on the evolution of the magnetization during the acquisition. The Point Spread Function (PSF) is specific to the encoding scheme used, the sequence used as well as the NMR properties of the imaged volume. Comparison between acquisition and sim-

ulation of sharp edges coming from a quadrant phantom is shown in fig. 5.13. The imaging sequence is a 3D MPRAGE sequence, with a flip angle of $8°$, a TR of 7 ms and a TFE factor of 256.

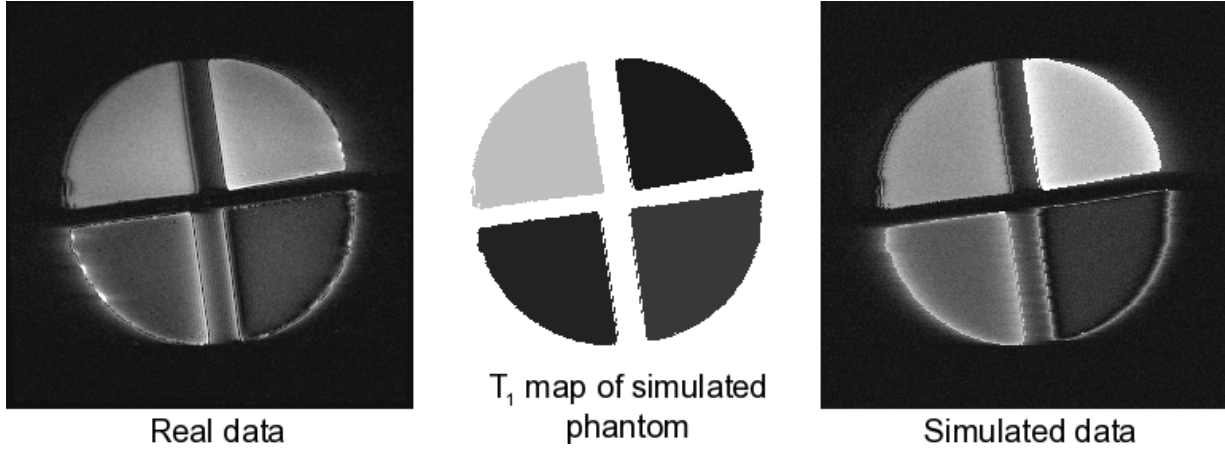T$_1$ map of simulated
phantom

Real data   Simulated data

Figure 5.13: Real image (left) of a phantom acquired with linear phase encoded MPRAGE, T_1 map (middle) used as input to the simulator and simulated image (right). The inversion time was set to 300ms, the image being acquired at 3T.

Each quadrant contained a mix of agar gel and gadolinium, producing specific T_1 and T_2 combination. The effect of the phase encoding scheme was examined on the quadrant phantom, and successfully reproduced with the simulator. Fig. 5.13 shows an example of the linear encoding scheme (acquisition of the k-space via a linear profile, *i.e.* -$k$max ...,-2,-1,0,+1,+2,...,+$k$max), via both the MRI acquisition and the simulator. Close similarities can be observed, especially at the edges of the quadrants where the profile order determines the fidelity of the image.

Brain simulation   After acquiring a series of MPRAGE images with different T_1-weighting of a volunteer's brain, the one closest to a standard T_1-weighted scan was used for tissue segmentation. This served to create tissue maps where the appropriate relaxation times and proton density were assigned to each isochromat. Standard T_1-weighted MPRAGE images were simulated for different inversion time and with presence of an inhomogeneous B_1 field.

Visual inspection of fig. 5.14 shows a promising similarity between the simulated and original images, particularly at the border between the CSF and the WM in fig. 5.14 b and 5.14 e, where the partial volume effect is clearly visible in both zoomed inserts. The 'hotspot' effect can also be simulated by introducing a B_1 map (fig. 5.14 c) in the simulation. This creates a strong inhomogeneity
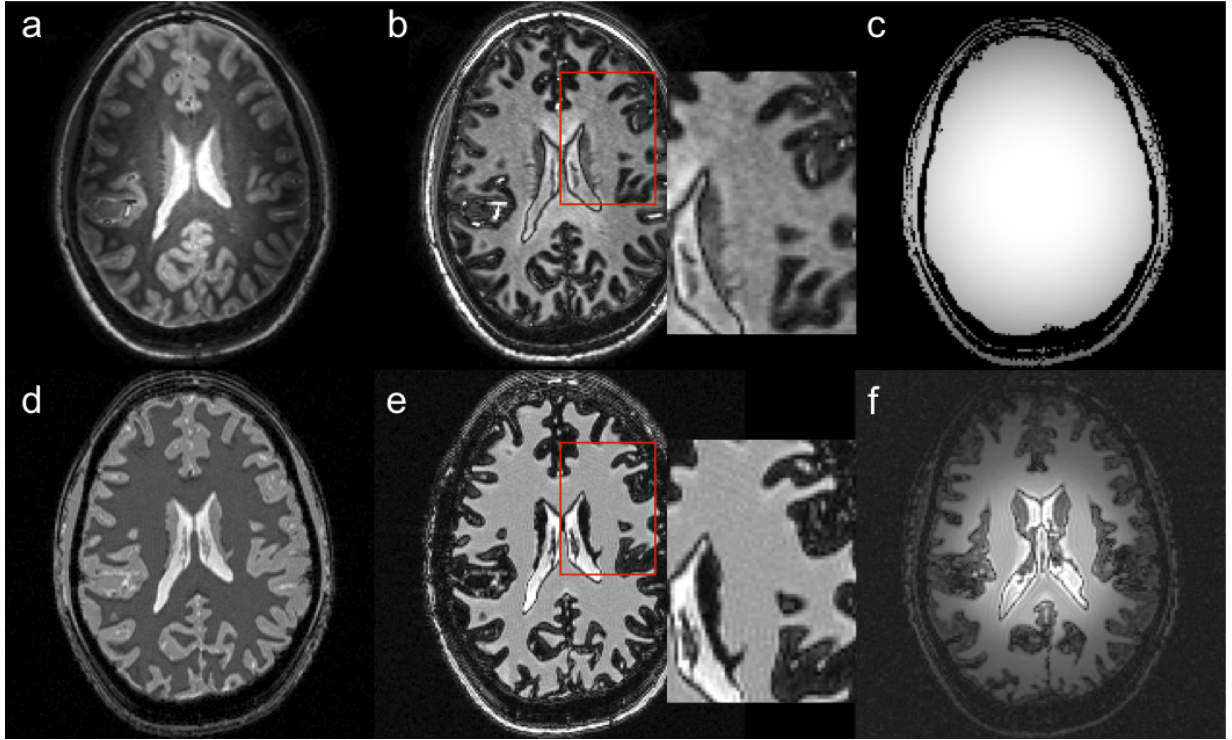
170

Figure 5.14: MPRAGE acquisitions (a and b) and simulations (d and e): 1 mm isotropic with 300 ms inversion time (left); 1 mm isotropic with 850 ms inversion time: the grey and white matter signals are inverted, leading to lower signal in partial volumed pixels (inserts of b and e); simulated B_1 map (c) used as B_1 inhomogeneity input for the simulation of the corresponding MPRAGE image (f) with added noise.

in contrast (as presented in fig. 5.14f) between the centre of the brain (where the flip angle is correct) and the cortical areas (with a flip angle of approximately 70% of the nominal value).

Sophisticated sphere   With the simulations showing close similarities to artefacts seen in reality, more specific problems can be addressed via the simulator, as for example, the detection of small objects. This is especially relevant for the MT-TFE sequence, since its PSF has not been optimized, contrary to the more common MPRAGE sequence.

For the MT-TFE sequence, results from previous simulations presented in 5.3.1 are used to set the magnetization at the start of the imaging part. It is assumed that a train of 20 saturation pulses applied at an offset frequency of -1050Hz and with a bandwidth of 200Hz was used during the saturation part. The imaging part is then composed of a train of 256 FFE readouts, with a flip angle of 8° and a TR of 11 ms. The reconstructed matrix is 64 pixels in the three directions, while the

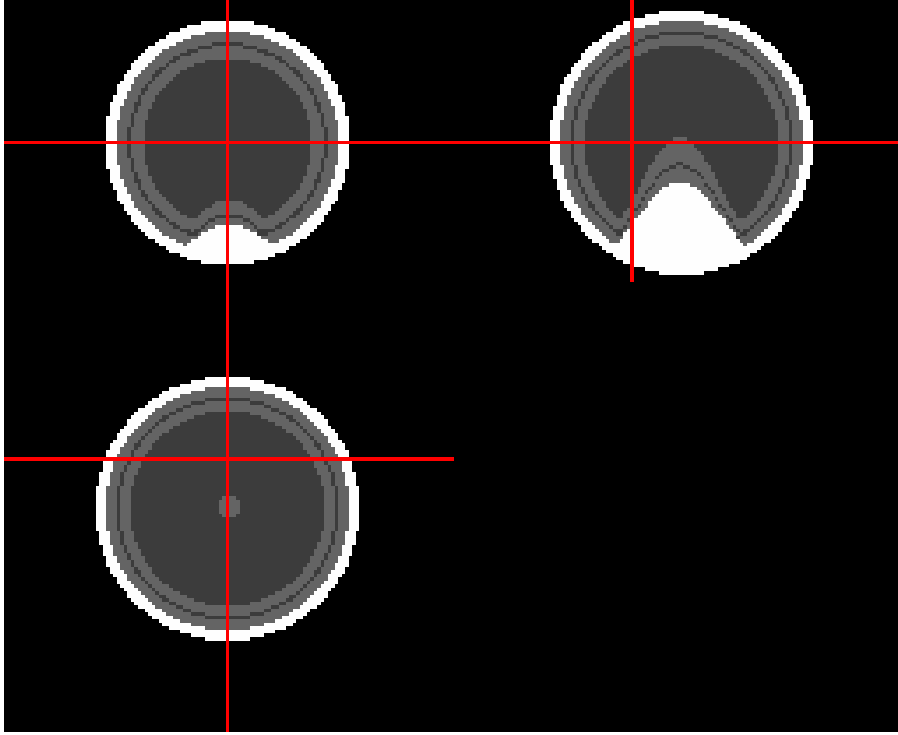## 5.3. Modelling contrast and artefacts in MT experiment

Figure 5.15: T_1 map used as an input for the MTR simulation of the sophisticated sphere, with the white pixels representing the CSF, the light grey the grey matter and the dark grey the white matter.

original maps were double the size in the three directions. As for the MPRAGE sequence, a complex encoding scheme was used, as presented in 3.2.2.1. The phantom used is a sphere with additional features inside, as presented in 5.15. A stria of white matter is introduced inside the grey matter layer, with a width of one voxel (corresponding to half-a-voxel in the reconstructed image).

Detecting the stria of Gennari, a small myelinated region enclosed inside the cortical layer, depends on the exact imaging sequence used, as the stria is only 0.3 mm thick, *i.e.* of the order of the lowest in-plane resolution possible at the moment on the 7T scanner for human applications. It has been showed that this band can be detected in vivo via MRI [11, 3, 7], but the proximity of the edge of the brain can also produce a Gibbs artefact of this kind in the grey matter, as explained in [73].

For this purpose, additional layers and features were added in the phantom shown in fig. 5.15, with for example a 'sulcus-like' shape as well as a line (stria) with white matter NMR properties positioned inside the grey matter layer. To quantify the actual detection possibility, both phantom with and without a stria inside the cortex layer were simulated, with the stria having a width corresponding to half a reconstructed image voxel and are represented in fig. 5.17. While the stria is not easily

detectable in the saturated image (due to the Gibbs artefact producing a destructive interference at the same location), the MTR maps show a clear difference between the two phantoms. Detectability of the stria was independent of the orientation, and could be seen from any angle inside the grey matter layer of the sphere. Profiles analysis shown in fig. 5.17 contains two peaks in the case of the phantom with stria (as presented by the red arrows), while for the case of the phantom without the stria, those peaks are non-existent. However other peaks can be seen in both profiles and are created by the PSF
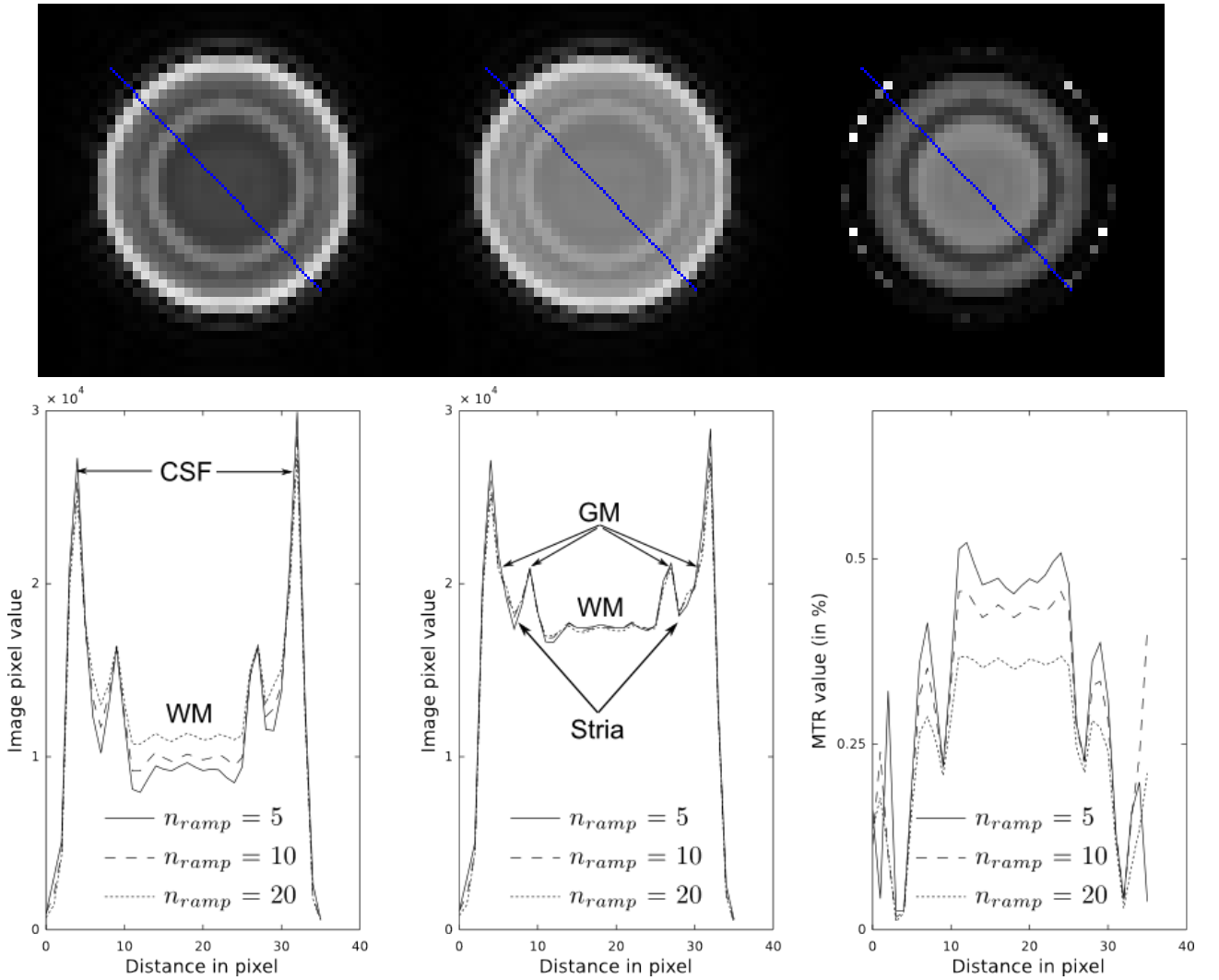

Figure 5.16: Images in the top row were obtained with saturation (M_{sat} on the left) and without saturation (M_0 in the middle), together with the MTR map (on the right) obtained via the simulator for a number of pulses n_{ramp} = 5. The bottom row represents the corresponding profiles (M_{sat} on the left, M_0 in the middle and MTR on the right), obtained at the level of the blue line. The stria is visible on the three images (and profiles) but creates an inhomogeneous pattern in the MTR maps at the boundary between white matter and grey matter (also shown in fig. 5.17).
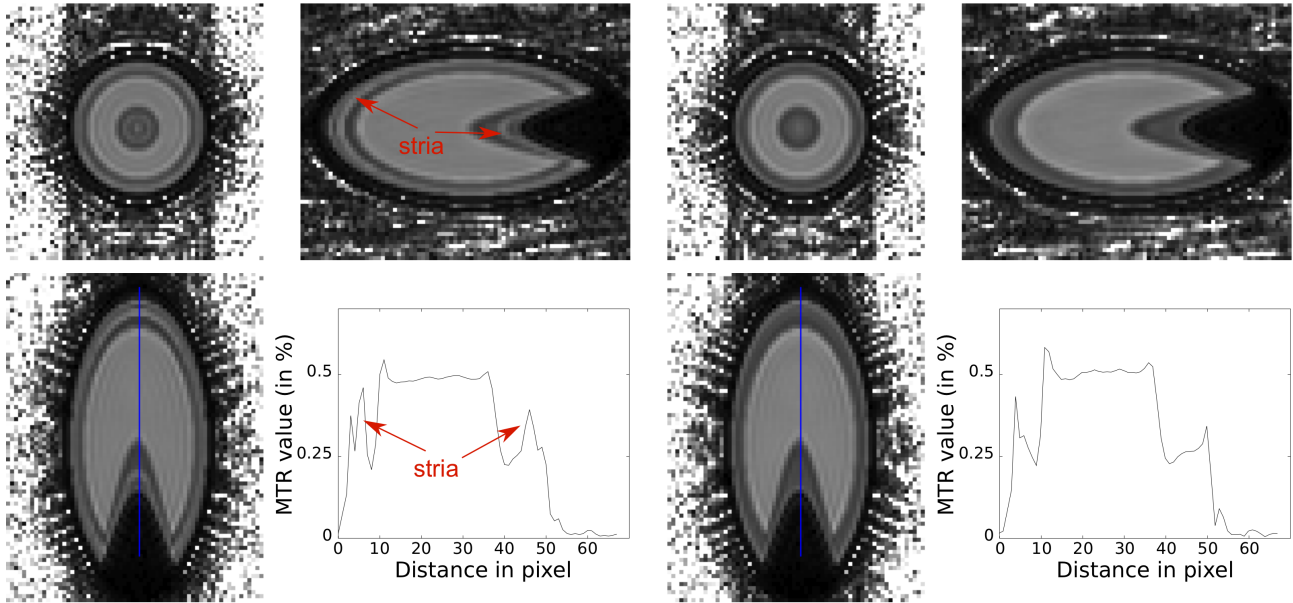
Figure 5.17: 3D MTR maps simulated by the acquisition of a ′stria phantom′, with the three orthogonal views presented as well as profiles drawn from the blue lines. The lefts images were simulated with the stria present in the phantom, while the right ones are without the stria (the grey matter is surrounding the white matter, with a CSF ring present in the outside). Acquisition parameters are a flip angle of 8°, a TR of 11ms, a TFE factor of 64 and a SSi of 10s.

of the imaging sequence, not sharp enough and thus creating partial volume effects, for example at the edge of the grey matter.

5.3.3.5 MTR map simulation

The same maps were used to produce realistic MT-weighted brain images (both without and with saturation). Due to the high computational cost of the simulation, the data parallelism was performed on the High Performance Computing facility present at the University of Nottingham (offering a total of over 2400 compute cores). A number of isochromats corresponding to the volume of a slice necessitated around 10 hours on a single core. Performing the simulation of a complete brain could thus be performed in a day on the supercomputer, instead of several weeks on a normal computer. The amount of saturation was not simulated during the imaging part, but obtained beforehand from the simulations of the three pool model performed for each tissue separately. Only the initial magnetization was obtained this way, the magnetization being only driven by RF pulses and relaxation in the rest of the acquisition (assuming no influence of exchange during imaging as previously shown in

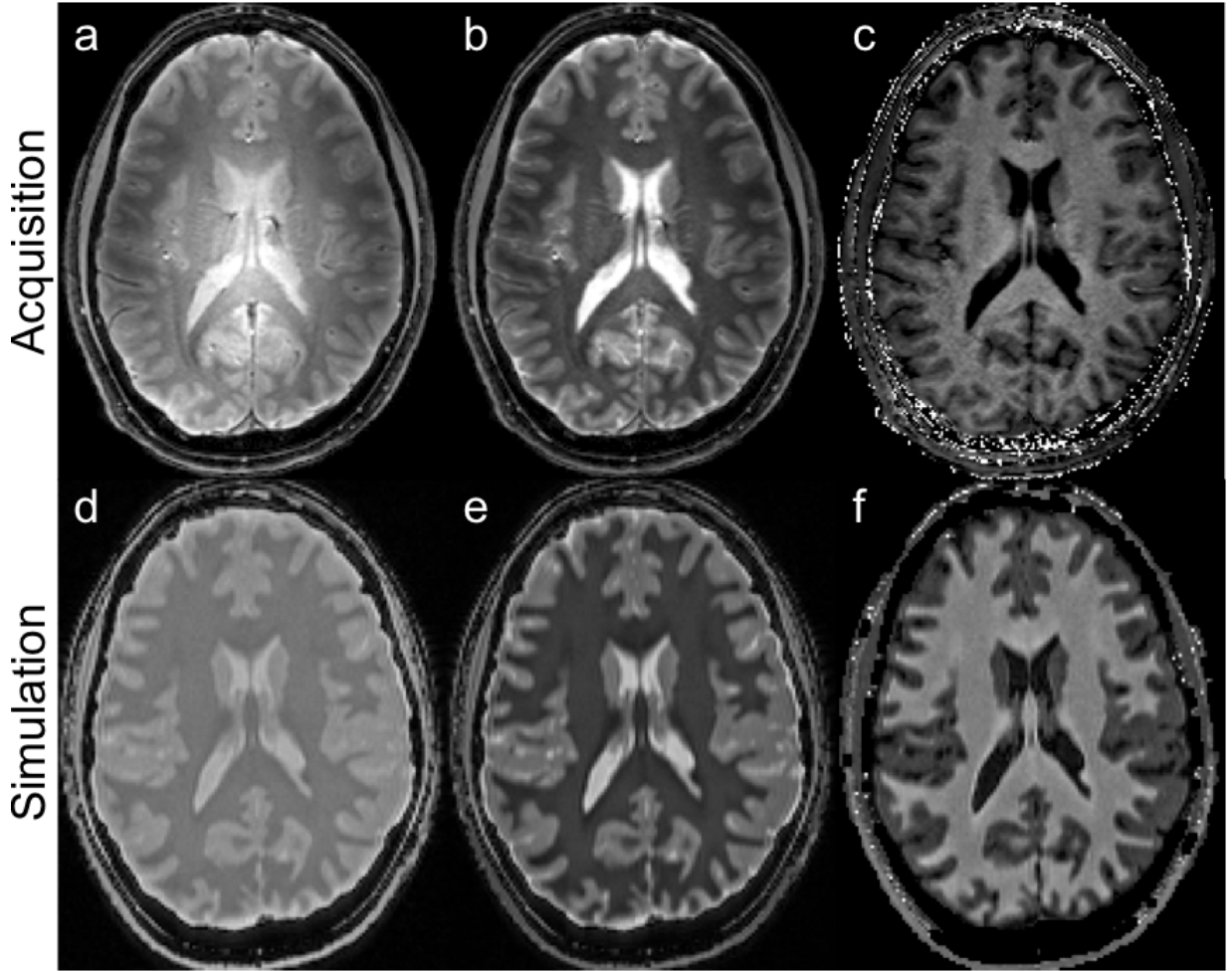## 5.3. Modelling contrast and artefacts in MT experiment

5.3.1).

Figure 5.18: Images in the top row are the acquired images (a) M_0 and (b) M_{sat}, together with (c) the MTR map. The bottom row represent the same images (d: M_0, e: M_{sat} and f: MTR map), but obtained via the simulator, with an added noise corresponding to a SNR of 140 in the raw images, and a constant value of MT for the white matter and the grey matter.

Differentiation between the WM and the GM is clearly visible on fig. 5.18, providing a good similarity with the acquired images. Delineation of small cortex features is possible, as well as visualization of small CSF volume at the interface with the GM, particularly at the outer surface of the brain. Additionally, features such as the cortical U-fibers or part of the corpus callosum closed to the ventricles appears brighter on the MTR maps on both the acquired images and the simulated ones. As a constant white matter MT was simulated inside all the brain, this effect could not be due to anatomical variation but would rather be an acquisition artefact. This effect is in fact due to the PSF of the MT-TFE sequence, which is different for the saturated and the non-saturated sequence. Close

to sharp edges, the ratio between the two gives a wrong value which can be misleading for clinical use. Reducing this artefact is important, and may be possible by using a more complex ramp at the startup of the TFE train, as described in [48], with possible validation via the simulator.

5.4 High resolution MT Imaging *in vivo*

As both the simulation and the first *in vivo* results of chapter 4 suggest, MTR maps at sub-millimetric resolution can be acquired at 7T. This section focuses on the actual resolution achievable, together with the detection sensitivity of the sequence, via evaluation of the Point Spread Function compared to the simulations, together with detection of the Stria of Gennari via *in vivo* scanning experiments as well as first clinical applications of the MTR sequence.

5.4.1 APT and MT asymmetry imaging

As described in 4.4.2, asymmetry of the MT effects can be seen on the z-spectra. This asymmetry is greatly enhanced (+50%) at 7T compared to 3T when looking at the resonance frequency of the amides protons in proteins at +3.5ppm from water (Amide Proton Transfer, APT imaging), and has proved useful in imaging tumours [82, 81].

APT imaging relies on the measurement of the exchange/transfer of magnetization between the amide protons of intracellular mobile proteins and peptides with the surrounding water protons. To normalize the measured effect (and subsequently remove the direct effect and the conventional MT effect), another measurement is done on the opposite side of the spectra, *i.e.* at -3.5ppm. APT has been shown to be sensitive to pH change [84, 29], as the quantity of available ions (H^+ and OH^-) can influence the transfer of protons from one pool to the other. Assuming that the main magnetic field is homogeneous and that the conventional magnetization transfer is symmetric to the water resonance frequency (still a matter of debate), considering as well that the direct effect due to the saturation of the water is symmetric, the APT ratio reflects the amide content in tissues as well as its rate of exchange with the surrounding water.

Fig. 5.19 and 5.8 show very high resolution MT images acquired of the human brain *in vivo*. A
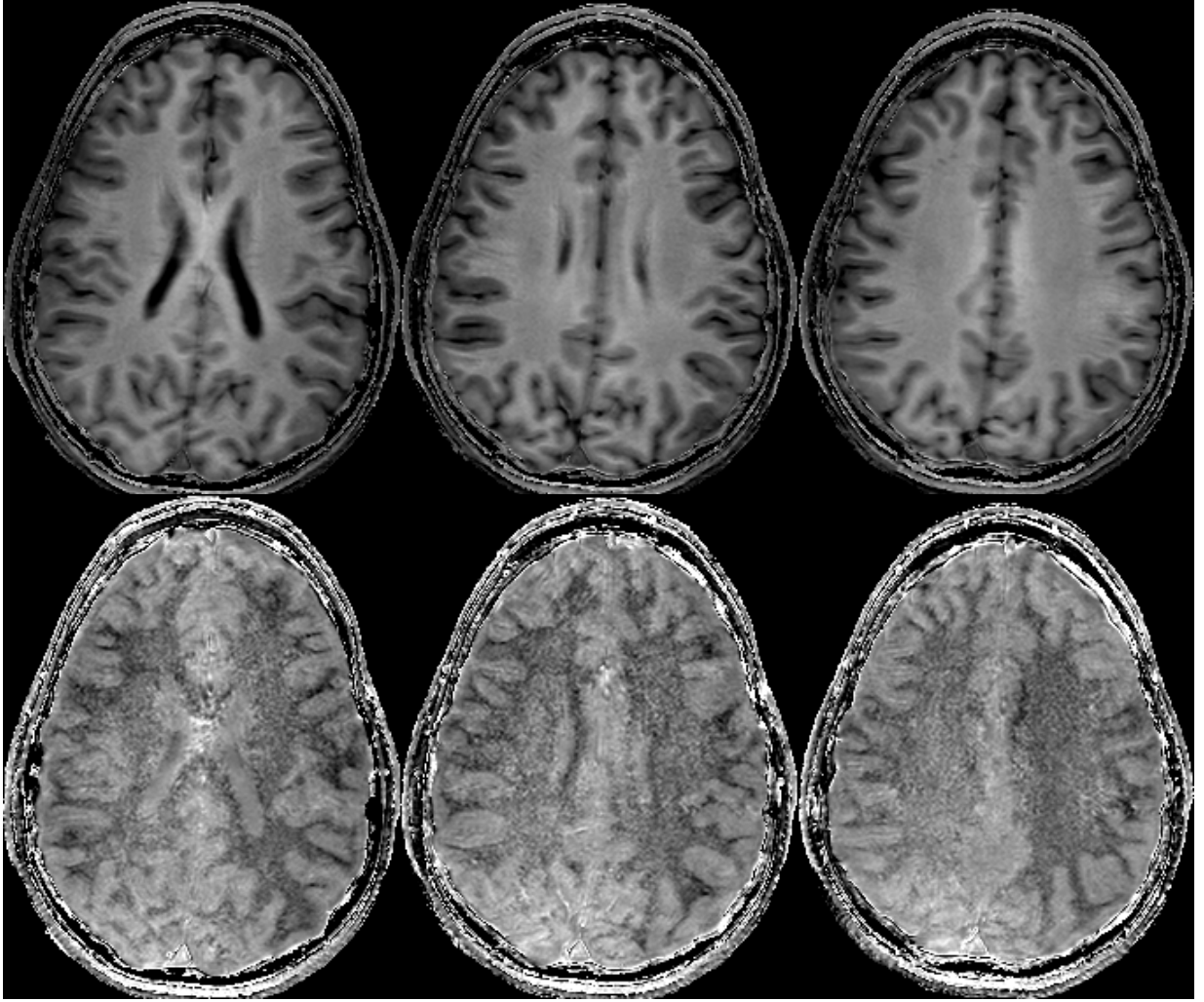
Figure 5.19: High resolution MT data acquired at 7T. Resolution of 0.7x0.7x1 mm^3, NSA = 2, 10 slices, T_{acq}= 5:50 min. First row represents MTR maps while the second row represent the MT_{asym} maps, both of an healthy volunteer.

good contrast to noise ratio is achieved in both MTR and APT maps by making the Number of Signal Average (NSA) equal to 2 (images in fig. 5.19). The differentiation between the cortical grey matter and the surrounding white matter is greatly enhanced, and shows clearly the difference of internal structure of the tissues due to the macromolecular compound, especially the larger amount of myelin of the white matter. Those high resolution images show also some regional difference inside the white matter tracts, especially in the corpus callosum, but also in the region of the corticospinal tracts. More specific images could reveal these differentiation already observed at lower field strengths [80, 62] as well as with another modality [35]. Simulation of the Z-spectrum with different amount of myelin and/or amides based on histological studies could facilitate the optimization of the contrast inside

the white matter, as well as inside the deep grey nuclei where the fibre tracts traverse the caudate nuclei for example. A first try on the deep nuclei of a post mortem brain also showed a possible differentiation of the different nucleus inside the thalamus thanks to the high resolution achieved via the possibility of averaging several images. Further investigation could help to optimize this modality in order to correlate better the source of contrast in certain regions via multi-modality studies and/or quantification.

5.4.2   High resolution: *in vivo* results

Following the encouraging first results obtained on healthy subjects, more specific problems are addressed, such as the achievable detectability of the sequence, both in the cortex of healthy subjects and in the cortex of Multiple Sclerosis patients.

5.4.2.1   Detection of the Stria of Gennari with MTR maps

Myelination is known to vary across the thickness of the cortex, for instance the calcarine sulcus can be distinguished by the presence of the stria of Gennari, a dense band of myelination within the cortical grey matter of 0.3 mm thickness. Detection of contrast in the grey matter has previously been achieved using high resolution MRI [11] for instance using MPRAGE [10] and Turbo Spin Echo [3] optimized for grey/white matter contrast. Magnetization Transfer Imaging is generally used to study variations in myelination in the white matter (WM) but provides a method for potentially quantifying variations in myelination across the cortex. However to provide adequate sensitivity in high spatial resolution MT imaging, the data must be acquired at ultrahigh field (*e.g.* 7T). Pulsed train magnetization transfer is used here (and presented in [46]) in conjunction with Turbo Field Echo at 7T to quantify changes in MTR across the cortical layer in vivo in humans.

To increase SNR in the quantitative data, data were averaged along the stria for quantitative analysis. Curves of $\approx$ 1.5cm were drawn parallel to the cortex surface on the M_0 images and applied to the M_{sat} images, averaged and then used to calculate an MTR for the curve. This was repeated with the curve moved progressively from the pial surface to the WM surface to give a spatially averaged profile across the cortex. Profiles were spatially normalized before averaging across subjects (0 being
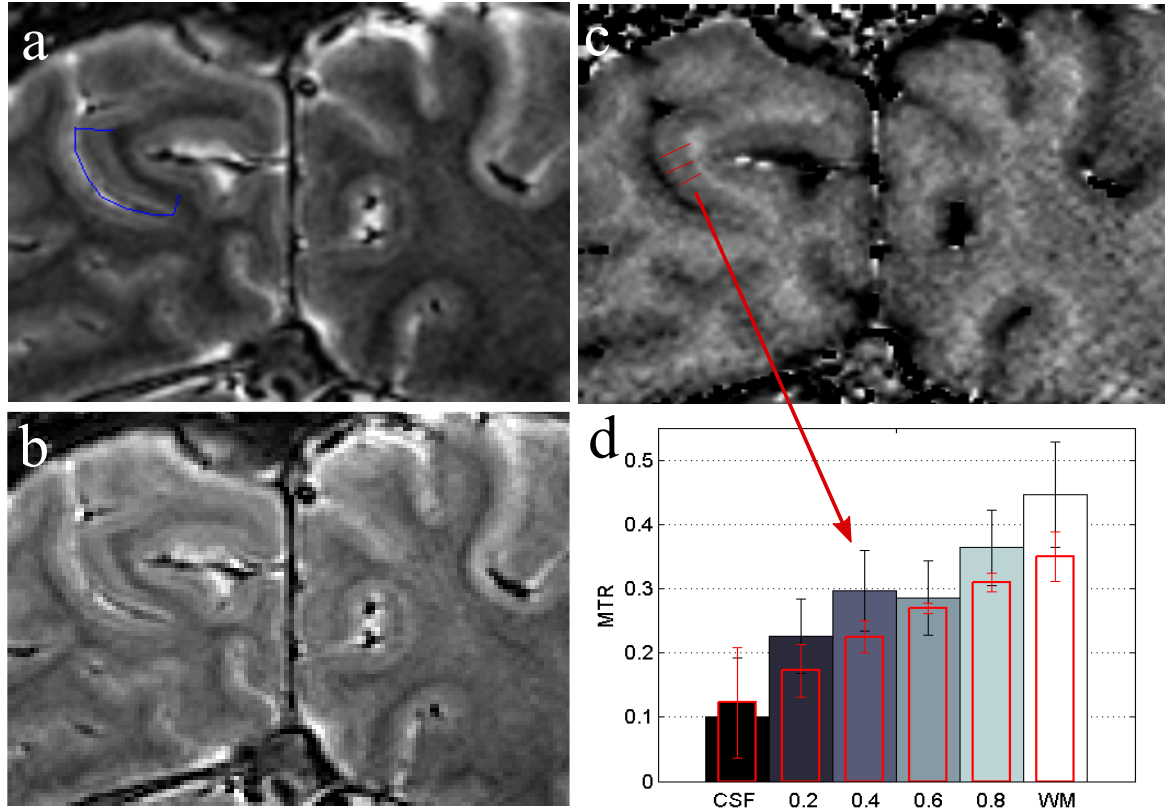
Figure 5.20: (a) M_{sat} and (b) M_0 image of part of the visual cortex of an healthy volunteer, together with (c) the corresponding MTR maps formed from MT-TFE images acquired at 7T. Image resolution is 0.4x0.4x1mm^3. On (c) the red lines and arrows are showing an example of where lines were drawn parallel to the cortex on a and b. The measured lines were spatially normalised and average across subjects to give an overall profile of the cortex (d), both with (black contour) and without (red contour) visible stria. A peak and dip in the profile can be seen corresponding to the stria (red arrow) not visible in the red bars. All results from [46]

the CSF and 1 the WM surface) and showed a small peak and dip in the profile, as shown on fig. 5.20d

. Variations in MTR can thus be detected in GM and probably correspond to intracortical variations in myelination. These results are confirmed by the possibility to detect a small layer of white matter inside the grey matter, despite the rather weak sharpness of the PSF of the TFE sequence, as presented in 5.3.3.4.

5.4.2.2   Preliminary results from MS patients: cortical lesions evaluation

Multiple Sclerosis (MS) is a disease affecting the myelin principally situated in the Central Nervous System, mainly inside the white matter (WM) and the spinal cord. However, grey matter (GM)
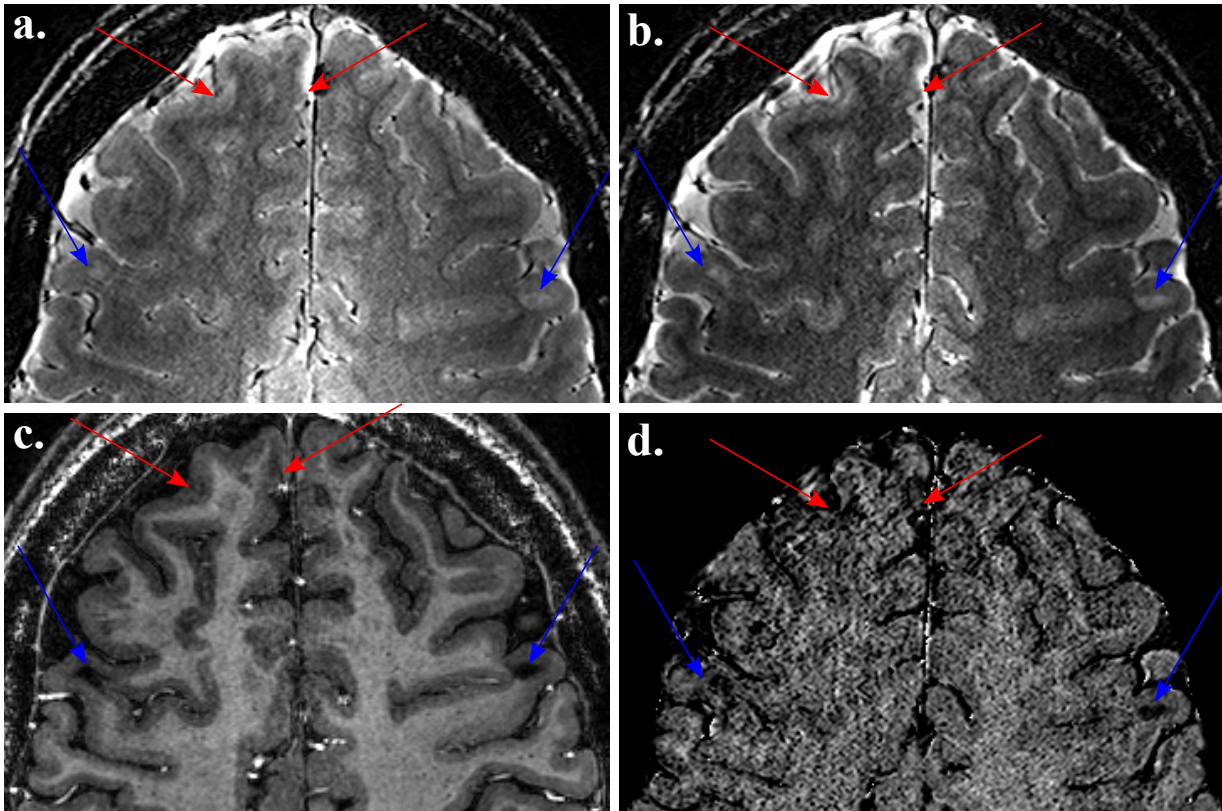
Figure 5.21: The MPRAGE image (c) shown some abnormalities on the cortex of the patient, but not easily detectable. The MT-TFE images with M_0 (a) and M_{sat} (b) versions, with the corresponding MTR map (d). Areas of the cortex which appears hyper-intense on both images are likely to be intra-cortical lesions. Red arrows shows cortical lesions, while blue arrow show mixed WM/GM lesions. All data from [46]

also possessed myelin in a fewer extent. The striking visibility of WM lesions, both pathologically and on MR images, eclipsed the importance of GM demyelination. MS research focused primarily on WM lesions load, but the later was found to be only moderately correlated with clinical disability [20]. Recent pathological evidence suggests that the extent of GM demyelination exceeds that of WM demyelination [23]. Visualization of the GM lesions is poor with conventional MR imaging techniques, but classification of the different types of lesions has been reported via Post-Mortem examination, mainly via histology [32, 8]. However, magnetization transfer (MT) imaging, which is already a useful maker of WM demyelination in MS, has recently been applied to the study of GM changes in MS. Patients with early relapsing remitting multiple sclerosis (RRMS) have been showing to have MT abnormalities in the GM, with MT histograms of the GM predicting disability [13]. High resolution MT imaging could give information about the diffusivity of the underlying pathology. It

could be possible to detect small intra-cortical lesions, with the most common observed *ex-vivo* being due to subpial demyelination, affecting the outer layers of the cerebral cortex.

Different type of lesions could be seen, both in the M_{sat} and M_0 images. The detection of intra-cortical lesions, as well as mixed white matter/ grey matter lesions was possible in the MT images, as well as in the MTR maps. However a better detection is possible if both images are analysed together (the MTR map providing contrast and the MPRAGE or base MT-TFE images providing delineation of the cortex). Using the classification system by Bø *et al.* [8], detection of lesions of class I, II and IV could be achieved *in vivo* in the MT images. The lesions had very high contrast on the MTR maps (5.21d) despite the fact that the contrast to noise ratio (CNR) of the MTR maps is low due to the ratio calculation. Quantitative comparison of the CNR of the isotropic and high in-plane resolution images was computed using the propagation of errors from the raw MT images [9]. The isotropic resolution images gave slightly better white-grey matter CNR than the high-res ones but with larger inter-subject standard deviation (0.16±0.10 versus 0.14±0.07). However lesions could be detected more easily in the high-res images due to a higher CNR between the grey matter and the lesions (0.12±0.07 compared to 0.08±0.06), probably due to reduced partial volume effects.

5.4.3 Amide proton transfer at high resolution

Combining the development and results presented in the previous chapter (section 4.4.2) as well as in this chapter (section 5.2.3 and 5.2.5.2), the possibility to image the amide proton transfer at high resolution is possible, even with (reasonable) inhomogeneous field. This can be used to map the amide quantity in the healthy brain as well as for pathological study, particularly to observe the demyelination, and possibly remyelination of the neurons.

5.4.3.1 *In vivo* z-spectra at high resolution

Chapter 4 presented measures of the z-spectrum at different power depositions (bandwidth of the pulses) and reveals regional differences in the parameters describing the CEST spectrum of the human brain in vivo [43]. Since EPI suffers from artefacts that limit effective spatial specificity, acquisition of z-spectrum via Turbo Field Echo readout (MT-TFE) give the possibility to increase the

spatial resolution. This can provide 3D z-spectra data in a reasonable imaging time at high resolution. The MT-TFE sequence thus allows MT parameters to be quantified *in vivo* with anatomical image quality, providing detailed analysis of the variation in the CEST parameters across the white matter and cortex. The next step is to improve the quantification process, as the imaging part influences the contrast in a way predicted in this chapter. Details of the study can be found in [44], and the principal results are shown in fig. 5.22. Four healthy subjects were scanned at 7T, and quantification was performed in the same way as described in chapter 4, on a set of 3 z-spectra of 16 off-frequency each with a bandwidth of 200Hz (acquired with 10 and 20 saturation pulses) and 300Hz (only acquired with 20 pulses).
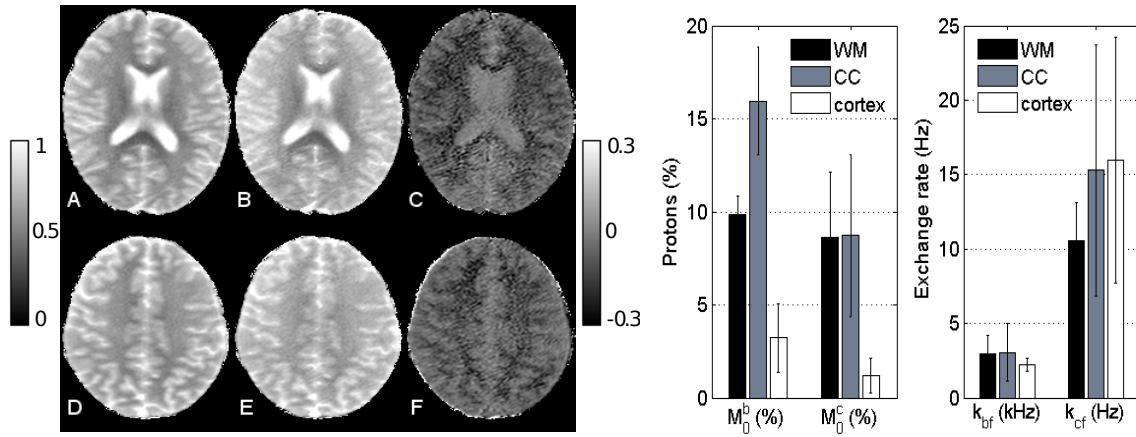

Figure 5.22: MT images at 7T showing more MT effects on negative offset (A,D: -1050Hz) compared to positive offset (B,E: +1050 Hz) with the corresponding MTasym map (C,F) calculated for $\pm$ 1050Hz using the equation 5.2. Image resolution is 1.25x1.25x1.25mm^3. The right graph shows results of the quantification of the exchange pool and the bound pool averaged over the four healthy subjects. Results are for white matter regions and cortex. While the amount of bound protons is increasing between the corpus callosum and the WM, the amount of exchangeable amide protons stays the same. No significant difference could be seen on the exchange rate. All results from [44].

The results do not quite agree with previous EPI results [42], but this is likely to be due to the effect of the additional pulses in the MT-TFE sequence and the different sensitivities to different water components of the EPI and TFE readouts. The fact that the echo time used for the MT-TFE readout is shorter ($\sim$5 ms) compared to the EPI readout ($\sim$15 ms) could in fact increase the sensitivity of the readout to protons having shorter T_2. Since the contrast in the image is not exclusively determined by the centre of the k-space, the TFE readout can also impair the obtained contrast. These effects will be investigated by including them in the 3 compartment model used to fit the data. This imaging protocol

could be applied on patients, producing the exchange parameters of specific pathological tissues. This could ultimately be used to optimize the MT imaging sequence to produce a better detectability of the tissue of interest, as for example to investigate the change of myelin in cortical lesions of MS patients.

5.4.3.2 APT and MT asymmetry imaging of NAWM in MS

A difference in contrast can clearly be seen in fig. 5.19 between the white matter and the grey matter, with darker regions (*i.e.* the white matter) indicating a stronger asymmetry in the side of the amide protons, while the grey regions (such as the grey matter and the CSF) show hardly no asymmetry. A study investigating the APT asymmetry in pathological brain tissue was performed on patients with Clinically Isolated Syndrome (CIS: a condition that is likely to lead to MS), focusing on the Normal Appearing White Matter (NAWM) only. For this purpose, patients (N=17) and age-sex matched healthy volunteers (N=15) were scanned on the 7T scanner, with protocols containing a MT-TFE sequence and a B_1 map (a complete description of the protocol is available in [1]). After segmentation of the white matter and B_1 correction, as described in 5.2.5.3, histograms of both population were compared. It was clear that the CEST effect was smaller in the NAWM of the CIS subjects (44% $\pm$ 3%) that for the healthy subjects (47% $\pm$ 2%), with a p-value inferior to 0.01. The CEST effect may thus provide additional contrast information in the white matter of MS patients, especially at 7T. A follow-up of these patients is in progress at the SPMMRC and is susceptible to provide more insight into the development of the plaques, and possibly their remyelination.

5.5 Conclusion

Simulation, imaging results and first clinical results show that the protocol designed here can be applied clinically. In particular, it gives a good contrast sensitive to myelin, the simulations shows a reasonable range of robustness to inhomogeneities, and the acquisition time is sensible for *in vivo* imaging. Further work is required, especially concerning the improvement of the sharpness of the Point Spread Function of the final MTR maps.

5.5. Conclusion

***In vivo* MT-TFE images** Standard clinical, pulsed saturation- fast field echo (FFE), MTR imaging sequences could not be used at 7T because sufficient saturation power could not be obtained without exceeding SAR limits. An MT-TFE sequence was developed to overcome this problem, and although the MTR achievable was lower at 7T than 3T, 7T provides considerably improved contrast to noise ratio in magnetization transfer imaging compared to 3T. Further work is required to evaluate the efficiency of this sequence compared to standard MTR FFE sequences at lower field. This contrast to noise ratio has been used to provide high spatial resolution MTR maps and we are not aware of any MTR maps of the brain acquired at this spatial resolution before. Fig. 5.3 shows considerable variation in the white matter MTR at 7T. The length of this 3D scan is similar to a standard T_1 weighted MPRAGE scan, repeated to provide the reference scan, so that high resolution whole brain MTR is clinically feasible at ultrahigh field. Moreover, the large CEST effect at high field makes it possible to produce maps of MT-asymmetry (APT effects) with reasonable contrast in a reasonable imaging time with this sequence. Further work based on the simulations presented in fig. 5.6 and 5.18 will allow improved image contrast to noise ratio of MT_{asym} maps.

Contrast sensitivity Depending on the structure to image/detect, the possibility to simulate the exact imaging parameters has enable the optimization of the sensitivity in the final images. This has been further improved by using higher resolution, and did not suffer from increase of T_1 at high field. Further acceleration of the sequence is possible (via parallel imaging for example), but would affect the final contrast in a non-trivial way. Based on the different simulations implemented for the design of the high-resolution MT imaging, optimization for more specific applications could be performed, both for anatomical research as well as clinical outcomes. As the scanner of choice in the clinic at the moment is the 3T, simulations with specific relaxation times, frequency offset and SNR would predict if the phenomenon seen and quantified at 7T could be viewed at 3T. Study on APT imaging have been carried out on 3T clinical scanners [81], showing a small but significant detection of the amide proton transfer, especially in brain tumor.

Bibliography

[1] A. Al-Radaideh, O. Mougin, S.-Y. Lim, C. Tench, C. Constantinescu, and P. Gowland. Magnetization transfer (mt) and endogenous chemical exchange saturation transfer (cest) effects in patients with clinically isolated syndrome. In *Proceeding of the International Society of Magnetic Resonance in Medicine, 18th Annual Meeting, Stockholm*, 2010.

[2] R. S. Balaban and T. L. Ceckler. Magnetization transfer contrast in magnetic resonance imaging. *Magn Reson Q*, 8(2):116–137, Jun 1992.

[3] E. L. Barbier, S. Marrett, A. Danek, A. Vortmeyer, P. van Gelderen, J. Duyn, P. Bandettini, J. Grafman, and A. P. Koretsky. Imaging cortical anatomy by high-resolution mr at 3.0t: detection of the stripe of gennari in visual area 17. *Magn Reson Med*, 48(4):735–738, Oct 2002.

[4] A. J. Barkovich. Magnetic resonance techniques in the assessment of myelin and myelination. *J Inherit Metab Dis*, 28(3):311–343, 2005.

[5] H. Benoit-Cattin, G. Collewet, B. Belaroussi, H. Saint-Jalmes, and C. Odet. The simri project: a versatile and interactive mri simulator. *J Magn Reson*, 173(1):97–115, Mar 2005.

[6] A. R. Brenner, J. Kürsch, and T. G. Noll. Distributed large-scale simulation of magnetic resonance imaging. *MAGMA*, 5(2):129–138, Jun 1997.

[7] H. Bridge, S. Clare, M. Jenkinson, P. Jezzard, A. J. Parker, and P. M. Matthews. Independent anatomical and functional measures of the v1/v2 boundary in human visual cortex. *J Vis*, 5(2):93–102, 2005.

[8] L. Bø, C. A. Vedeler, H. I. Nyland, B. D. Trapp, and S. J. Mørk. Subpial demyelination in the cerebral cortex of multiple sclerosis patients. *J Neuropathol Exp Neurol*, 62(7):723–732, Jul 2003.

[9] M. Cercignani, M. R. Symms, M. Ron, and G. J. Barker. 3d mtr measurement: from 1.5 t to 3.0 t. *Neuroimage*, 31(1):181–186, May 2006.

[10] S. Clare and H. Bridge. Methodological issues relating to in vivo cortical myelography using mri. *Hum Brain Mapp*, 26(4):240–250, Dec 2005.

[11] V. P. Clark, E. Courchesne, and M. Grafe. In vivo myeloarchitectonic analysis of human striate and extrastriate cortex using magnetic resonance imaging. *Cereb Cortex*, 2(5):417–424, 1992.

[12] A. Compston and A. Coles. Multiple sclerosis. *Lancet*, 372(9648):1502–1517, Oct 2008.

BIBLIOGRAPHY

[13] G. R. Davies, D. R. Altmann, A. Hadjiprocopis, W. Rashid, D. T. Chard, C. M. Griffin, P. S. Tofts, G. J. Barker, R. Kapoor, A. J. Thompson, and D. H. Miller. Increasing normal-appearing grey and white matter magnetisation transfer ratio abnormality in early relapsing-remitting multiple sclerosis. *J Neurol*, 252(9):1037–1044, Sep 2005.

[14] V. Dousset, R. I. Grossman, K. N. Ramer, M. D. Schnall, L. H. Young, F. Gonzalez-Scarano, E. Lavi, and J. A. Cohen. Experimental allergic encephalomyelitis and multiple sclerosis: lesion characterization with magnetization transfer imaging. *Radiology*, 182(2):483–491, Feb 1992.

[15] I. Drobnjak, D. Gavaghan, E. Süli, J. Pitt-Francis, and M. Jenkinson. Development of a functional magnetic resonance imaging simulator for modeling realistic rigid-body motion artifacts. *Magn Reson Med*, 56(2):364–380, Aug 2006.

[16] Y. P. Du, D. L. Parker, W. L. Davis, and G. Cao. Reduction of partial-volume artifacts with zero-filled interpolation in three-dimensional mr angiography. *J Magn Reson Imaging*, 4(5):733–741, 1994.

[17] U. Duvvuri, D. A. Roberts, J. S. Leigh, and L. Bolinger. Magnetization transfer imaging of the brain: A quantitative comparison of results obtained at 1.5 and 4.0 t. *J Magn Reson Imaging*, 10(4):527–532, Oct 1999.

[18] R. R. Edelman, S. S. Ahn, D. Chien, W. Li, A. Goldmann, M. Mantello, J. Kramer, and J. Kleefield. Improved time-of-flight mr angiography of the brain with magnetization transfer contrast. *Radiology*, 184(2):395–399, Aug 1992.

[19] D. A. Finelli, G. C. Hurst, R. P. Gullapali, and E. M. Bellon. Improved contrast of enhancing brain lesions on postgadolinium, t1-weighted spin-echo images with use of magnetization transfer. *Radiology*, 190(2):553–559, Feb 1994.

[20] L. K. Fisniku, P. A. Brex, D. R. Altmann, K. A. Miszkiel, C. E. Benton, R. Lanyon, A. J. Thompson, and D. H. Miller. Disability and t2 mri lesions: a 20-year follow-up of patients with relapse onset of multiple sclerosis. *Brain*, 131(Pt 3):808–817, Mar 2008.

[21] A. Gass, G. J. Barker, D. Kidd, J. W. Thorpe, D. MacManus, A. Brennan, P. S. Tofts, A. J. Thompson, W. I. McDonald, and D. H. Miller. Correlation of magnetization transfer ratio with clinical disability in multiple sclerosis. *Ann Neurol*, 36(1):62–67, Jul 1994.

[22] Y. Ge, R. I. Grossman, J. S. Babb, M. L. Rabin, L. J. Mannon, and D. L. Kolson. Age-related total gray matter and white matter changes in normal adult brain. part ii: quantitative magneti-

zation transfer ratio histogram analysis. *AJNR Am J Neuroradiol*, 23(8):1334–1341, Sep 2002.

[23] C. P. Gilmore, G. C. DeLuca, L. Bö, T. Owens, J. Lowe, M. M. Esiri, and N. Evangelou. Spinal cord neuronal pathology in multiple sclerosis. *Brain Pathol*, 19(4):642–649, Oct 2009.

[24] X. Golay, M. Stuber, K. Pruessmann, D. Meier, and P. Boesiger. Transfer insensitive labeling technique (tilt): application to multislice functional perfusion imaging. *Journal of magnetic resonance imaging: JMRI*, 9(3):454, 1999.

[25] S. J. Graham and R. M. Henkelman. Understanding pulsed magnetization transfer. *J Magn Reson Imaging*, 7(5):903–912, 1997.

[26] L. G. Hanson. A graphical simulator for teaching basic and advanced mr imaging techniques. *Radiographics*, 27(6):e27, 2007.

[27] H. Hanyu, T. Asano, T. Iwamoto, M. Takasaki, H. Shindo, and K. Abe. Magnetization transfer measurements of the hippocampus in patients with alzheimer's disease, vascular dementia, and other types of dementia. *AJNR Am J Neuroradiol*, 21(7):1235–1242, Aug 2000.

[28] M. A. Horsfield. Magnetization transfer imaging in multiple sclerosis. *Journal of Neuroimaging*, 15(s4):58S–67S, 2005.

[29] K. T. Jokivarsi, H. I. Gröhn, O. H. Gröhn, and R. A. Kauppinen. Proton transfer ratio, lactate, and intracellular ph in acute cerebral ischemia. *Magn Reson Med*, 57(4):647–653, Apr 2007.

[30] C. K. Jones, M. J. Schlosser, P. C. M. van Zijl, M. G. Pomper, X. Golay, and J. Zhou. Amide proton transfer imaging of human brain tumors at 3t. *Magn Reson Med*, 56(3):585–592, Sep 2006.

[31] Z. Khaleeli, D. R. Altmann, M. Cercignani, O. Ciccarelli, D. H. Miller, and A. J. Thompson. Magnetization transfer ratio in gray matter: a potential surrogate marker for progression in early primary progressive multiple sclerosis. *Arch Neurol*, 65(11):1454–1459, Nov 2008.

[32] D. Kidd, F. Barkhof, R. McConnell, P. R. Algra, I. V. Allen, and T. Revesz. Cortical lesions in multiple sclerosis. *Brain*, 122 (Pt 1):17–26, Jan 1999.

[33] R. K. Kwan, A. C. Evans, and G. B. Pike. Mri simulation-based evaluation of image-processing and classification methods. *IEEE Trans Med Imaging*, 18(11):1085–1097, Nov 1999.

[34] H. Lassmann, W. Brück, and C. F. Lucchinetti. The immunopathology of multiple sclerosis: an overview. *Brain Pathol*, 17(2):210–218, Apr 2007.

[35] T.-Q. Li, P. van Gelderen, H. Merkle, L. Talagala, A. P. Koretsky, and J. Duyn. Extensive

heterogeneity in white matter intensity in high-resolution t2*-weighted mri of the human brain at 7.0 t. *Neuroimage*, 32(3):1032–1040, Sep 2006.

[36] W. I. McDonald, A. Compston, G. Edan, D. Goodkin, H. P. Hartung, F. D. Lublin, H. F. McFarland, D. W. Paty, C. H. Polman, S. C. Reingold, M. Sandberg-Wollheim, W. Sibley, A. Thompson, S. van den Noort, B. Y. Weinshenker, and J. S. Wolinsky. Recommended diagnostic criteria for multiple sclerosis: guidelines from the international panel on the diagnosis of multiple sclerosis. *Ann Neurol*, 50(1):121–127, Jul 2001.

[37] R. C. Mehta, G. B. Pike, and D. R. Enzmann. Magnetization transfer mr of the normal adult brain. *AJNR Am J Neuroradiol*, 16(10):2085–2091, 1995.

[38] R. C. Mehta, G. B. Pike, and D. R. Enzmann. Measure of magnetization transfer in multiple sclerosis demyelinating plaques, white matter ischemic lesions, and edema. *AJNR Am J Neuroradiol*, 17(6):1051–1055, 1996.

[39] R. Mekle, A. F. Laine, and E. X. Wu. Combined mr data acquisition of multicontrast images using variable acquisition parameters and k-space data sharing. *IEEE Trans Med Imaging*, 22(7):806–823, Jul 2003.

[40] E. Melhem, H. Jara, and E. Yucel. Multislice T1-weighted hybrid RARE in CNS imaging: assessment of magnetization transfer effects and artifacts. *Journal of magnetic resonance imaging: JMRI*, 6(6):903, 1996.

[41] J. P. Mottershead, K. Schmierer, M. Clemence, J. S. Thornton, F. Scaravilli, G. J. Barker, P. S. Tofts, J. Newcombe, M. L. Cuzner, R. J. Ordidge, W. I. McDonald, and D. H. Miller. High field mri correlates of myelin content and axonal density in multiple sclerosis–a post-mortem study of the spinal cord. *J Neurol*, 250(11):1293–1301, Nov 2003.

[42] O. E. Mougin, R. C. Coxon, A. Pitiot, and P. A. Gowland. Magnetization transfer phenomenon in the human brain at 7 t. *Neuroimage*, 49(1):272–281, Jan 2010.

[43] O. E. Mougin, J. Dixon, I. Donaldson, E. Tallantyre, N. Evangelou, and P. A. Gowland. High resolution magnetization transfer imaging at 7t: detection of cortical lesions in ms patient. In *Proceeding of the International Society of Magnetic Resonance in Medicine, 18th Annual Meeting, Stockholm*, 2010.

[44] O. E. Mougin and P. A. Gowland. Quantification of the magnetization transfer phenomenon in the human head at 7t. In *Proceeding of the International Society of Magnetic Resonance in*

Medicine, 18th Annual Meeting, Stockholm, 2010.

[45] O. E. Mougin, P. A. Gowland, and A. Pitiot. Vermagris, a versatile and realistic magnetic resonance imaging simulator. In *MIUA*, 2010.

[46] O. E. Mougin, A. Pitiot, and P. A. Gowland. Detection of cortical layers via magnetization transfer imaging at 7t. In *Proceeding of the International Society of Magnetic Resonance in Medicine, 18th Annual Meeting, Stockholm*, 2010.

[47] J. P. Mugler and J. R. Brookeman. Three-dimensional magnetization-prepared rapid gradient-echo imaging (3d mp rage). *Magn Reson Med*, 15(1):152–157, Jul 1990.

[48] J. P. Mugler, F. H. Epstein, and J. R. Brookeman. Shaping the signal response during the approach to steady state in three-dimensional magnetization-prepared rapid gradient-echo imaging using variable flip angles. *Magn Reson Med*, 28(2):165–185, Dec 1992.

[49] J. Pekar, P. Jezzard, D. A. Roberts, J. S. Leigh, J. A. Frank, and A. C. McLaughlin. Perfusion imaging with compensation for asymmetric magnetization transfer effects. *Magn Reson Med*, 35(1):70–79, Jan 1996.

[50] J. Pfeuffer, P.-F. van de Moortele, E. Yacoub, A. Shmuel, G. Adriany, P. Andersen, H. Merkle, M. Garwood, K. Ugurbil, and X. Hu. Zoomed functional imaging in the human brain at 7 tesla with simultaneous high spatial and high temporal resolution. *Neuroimage*, 17(1):272–286, Sep 2002.

[51] A. Pitiot, J. Totman, and P. Gowland. Null point imaging: a joint acquisition/analysis paradigm for mr classification. *Med Image Comput Comput Assist Interv*, 10(Pt 1):759–766, 2007.

[52] J. Rademacher, V. Engelbrecht, U. Bürgel, H. Freund, and K. Zilles. Measuring in vivo myelination of human white matter fiber tracts with magnetization transfer mr. *Neuroimage*, 9(4):393–406, Apr 1999.

[53] B. H. Ridha, M. R. Symms, D. J. Tozer, K. C. Stockton, C. Frost, M. M. Siddique, E. B. Lewis, D. G. MacManus, P. A. Boulby, G. J. Barker, M. N. Rossor, N. C. Fox, and P. S. Tofts. Magnetization transfer ratio in alzheimer disease: comparison with volumetric measurements. *AJNR Am J Neuroradiol*, 28(5):965–970, May 2007.

[54] M. D. Robson, J. C. Gore, and R. T. Constable. Measurement of the point spread function in mri using constant time imaging. *Magn Reson Med*, 38(5):733–740, Nov 1997.

[55] S. Ropele, M. Filippi, P. Valsasina, T. Korteweg, F. Barkhof, P. S. Tofts, R. Samson, D. H. Miller,

and F. Fazekas. Assessment and correction of b1-induced errors in magnetization transfer ratio measurements. *Magn Reson Med*, 53(1):134–140, Jan 2005.

[56] M. Rovaris, F. Agosta, M. P. Sormani, M. Inglese, V. Martinelli, G. Comi, and M. Filippi. Conventional and magnetization transfer mri predictors of clinical multiple sclerosis evolution: a medium-term follow-up study. *Brain*, 126(Pt 10):2323–2332, Oct 2003.

[57] M. Rovaris, G. Iannucci, M. Cercignani, M. P. Sormani, N. D. Stefano, S. Gerevini, G. Comi, and M. Filippi. Age-related changes in conventional, magnetization transfer, and diffusion-tensor mr imaging findings: study with whole-brain tissue histogram analysis. *Radiology*, 227(3):731–738, Jun 2003.

[58] K. Schmierer, F. Scaravilli, D. R. Altmann, G. J. Barker, and D. H. Miller. Magnetization transfer ratio and myelin in postmortem multiple sclerosis brain. *Ann Neurol*, 56(3):407–415, Sep 2004.

[59] K. Schmierer, D. J. Tozer, F. Scaravilli, D. R. Altmann, G. J. Barker, P. S. Tofts, and D. H. Miller. Quantitative magnetization transfer imaging in postmortem multiple sclerosis brain. *J Magn Reson Imaging*, 26(1):41–51, Jul 2007.

[60] K. Schmierer, C. A. M. Wheeler-Kingshott, D. J. Tozer, P. A. Boulby, H. G. Parkes, T. A. Yousry, F. Scaravilli, G. J. Barker, P. S. Tofts, and D. H. Miller. Quantitative magnetic resonance of postmortem multiple sclerosis brain before and after fixation. *Magn Reson Med*, 59(2):268–277, Feb 2008.

[61] A. Simmons, S. R. Arridge, G. J. Barker, and S. C. Williams. Simulation of mri cluster plots and application to neurological segmentation. *Magn Reson Imaging*, 14(1):73–92, 1996.

[62] J. G. Sled, I. Levesque, A. C. Santos, S. J. Francis, S. Narayanan, S. D. Brass, D. L. Arnold, and G. B. Pike. Regional variations in normal brain shown by quantitative magnetization transfer imaging. *Magn Reson Med*, 51(2):299–303, Feb 2004.

[63] J. G. Sled and G. B. Pike. Quantitative imaging of magnetization transfer exchange and relaxation properties in vivo using mri. *Magn Reson Med*, 46(5):923–931, Nov 2001.

[64] A. W. Song, S. D. Wolff, R. S. Balaban, and P. Jezzard. The effect of off-resonance radiofrequency pulse saturation on fmri contrast. *NMR Biomed*, 10(4-5):208–215, 1997.

[65] P. Z. Sun, C. T. Farrar, and A. G. Sorensen. Correction for artifacts induced by b(0) and b(1) field inhomogeneities in ph-sensitive chemical exchange saturation transfer (cest) imaging. *Magn*

Reson Med, 58(6):1207–1215, Dec 2007.

[66] P. Z. Sun, J. Zhou, J. Huang, and P. van Zijl. Simplified quantitative description of amide proton transfer (apt) imaging during acute ischemia. *Magn Reson Med*, 57(2):405–410, Feb 2007.

[67] I. Tkác, G. Oz, G. Adriany, K. U?urbil, and R. Gruetter. In vivo 1h nmr spectroscopy of the human brain at high magnetic fields: metabolite quantification at 4t vs. 7t. *Magn Reson Med*, 62(4):868–879, Oct 2009.

[68] P. Tofts, S. Steens, M. Cercignani, F. Admiraal-Behloul, P. Hofman, M. van Osch, W. Teeuwisse, D. Tozer, J. van Waesberghe, R. Yeung, et al. Sources of variation in multi-centre brain mtr histogram studies: body-coil transmission eliminates inter-centre differences. *Magnetic Resonance Materials in Physics, Biology and Medicine*, 19(4):209–222, 2006.

[69] D. J. Tozer, G. R. Davies, D. R. Altmann, D. H. Miller, and P. S. Tofts. Correlation of apparent myelin measures obtained in multiple sclerosis patients and controls from magnetization transfer and multicompartmental t2 analysis. *Magn Reson Med*, 53(6):1415–1422, Jun 2005.

[70] M. A. van Buchem, S. C. Steens, H. A. Vrooman, A. H. Zwinderman, J. C. McGowan, M. Rassek, and V. Engelbrecht. Global estimation of myelination in the developing brain on the basis of magnetization transfer imaging: a preliminary study. *AJNR Am J Neuroradiol*, 22(4):762–766, Apr 2001.

[71] M. Van Der Knaap and J. Valk. *Magnetic resonance of myelination and myelin disorders.* Springer, 2005.

[72] R. L. Vold, R. R. Vold, and H. E. Simon. Errors in measurements of transverse relaxation rates. *Journal of Magnetic Resonance*, 11:283–298, 1973.

[73] L. L. Wald, B. Fischl, and B. R. Rosen. *High-Resolution and Microscopic Imaging at High Field*, volume 26, chapter 11, pages 343–366. Springer, 2006.

[74] K. M. Ward, A. H. Aletras, and R. S. Balaban. A new class of contrast agents for mri based on proton chemical exchange dependent saturation transfer (cest). *Journal of Magnetic Resonance*, 143(1):79 – 87, 2000.

[75] K. P. Whittall, A. L. MacKay, D. A. Graeb, R. A. Nugent, D. K. Li, and D. W. Paty. In vivo measurement of t2 distributions and water contents in normal human brain. *Magn Reson Med*, 37(1):34–43, Jan 1997.

[76] S. D. Wolff and R. S. Balaban. Magnetization transfer contrast (mtc) and tissue water proton

relaxation in vivo. *Magn Reson Med*, 10(1):135–144, Apr 1989.

[77] P. J. Wright, O. E. Mougin, J. J. Totman, A. M. Peters, M. J. Brookes, R. Coxon, P. E. Morris, M. Clemence, S. T. Francis, R. W. Bowtell, and P. A. Gowland. Water proton t1 measurements in brain tissue at 7, 3, and 1.5 t using ir-epi, ir-tse, and mprage: results and optimization. *MAGMA*, 21(1-2):121–130, Mar 2008.

[78] V. L. Yarnykh. Pulsed z-spectroscopic imaging of cross-relaxation parameters in tissues for human mri: theory and clinical applications. *Magn Reson Med*, 47(5):929–939, May 2002.

[79] V. L. Yarnykh. Actual flip-angle imaging in the pulsed steady state: a method for rapid three-dimensional mapping of the transmitted radiofrequency field. *Magn Reson Med*, 57(1):192–200, Jan 2007.

[80] V. L. Yarnykh and C. Yuan. Cross-relaxation imaging reveals detailed anatomy of white matter fiber tracts in the human brain. *Neuroimage*, 23(1):409–424, Sep 2004.

[81] J. Zhou, J. O. Blakeley, J. Hua, M. Kim, J. Laterra, M. G. Pomper, and P. C. M. van Zijl. Practical data acquisition method for human brain tumor amide proton transfer (apt) imaging. *Magn Reson Med*, 60(4):842–849, Oct 2008.

[82] J. Zhou, B. Lal, D. A. Wilson, J. Laterra, and P. C. M. van Zijl. Amide proton transfer (apt) contrast for imaging of brain tumors. *Magn Reson Med*, 50(6):1120–1126, Dec 2003.

[83] J. Zhou, J.-F. Payen, and P. C. M. van Zijl. The interaction between magnetization transfer and blood-oxygen-level-dependent effects. *Magn Reson Med*, 53(2):356–366, Feb 2005.

[84] J. Zhou, J.-F. Payen, D. A. Wilson, R. J. Traystman, and P. C. M. van Zijl. Using the amide proton signals of intracellular proteins and peptides to detect ph effects in mri. *Nat Med*, 9(8):1085–1090, Aug 2003.

CONCLUSION

The work presented in this thesis investigates the implementation and use of a variety of quantitative sequences. Modelling of the complex MPRAGE (or IR-TFE) sequence is presented and used to provide similar measurements to the more traditional IR-EPI method, but with higher spatial resolution. Results obtained via the IR-TSE method (*i.e.* based on a Turbo Spin Echo sequence) show a reduced T_1 in the white matter, probably due to magnetisation transfer saturation due to the use of multiple refocusing pulses. Quantitative imaging provides more robust information than simple anatomical imaging, especially at high field, due to the possibility of detecting smaller changes in the observed tissues. The measure was robust enough to apply it to various applications, such as detection of the asymmetry in the cortico-spinal tract due to handedness, or detection of abnormal T_1 values inside the normal appearing white matter of CIS patients. Several other studies (conducted in the SPMMRC) are using this protocol, such as evolution of the T_1 with age as well as the effect of premature delivery on brain development. Further improvements of the fitting procedure could lead to smaller error with lower noise level, making it appropriate for lower field strength studies as well.

The investigation of the magnetization transfer phenomenon at high field was carried out via z-spectrum acquisition in vivo at 7T, within SAR limits. It showed surprising results at the level of the amide protons, and necessitated further investigation. A three compartment model was proposed and developed to measure chemical exchange and magnetization transfer parameters from the z-spectrum data. Quantitative APT results varied between the corpus callosum and other white matter structures, suggesting that quantitative APT imaging could be used as a method of measuring myelination. Exchange rate and amount of protons in the different pools could be resolved via the

numerical model implemented, but further improvement is possible via optimization of the acquisition, especially the different saturation parameters. The long timing of the sequence, together with the long post-processing quantification, restricts at the moment this protocol to research investigations. However a more clinically friendly protocol was desired to investigate the efficiency of the method, and has been presented in the chapter 5.

Based on the IR-TFE protocol used in the chapter 3, a MT-TFE protocol was designed and tested on healthy volunteers. Simulation, imaging results and first clinical results show that the proposed protocol can be applied clinically. In particular, it gives a good contrast sensitive to myelin, the simulations show a reasonable range of robustness to inhomogeneities, and the acquisition time is sensible for clinical *in vivo* imaging. The bandwidth of the pulses used in the saturation train is particularly important, both in terms of contrast but also in terms of robustness to inhomogeneities. While the effect of reasonable inhomogeneities has been minimized via simulation, further work is required, especially concerning the improvement of the sharpness of the Point Spread Function of the final MTR maps. The use of a 32 channel receiver coil could probably improve the detectability of abnormality inside cortex of MS patients, but additional optimization specifically designed to increase the contrast of cortical grey matter lesions compared to normal grey matter will further improve its use in diagnosis.